Contribution of autonomous underwater gliders to monitor suspended particulates matter dynamics in the coastal zone

Mathieu Gentil

THÈSE

Pour obtenir le grade de

Docteur

Délivré par

UNIVERSITE DE PERPIGNAN VIA DOMITIA

Préparée au sein de l'école doctorale

Energie et Environnement (ED 305)

Et de l'unité de recherche

CEFREM UMR5110

Spécialité : **Océanologie**

Présentée par

Mathieu GENTIL

Contribution of autonomous underwater glider observations to monitor hydro-sedimentary processes in the coastal zone

Soutenue le **15/12/2021** devant le jury composé de

M. Jean-Luc DÉVENON, Professeur, Univ. Aix-Marseille	*Rapporteur*
M. Pierre GARREAU, Chercheur-HDR, IFREMER	*Rapporteur*
Mme. Anne PETRENKO, Maître de Conférences-HDR, Univ. Aix-Marseille	*Examinatrice*
M. Frédéric MARIN, Directeur de Recherche, IRD	*Examinateur*
M. Wolfgang LUDWIG, Professeur, Univ. de Perpignan Via Domitia	*Examinateur*
M. Xavier DURRIEU de MADRON, Directeur de Recherche, CNRS	*Directeur de Thèse*
M. François BOURRIN, Maître de Conférences-HDR, Univ. de Perpignan Via Domitia	*Co-directeur*

Remerciements

"***On ne va jamais aussi loin que lorsqu'on ne sait pas où l'on va".***

(Christophe Colomb)

Je profite de ces quelques lignes au début de ce manuscrit pour remercier toutes les personnes avec qui j'ai pu collaborer de près ou de loin.

Le présent travail a vu le jour grâce au financement de la Région Occitanie et de l'Université de Perpignan Via Domitia, je tiens donc à remercier ces deux institutions. Un grand merci aux membres du jury, en particulier à MM. Jean-Luc Dévenon et Pierre Garreau qui ont accepté de rapporter ce manuscrit. Vos commentaires et suggestions m'ont été d'une grande utilité.

Un immense merci à mes directeurs de thèse : Xavier et François. Vous m'avez offert une opportunité unique et taillée sur-mesure à mes envies d'océanographie physique de terrain. Merci de m'avoir permis de partir en mer à plusieurs reprises ainsi qu'en conférence en Europe et Outre-Atlantique. Merci à vous deux pour votre patience, votre disponibilité durant nos longues réunions où j'ai appris le métier de chercheur à votre contact. Au-delà de nos échanges scientifiques, vos qualités humaines m'ont permis de traverser ces trois années de thèse avec plaisir. Ce n'est que le début d'une longue collaboration au Mexique et ailleurs !

Je tiens à remercier les nombreuses personnes ayant nourri ma réflexion scientifique sur ce travail : Gaël, Romaric, Pierre, Lucas, Travis, Félix, France, Ivane, Serge, Pere, Serge, Sébastien (et d'autres que j'ai sûrement oublié…). Merci à Claude de m'avoir consacré tant de temps en cette dernière année de thèse pour suivre mon travail et à toi Frédéric pour tes conseils avisés sur mes travaux et perspectives de recherche.

Merci aux membres d'équipage et scientifique des navires sur lesquels j'ai eu la chance d'embarquer ces dernières années (le *TéThys II*, le *Pourquoi Pas* et le *Thalassa*). Mention spéciale à Micka pour nos discussions trail, à Nagib la force tranquille du quart, à Romain fidèle compagnon de chambrée et enfin à Paulo pour nous rappeler que la Méditerranée peut nous cueillir sans prévenir !

Merci à tous les membres du laboratoire pour leur accueil chaleureux. Un grand merci à toute l'équipe administrative, toujours bienveillante pour m'accompagner dans ce "millefeuille" si complexe. Spéciale dédicace à toi mon Bruno, ou dirai-je le "Messi Catalan" qui m'a enseigné les ficelles du métier avec roublardise. On ne saura définitivement jamais qui était responsable de ces échantillons… mais une chose est sûre le vin est arrivé à bon port !

Merci à l'équipe des docs du CEFREM, aux anciens comme aux nouveaux, Eléonore, Camille, Méryl, Florian, Margot, Mégane, Pierrick et Lisa pour votre bonne humeur et nos échanges si nombreux à la machine à café qui nous aura tous mis sur la paille ! Spéciale dédicace à Pierre le kanak, l'ouvreur des spots, l'amoureux de l'Ouille jamais avare en distribution de "documents de travail", et à Sébi le dauphin, célèbre filtreur des profondeurs de la côte catalane.

Je remercie aussi le Canet Surf Crew, ma famille catalane, avec qui j'ai partagé un bon nombre de sessions m'ayant apporté bien-être et sérénité. Un immense merci à vous deux Emile et Pierrot, les aficionados de la première heure, les lascars de la Méd et aujourd'hui des amis infaillibles. Je repense avec nostalgie à nos soirées sans fins à parler de tout et de rien pour toujours revenir aux fondamentaux : "On surf demain ! Session le matin, midi ou soir ? Les 3 évidemment, je pense même qu'on peut en caler une quatrième !"

Un grand merci à ma famille (mes frères et mes parents) présente depuis le début et qui m'a toujours soutenu dans mes choix afin de faire ce qui me plaisait. Mention spéciale à "p'tit gris" nouvelle venue dans cette famille, et qui par sa joie de vivre m'a permis de décompresser (et non Florian ce n'est pas un caniche !).

Enfin, même si nos chemins ont divergé, un immense merci à toi Karine, ma moitié durant de nombreuses années, pour m'avoir soutenu durant cette thèse et avant, ce qui m'a donné suffisamment de confiance pour toujours aller plus loin.

Table of Contents

Chapter 1.

General introduction

Table of Contents

Table of figures

Index of tables

1.1. The coastal ocean

1.1.1. Definition

The coastal ocean, at the interface between continents and deep oceans, are complex areas featuring diverse bio-physical-geomorphological environments, where land, ocean, and atmosphere strongly interact (Cocquempot et al., 2019; Gattuso et al., 2009). Due to their complexity, multiple definitions of the coastal ocean can be found through the bibliography (Baschek et al., 2017; Davis and Ethington, 1976; Lorenzoni and Benway, 2013; Petihakis et al., 2018). This study considers the coastal ocean, as the continental shelf waters located between the surface and 200 m depths, from the shoreline to the outer edge of the continental margin.

1.1.2. Key features

These small regions (~7% of the total ocean, i.e., 26×10^6 km^2) play a disproportionately large role for humanity, with numerous strategic economic and ecological stakes (Cocquempot et al., 2019; Schofield et al., 2015). They are the receptacle areas for land-derived organic, inorganic, natural, and anthropogenic material (as sediments, dissolved and particulate nutrients). They act as a sink and store a part of the material received, while under some conditions, they can be a source of material for the open ocean. Coastal areas play a main role in the sequestration of chemical elements (carbon), the sedimentary budget of continental margins, as well as the structure of benthic habitats (Durrieu de Madron et al., 2008). Although relatively small, they represent 10% up to 30% of global ocean primary productivity (Salgado-Hernanz et al., 2021), 80% of organic matter burial, 75–90% of the oceanic sink of suspended river load (Gattuso et al., 1998), and 90% of the world fishery catches (Pauly et al., 2002; Pauly and Christensen, 1995). Furthermore, about ~35% of the world's population lives within 100 km of the coastline (Vitousek et al., 1997), and this percentage is expected to grow to 75% over the next few decades. The increase of the human coastal zone

population brings a greater demand for food, marine resources, recreational and commercial uses of the shore, increasing pressures and environmental impacts (De Souza et al., 2003; Rockström et al., 2009).

1.1.3. Observation challenges

An integrated management and sustainable exploitation of coastal ocean resources rely on a detailed knowledge of the functioning of the ecosystem and the main factors affecting its variability and its state of health. An ability to observe and forecast the coastal ocean and its links to weather, climate and biogeochemical phenomena is required to reduce the environmental impact (Tanhua et al., 2019). In this context, scientific interest in coastal ocean observation is growing, as shown by the exponential increase in publications from 1950 to 2020 (Figure 1.1). A search in "all fields" of Pubmed (https://pubmed.ncbi.nlm.nih.gov/) including the words "coastal ocean" and "observation" showed 1 publication in 1952, reaching up to 1194 in 2020. This growing interest is also observed in the public policies as shown by the recent proclamation by the United Nations of a Decade of

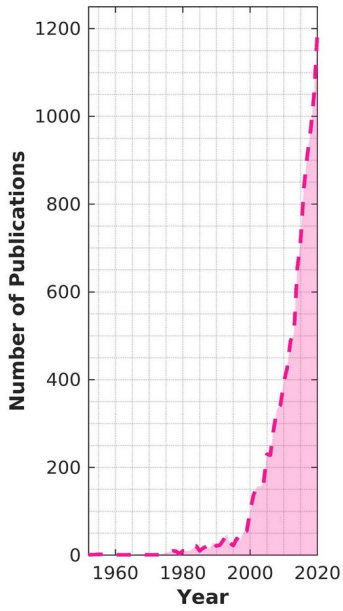

Figure 1.1: Number of publications per year for the period 1952-2020 including the words "coastal ocean" and "observation", from the pubmed database.

Ocean Science for Sustainable Development (2021–2030) (https://ioc.unesco.org/ocean-decade). International efforts, such as the Global Ocean Observing System (GOOS), lead actions towards a more integrated and sustainable ocean observing system (Visbeck, 2018). These efforts are also declined at the regional scale from MONGOOS (Mediterranean Oceanography Network for the Global Ocean Observing System) or EuroGOOS, involved in several programs such as JERICO (Joint European Research Infrastructure network for Coastal Observatories, www.jerico-ri.eu), which aims to structure the observations for the coastal area at the European scale. In addition, a legislative framework is also applied, as in Europe from 2008, with Marine Strategy Framework Directive (DCSMM) to establish a framework for community action in the field of marine

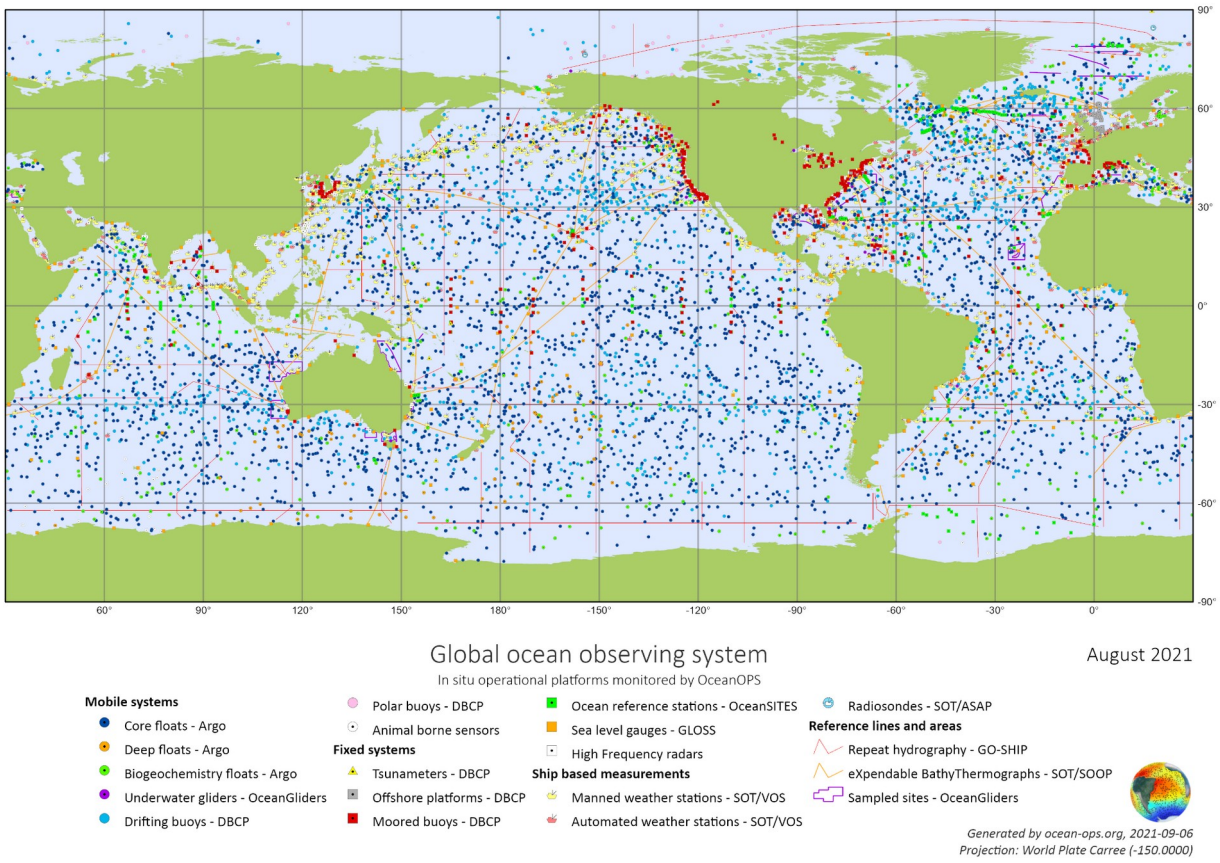

Figure 1.2: Summary map of all available *in-situ* data as reported by JCOMMOPS in August 2021 (see http://www.jcommops.org/).

environmental policy. These organizations, programs, and directives tend to federate national scientific orientations around common observation objectives concerning fundamental aspects as the actual responses of coastal marine ecosystems to anthropic and climate forcings.

Monitoring the ocean in four dimensions and across disciplines, therefore, requires the integration of data collected from a multiplatform system. Tremendous progress was made in our ability to observe the ocean globally between the creation of GOOS in 1991 and the second international Conference on Ocean Observing held in September 2009 (Ocean Obs'09) (Anderson, 2010; Moltmann et al., 2019). Currently, GOOS comprises observing efforts carried out by ships, moorings, floats, surface drifters, marine mammals, and sea-level observatories (e.g., Fig. 1.2). Despite the development of capacity and associated funding for the ocean observing system over the past 30 years, our knowledge of coastal ocean dynamics remains partial. Ocean processes operate on time scales from fractions of a second to multiple decades temporally and from millimeters to thousands of kilometers spatially (Ruhl et al., 2011) (Fig. 1.3). The interlocking spatial and temporal scales of the processes make sampling particularly challenging. Furthermore, anthropogenic forcing contributes an added layer of complexity. Depending on the time—and spatial scale of processes involved in coastal zones, different types of observations are required to monitor and understand the response of coastal zones to the forcing agents. In this thesis, we focus on the hydro-sedimentary processes and issues, especially those related to the suspended particulate matter (SPM) on continental shelves (section 1.2).

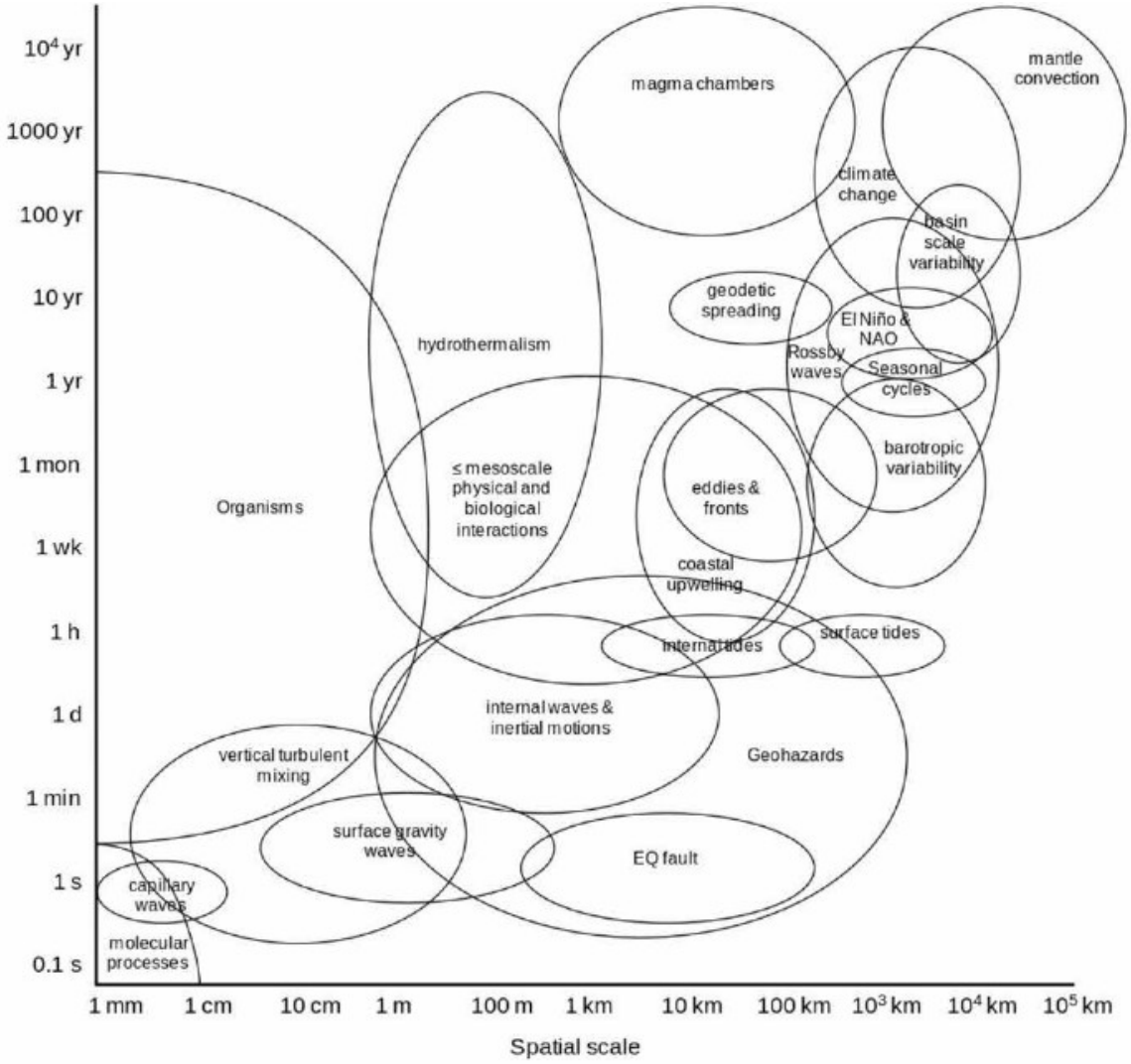

Figure 1.3: Processes in the ocean happen on a number of varying temporal and spatial scales, and these events often affect one other, from Ruhl et al. (2011).

1.2. Case of SPM dynamics on continental shelves

1.2.1. Processes

Sediment transport on continental margins depends on a wide variety of processes, summarized in the continuum land-sea by the Figure 1.4.

SPM inputs on the coastal zone, due to the erosion of the watersheds, are dominated by the balance between gravity and friction processes. The former acts to keep sediment immobile, while the latter, represents the turbulent shear that acts to keep sediment in suspension in the water

column. At the continent-ocean interface, SPM is transported by hydrodynamic agents, through river plumes, bottom nepheloid layers, and ROFI (region of freshwater influence) (Fig. 1.4). The transported materials are mainly of two types: (i) coarse sediments or sands which have a non-cohesive character and (ii) fine sediments which have a cohesive character.

On continental margins, the sand, mainly transported by "bedload", quickly settles in the estuarine zone or is generally transported along the shore in the littoral zone, where it aliments the local beach (Many, 2016). The littoral zone is governed locally by wind, wave, tidal forcing, and the Coriolis force (Ouillon, 2018). However, it is generally assumed that the resuspension and transport of sand are limited for depths smaller than 10 m (Durand, 1999; Sabatier et al., 2005), because waves and currents action drastically decreases with the increase of depth, except for extreme events, such as storm and flood.

The fine particles undergo significant changes when passing from the fluvial environment to the marine environment which affects their fate in coastal areas. They are transformed into flocs/aggregates (Fig. 1.4) of various sizes and shapes under the effect of salinity, concentration, turbulence, and organic matter content (Maggi, 2005; Many et al., 2019). The phenomena of flocculation/aggregation change the properties of SPM by modifying their effective density but also their settling velocity (Many et al., 2019). The fine-grained sediment is commonly transported over depth greater than 10 m within the nepheloid layer (bottom or intermediate) and river plume, before settling with the decrease of hydrodynamic forcing (Many, 2016). However, on the continental shelf multiple processes may lead to resuspension and advection of recent sediment deposits such as the intrusion of mesoscale eddies, storms, cascading of dense water, near-bottom currents, etc. (Nittrouer and Wright, 1994; Ouillon, 2018). In some cases, depending on the location over the shelf, suspended particles can then eventually be exported off-shelf (Fig 1.4) by gravity flow, downwelling, or advection.

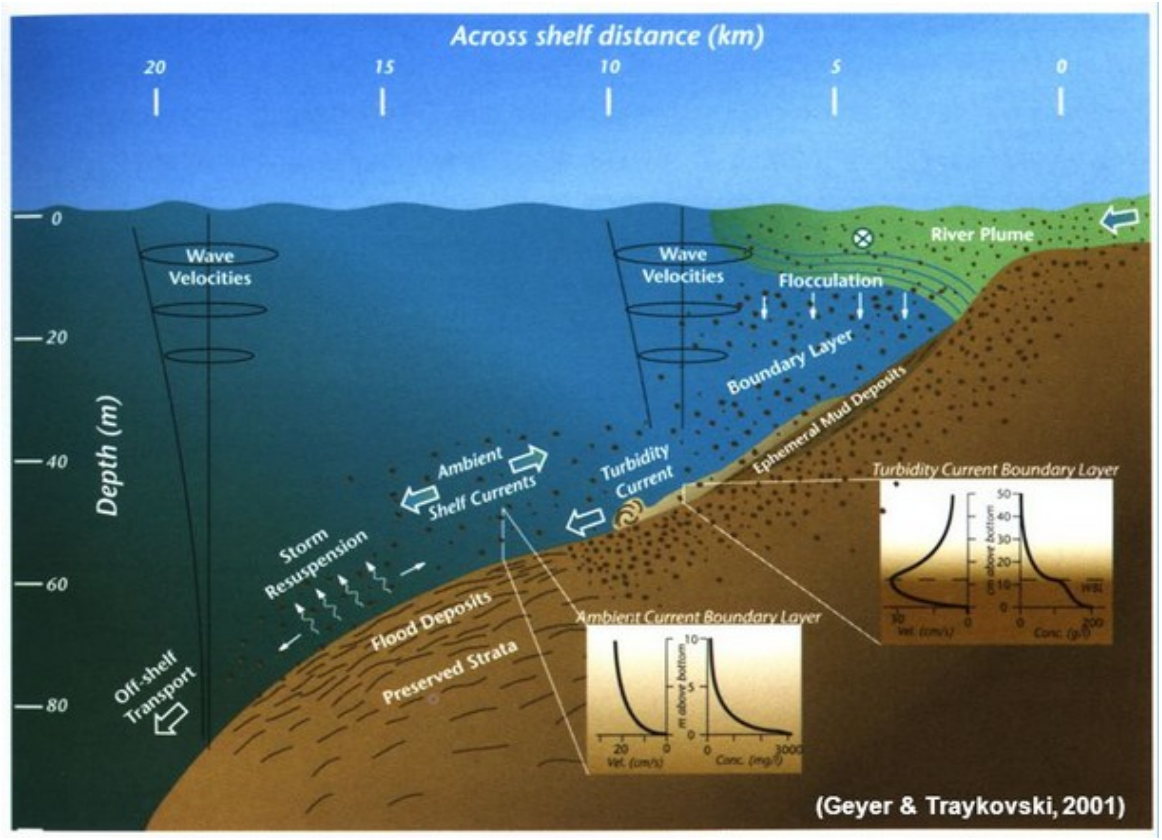

Figure 1.4: Schematic of the sediment transport processes on the shelf from Geyer et al, (2001).

1.2.2. Issues

The quantification of SPM and the investigation of its dynamics are of major importance to understand water quality, carbon flux, and ecosystem dynamics among other ocean processes in the coastal ocean (Miles et al., 2021). Like the processes shown in Figure 1.3, SPM dynamics presents very disparate spatiotemporal scales highlighted by the following examples.

Rivers are major vectors of (micro/macro) waste and chemical contaminants to the coastal environment. Contaminants transported by rivers are either in dissolved form or adsorbed onto SPM which plays an important role in determining their ultimate fate (Balls, 1986). The SPM sedimentation can lead to the trapping of some contaminants in the sediment layers. This trapping may only be temporary as resuspension phenomena may occur, under the action of sea currents and waves, remobilizing these contaminated sediments. When the sediment is in suspension, the

contaminants can dissociate from it by physicochemical processes and become free in the water column, thus being more easily dispersed and more easily assimilated by living organisms (Brown et al., 2019). Understanding the SPM transfer from sources (catchment areas) to sinks (deep basins) is also essential to better understanding the formation and evolution of new sediment strata on continental shelves. Sedimentary strata are the main source of geo-historical information. Sediment records can be used to analyze the variability of past environmental conditions and their processes over a large time scale to better understand the modern dynamics and predict future evolution, such as the impact of sea-level rise (Grant et al., 2019; Guilderson et al., 2000).

These examples show that operational monitoring of SPM dynamics is essential to capture actual and long-term issues, such as the dispersion of land-derived chemical elements (contaminants), and the evolution of continental shelf morphology in the coastal ocean.

1.3. A science field that evolves with technology

1.3.1. Historic evolution

Investigating coastal physical processes and changes is strongly based on the application of methods such as field measurements, remote sensing, and numeric modeling. They all contribute in a complementary way to better characterize and understand hydrodynamics and sediment transport processes in continental margins. The objective of this section is to provide an overview of technology evolution in research and applications in hydro-sedimentary studies. For this purpose, 3 major periods are defined to trace the main technological and instrumental developments (for a detailed overview of each process in the main geomorphological units, see the review by Ouillon [2018]).

(i) 1930s to 1960s: The ocean is a hostile environment, difficult to access, and opaque. The properties of the ocean have long remained mysterious. For example, the first large-scale expedition

organized primarily to gather physical oceanographic data was carried out in the Atlantic Ocean from 1925 to 1927 (Talley, 2011). In this period, ocean observations were extremely rare. In the coastal zone, the hydro-sedimentary mechanisms and processes were mainly approached from dimensional analyses, theoretical and/or statistical developments, and experiments in channels (Ouillon, 2018). As highlighted by Ouillon (2018), many of the theories developed in this period are still used in the models of the sediment transport as the Shield critical shear stress for non-cohesive sediments transport (Shields, 1936); the Rouse's profiles for suspension flux (Rouse, 1937); bedload estimate from the excess of shear stress (Meyer-Peter and Müller, 1948) or the formulae of total sediment transport (Ackers and White, 1973; Engelund and Hansen, 1967).

(ii) 1970s to 1990s: These two decades are marked by important technological developments that lead to fast progress in sediment dynamics and processes involved. The development of coastal buoys (Fig. 1.5b), moorings, and benthic tripods equipped with a suite of new sensors such as current meters using acoustic Doppler principles, CTD (Conductivity, Temperature, Depth) probes, and turbidimeters or optical backscattering sensors allowed to acquire measurements at fixed geographic locations and with instruments mounted at fixed depths. Also, the possibility of continuously measuring the vertical properties of the ocean was a real revolution. This came with the development of the bathythermograph, and then the bathysonde for shipboard measurements in the 1970s. The bathysonde is an electronic system for continuous acquisition of *in-situ* measurements of ocean parameters (Fig. 1.5c). They are operated in research vessels, which are important components of the ocean observing system (Fig. 1.5a), in particular for multidisciplinary studies by allowing multivariate sampling (CTD deployment, turbidimeters, ADCP, water sampling, coring, etc.). This period is also marked by the first oceanographic measurements of satellites (starting in the 1970s) (Fig. 1.5d), and high-frequency radars (starting at the end of 1990s) (Fig. 1.5e) to measure the geophysical quantities at the sea surface, as the SPM concentration and

currents. These surface measurements can describe with a high spatial resolution and over regional scales the SPM dynamics in the river plumes and coastal areas (Amos and Topliss, 1985; Bishop, 1986) or to determine shallow water bathymetry (Lyzenga, 1978). Research vessels, HF radars, and satellite measurements allowed to address the spatial component compared to buoy and moorings. These technological developments allowed to transpose studies carried out in the laboratory into the real environment to estimate the sediment dynamics. Many of the observation techniques developed in these decades are still widely used in coastal zone monitoring, such as benthic tripods to measure hydro-sedimentary processes in the bottom boundary layer (Cacchionne et al., 2006; Stenberg, 2005).

Finally, from the 1980s the "computer boom" began with the emergence of the first microprocessors, which allowed the development of 1D numerical models to study hydro-sedimentary processes in the bottom boundary layer (Glenn and Grant, 1987; Sheng, 1986; Styles and Glenn, 2000; Weatherly and Martin, 1978).

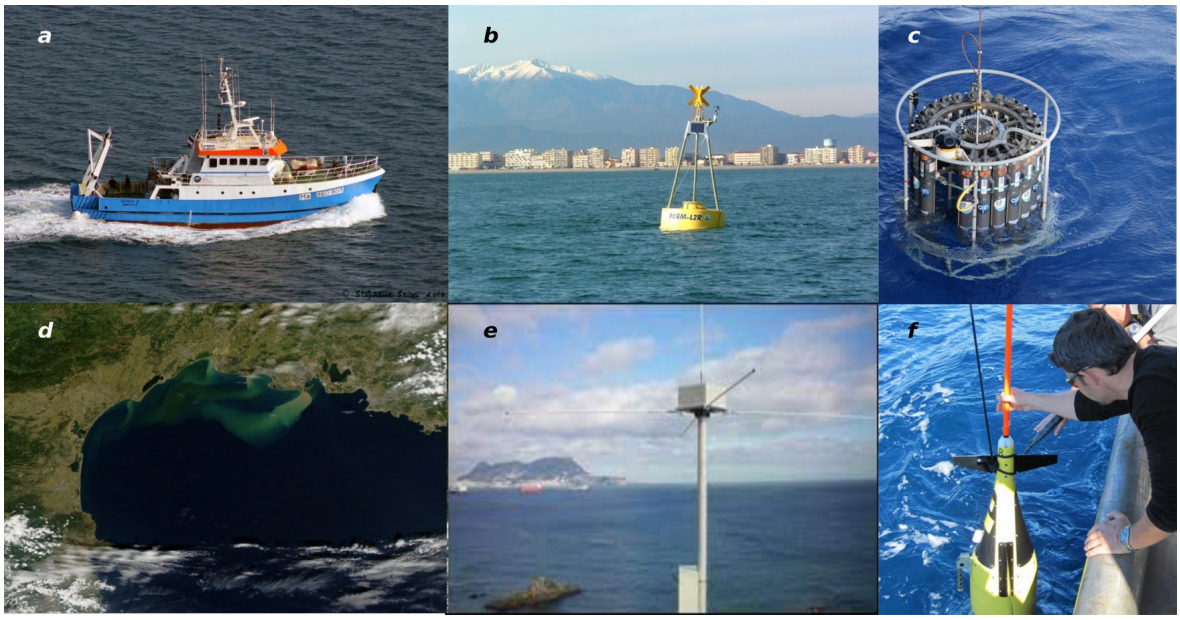

Figure 1.5: Images of different *in-situ* coastal ocean observing platforms used for SPM monitoring. (a) Shipborne observations where a bathysonde can be deployed (c). (b) Coastal buoy. (d) Satellite observations. (e) High Frequency Radar. (f) Launching a SeaExplorer glider. [Photo credits: (a) http://www.shipspotting.com/; (b) and (d) François Bourrin ; (c) Christophe Cassou (d) https://worldview.earthdata.nasa.gov; and (e) http://www.mongoos.eu/hf-radars].

(iii) *From 2000s*: Significant progress made during these decades reflects support from federal agencies, some foundations, and many nations (Ouillon, 2018). The continuous improvement of the computational means has allowed coupling the one-dimensional bottom boundary layer models to three-dimensional dynamics models to understand complex processes, such as particle dynamics in the presence of mixed sediments (Le Hir et al., 2011), formation and dynamics of estuarine turbidity maximum (Brenon and Le Hir, 1999; Sottolichio et al., 2000) and also to understand the broader scale erosion and deposition at regional scales (Blaas et al., 2007; Papanicolaou et al., 2008). The 2000s marked the beginning of an exponential growth of publications related to ocean observation (Fig. 1.1), proof of the growing interest of the scientific community in this field thanks to the technological developments. Indeed, these years are marked by a transition towards the robotization of observations. The novelty came from mobile platforms such as gliders (and other autonomous underwater vehicles) (Fig. 1.5f), and drones or UAVs (Unmanned Aerial Vehicles).

1.3.2. Emergence of underwater glider platform

Glider systems (Davis et al., 2002) are a low-power long-term duration (>30 days) autonomous underwater vehicle that can carry a range of interchangeable sensor packages and sample the water column on large spatial scales (>100 km). Many sensors developed for fixed platforms during the 1970s–1990s have been miniaturized and integrated into these mobile platforms. Gliders have no propellers and are driven primarily through small changes in buoyancy that allow them to “glide” forward through the water column on descent, to typically 2 m above the bottom, and ascend to 0–1 m from the surface. They provide a high density of spatio-temporal *in-situ* measurement illustrated in Fig. 1.6. As reported by Many (2016), gliders can monitor coastal waters with a cast every 100 m (depending on bottom depth, ~150 casts per day) whereas ship observations are limited to ~10 casts per day, as shown by the example in the Rhone River ROFI

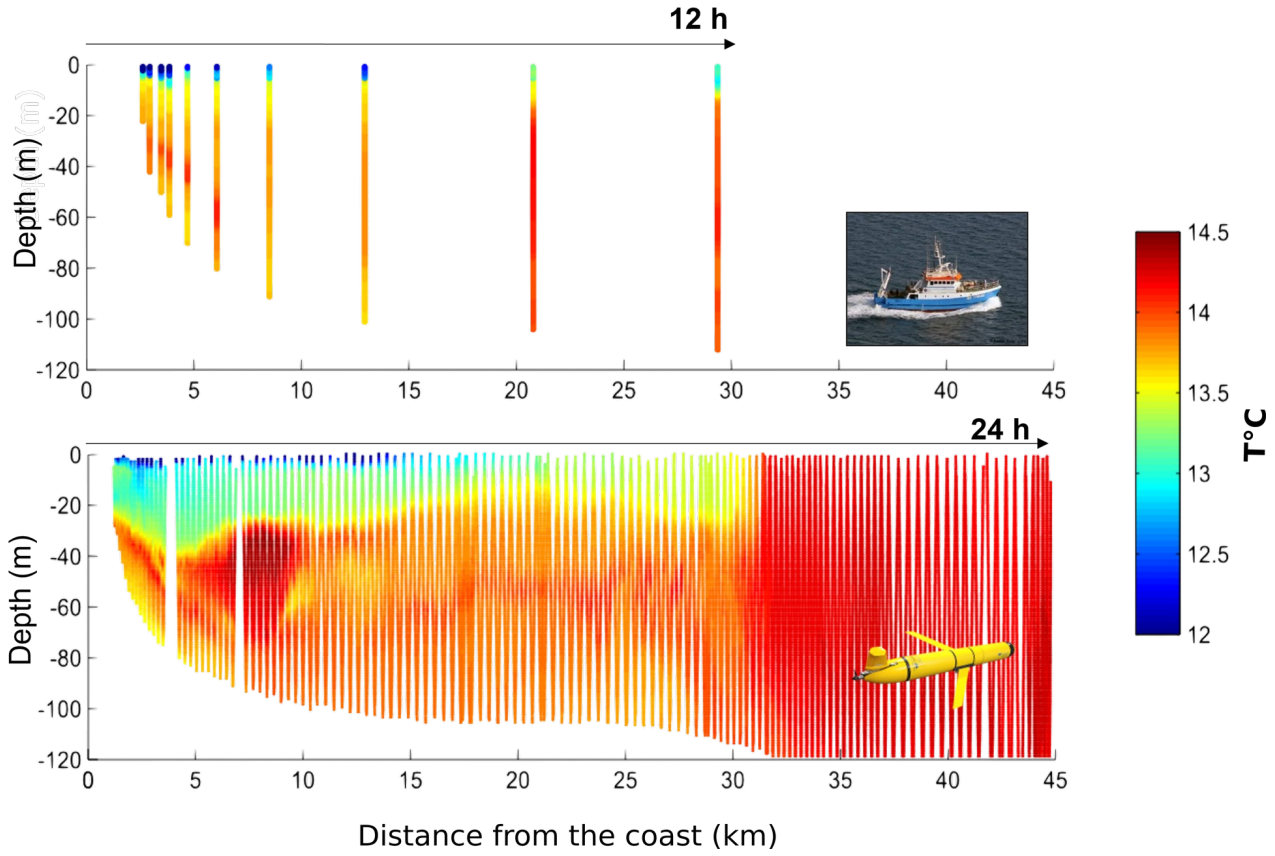

Figure 1.6: Comparison of one-day ship-based observations (top), with one-day glider cross-shelf deployment (bottom). Cross-shelf section of temperature conditions within the Rhone River ROFI from Many (2016).

(Fig. 1.6). The related cost efficiency of glider observations is very low (<10 €/cast) compared to ship observations (~100 €/cast) and shows the "middle-cost for a high efficiency" character of gliders (Many, 2016). Gliders markedly supplement the fixed measurements of buoys and moorings, as well as data collected during shipborne surveys, which are shorter, potentially less frequent, and weather-sensitive.

Underwater gliders became increasingly important for the collection of oceanographic measurements in observing programs during the last decade (Liblik et al., 2016; Rudnick, 2016; Testor et al., 2010). European and American databases via Global Data Assembly Center (GDAC) and IOOS (Integrated Ocean Observing System) have been harmonized to show the evolution of gliders data globally. Glider missions provided a considerable amount of ocean data during the last

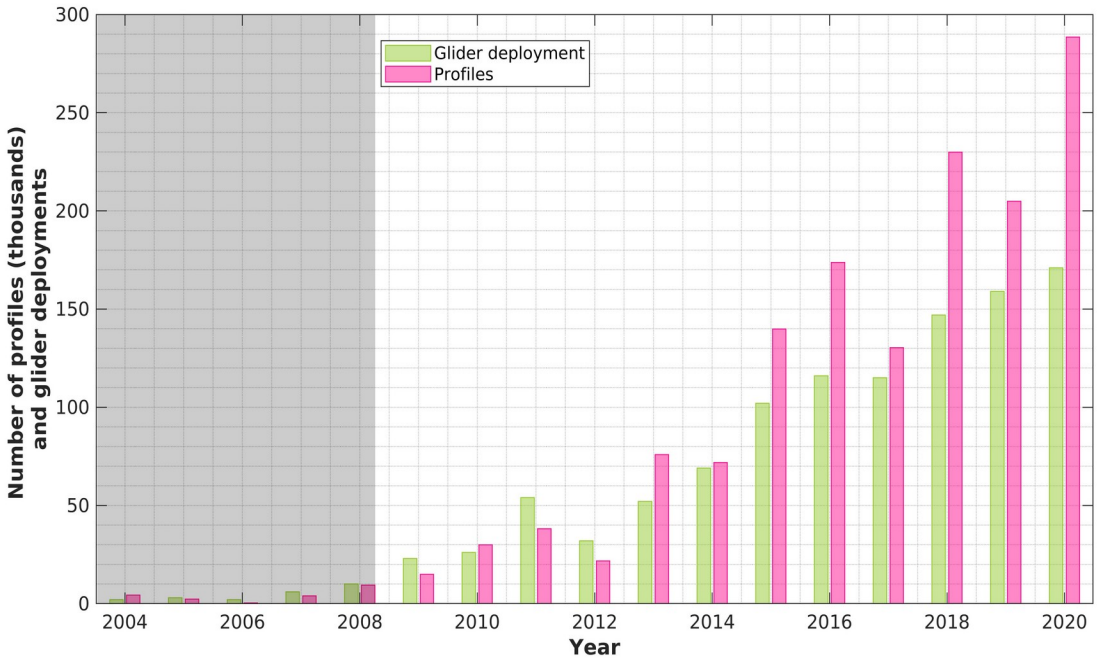

Figure 1.7: Gliders-acquired profiles and number of glider deployments from European GDAC (http://www.ifremer.fr/co/ego/ego/v2/glider_prof_index.txt) and American IOOS (https://marine.rutgers.edu/cool/data/gliders/dac/status/api/data/all.csv) Databases. From 2004 to 2008, only European data are available (indicated by the black shaded area).

decade as shown by Fig. 1.7. The amount of data has grown exponentially over the past decade, with a maximum of ~300,000 profiles acquired in 2020 from 170 glider deployments. Figure 1.7 provides an overview of the evolution of the gliders platform in oceanographic data acquisition over time. However, some American and European deployments are not included in these databases, and Australian glider information is also missing.

Since OceanObs'09, autonomous underwater gliders have reached a mature state and are now operated routinely (Testor et al., 2019). As a result, gliders have been deployed in a wide range of environments: from continental boundary currents to the polar seas, to study aspects ranging from long-term climate variability to fine-scale submesoscale processes (Testor et al., 2019, for a full list of studies and their references) (Fig. 1.8). The ability of the glider to autonomously operate

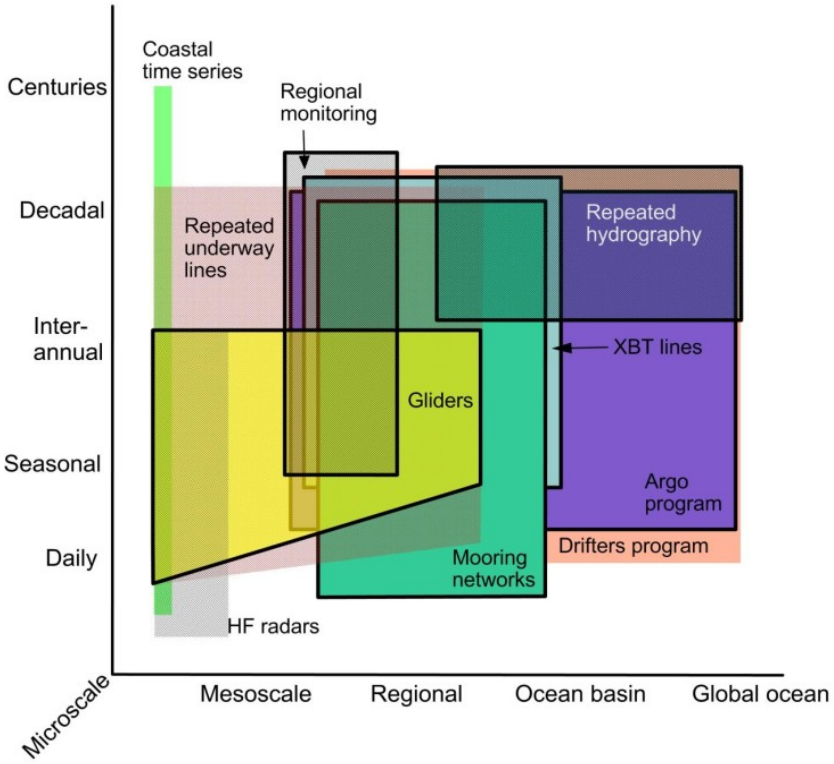

Figure 1.8: Spatial and temporal coverage of various observatories. Horizontal-spatial scales are represented on x-axis and temporal scales on y-axis. Systems that acquire vertical profiles are surrounded by black bold lines from Liblik et al. (2016).

in all weather conditions, for missions of up to several months, and with high sampling resolution has enabled major scientific advances, revealing new insights into physical, biogeochemical, and biological processes over the past decade (Table 1.1) (Testor et al., 2019). Recent studies (Bourrin et al., 2015; Glenn et al., 2008; Many et al., 2018; Miles et al., 2013) highlighted the ability of autonomous underwater gliders to study the spatiotemporal variability of sediment resuspension on continental shelves. Indeed, a new generation of measurement instruments became available for gliders, with (i) smaller optical sensors, which made it possible to characterize properties of SPM (Bourrin et al., 2015); (ii) smaller acoustic Doppler current profiler (ADCP) to measure currents and turbidity (Miles et al., 2015), and (iii) smaller laser *in-situ* scattering and transmissometry (LISST) particle analyzer sensors to enable observations of the details of particles size and concentration (Miles et al., 2021).

These technological developments open up new perspectives in the understanding of hydro-sedimentary processes with increasing measurements of a variety of variables. However, a need exists to operate and manage the data from these new complex sensors. Furthermore, the study of hydro-sedimentary dynamics and processes on continental shelves from new gliders platforms seems to be underrepresented compared to other fields such as mesoscale and submesoscale processes, phytoplankton phenology, and biogeochemistry, etc. as shown in Table 1.1 by (Testor et al., 2019).

Table 1.1: Highlights on publications during the past decade using glider technology by Testor et al. (2019).

High latitudes oceanography, air-sea-ice interactions, or intermediate/deep convection	Beszczynska-Möller et al., 2011; Frajka-Williams et al., 2011; Beaird et al., 2012, 2013; Evans et al., 2013; Fan et al., 2013; Høydalsvik et al., 2013; Kohut et al., 2013; Queste et al., 2013; Guihen et al., 2014; Heywood et al., 2014; Carvalho et al., 2016; Houpert et al., 2016; Nelson et al., 2016; Azaneu et al., 2017; Couto et al., 2017; Jones and Smith, 2017; Lee et al., 2017; Timmermans and Winsor, 2013; Weingartner et al., 2013; Thompson et al., 2014; Ullgren et al., 2014; Venables and Meredith, 2014; Schofield et al., 2015; Swart et al., 2015; Thomalla et al., 2015; Testor et al., 2018; Våge et al., 2018; Viglione et al., 2018
Variability of boundary currents	Pascual et al., 2010; Pattiaratchi et al., 2010, 2017; Ramp et al., 2011; Todd et al., 2011a,b, 2016, 2018; Albretsen et al., 2012; Davis et al., 2012; McClatchie et al., 2012; Sherwin et al., 2012; Høydalsvik et al., 2013; Johnston et al., 2013; Lien et al., 2014, 2015; Pietri et al., 2014; Schaeffer and Roughan, 2015; Schönau et al., 2015; Yang et al., 2015; Lee et al., 2016; Mensah et al., 2016; Schaeffer et al., 2016a; Zaba and Rudnick, 2016; Andres et al., 2017; Anutaliya et al., 2017; Durand et al., 2017; Todd, 2017; Todd and Locke-Wynn, 2017; Aulicino et al., 2018; Houpert et al., 2018; Krug et al., 2018; Seim and Edwards, 2019
Mesoscale and submesoscale processes	Bouffard et al., 2010, 2012; Baird et al., 2011; Baird and Ridgway, 2012; Heslop et al., 2012; Mahadevan et al., 2012; Ruiz et al., 2012; Todd et al., 2012, 2013; Alvarez et al., 2013; Pelland et al., 2013, 2014, 2016, 2018; Pietri et al., 2013; Piterbarg et al., 2013; Timmermans and Winsor, 2013; Caldeira et al., 2014; Hristova et al., 2014; Bosse et al., 2015, 2016; Everett et al., 2015; Farrar et al., 2015; Omand et al., 2015; Schönau and Rudnick, 2015, 2017; Sherwin et al., 2015; Borrione et al., 2016; Caballero et al., 2016; Freitas et al., 2016; Mauri et al., 2016; Thompson et al., 2016; Thomsen et al., 2016; Brannigan et al., 2017; Buffett et al., 2017; Du Plessis et al., 2017; Gourdeau et al., 2017; Itoh and Rudnick, 2017; Karstensen et al., 2017; Kokkini et al., 2017; Krug et al., 2017; Mancero-Mosquera et al., 2017; Margirier et al., 2017; Morrow et al., 2017; Pascual et al., 2017; Ruan et al., 2017; Yu et al., 2017; Zacharia et al., 2017; Gula et al., 2019
Phytoplankton phenology and biogeochemistry	Asper et al., 2011; Briggs et al., 2011; Martin et al., 2011; Xu et al., 2011; Alkire et al., 2012, 2014; Cetinić et al., 2012, 2015; Pierce et al., 2012; Gower et al., 2013; Zhao et al., 2013; Foloni-Neto et al., 2014; Kaufman et al., 2014, 2017; Olita et al., 2014, 2017; Biddle et al., 2015; Evans et al., 2015; Hemsley et al., 2015; Nicholson et al., 2015; Queste et al., 2015; Seegers et al., 2015; Adams et al., 2016; Cotroneo et al., 2016; Fiedler et al., 2016; Jacox et al., 2016; Loginova et al., 2016; Pizarro et al., 2016; Porter et al., 2016; Schaeffer et al., 2016b; Schuette et al., 2016; Thomsen et al., 2016; Bosse et al., 2017; Hemming et al., 2017; Mayot et al., 2017; Ross et al., 2017; Thomalla et al., 2017; Little et al., 2018
Higher trophic levels and biology	Kahl et al., 2010; Klinck et al., 2012; McClatchie et al., 2012; Powell and Ohman, 2012, 2015; Wall et al., 2012; Baumgartner et al., 2013, 2014; Ohman et al., 2013; Oliver et al., 2013; Guihen et al., 2014; Kohut et al., 2014a; Pelland et al., 2014; Ainley et al., 2015; Goericke and Ohman, 2015; Swart et al., 2016; Kusel et al., 2017; Taylor and Lembke, 2017; Benoit-Bird et al., 2018; Chave et al., 2018
Shallow and marginal seas	Castelao et al., 2010; Shulman et al., 2010; Karstensen et al., 2014; Kohut et al., 2014b; Mazzini et al., 2014; Schaeffer et al., 2014; Piero Mazzini et al., 2015; Qiu et al., 2015; Dever et al., 2016; Mahjabin et al., 2016; Saldias et al., 2016; Heslop et al., 2017; Zarokanellos et al., 2017
Climate and variability of the water column	Cole and Rudnick, 2012; Schlundt et al., 2014; Domingues et al., 2015; Farrar et al., 2015; Houpert et al., 2015; Damerell et al., 2016; Schaeffer et al., 2016a; Rudnick et al., 2017; Portela et al., 2018
Internal waves, turbulence, tides, diffusivity and vertical mixing	Alford et al., 2012; Thorpe, 2012; Beaird et al., 2013; Johnston et al., 2013; Rainville et al., 2013, 2017; Fer et al., 2014; Peterson and Fer, 2014; Boettger et al., 2015; Cronin et al., 2015; Johnston and Rudnick, 2015; Palmer et al., 2015; Klymak et al., 2016; Hall et al., 2017; Schultze et al., 2017; St Laurent and Merrifield, 2017; Todd, 2017; Evans et al., 2018; Ma et al., 2018; Scheifele et al., 2018
Particles fluxes and sedimentology	Briggs et al., 2011; Miles et al., 2013; Bourrin et al., 2015; Omand et al., 2015; Many et al., 2016; Churnside et al., 2017; Durrieu de Madron et al., 2017
Ocean forecasting, climatology, and state estimates	Dobricic et al., 2010; Oke et al., 2010, 2015; Zhang et al., 2010a,b; Chudong et al., 2011; Ramp et al., 2011; Todd et al., 2011a, 2012; Yaremchuk et al., 2011; Jones et al., 2012; Melet et al., 2012; Mourre and Alvarez, 2012; Gangopadhyay et al., 2013; L'Heveder et al., 2013; Li et al., 2013; Rayburn and Kamenkovich, 2013; Wilkin and Hunter, 2013; Alvarez and Mourre, 2014; Chen et al., 2014; Drillet et al., 2014; Mourre and Chiggiato, 2014; Ngodock and Carrier, 2014; Pan et al., 2014, 2017; Durski et al., 2015; Miles et al., 2015; Rudnick et al., 2015; Estournel et al., 2016a,b; Fragoso et al., 2016; Kerry et al., 2016, 2018; Chao et al., 2017a,b; Damien et al., 2017; Dong et al., 2017; Goni et al., 2017; Halliwell et al., 2017; Kurapov et al., 2017; Onken, 2017; Todd and Locke-Wynn, 2017; Verdy et al., 2017

1.4. Scientific barriers and methodology

1.4.1. Traditional observation limits for SPM monitoring

In this introduction, we showed that monitoring SPM dynamics involves: (i) estimating sediment fluxes between or within compartments of the coastal zone and (ii) analyzing their spatiotemporal variability at different scales (Ouillon, 2018). Monitoring these processes is essential to achieve sustainable societal use of the coastal ocean for fishing, transportation, and recreation. However, the interlocking spatial and temporal scales of ocean processes make the study of hydro-sedimentary dynamics challenging, especially during extreme events such as storms and floods, which are the main drivers of sediment dynamics in the coastal ocean. Many field programs during these decades used coastal buoys, moorings equipped with optical and acoustic sensors to understand sediment resuspension and transport on continental shelves (Agrawal and Pottsmith, 2000; Drake et al., 1992; Drake and Cacchione, 1986; Palinkas et al., 2010; Trowbridge and Nowell, 1994). Such observations provide precise information on the temporal variability of a narrow water column but are not able to describe the spatial gradients across the entire shelf and evaluate the overall suspended particle transport. In addition, traditional platform measurements as shipborne surveys are weather-sensitive and can only be carried out in calm weather, while remote-sensing observations provide snapshots of the distribution of suspended particles, which are, however, restricted to the surface layer and cloud-free days. To fill these gaps and then understand sediment dynamics at regional scales, three-dimensional hydrodynamic models have been used (Dalyander et al., 2013; Dufois et al., 2008; King et al., 2019; Styles and Glenn, 2005). With the development of these regional-scale sediment resuspension and transport studies, new technologies are necessary to supplement single-point measurements of sediment resuspension and transport on continental shelves (Miles et al., 2015). Improving our ability to understand, simulate and predict sediment dynamics in the coastal zone requires improving the resolution, extent, and duration of

oceanographic measurements. The recent integration of new sensors, such as ADCP and LISST on gliders, open up new perspectives in the understanding of hydro-sedimentary processes. In this context, the contribution of autonomous underwater gliders, allowing the observation of fine-scale hydrology and hydrodynamics over part or all of the continental shelf, and over long periods, is investigated.

1.4.2. Problematic and plan of the thesis

The work of this Ph.D. carried out in the "Centre de Formation et de Recherche sur les Environnements Méditerranéens" (CEFREM – UMR 5110 CNRS/UPVD) of the University of Perpignan (France), is linked to the French research projects MATUGLI (Autonomous coastal TUrbidity Measurements using GLiders) and CHIFRE (Coastal High-Frequency Response to Extreme Events, storms, and floods), in which an ADCP was integrated onto a Slocum glider. The main purpose of this Ph.D. is to develop the processing chain and to explore the capability of a glider newly equipped with an acoustic Doppler current profiler to study hydro-sedimentary processes, particularly during extreme events. It follows the work carried out during projects CASCADE (CAscading, Storm, Convection, Advection, and Downwelling Events) and TUCPA (Coastal Turbidity and Autonomous Platforms) projects in which gliders equipped with physical and bio-optical sensors were deployed in the coastal zone of the Gulf of Lions to describe the SPM properties over the shelf.

Key questions developed forward this work can be resumed as follows:

(i) Is the glider-ADCP a suitable tool to measure currents, turbidity, and in-fine SPM fluxes in the coastal zone?

(ii) Is the glider-ADCP a suitable tool for monitoring the spatiotemporal variability of SPM dynamics in different compartments such as:

- ***Case 1: the region of freshwater influence (ROFI)?***
- ***Case 2: the continental shelf?***

The study area chosen to answer these issues is the GoL located in the northwestern part of the Mediterranean Sea. The coastline, a highly anthropized region with a high level of summer tourist activity (see maps 3.5 in European Environment Agency [1999]), is subject to significant discharges of organic matter and contaminants from rivers. All these inputs make the coastal zone of the GoL a changing environment requiring increased monitoring for its preservation and sustainable management. The GoL dynamic is essentially controlled by intense hydrometeorological events (e.g., floods, southeast storms, cascading of dense water). These hydro-climatic events can occur over very short periods (one day or even a few hours for floods and storms) but sometimes over longer periods (a few weeks to a few months for dense waters), which makes them difficult to sample. The characteristics of the GoL make it a particularly interesting area for monitoring the SPM dynamics. The results obtained in the GoL could be then applied to other highly anthropized coastal areas with similar forcings.

To answer these issues, we will structure our manuscript around 6 chapters, including this general introduction.

In the second chapter, we will define the functioning of the coastal hydro-systems of the GoL. After a state of the art on the main hydrodynamical and sedimentological features of the area, we will detail the multi-platform approach used in the GoL to monitor SPM dynamics.

Chapter three, entitled "*Glider-ADCP toolbox: a MATLAB toolbox for processing active acoustic data onto underwater glider"*, deals with the processing of glider data from physical, bio-optical, and acoustic sensors. In the absence of an available processing chain, we developed a toolbox to process ADCP glider data, to be able to analyze and interpret the current and acoustic backscatter data for hydro-sedimentary issues.

Chapter four, entitled "*Glider-based active acoustic monitoring of currents and turbidity in the coastal zone"*, deals with the capacity of gliders to monitor the interplay of hydrographic features, water circulation, and particulate matter distribution over endurance deployments (>1 month) to capture sporadic events (storms and floods), which are the key mechanisms involved in the SPM transfer in the coastal zone. The quantification of currents, SPM concentration, and ultimately the fluxes, will be carried out in a strategic area, the ROFI of the Rhone River, which plays a major role in the sediment dynamics of the GoL.

Chapter five is entitled '*Sediment dynamics on the outer-shelf of the Gulf of Lions during an onshore storm: an approach based on acoustic glider and numerical modelling'*. In this chapter, we will discuss the impact of a storm on resuspension and advection processes on the GoL continental shelf. An endurance glider deployment has been carried out in winter 2018 and allowed to capture a major storm event (5-year return period) over the outer shelf, where observations are missing due to the trawling activity. The role of wave-current interaction in sediment dynamic processes will be highlighted using the glider-ADCP and spatialized at the Gulf of Lion scale using the SYMPHONIE numerical model.

Finally, in chapter six, a synthesis of the results obtained will be carried out to answer the questions mentioned in this introduction. An extension of the usefulness of the glider-ADCP on major coastal issues will be discussed. Finally, a general synthesis will be drawn up and perspectives will be given as conclusions to this study.

This research work led to the writing of two scientific papers which form two of the chapters of this manuscript (Chapters. 4 and 5). In addition, we developed a MATLAB toolbox (Chapter. 3) for processing physical, bio-optical, and ADCP sensors integrated on gliders, available in open access from GitHub (https://github.com/mgentil17/mgentil17/tree/master), without any registration or login required.

References

Ackers, P., White, W. R., 1973. Sediment transport: new approach and analysis. Journal of the Hydraulics Division 99, 2041–2060.

Agrawal, Y. C., Pottsmith, H.C., 2000. Instruments for particle size and settling velocity observations in sediment transport. Marine Geology 168, 89–114.

Amos, C.L., Topliss, B. J., 1985. Discrimination of Suspended Particulate Matter in the Bay of Fundy Using the Nimbus 7 Coastal Zone Color Scanner. Canadian Journal of Remote Sensing 11, 85–92. https://doi.org/10.1080/07038992.1985.10855080

Anderson, D., 2010. Early successes: El Nino, Southern oscillation, and seasonal forecasting. Presented at the Proc. OceanObs' 09: Sustained Ocean Observations and Information for Society Conf, p. 01.

Balls, P., 1986. Composition of suspended particulate matter from Scottish coastal waters—geochemical implications for the transport of trace metal contaminants. Science of the total environment 57, 171–180.

Baschek, B., Schroeder, F., Brix, H., Riethmüller, R., Badewien, T.H., Breitbach, G., Brügge, B., Colijn, F., Doerffer, R., Eschenbach, C., 2017. The coastal observing system for northern and arctic seas (COSYNA). Ocean science 13, 379–410.

Bishop, J. K. B., 1986. The correction and suspended particulate matter calibration of Sea Tech transmissometer data. Deep-Sea Research Part A. Oceanographic Research Papers 33, 121–134. https://doi.org/10.1016/0198-0149 (86)90111-1

Blaas, M., Dong, C., Marchesiello, P., McWilliams, J.C., Stolzenbach, K. D., 2007. Sediment-transport modeling on Southern Californian shelves: A ROMS case study. Continental shelf research 27, 832–853.

Bourrin, F., Many, G., De Madron, X. D., Martín, J., Puig, P., Houpert, L., Testor, P., Kunesch, S., Mahiouz, K., Béguery, L., 2015. Glider monitoring of shelf suspended particle dynamics and transport during storm and flooding conditions. Continental Shelf Research 109, 135–149.

Brenon, I., Le Hir, P., 1999. Modelling the turbidity maximum in the Seine estuary (France): identification of formation processes. Estuarine, coastal and shelf science 49, 525–544.

Brown, D. A., Gossett, R. W., Hershelman, P., Schaefer, H. A., Jenkins, K. D., Perkins, E. M., 2019. Bioaccumulation and detoxification of contaminants in marine organisms from southern California coastal waters, in: Waste Disposal in the Oceans. Routledge, pp. 171–193.

Cacchione, D. A., Sternberg, R. W., & Ogston, A. S. (2006). Bottom instrumented tripods: History, applications, and impacts. *Continental Shelf Research*, *26*(17-18), 2319-2334.

Cocquempot, L., Delacourt, C., Paillet, J., Riou, P., Aucan, J., Castelle, B., Charria, G., Claudet, J., Conan, P., Coppola, L., 2019. Coastal ocean and nearshore observation: A French case study. Frontiers in Marine Science 6, 324.

Dalyander, P.S., Butman, B., Sherwood, C.R., Signell, R.P., Wilkin, J.L., 2013. Characterizing wave-and current-induced bottom shear stress: US middle Atlantic continental shelf. Continental Shelf Research 52, 73–86.

Davis, R. A., Ethington, R. L., 1976. Beach and nearshore sedimentation. SEPM Soc. Sediment. Geol. 24. https://doi.org/10.2110/pec.76.24

Davis, R.E., Eriksen, C.C., Jones, C.P., 2002. Autonomous buoyancy-driven underwater gliders. The technology and applications of autonomous underwater vehicles 37–58.

De Souza, R.-M., Williams, J. S., Meyerson, F.A.B., 2003. Critical links: Population, health, and the environment.

Drake, D. E., Cacchione, D. A., 1986. Field observations of bed shear stress and sediment resuspension on continental shelves, Alaska and California. Continental Shelf Research 6, 415–429.

Drake, D. E., Cacchione, D. A., Grant, W. D., 1992. Shear stress and bed roughness estimates for combined wave and current flows over a rippled bed. Journal of Geophysical Research: Oceans 97, 2319–2326.

Dufois, F., Garreau, P., Le Hir, P., Forget, P., 2008. Wave-and current-induced bottom shear stress distribution in the Gulf of Lions. Continental Shelf Research 28, 1920–1934.

Durand, P., 1999. L'evolution des plages de l'ouest du golfe du lion au xxeme siecle. Cinematique du trait de cote, dynamique sedimentaire, analyse previsionnelle.

Durrieu de Madron, X., Wiberg, P. L., Puig, P., 2008. Sediment dynamics in the Gulf of Lions: The impact of extreme events.

Engelund, F., Hansen, E., 1967. A monograph on sediment transport in alluvial streams. Technical University of Denmark 0stervoldgade 10, Copenhagen K.

European Environment Agency, 1999. State and pressures of the marine and coastal Mediterranean environment. Office for Official Publ. of the European Comm.

Gattuso, J.P., Frankignoulle, M., Wollast, R., 1998. Carbon and carbonate metabolism in coastal aquatic ecosystems. Annual Review of Ecology and Systematics 29, 405–434.

Gattuso, J. P., Smith, S. V., Hogan, C. M., Duffy, J. E., 2009. Coastal zone. Encyclopedia of Earth. Environmental Information Coalition. National Council for Science and the Environment, Washington, DC. (First published in the Encyclopedia of Earth, see http://www. eoearth. org/article/Coastal_zone).

Geyer, W. R., Woodruff, J. D., & Traykovski, P. (2001). Sediment transport and trapping in the Hudson River estuary. Estuaries, *24*(5), 670-679.

Glenn, S., Jones, C., Twardowski, M., Bowers, L., Kerfoot, J., Kohut, J., Webb, D., Schofield, O., 2008. Glider observations of sediment resuspension in a Middle Atlantic Bight fall transition storm. Limnology and Oceanography 53, 2180–2196.

Glenn, S. M., Grant, W. D., 1987. A suspended sediment stratification correction for combined wave and current flows. Journal of Geophysical Research: Oceans 92, 8244—8264. https://doi.org/10.1029/JC092iC08p08244

Grant, G., Naish, T., Dunbar, G., Stocchi, P., Kominz, M., Kamp, P.J., Tapia, C., McKay, R., Levy, R., Patterson, M., 2019. The amplitude and origin of sea-level variability during the Pliocene epoch. Nature 574, 237–241.

Guilderson, T., Burckle, L., Hemming, S., Peltier, W., 2000. Late Pleistocene sea-level variations derived from the Argentine Shelf. Geochemistry, Geophysics, Geosystems 1.

King, E., Conley, D., Masselink, G., Leonardi, N., McCarroll, R., Scott, T., 2019. The impact of waves and tides on residual sand transport on a sediment-poor, energetic, and macrotidal continental shelf. Journal of Geophysical Research: Oceans 124, 4974–5002.

Le Hir, P., Cayocca, F., Waeles, B., 2011. Dynamics of sand and mud mixtures: A multiprocess-based modelling strategy. Continental Shelf Research 31, S135—S149.

Liblik, T., Karstensen, J., Testor, P., Alenius, P., Hayes, D., Ruiz, S., Heywood, K., Pouliquen, S., Mortier, L., Mauri, Ejm., 2016. Potential for an underwater glider component as part of the Global Ocean Observing System. Methods in Oceanography 17, 50–82.

Lorenzoni, L., Benway, H., 2013. Global Intercomparability in a Changing Ocean: an international time-series methods workshop, November 28–30, 2012 (Bermuda Institute of Ocean Sciences, St. Georges, Bermuda).

Lyzenga, D. R., 1978. Passive remote sensing techniques for mapping water depth and bottom features. Appl. Opt., AO 17, 379–383. https://doi.org/10.1364/AO.17.000379

Maggi, F., 2005. Flocculation dynamics of cohesive sediment.

Many, G., 2016. Impacts of storm and flood events on suspended particulate matter dynamics in the Gulf of Lions. Contributions of gliders to a multi-platform approach.

Many, G., Bourrin, F., de Madron, X.D., Ody, A., Doxaran, D., Cauchy, P., 2018. Glider and satellite monitoring of the variability of the suspended particle distribution and size in the Rhône ROFI. Progress in oceanography 163, 123–135.

Many, G., de Madron, X.D., Verney, R., Bourrin, F., Renosh, P., Jourdin, F., Gangloff, A., 2019. Geometry, fractal dimension, and settling velocity of flocs during flooding conditions in the Rhône ROFI. Estuarine, Coastal and Shelf Science 219, 1–13.

Meyer-Peter, E., Müller, R., 1948. Formulas for bed-load transport. Presented at the IAHSR 2nd meeting, Stockholm, appendix 2, IAHR.

Miles, T., Glenn, S. M., Schofield, O., 2013. Temporal and spatial variability in fall storm induced sediment resuspension on the Mid-Atlantic Bight. Continental Shelf Research 63, S36—S49.

Miles, T., Seroka, G., Kohut, J., Schofield, O., Glenn, S., 2015. Glider observations and modeling of sediment transport in Hurricane Sandy. Journal of Geophysical Research: Oceans 120, 1771–1791.

Miles, T., Slade, W., Glenn, S., 2021. Sediment resuspension and transport from a glider integrated Laser In Situ Scattering and Transmissometry (LISST) particle analyzer. Journal of Atmospheric and Oceanic Technology.

Moltmann, T., Turton, J., Zhang, H.-M., Nolan, G., Gouldman, C., Griesbauer, L., Willis, Z., Piniella, A.M., Barrell, S., Andersson, E., 2019. A Global Ocean Observing System (GOOS), delivered through enhanced collaboration across regions, communities, and new technologies. Frontiers in Marine Science 6, 291.

Nittrouer, C. A., Wright, L. D., 1994. Transport of particles across continental shelves. Reviews of Geophysics 32, 85–113.

Ouillon, S., 2018. Why and how do we study sediment transport? Focus on coastal zones and ongoing methods. Water 2018, 10(4), 390; https://doi.org/10.3390/w10040390.

Palinkas, C., Ogston, A., Nittrouer, C., 2010. Observations of event-scale sedimentary dynamics with an instrumented bottom-boundary-layer tripod. Marine Geology 274, 151–164.

Papanicolaou, A. (Thanos) N., Elhakeem, M., Krallis, G., Prakash, S., Edinger, J., 2008. Sediment transport modeling review—current and future developments. Journal of hydraulic engineering 134, 1–14.

Pauly, D., Christensen, V., 1995. Primary production required to sustain global fisheries. Nature 374, 255–257.

Pauly, D., Christensen, V., Guénette, S., Pitcher, T.J., Sumaila, U. R., Walters, C. J., Watson, R., Zeller, D., 2002. Towards sustainability in world fisheries. Nature 418, 689–695.

Petihakis, G., Perivoliotis, L., Korres, G., Ballas, D., Frangoulis, C., Pagonis, P., Ntoumas, M., Pettas, M., Chalkiopoulos, A., Sotiropoulou, M., 2018. An integrated open-coastal biogeochemistry, ecosystem and biodiversity observatory of the eastern Mediterranean—the Cretan Sea component of the POSEIDON system. Ocean Science 14, 1223–1245.

Rockström, J., Steffen, W., Noone, K., Persson, Å., Chapin, F.S., Lambin, E.F., Lenton, T.M., Scheffer, M., Folke, C., Schellnhuber, H.J., 2009. A safe operating space for humanity. nature 461, 472–475.

Rouse, H., 1937. Modern conceptions of the mechanics of fluid turbulence. Transactions of the American Society of Civil Engineers 102, 463–505.

Rudnick, D. L., 2016. Ocean research enabled by underwater gliders. Annual review of marine science 8, 519–541.

Ruhl, H.A., André, M., Beranzoli, L., Çağatay, M.N., Colaço, A., Cannat, M., Dañobeitia, J.J., Favali, P., Géli, L., Gillooly, M., 2011. Societal need for improved understanding of climate change, anthropogenic impacts, and geo-hazard warning drive development of ocean observatories in European Seas. Progress in Oceanography 91, 1–33.

Sabatier, F., Stive, M., Pons, F., 2005. Longshore variation of depth of closure on a micro-tidal wave-dominated coast, in: Coastal Engineering 2004: (In 4 Volumes). World Scientific, pp. 2327–2339.

Salgado-Hernanz, P.M., Regaudie de Gioux, A., Antoine, D., Basterretxea, G., 2021. Pelagic primary production in the coastal Mediterranean Sea: variability, trends and contribution to basin scale budgets. Biogeosciences Discussions 1–35.

Schofield, O., Jones, C., Kohut, J., Kremer, U., Miles, T., Saba, G., Webb, D., Glenn, S., 2015. Developing coordinated communities of autonomous gliders for sampling coastal ecosystems. Marine Technology Society Journal 49, 9–16.

Sheng, Y. P., 1986. Modeling bottom boundary layer and cohesive sediment dynamics in estuarine and coastal waters, in: Estuarine Cohesive Sediment Dynamics. Springer, pp. 360–400.

Shields, A., 1936. Application of similarity principles and turbulence research to bed-load movement.

Sottolichio, A., Le Hir, P., Castaing, P., 2000. Modeling mechanisms for the stability of the turbidity maximum in the Gironde estuary, France, in: Proceedings in Marine Science. Elsevier, pp. 373–386.

Sternberg, R. (2005). Sediment transport in the coastal ocean: a retrospective evaluation of the benthic tripod and its impact, past, present, and future. *Scientia Marina*, *69*(S1), 43-54.

Styles, R., Glenn, S. M., 2005. Long-term sediment mobilization at a sandy inner shelf site, LEO-15. Journal of Geophysical Research: Oceans 110.

Styles, R., Glenn, S. M., 2000. Modeling stratified wave and current bottom boundary layers on the continental shelf. Journal of Geophysical Research: Oceans 105, 24119–24139.

Talley, L. D., 2011. Descriptive physical oceanography: an introduction. Academic press.

Tanhua, T., McCurdy, A., Fischer, A., Appeltans, W., Bax, N., Currie, K., DeYoung, B., Dunn, D., Heslop, E., Glover, L.K., 2019. What we have learned from the framework for ocean observing: Evolution of the global ocean observing system. Frontiers in Marine Science 6, 471.

Testor, P., de Young, B., Rudnick, D. L., Glenn, S., Hayes, D., Lee, C. M., Pattiaratchi, C., Hill, K., Heslop, E., Turpin, V., 2019. OceanGliders: a component of the integrated GOOS. Frontiers in Marine Science 6, 422.

Testor, P., Meyers, G., Pattiaratchi, C., Bachmayer, R., Hayes, D., Pouliquen, S., Petit de la Villeon, L., Carval, T., Ganachaud, A., Gourdeau, L., 2010. Gliders as a component of future observing systems. OceanObs' 09.

Trowbridge, J.H., Nowell, A. R. M., 1994. An introduction to the Sediment TRansport Events on Shelves and Slopes (STRESS) program. Continental Shelf Research, 14, 1057–1061. https://doi.org/10.1016/0278-4343 (94)90028-0

Visbeck, M., 2018. Ocean science research is key for a sustainable future. Nature communications 9, 1–4.

Vitousek, P. M., Mooney, H. A., Lubchenco, J., Melillo, J. M., 1997. Human domination of Earth's ecosystems. Science 277, 494–499.

Weatherly, G.L., Martin, P. J., 1978. On the structure and dynamics of the oceanic bottom boundary layer. Journal of Physical Oceanography 8, 557–570.

Chapter 2.

Regional settings: The Gulf of Lions

Table of Contents

Table of figures

Index of tables

2.1. General description

The Gulf of Lions (GoL), located in the northwestern Mediterranean, is a wide continental shelf surrounded by the Alps, the Massif Central, and the Pyrenees (Fig. 2.1). It has a crescent-shaped form and extends over 6700 km² from Cap Croisette at the eastern end to Cap Creus at its southwestern end. The width of its continental shelf reaches a maximum of 70 km with an average depth of 90 m. Its Southern limit is associated with the steep continental slope connecting it to an abyssal plain with an average depth of about 2500 m. This slope is notably incised by several submarine canyons, an area where water and particles transit towards the open sea (Bonnin et al., 2008 ; Durrieu de Madron et al., 1999, 1990 ; Flexas et al., 2002 ; Palanques et al., 2008, 2006).

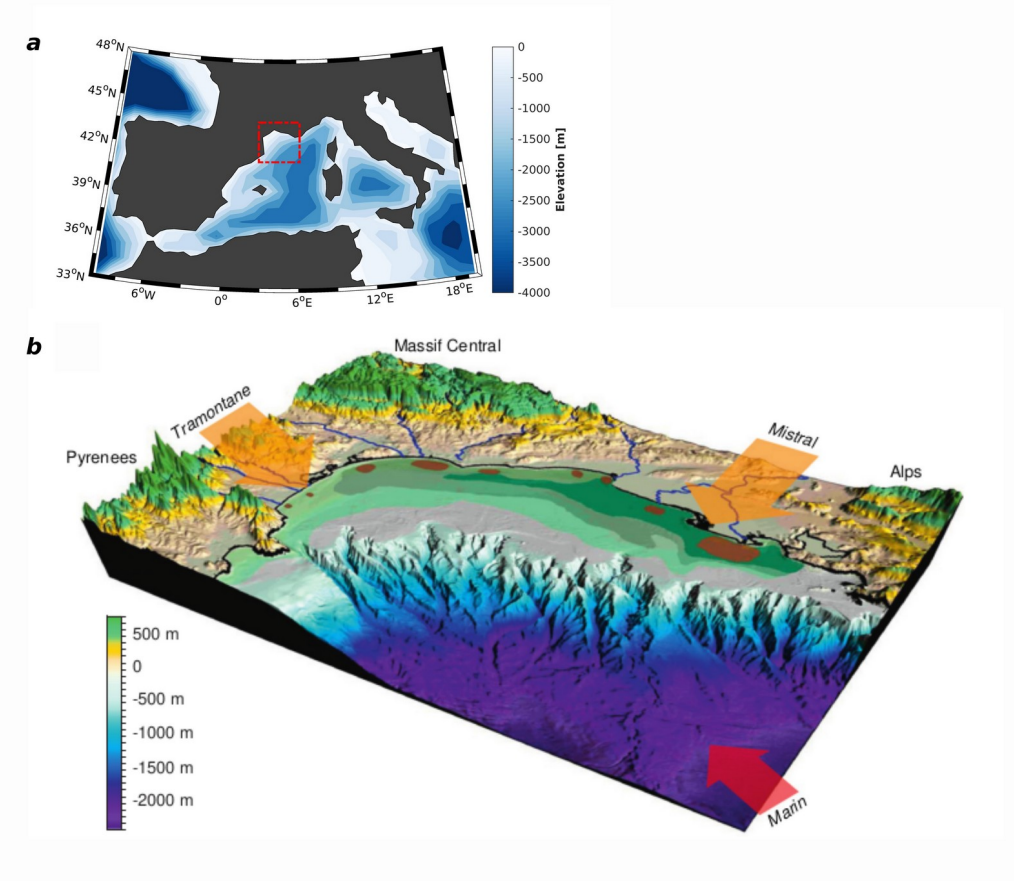

Figure 2.1: (a) General map of western Mediterranean, where the Gulf of Lions is located by a red square. (b) Bathymetric and topographic map of the Gulf of Lions showing the main rivers (in blue) and the prevailing winds (arrows) from Durrieu de Madron et al. (2008).

2.2. Overview

2.2.1. Wind regimes

The dominant winds in the GoL are of two main origins: offshore (Tramontane and Mistral), and onshore (marine) winds (Fig. 2.1 arrows). Tramontane is a north-westerly air flux coming from the Atlantic and channeled by the Pyrenees and the Massif Central. The Mistral is a northerly cold and dry wind channeled by the Massif Central and the Alps. It comes from the confrontation of a high pressure located between Spain and the Bay of Biscay and a low pressure located around the Gulf of Genoa. These continental winds can be strong around 10–15 m s^{-1} on average (Millot, 1990). Marine winds, generally from the east or southeast, are less frequent than continental winds but can be strong all year outside the summer period, reaching speeds of 20–25 m s^{-1} (Andre et al., 2005; Dufois et al., 2014; Millot, 1990).

2.2.2. Hydrodynamical conditions

The hydrodynamics of the shelf involves numerous physical processes, with heterogeneous spatiotemporal scales. The Mediterranean Sea is a micro-tidal environment, where tides have small amplitudes, in order of 30 cm in the GoL (Fanget et al., 2013), and associated currents are weak by a few mm s^{-1} (Carrère et al., 2012). In the GoL, most hydrodynamical processes are generated directly in response to wind forcing. Wind induces stress at the air-sea interface, shearing the water layer and setting it in motion. Depending on the direction, intensity, and duration of the wind, different hydrodynamic processes will be generated, such as barotropic circulation, mesoscale structures, upwellings, and inertial currents. The dimension of the Mediterranean system is presented below before focusing on the shelf circulation scenarios, according to the main winds.

2.2.2.1. Circulation induced by the NW Mediterranean system

The North Current or Liguro-Provençal Current (LPC) is the northern part of the Mediterranean surface water gyre (cyclonic circulation) of the western basin. This vein of warm water, less salty compared to the open sea waters (Millot, 1990), reaches speeds of several tens of cm s^{-1} (Millot and Taupier-Letage, 2005) in winter, and spreads in the GoL shelf over a width of several tens of km. In the GoL, this current follows the upper part of the continental slope and is therefore constrained by the bathymetry (Petrenko, 2003).

2.2.2.2. Circulation induced by offshore winds

Barotropic circulation—Estournel et al. (2001) showed from numerical simulations that the Mistral alone induces an anticyclonic circulation at the shelf scale, which tends to isolate the shelf waters from the slope waters. While Tramontane alone induces a cyclonic circulation only on the western part of the shelf. These winds generate waves of small amplitude and period (<2 m and <6 s), due to the short fetch.

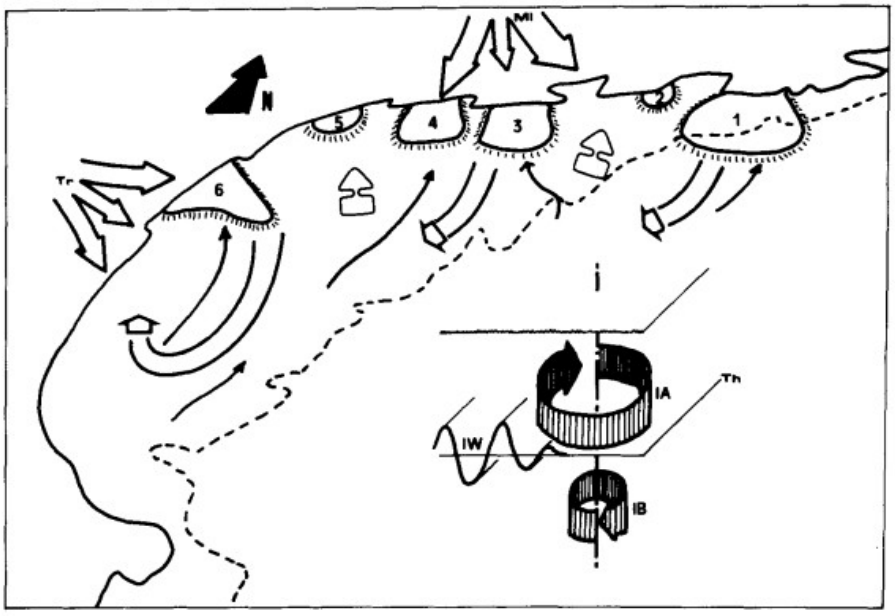

Figure 2.2: Schematic representation of the phenomena induced by offshore winds from Millot (1990), where the six coastal upwellings zones are represented (1-6). The arrows represent induced currents (wide: surface; narrow: bottom).

Upwellings—Estournel et al. (2001) showed that Mistral and Tramontane induce coastal currents that export shelf water and prompt, in turn, compensating the inflow of the slope water onto the shelf (upwellings). These offshore winds also lead to upwellings on the coasts of Provence and Hérault, as observed in summer by Millot (1990) (Fig. 2.2), where the surface water is drained to the southwest and the shelf waters are upwelled.

Dense shelf waters—In winter, wintry heat losses as well as evaporation—caused by cold and dry northerly winds—induce cooling and mixing of the shelf waters which may cascade along the slope (Durrieu de Madron et al., 2005; and the references therein) (Fig. 2.3). As reported by Durrieu de Madron et al. (2008), these events are unusual but very important in the export of suspended particulates matter (SPM) from the shelf to the deep ocean.

Mesoscale eddies—Several studies (Forget et al., 2008; Rubio et al., 2009, 2005) have revealed the presence of isolated but recurrent eddies over the GoL shelf. For instance (Rubio et al., 2009) showed an eddy of 25 to 40 km of diameter with a vertical extension of 80–100 m depth, and

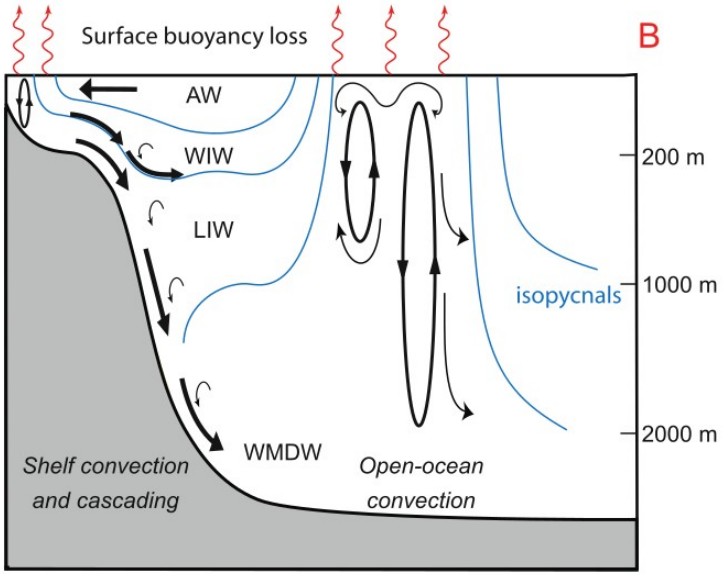

Figure 2.3: Schematic diagram depicting the dense shelf water cascading and open sea convection processes across the margin from Puig et al. (2013).

surface velocities around 0.2-0.3 m s^{-1} over the Catalan shelf (West of the GoL). It would be generated by the detachment to the south of Cap Creus of a coastal current formed during a strong Tramontane (Rubio et al., 2009).

2.2.2.3. Circulation induced by onshore winds

In fall and winter, intense onshore winds (higher than 10 m s^{-1}) may generate storms. As reported by Ulses et al. (2008a), these intense winds are generally brief (3 days) and rare (6% of the time). However, storms can produce east to southeast significant wave heights of up to 10 m with a period of 12 s (Guizien, 2009), associated with strong near-bottom currents. At the shelf scale, storms induce a cyclonic circulation (Fig. 2.4) and can generate coastal downwelling (surface water sinking due to its accumulation near the coast). This coastal water can then be exported deep into the Cap de Creus Canyon due to the narrowing of the shelf, which is only a few kilometers wide at the cap (Ulses et al., 2008a). In winter, these exports can be enhanced by the presence of dense cold

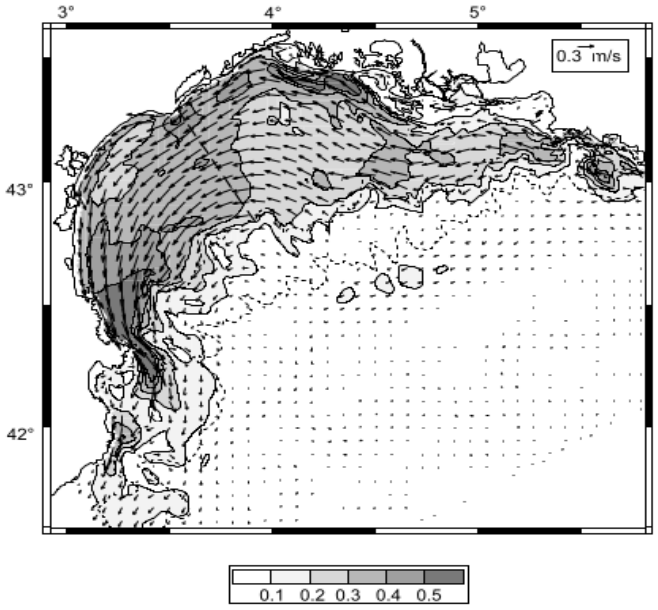

Figure 2.4: Simulated depth-averaged current field (m s^{-1}) on the storm of 4 December 2003, showing the cyclonic circulation in the Gulf of Lions from Ulses et al. (2008a).

waters on the shelf and the weak stratification of the water column on the slope (Palanques et al., 2006). In the GoL, where tide forcing can be neglected, various observational (Bonnin et al., 2008 ; Bourrin et al., 2015, 2008b, 2008a ; Ferré et al., 2005 ; Guillén et al., 2006 ; Martín et al., 2013 ; Ogston et al., 2008 ; Palanques et al., 2008, 2006) and modeling (Dufois et al., 2008 ; Ferré et al., 2008 ; Ulses et al., 2008b) studies emphasized the role of east, southeast storms induced by onshore winds in the resuspension and redistribution of the shelf sediments. These marine storms may also be combined with river floods due to the transport of humidity over coastal relief (Pyrenees, Massif Central, Alps) which induces high precipitation.

2.2.3. Rivers influence

In the GoL, riverine inputs can be separated into two main categories: (i) the seasonal inflow from the Rhone River, and (ii) the inflow from the coastal rivers with torrential character.

The Rhone River—is one of the largest rivers in terms of liquid and solid contributions to the Mediterranean Sea, along with the Po in Italy and, to a lesser extent, the Ebro in Spain, as reported by Bourrin (2007) in Table 2.1, and confirmed by the recent update of Sadaoui et al. (2018). The Rhone River (Fig. 2.5b) presents a highly seasonal variability (mean annual discharge of 1,700 $m^3 s^{-1}$) with maximum discharges observed in autumn and winter, during which the largest floods generally occur, or during the melting snow period in spring. The river supplies 80% of the sedimentary input to the GoL (Bourrin and Durrieu de Madron, 2006 ; Courp and Monaco, 1990), with an average annual particle flux of 8 +/- 4.5 $\times 10^6$ t y^{-1} (1977–2013 period) (Sadaoui et al., 2016). The contribution of sediments during a flood event is estimated at 70% (Pont, 1996), highlighting the role of these episodic events in the SPM delivery to the shelf.

Table 2.1: Characteristics of the Rhone River in comparison to some of the larger rivers in the Mediterranean (Bourrin, 2007; and references therein).

Rivers	Liquid Discharge (m^3 s^{-1})			Solid Discharge (x 10^6 m^3 an)	Temporal Window (year)
	0	0	0		
Rhone	234	11,000	1,700	8	1920–2004
Po	275	11,580	1,480	10.4	1919–1996
Ebre	136	712	426	0.1	1960–1999
Nile	/	/	951	~0	1871–1999

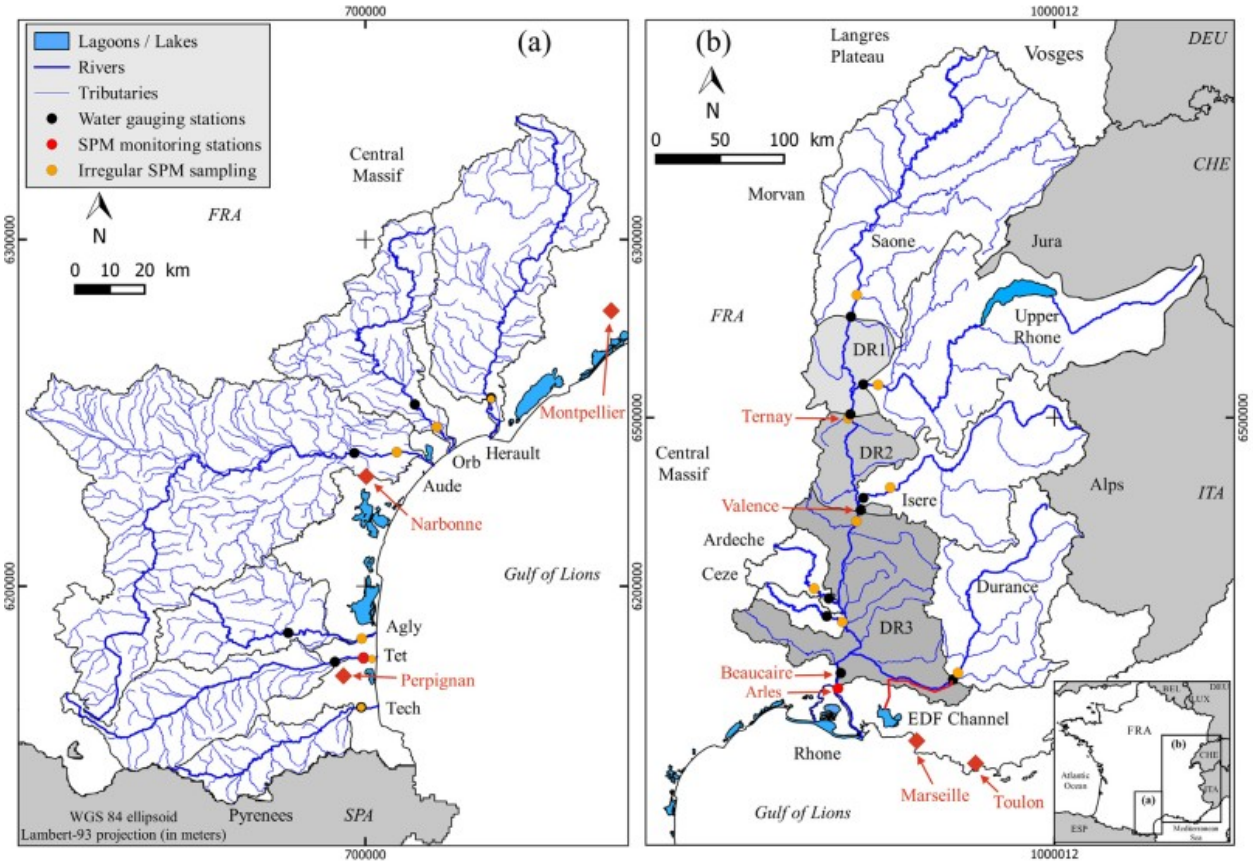

Figure 2.5: GoL maps showing the watersheds of (a) the coastal rivers (Hérault, Orb, Aude, Agly, Têt, Tech), and (b) the Rhone River, from Sadaoui et al. (2016).

The Coastal Rivers—of the GoL (i.e., from east to west: Vidourle, Lez, Hérault, Orb, Aude, Agly, Têt, and Tech [Fig. 2.5a]), have a high seasonal variability and their functioning is close to the North African Wadis. These small mountainous rivers present low discharges during summer and large flood events in winter, fall, and also spring season (Serrat et al., 2001). Most of the sedimentary material of these coastal rivers is therefore brought during episodic events such as floods. For instance, Bourrin et al. (2008b) estimated, during a 5-year flood, to ~25 and ~75% the fraction of sands and clays/silts in the total year SPM delivered by small rivers to the GoL shelf.

2.2.4. Morpho-bathymetry and sedimentary properties

The GoL is composed of different sedimentary units that we will name by their location: inner-, mid- and outer-shelf. The main part of the sediments brought by the rivers is stored, sometimes temporarily, on the GoL sediment units.

The inner shelf (~20 m) is mainly composed of coastal sands (Fig. 2.6). This material is mobilized during storm events and moved along the longshore drift. There are several cells with different drift directions along the GoL coastline which depend on the angle of incidence of the main waves with the coast. The main cells and directions of these longshore drifts are well known and have been established by bathymetric methods (Certain, 2002) or radioactive tracing (Courtois and Monaco, 1969).

The mid shelf is mainly composed of a mud belt from silt to clay (Fig. 2.6). This sedimentary unit is located between 30 and 90 m depth and corresponds to the average wave action limit (Jago and Barusseau, 1981). This median mudflat is directly connected to the Rhône pro-delta but detached from the prodeltas of other coastal rivers (Fig. 2.6).

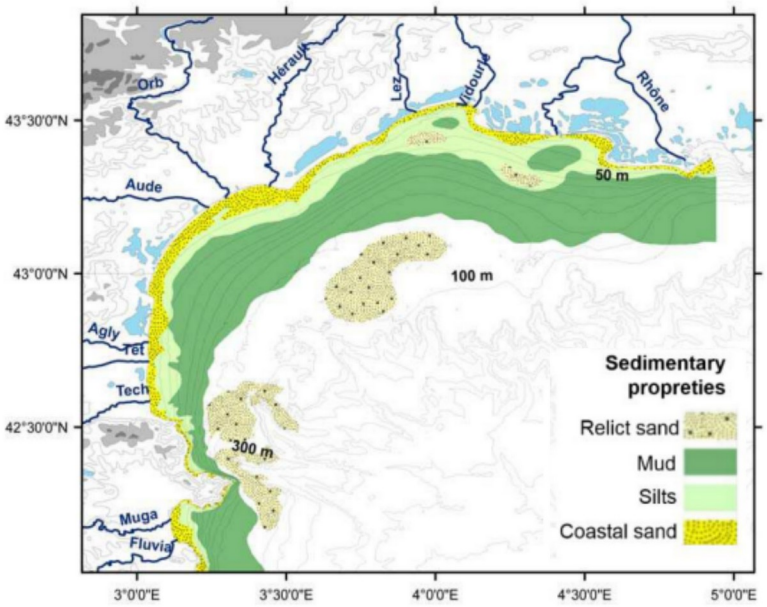

Figure 2.6: Morphological and bathymetric map of the Gulf of Lions' shelf, from Bourrin, (2007). This map compiled several sedimentary studies carried out during past decades (Aloısi, 1986; Got, 1973; Monaco, 1971).

The outer shelf (>90 m) is mainly composed of muddy sands, which are homogeneous and bioturbated (Bassetti et al., 2006). The sandy fraction corresponds to relict "offshore sands", which cover many continental shelves around the world, at water depths generally between 80 and 120 m (Emery, 1968). These sediments represent littoral relict formations from the last eustatic low stage that were reworked during the first phase of the eustatic sea-level rise (Berne et al., 1998; Perez Belmonte, 2003). The muddy fraction has a more recent origin and is mainly sourced from the Rhone River. In the GoL, sand ripples blanketed with mud may be remobilized from the outer-shelf and supply sediments to canyon heads (Gaudin et al., 2006).

2.2.5. Suspended particle dynamics

In the GoL, the SPM is distributed in nepheloid layers, whose characteristics (concentration, extent, thickness) depend on the river discharge and the physical forcings (stratification, wind, currents and waves) affecting the coastal zone.

During flood events of the Rhone River, the delivery of particles to the shelf is strongly enhanced, until 70% of the total solid discharge (Pont, 1996). These particles are dispersed by the Rhone River plume in the coastal zone. The Rhone River plume responds to the wind forcing (~5-10 h according to Demarcq and Wald (1984)) and is advected through the shelf by the surface currents enhanced by continental (i.e. north-northwesterly) wind or along the coast during marine (i.e. east-southeasterly) wind (Broche et al., 1998; Estournel et al., 2001; Forget and Ouillon, 1998; Naudin et al., 1997; Ody et al., 2016).

Over the shelf, deposited surface sediments are resuspended by waves and currents and dispersed by bottom currents. Several studies highlight the presence of a bottom nepheloid layer (1-5 mg L^{-1}) up to 15 m thick over the shelf (Aloisi et al., 1979; Durrieu de Madron et al., 1990; Durrieu de Madron and Panouse, 1996). This nepheloid layer highly participates to the particulate transport over the shelf during all year. Marine storm events have been described as a principal factor producing sediment resuspension and redistribution overt the shelf (Dufois, 2008; Ferré et al., 2008; Ulses et al., 2008a,b) (Fig. 2.7). The sediment erosion induced by waves and strong currents, which can reach several centimeters, enhances the SPM concentration (>30 mg L^{-1}) in the water column (Ferré et al., 2005; Guillén et al., 2006; Bourrin al., 2008b). Also, the SPM dynamics is accentuated by the cyclonic circulation (∼ 50-70 cm s^{-1} close to the coast), which favors the suspended particle transport along the shelf (see red arrow on the map in Fig. 2.7).

Over the SW part of the shelf, the export of suspended particles offshelf occurs by downwelling through the Cap de Creus and Lacaze-Duthier submarine canyons as well as by bypassing the Cap de Creus to the Catalan shelf (Palanques et al., 2006, 2008; Bonnin et al., 2008; Martín et al., 2013).

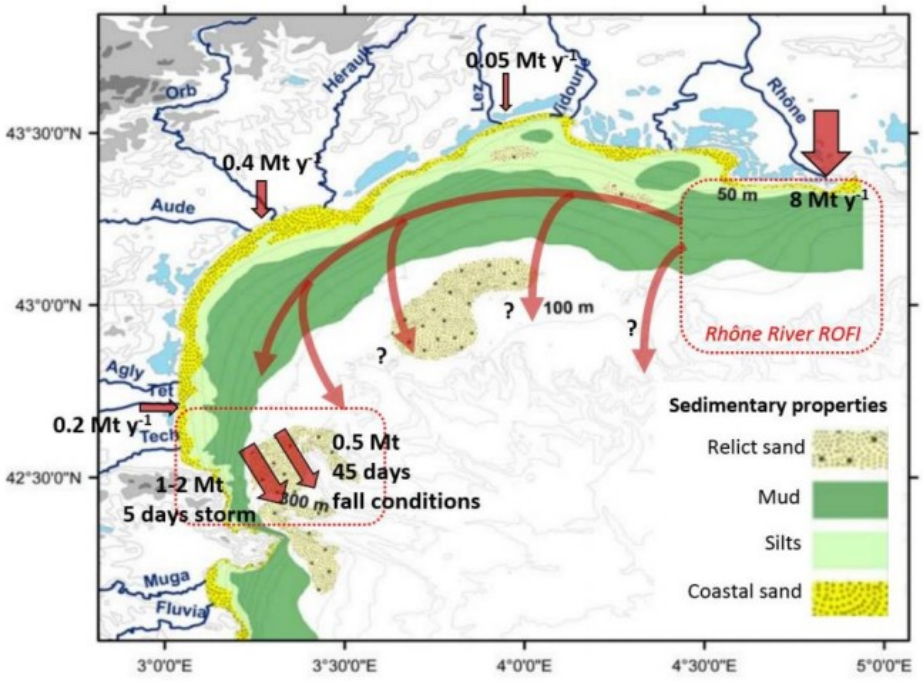

Figure 2.7: Sediment budget of the GoL shelf. The morphology of the sediment is specified. The red rectangles highlight the main areas of SPM source (Rhone River ROFI) and export (Catalan shelf).

2.3. Historical observations of hydro-sedimentary processes

In section 2.2, we defined the main hydro-sedimentary characteristics of the Gulf of Lions and their dynamics. The knowledge of the GoL's dynamics is intimately linked to our ability to accumulate physical, sedimentological, and geological measurements. Main observations carried out in the GoL are resumed in Table 2.2 and 2.3 for hydrodynamic and sediment dynamics respectively, as a function of their programmatic context. As on a larger scale (see Chapter 1.), the GoL is experiencing an increase in measurements at different spatiotemporal scales, thanks to technological developments. Indeed, until 2015, most in situ observations were gathered at few fixed locations over one or some components of the shelf (inner-, mid-, outer-, and shelf break) (Table 2.2 and 2.3). Since 2015, autonomous underwater gliders have been used in several projects (CASCADE, TUCPA, MATUGLI, CHIFRE), especially for the study of the SPM dynamics in the

Table 2.2: Previous published papers related to the Gulf of Lions' hydrodynamics, in their programmatic context.

Hydrodynamic						
Author/year	**Title**	**Processes Studied**	**Area**	**Programs**	**Observations – *Platforms***	**Other Publications In similar fields**
Millot, (1990)	The Gulf of Lions' hydrodynamics	Upwelling – intertial oscillations – Formation of dense water – wind-forced circulation – slope dynamics – River plume dynamics	Continental Shelf	ECOMARGE	Sea Surface Temperature (SST) – *Satellite* Rotor Current Meter (RCM) and Thermistor – *Mooring*	Millot and Wald, (1980) Millot and Crepon, (1981) Millot, (1982) Demarq and Wald, (1984) Devenon et al., (1992) Naudin et al., (2001) Petrenko, (2003) Bourrin et al., (2008) Schaeffer et al., (2011) Nencioli et al., (2016)
Millot, (1991)	Mesoscale and seasonal variabilities of the circulation in the western Mediterranean	Geostropgic circulation (the Northern Current)	Shelf and slope	ECOMARGE	SST – *Satellite* RCM and thermistor – *Mooring* CTD – *Research vessel* Currents – *Drifter buoys*	
Estournel et al., (2001)	The Rhone River plume in Unsteady conditions: Numerical and experimental results	River plume dynamics	ROFI	PNEC	Currents – *VHF radars and Drifter buoys* CTD – *Research vessel* *Model (Symphonie)*	
Estournel et al., (2003)	Observation and modeling of the winter coastal oceanic circulation in the GoL under wind conditions influenced by The continental orography (FETCH experiment)	Wind-forced circulation	Continental Shelf	FETCH	Currents and CTD – *Research vessel* *Model (Symphonie)*	
Raimbault and Durrieu de Madron, (2003)	Research activities in the Gulf of Lion (NW Mediterranean) within the 1997 – 2001 PNEC project	Wind-forced circulation	Continental Shelf	PNEC	Currents – *VHF radars and Drifter buoys* CTD – *Research vessel* *Model (Symphonie)*	
Petrenko et al., (2005)	Circulation in a stratified and wind-forced Gulf of Lions, NW Mediterranean Sea: in situ And modeling data	Wind-forced circulation	Shelf and slope	SARHYGOL	CTD, ADCP (Acoustic Doppler Current Profiler), and Sippican Expandable Bathy Thermograph (XBT) – *Research vessel* *Model (Symphonie)*	
Ulse et al., (2008a)	Impact of storms and dense water cascading on shelf-slope Exchanges in the Gulf of Lion (NW Mediterranean)	Formation of dense water And storm circulation	Shelf and slope	EUROSTRATFORM	CTD and ADCP – *Moorings* *Model (Symphonie)*	
Michaud et al., (2013)	Modelling and in-situ measurements of intense currents during a winter storm In the Gulf of Aigues-Mortes (NW Mediterranean Sea)	Storm circulation	Shelf	/	CTD and ADCP – *Moorings* *Model (Symphonie)*	
Petrenko et al., (2017)	A review of the LATEX project: mesoscale to submesoscale Processes in a coastal environment	Eddies circulation	Shelf	LATEX	SST – *Satellite* CTD and ADCP – *Research vessel* Currents and transport – *Drifter buoys, SF6 tracer Experiment (gaseous electrical insulator)*	
Mikolajczak et al., (2020)	Impact of storms on residence times and export of coastal Waters during a mild autumn/winter Period in the Gulf of Lion	Storm circulation	Shelf	AMORAD MISTRAL – MERMEX CASCADE	CTD and ADCP – *Moorings and Research vessel* *Model (Symphonie)* CTD and depth-averaged current – ***Glider***	

Table 2.3: Previous published papers related to the Gulf of Lions' sedimentary dynamics, in their programmatic context.

Sediment Dynamics						
Author/year	**Title**	**Processes Studied**	**Area**	**Programs**	**Observations – *Platforms***	**Other Publications In similar fields**
Aloisi et al., (1982)	Origine et rôle du néphéloide profond dans Le transfert des particules en milieu marin. Application au Golfe du Lion	River plume dynamics Bottom Nepheloid Layer (BNL)	Coastal Rivers Mouth	DYPOL	CTD, Turbidity And water samples – *Research vessel* CTD and RCM – *Mooring*	Monaco et al., (1990a) Monaco et al., (1990b) Courp and Monaco, (1990) Durrieu de Madron and Panouse, (1996) Canals et al., (2006) Guillen et al., (2006) Bassetti et al., (2006) Bourrin et al., (2008) Palanques et al., (2008) Ogston et al., (2008) Ferré et al., (2008) Dufois et al., (2008) Many et al., (2016) Pruski et al., (2019)
Heussner et al., (1990)	ECOMARGE: flux of particulate Matter in the Northwestern Mediterranean (Golfe du Lion)	Vertical SPM fluxes (transport)	Shelf and slope	ECOMARGE	RCM and sediment traps– *Mooring*	
Durrieu de Madron et al., (1990)	Hydrographic structure and nepheloid Spatial distribution in the Gulf of Lions continental margin	SPM Bottom Nepheloid Layer (BNL)	Shelf and slope	ECOMARGE	CTD, Turbidity and Water samples – *Research vessel*	
Naudin et al., (2001)	The Rhone River plume in Unsteady conditions: Numerical and experimental results	River plume dynamics Surface Nepheloid Layer (SNL)	ROFI	PNEC	Currents – *VHF radars and Drifter buoys* CTD, water samples – *Research vessel*	
Durrieu de Madron et al., (2005)	Trawling-induced resuspension and dispersal Of muddy sediments and dissolved Elements in the Gulf of Lion (NW Mediterranean)	Sediment transport under Human activities	Continental Shelf	INTERPOL	Trawling net, CTD, Turbidiy, water samples, ADCP, and corer – *Research vessels*	
Palanques et al., (2006)	Suspended sediment fluxes and transport Processes in the Gulf of Lions submarine Canyons. The role of storms and dense Water cascading	Sediment transport forced by: Storm and dense water cascading	Shelf and slope	EUROSTRATAFORM	CTD, Turbidity – *Mooring* CTD, Turbidity – *Research vessel*	
Ulses et al., (2008c)	Suspended sediment transport in the Gulf of Lions (NW Mediterranean): Impact of Extreme storms and floods	Seabed erodibility under extreme events (storm and flood)	Shelf and slope	EUROSTRATAFORM	CTD, ADCP and sediment traps – *Mooring* Currents – *Coastal buoys* *Model (Symphonie)*	
Bourrin et al., (2015)	Glider monitoring of shelf suspended Particle dynamics and transport During storm and flooding conditions	Sediment transport forced by: Storm and flood	Continental Shelf	CASCADE	CTD, ADCP, and Turbidity – *Coastal buoy and Mooring* CTD and Turbidity – *Research vessel and* ***Glider***	
Many et al., (2018)	Glider and satellite monitoring of the variability Of the suspended particle distribution And size in the Rhône ROFI	SPM dynamics	ROFI	TUCPA	SPM concentration – *Satellite* Currents – *Coastal buoy* CTD and Turbidity – ***Glider***	
Many et al., (2019)	Geometry, fractal dimentsion and settling velocity of flocs during flooding conditions In the Rhône ROFI	SPM dynamics	ROFI	MISTRAL-MERMEX MATUGLI	SPM concentration – *Satellite* Currents – *Coastal buoy* CTD, Turbidity, LISST – *Research vessel*	
Gentil et al., (2020)	Glider-based active acoustic monitoring Of currents and turbidity in the Coastal zone	SPM dynamics	ROFI	MATUGLI	SPM concentration – *Satellite* CTD, Turbidity, **ADCP – *Glider***	
Gentil et al., (2021) In prep	Sediment dynamics on the outer-shelf of the Gulf of Lions during an onshore storm: An approach based on acoustic glider And numerical modelling	Sediment transport forced By storm	Continental Shelf	CHIFRE	Granulometric samples corer – *Research vessel* Currents – *Coastal buoy* CTD, Turbidity, **ADCP – *Glider*** *Model (Symphonie)*	

coastal zone during extreme events (Table 2.3). Over the last decade, the use of a holistic approach in projects has been developed, thanks to technological advances, through a multi-platform strategy (mooring, research vessel, satellite, glider, model) to better understand and quantify sediment dynamics in the Gulf of Lions (Durrieu de Madron et al., 2008 ; Many, 2016 ; Weaver et al., 2006).

2.4. Datasets of the thesis work

Section 2.3 shows that the evolution of technologies and the robotization of instruments have allowed the use of gliders to improve knowledge of hydro-sedimentary dynamics in the GoL. However, the rapid evolution of technologies with the integration of new sensors such as the ADCP onto underwater gliders needs to be investigated. The objective of this thesis is to develop the processing chain and to explore the capability of a glider newly equipped with an acoustic Doppler current profiler to study hydro-sedimentary processes, particularly during extreme events.

The glider-ADCP data acquired during two experiments conducted respectively in 2016 and 2017 at the level of the Rhone plume (Site 1; Fig. 2.8a) and in 2018 on the continental shelf (Site 2; Fig. 2.8a) of the GoL, were analyzed by combining them with other data from traditional platforms (coastal buoys, ships, satellites) or numerical simulations (Table 2.4). Figure 2.8b-d shows glider deployments carried out during these two experiments and Table 2.4 summarizes the platforms used according to the study sites. The observations acquired by these different platforms and their processing will be detailed in chapters 3, 4, and 5.

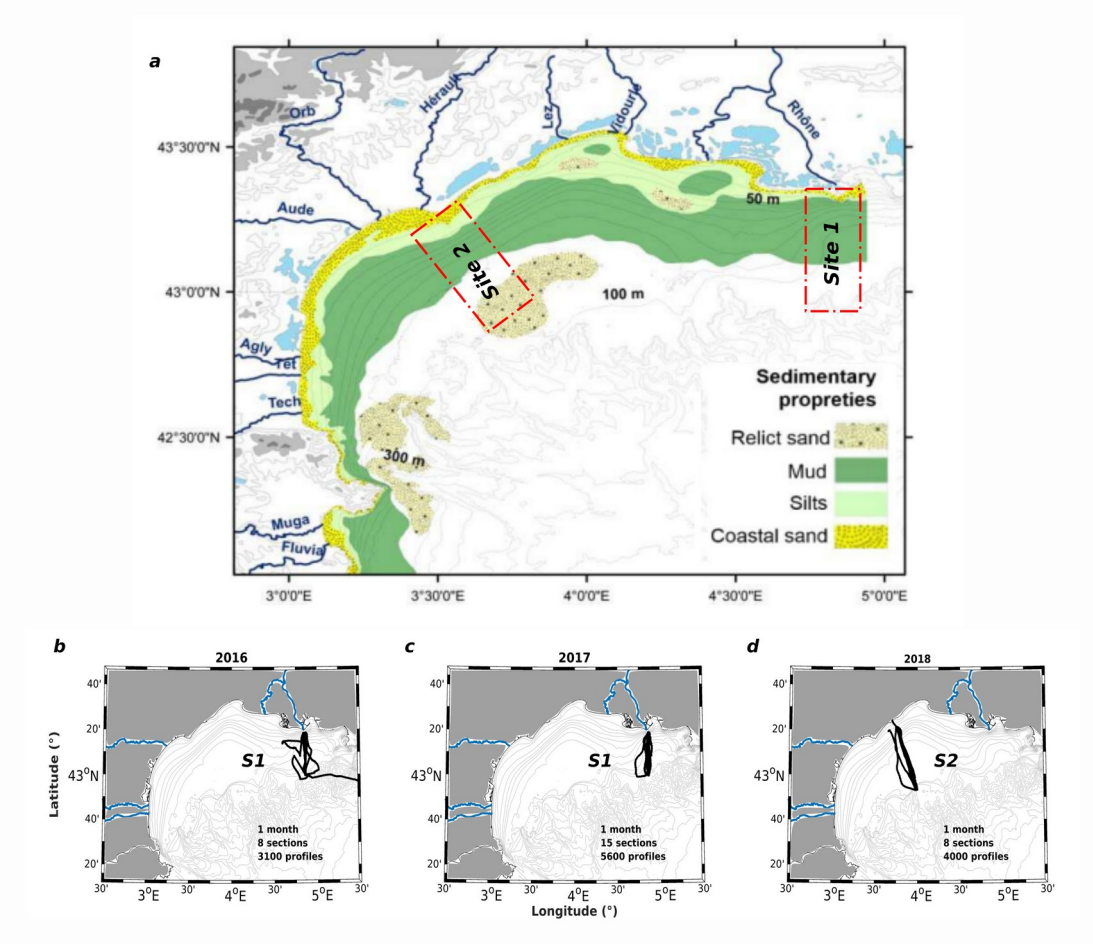

Figure 2.8: (a) Morphological and bathymetric map of the Gulf of Lions' shelf, from Bourrin, (2007). Red dash-line rectangles show the Rhone River ROFI (right; Site 1) and the Languedoc shelf (left; Site 2), study areas of Chapter 3–4 and 5 respectively. (b-d) Glider deployments according to study area, S1 and S2 for ROFI and continental shelf, respectively.

Table 2.4: List of platforms used in this thesis work as a function of programmatic context.

Project	Platform	Name	Source	Date	Days	Area	Observation
MATUGLI (leg 1)	Satellite	Modis – Aqua	Ifremer				
	Glider	Theque	/				
	Météo-France (Wind)	Cap Couronne	https://donneespubliques.meteofrance.fr/	26 Oct – 21 Nov 2016	30	ROFI	SPM dynamics and Properties during flooding conditions
	River Discharges	Beaucaire Tarascon	http://www.hydro.eaufrance.fr				
	Ship	Tethys II	/	01 – 11 Nov 2016	10		
MATUGLI (leg 2)	Satellite	Modis – Aqua	Ifremer				
	Glider	Theque	/				
	Météo-France (Wind)	Cap Couronne	https://donneespubliques.meteofrance.fr/	30 Jan – 03 Mar 2017	35	ROFI	SPM dynamics and Properties during flooding conditions
	River Discharges	Beaucaire Tarascon	http://www.hydro.eaufrance.fr				
	Ship	Tethys II	/	25 Jan – 01 Feb 2017 24 Feb – 03 Mar 2017	10		
CHIFRE	Glider	Theque	/				
	Météo-France (Wind)	Sète	https://donneespubliques.meteofrance.fr/	23 Feb – 20 Mar 2018	30	Continental Shelf	Coastal high frequency esponse to extreme events Storms and floods
	Coastal buoy	Sète	http://candhis.cetmef.developpement-durable.gc				
	ROV	MEDSEACAN	Agence des aires marines protégées	2008 -2012	/		
	Granulometric Samples	/	CEFREM	1980 – 2020	/		
	Model	SYMPHONIE	/	23 Feb – 20 Mar 2018	30		

References

Aloisi, J. C., C. Millot, A. Monaco, and H. Pauc. 1979. Dynamique des suspensions et mécanismes sédimentogénétiques sur le plateau continental du Golfe du Lion. CR Acad. Sc 289 (13): 879-82.

Aloisi, J., Cambon, J., Carbonne, J., Cauwet, G., Millot, C., Monaco, A., Pauc, H., 1982. Origine et rôle du néphéloïde profond dans le transfert des particules au milieu marin. Application au Golfe du Lion. Oceanologica Acta 5, 481–491.

Aloisi, J., 1986. Sur un modèle de sédimentation deltaıque : contribution a la connaissance des marges passives. Thèse de Doctorat d'Etat, Université de Perpignan.

Andre, G., Garreau, P., Garnier, V., Fraunie, P., 2005. Modelled variability of the sea surface circulation in the North-western Mediterranean Sea and in the Gulf of Lions. Ocean Dynamics 55, 294–308.

Bassetti, M.-A., Jouet, G., Dufois, F., Berné, S., Rabineau, M., Taviani, M., 2006. Sand bodies at the shelf edge in the Gulf of Lions (Western Mediterranean): Deglacial history and modern processes. Marine Geology 234, 93–109.

Berne, S., Lericolais, G., Marsset, T., Bourillet, J.F., De Batist, M., 1998. Erosional offshore sand ridges and lowstand shorefaces; examples from tide-and wave-dominated environments of France. Journal of Sedimentary Research 68, 540–555.

Bonnin, J., Heussner, S., Calafat, A., Fabres, J., Palanques, A., De Madron, X.D., Canals, M., Puig, P., Avril, J., Delsaut, N., 2008. Comparison of horizontal and downward particle fluxes across canyons of the Gulf of Lions (NW Mediterranean): Meteorological and hydrodynamic forcing. Continental Shelf Research 28, 1957–1970.

Bourrin, F., 2007. Variabilité et devenir des apports sédimentaires par les fleuves côtiers : cas du système Têt-Littoral roussillonnais dans le golfe du Lion.

Bourrin, F., de Madron, X. D., Heussner, S., Estournel, C., 2008a. Impact of winter dense water formation on shelf sediment erosion (evidence from the Gulf of Lions, NW Mediterranean). Continental Shelf Research 28, 1984–1999.

Bourrin, F., Durrieu de Madron, X., 2006. Contribution to the study of coastal rivers and associated prodeltas to sediment supply in gulf of lions (NW Mediterranean Sea). Vie et Milieu/Life & Environment 307–314.

Bourrin, F., Friend, P. L., Amos, C.L., Manca, E., Ulses, C., Palanques, A., De Madron, X. D., Thompson, C.E., 2008b. Sediment dispersal from a typical Mediterranean flood: the Têt River, Gulf of Lions. Continental Shelf Research 28, 1895–1910.

Bourrin, F., Many, G., De Madron, X. D., Martín, J., Puig, P., Houpert, L., Testor, P., Kunesch, S., Mahiouz, K., Béguery, L., 2015. Glider monitoring of shelf suspended particle dynamics and transport during storm and flooding conditions. Continental Shelf Research 109, 135–149.

Broche, P., J. L. Devenon, P. Forget, J. C. de Maistre, J. J. Naudin, et G. Cauwet. 1998. Experimental study of the Rhone plume. Part I: physics and dynamics. Oceanologica Acta 21 (6): 725-38.

Canals, M., Puig, P., de Madron, X. D., Heussner, S., Palanques, A., Fabres, J., 2006. Flushing submarine canyons. Nature 444, 354–357.

Carrère, L., Lyard, F., Cancet, M., Roblou, L., Guillot, A., 2012. FES 2012: a new tidal model taking advantage of nearly 20 years of altimetry measurements. Presented at the ocean surface topography science team 2012 meeting, Venice-Lido, Italy, pp. 22–29.

Certain, R., 2002. Morphodynamique d'une côte sableuse microtidale à barres : le golfe du Lion (Languedoc-Roussillon).

Courp, T., Monaco, A., 1990. Sediment dispersal and accumulation on the continental margin of the Gulf of Lions: sedimentary budget. Continental Shelf Research 10, 1063–1087.

Courtois, G., Monaco, A., 1969. Radioactive methods for the quantitative determination of coastal drift rate. Marine Geology 7, 183–206.

Demarcq, H., Wald, L., 1984. La dynamique superficielle du panache du Rhône d'après l'imagerie infrarouge satellitaire. Oceanologica Acta 7, 159–162.

Devenon, J., Broche, P., De Maistre, J., Forget, P., Gagelli, J., Rougier, G., 1992. VHF radar measurements in the Rhone river plume. Water Pol 75–87.

Dufois, F. 2008. Modélisation du transport particulaire dans le Golfe du Lion en vue d'une application au devenir des traceurs radioactifs issus du Rhône. Thèse de Doctorat. Institut de Radioprotection et de Sûreté Nucléaire. 414 p.

Dufois, F., Garreau, P., Le Hir, P., Forget, P., 2008. Wave-and current-induced bottom shear stress distribution in the Gulf of Lions. Continental Shelf Research 28, 1920–1934.

Dufois, F., Verney, R., Le Hir, P., Dumas, F., Charmasson, S., 2014. Impact of winter storms on sediment erosion in the Rhone River prodelta and fate of sediment in the Gulf of Lions (North Western Mediterranean Sea). Continental Shelf Research 72, 57–72.

Durrieu de Madron, X., Ferré, B., Le Corre, G., Grenz, C., Conan, P., Pujo-Pay, M., Buscail, R., Bodiot, O., 2005. Trawling-induced resuspension and dispersal of muddy sediments and dissolved elements in the Gulf of Lion (NW Mediterranean). Continental Shelf Research 25, 2387—2409. https://doi.org/10.1016/j.csr.2005.08.002

Durrieu de Madron, X., Nyffeler, F., Godet, C. H., 1990. Hydrographic structure and nepheloid spatial distribution in the Gulf of Lions continental margin. Continental Shelf Research 10, 915–929.

Durrieu de Madron, X., Panouse, M., 1996. Transport de matière particulaire en suspension sur le plateau continental du Golfe du Lion. Situation estivale et hivernale. Comptes rendus de l'Académie des sciences. Série 2. Sciences de la terre et des planètes 322, 1061–1070.

Durrieu de Madron, X., Radakovitch, O., Heussner, S., Loye-Pilot, M., Monaco, A., 1999. Role of the climatological and current variability on shelf-slope exchanges of particulate matter: Evidence from the Rhône continental margin (NW Mediterranean). Deep Sea Research Part I: Oceanographic Research Papers 46, 1513–1538.

Durrieu de Madron, X., Wiberg, P. L., Puig, P., 2008. Sediment dynamics in the Gulf of Lions: The impact of extreme events.

Durrieu de Madron, X, Zervakis, V., Theocharis, A., Georgopoulos, D., 2005. Comments on "Cascades of dense water around the world ocean." Progress in Oceanography 64, 83–90.

Emery, K., 1968. Relict sediments on continental shelves of world. AAPG Bulletin 52, 445–464.

Estournel, C., Broche, P., Marsaleix, P., Devenon, J.-L., Auclair, F., Vehil, R., 2001. The Rhone River plume in unsteady conditions: numerical and experimental results. Estuarine, Coastal and Shelf Science 53, 25–38.

Estournel, C., Durrieu de Madron, X., Marsaleix, P., Auclair, F., Julliand, C., Vehil, R., 2003. Observation and modeling of the winter coastal oceanic circulation in the Gulf of Lion under wind conditions influenced by the continental orography (FETCH experiment). Journal of Geophysical Research: Oceans 108.

Fanget, A.-S., Bassetti, M.-A., Arnaud, M., Chiffoleau, J.-F., Cossa, D., Goineau, A., Fontanier, C., Buscail, R., Jouet, G., Maillet, G., 2013. Historical evolution and extreme climate events during the last 400 years on the Rhone prodelta (NW Mediterranean). Marine Geology 346, 375–391.

Ferré, B., Durrieu de Madron, X., Estournel, C., Ulses, C., Le Corre, G., 2008. Impact of natural (waves and currents) and anthropogenic (trawl) resuspension on the export of particulate matter to the open ocean. Continental Shelf Research 28, 2071—2091. https://doi.org/10.1016/j.csr.2008.02.002

Ferré, B., Guizien, K., De Madron, X.D., Palanques, A., Guillén, J., Grémare, A., 2005. Fine-grained sediment dynamics during a strong storm event in the inner shelf of the Gulf of Lion (NW Mediterranean). Continental Shelf Research 25, 2410–2427.

Flexas, M., De Madron, X. D., Garcia, M., Canals, M., Arnau, P., 2002. Flow variability in the Gulf of Lions during the MATER HFF experiment (March—May 1997). Journal of Marine Systems 33, 197–214.

Forget, P., et S. Ouillon. 1998. Surface suspended matter off the Rhone river mouth from visible satellite imagery. Oceanologica acta 21 (6) : 739-49.

Forget, P., Barbin, Y., Andre, G., 2008. Monitoring of surface ocean circulation in the Gulf of Lions (north-west Mediterranean Sea) using WERA HF radars. Presented at the IGARSS 2008-2008 IEEE International Geoscience and Remote Sensing Symposium, IEEE, p. I—375.

Gaudin, M., Berné, S., Jouanneau, J.-M., Palanques, A., Puig, P., Mulder, T., Cirac, P., Rabineau, M., Imbert, P., 2006. Massive sand beds attributed to deposition by dense water cascades in the Bourcart canyon head, Gulf of Lions (northwestern Mediterranean Sea). Marine Geology 234, 111–128.

Gentil, M., Many, G., Durrieu de Madron, X., Cauchy, P., Pairaud, I., Testor, P., Verney, R., Bourrin, F., 2020. Glider-Based Active Acoustic Monitoring of Currents and Turbidity in the Coastal Zone. Remote Sensing 12, 2875.

Got, H., 1973. Etude des corrélations tectonique-sédimentation au cours de l'histoire quaternaire du Précontinent Pyrénéo-Catalan.

Guillén, J., Bourrin, F., Palanques, A., De Madron, X. D., Puig, P., Buscail, R., 2006. Sediment dynamics during wet and dry storm events on the Têt inner shelf (SW Gulf of Lions). Marine Geology 234, 129–142.

Guizien, K., 2009. Spatial variability of wave conditions in the Gulf of Lions (NW Mediterranean Sea). Vie et milieu 59, 261.

Heussner, S., Monaco, A., Fowler, S., Buscail, R., Millot, C., Bojanowski, R., 1988. Ecomarge: Flux of particulate matter in the Northwestern Mediterranean (golfe du Lion). Oceanologica Acta, Special issue.

Jago, C., Barusseau, J., 1981. Sediment entrainment on a wave-graded shelf, Roussillon, France. Marine Geology 42, 279–299.

Many, G., 2016. Impacts of storm and flood events on suspended particulate matter dynamics in the Gulf of Lions. Contributions of gliders to a multi-platform approach.

Many, G., Bourrin, F., de Madron, X.D., Ody, A., Doxaran, D., Cauchy, P., 2018. Glider and satellite monitoring of the variability of the suspended particle distribution and size in the Rhône ROFI. Progress in oceanography 163, 123–135.

Many, G., de Madron, X.D., Verney, R., Bourrin, F., Renosh, P., Jourdin, F., Gangloff, A., 2019. Geometry, fractal dimension and settling velocity of flocs during flooding conditions in the Rhône ROFI. Estuarine, Coastal and Shelf Science 219, 1–13.

Martín, J., Durrieu de Madron, X., Puig, P., Bourrin, F., Palanques, A., Houpert, L., Higueras, M., Sanchez-Vidal, A., Calafat, A.M., Canals, M., 2013. Sediment transport along the Cap de Creus Canyon flank during a mild, wet winter. Biogeosciences 10, 3221–3239.

Michaud, H., Leredde, Y., Estournel, C., Berthebaud, É., Marsaleix, P., 2013. Modelling and in-situ measurements of intense currents during a winter storm in the Gulf of Aigues-Mortes (NW Mediterranean Sea). Comptes Rendus Geoscience 345, 361–372.

Mikolajczak, G., Estournel, C., Ulses, C., Marsaleix, P., Bourrin, F., Martín, J., Pairaud, I., Puig, P., Leredde, Y., Many, G., 2020. Impact of storms on residence times and export of coastal waters during a mild autumn/winter period in the Gulf of Lion. Continental Shelf Research 207, 104192.

Millot, C., 1991. Mesoscale and seasonal variabilities of the circulation in the western Mediterranean. Dynamics of Atmospheres and Oceans 15, 179–214.

Millot, C., 1990. The gulf of Lions' hydrodynamics. Continental shelf research 10, 885–894.

Millot, C., 1982. Analysis of upwelling in the Gulf of Lions, in: Elsevier Oceanography Series. Elsevier, pp. 143–153.

Millot, C., Crépon, M., 1981. Inertial oscillations on the continental shelf of the Gulf of Lions—Observations and theory. Journal of Physical Oceanography 11, 639–657.

Millot, C., Taupier-Letage, I., 2005. Circulation in the Mediterranean sea, in: The Mediterranean Sea. Springer, pp. 29–66.

Millot, C., Wald, L., 1980. The effect of Mistral wind on the Ligurian current near Provence. Oceanologica Acta 3, 399–402.

Monaco, A., 1971. Contribution à l'étude géologique et sédimentologique du plateau continental du Roussillon (Golfe du Lion).

Monaco, Andre, Biscaye, P., Soyer, J., Pocklington, R., Heussner, S., 1990. Particle fluxes and ecosystem response on a continental margin: the 1985–1988 Mediterranean ECOMARGE experiment. Continental Shelf Research 10, 809–839.

Monaco, A, Courp, T., Heussner, S., Carbonne, J., Fowler, S., Deniaux, B., 1990. Seasonality and composition of particulate fluxes during ECOMARGE—I, western Gulf of Lions. Continental Shelf Research 10, 959–987.

Naudin, J.J., G. Cauwet, M.J. Chrétiennot-Dinet, B. Deniaux, J.L. Devenon, and H. Pauc. 1997. River Discharge and Wind Influence Upon Particulate Transfer at the Land–Ocean Interaction: Case Study of the Rhone River Plume. Estuarine, Coastal and Shelf Science 45 (3): 303-16. doi:10.1006/ecss.1996.0190.

Naudin, J. — J., Cauwet, G., Fajon, C., Oriol, L., Terzić, S., Devenon, J.-L., Broche, P., 2001. Effect of mixing on microbial communities in the Rhone River plume. Journal of Marine Systems 28, 203–227.

Nencioli, F., Petrenko, A., Doglioli, A., 2016. Diagnosing cross-shelf transport along an ocean front: An observational case study in the Gulf of Lion. Journal of Geophysical Research: Oceans 121, 7218–7243.

Ody, A., Doxaran, D., Vanhellemont, Q., Nechad, B., Novoa, S., Many, G., Bourrin, F., Verney, R., Pairaud, I., Gentili, B. 2016. Potential of high spatial and temporal ocean color satellite data to study the dynamics of suspended particles in a micro-Ttdal river plume. Remote Sensing 8 (3): 245.

Ogston, A.S., Drexler, T.M., Puig, P., 2008. Sediment delivery, resuspension, and transport in two contrasting canyon environments in the southwest Gulf of Lions. Continental Shelf Research 28, 2000–2016.

Palanques, A., de Madron, X. D., Puig, P., Fabres, J., Guillén, J., Calafat, A., Canals, M., Heussner, S., Bonnin, J., 2006. Suspended sediment fluxes and transport processes in the Gulf of Lions submarine canyons. The role of storms and dense water cascading. Marine Geology 234, 43–61.

Palanques, A., Guillén, J., Puig, P., de Madron, X. D., 2008. Storm-driven shelf-to-canyon suspended sediment transport at the southwestern Gulf of Lions. Continental Shelf Research 28, 1947–1956.

Perez Belmonte, L., 2003. Enregistrement de la dernière transgression dans le Golfe du Lion. DEA Thesis, Université Lille 1, 52.

Petrenko, A., Leredde, Y., Marsaleix, P., 2005. Circulation in a stratified and wind-forced Gulf of Lions, NW Mediterranean Sea: in situ and modeling data. Continental Shelf Research 25, 7–27.

Petrenko, A. A., 2003. Variability of circulation features in the Gulf of Lion NW Mediterranean Sea. Importance of inertial currents. Oceanologica acta 26, 323–338.

Petrenko, A.A., Doglioli, A.M., Nencioli, F., Kersalé, M., Hu, Z., d'Ovidio, F., 2017. A review of the LATEX project: mesoscale to submesoscale processes in a coastal environment. Ocean Dynamics 67, 513–533.

Pont, D., 1996. Evaluation of water fluxes and sediment supply. Oral Communication, MEDDELT, Final Meeting, Venezia.

Pruski, A.M., Buscail, R., Bourrin, F., Vétion, G., 2019. Influence of coastal Mediterranean rivers on the organic matter composition and reactivity of continental shelf sediments: The case of the Têt River (Gulf of Lions, France). Continental Shelf Research 181, 156–173.

Puig, P., De Madron, X. D., Salat, J., Schroeder, K., Martín, J., Karageorgis, A.P., Palanques, A., Roullier, F., Lopez-Jurado, J. L., Emelianov, M., 2013. Thick bottom nepheloid layers in the western Mediterranean generated by deep dense shelf water cascading. Progress in Oceanography 111, 1–23.

Raimbault, P., Durrieu de Madron, X., 2003. Research activities in the Gulf of Lion (NW Mediterranean) within the 1997–2001 PNEC project. Oceanologica Acta 26, 291–298.

Rubio, A., Arnau, P.A., Espino, M., del Mar Flexas, M., Jorda, G., Salat, J., Puigdefabregas, J., Agustín, S., 2005. A field study of the behaviour of an anticyclonic eddy on the Catalan continental shelf (NW Mediterranean). Progress in Oceanography 66, 142–156.

Rubio, A., Barnier, B., Jordá, G., Espino, M., Marsaleix, P., 2009. Origin and dynamics of mesoscale eddies in the Catalan Sea (NW Mediterranean): Insight from a numerical model study. Journal of Geophysical Research: Oceans 114.

Sadaoui, M., Ludwig, W., Bourrin, F., Raimbault, P., 2016. Controls, budgets and variability of riverine sediment fluxes to the Gulf of Lions (NW Mediterranean Sea). Journal of Hydrology 540, 1002–1015.

Sadaoui, M., Ludwig, W., Bourrin, F., Romero, E., 2018. The impact of reservoir construction on riverine sediment and carbon fluxes to the Mediterranean Sea. Progress in Oceanography 163, 94–111.

Schaeffer, A., Garreau, P., Molcard, A., Fraunié, P., Seity, Y., 2011. Influence of high-resolution wind forcing on hydrodynamic modeling of the Gulf of Lions. Ocean Dynamics 61, 1823–1844.

Serrat, P., Ludwig, W., Navarro, B., Blazi, J.-L., 2001. Variabilité spatio-temporelle des flux de matières en suspension d'un fleuve côtier méditerranéen : la Têt (France). Comptes Rendus de l'Académie des Sciences-Series IIA-Earth and Planetary Science 333, 389–397.

Ulses, C., Estournel, C., Bonnin, J., Durrieu de Madron, X., Marsaleix, P., 2008a. Impact of storms and dense water cascading on shelf-slope exchanges in the Gulf of Lion (NW Mediterranean). Journal of Geophysical Research: Oceans 113.

Ulses, C., Estournel, C., De Madron, X.D., Palanques, A., 2008 b. Suspended sediment transport in the Gulf of Lions (NW Mediterranean): Impact of extreme storms and floods. Continental shelf research 28, 2048–2070.

Weaver, P., Canals, M., Trincardi, F., 2006. EUROSTRATAFORM Vol 1: Source to Sink Sedimentation on the European Margin. Special issue of Marine Geology. Marine Geology 234, 1–292.

Chapter 3.

Glider-ADCP toolbox: a MATLAB toolbox for processing active acoustic data onto underwater glider

Chapter 3. Glider-ADCP toolbox: a MATLAB toolbox for processing active acoustic data onto underwater glider

---

Table of Contents

Table of figures

Index of table

3.1. Introduction

Autonomous underwater gliders (Davis et al., 2002) are becoming increasingly important for the collection of oceanographic measurements in observing programs, thanks to their capacity to operate autonomously in all weather conditions, for missions up to several months, and with higher sampling resolution than generally obtained with traditional platforms (Liblik et al., 2016; Rudnick, 2016; Testor et al., 2019). Glider vehicles can autonomously dive to typically up to 1000 m water depth and return to the surface navigating along predetermined sampling paths. It's a low power long duration AUV (up to approximately a year depending on sampling mode and sensors used), which is driven along a saw-tooth path primarily through small changes in buoyancy by altering the volume of the hull (air or oil). Pitch and steerage are enabled by adding wings and altering the center of mass by shifting the battery on the horizontal plane inside the hull (Rudnick et al., 2004). Gliders can carry a range of interchangeable sensor packages, and their low power consumption provides an incredibly detailed look at the water column (high-resolution measurements). As a result, they have been deployed in a wide range of environments: from continental boundary currents to the polar seas, to study aspects ranging from long-term climate variability to fine-scale submesoscale processes (Testor et al., 2019, for a full list of studies and their references). However, these technology platforms have not yet reached the same level of maturity as more traditional oceanographic monitoring platforms (Troupin et al., 2015). This implies that a newcomer to glider data analysis is exposed to many issues and time-consuming tasks that are not common when processing data from more traditional platforms.

Several initiatives as EGO (Everyone's Gliding Observatories, www.ego-network.org), GROOM (Gliders for Research, Ocean Observation, and Management), JERICO (Towards a Joint European Research Infrastructure network for Coastal Observatories, www.jerico-ri.eu), and OceanGliders (www.oceangliders.org) programs are involved in the sharing best practices,

requirements, and scientific knowledge needed to glider operations, data collection, and processing (Testor et al., 2019). As a result, several open-source user-written glider-specific softwares have become available for processing glider data. Notable open access examples include the Coriolis toolbox (EGO gliders data management team, 2017), UEA toolbox (http://www.byqueste.com/toolbox.html), SOCIB packages (Troupin et al., 2015), and more recently GliderTools developed in Python 3.7 (Gregor et al., 2019). Most of these open-source packages offer automated quality control (QC) for CTD (Conductivity, Temperature, Depth) sensors and glider navigation data. GliderTools expands these advances with modules for bio-optical data QC, vertical gridding, and two-dimensional interpolation. These developments cover the main stages of the data management process, including metadata aggregation, data download, advanced data processing, and the generation of data products and figures for the traditional sensors mounted on gliders. However, recent technological advances allowed the integration of more complex sensors onto underwater gliders such as Acoustic Doppler Current Profilers (ADCP) to measure currents (Gentil et al., 2020; Merckelbach et al., 2019; Todd et al., 2017), microstructure to measure turbulence (Merckelbach et al., 2019; Palmer et al., 2015; Wolk et al., 2009), or even Laser In Situ Scattering and Transmissometry (LISST) particle analyzer to characterize suspended particles populations (Miles et al., 2021, 2018) in the water column. A need exists to operate and manage the data streams in real-time and delayed mode, from these new complex sensors.

In the absence of an available processing chain, I had to develop at the beginning of my thesis work a toolbox to process ADCP glider data, to be able to analyze and interpret the current and acoustic backscatter data for hydro-sedimentary issues. In this study, a focus is carried out on the active acoustic glider sensor (ADCP) to derive absolute velocities and their baroclinic component (hydrodynamic), as well as backscatter index (proxy of particulates matter concentration) in the water column. This chapter, combined with a clear annotation of the code,

provides a framework to process acoustic glider data. The toolbox overview and glider setup are described in sections 3.2 and 3.3, respectively. Finally, section 3.4 presents the data chain processing step by step.

3.2. Toolbox overview

The toolbox is available from (https://github.com/mgentil17/mgentil17), without any registration or login required. A dataset is also provided to run the toolbox.

The glider-ADCP toolbox is composed of a set of MATLAB (MATLAB, 2018) scripts and functions designed to process the data collected by a Teledyne Webb Research Slocum glider from recent data-processing methods. Currently, the toolbox version supports the Slocum G1 model. This toolbox is designed to provide a delayed mode quality control on the physical, bio-optical, and acoustic sensor on the glider's suite. Delayed mode data includes all data collected from ocean gliders that are stored on the vehicle during its mission and need to be checked thoroughly by PI and against other measurements (ship-based observations, satellites). The toolbox operates on data conversion, advanced data processing, and the generation of data products and figures.

Figure 3.1 presents the workflow of the glider-ADCP toolbox, which is divided into 8 steps. The toolbox is organized around two main scripts (rectangles with red outlines). The former, *Glider_Adcp_main_program.m*, is summarized by the processing chain (step 0 to 7) and calls all the functions used in the toolbox. For each processing step, the external and internal data (circular boxes), the functions in the modules (grey rectangles) and their dependencies (arrows), as well as the outputs (figures and files) are made explicit. The toolbox is built to output 5 levels (L0 to L4) of MATLAB files (. mat), related to different levels of processing steps described in Figure 3.1 and

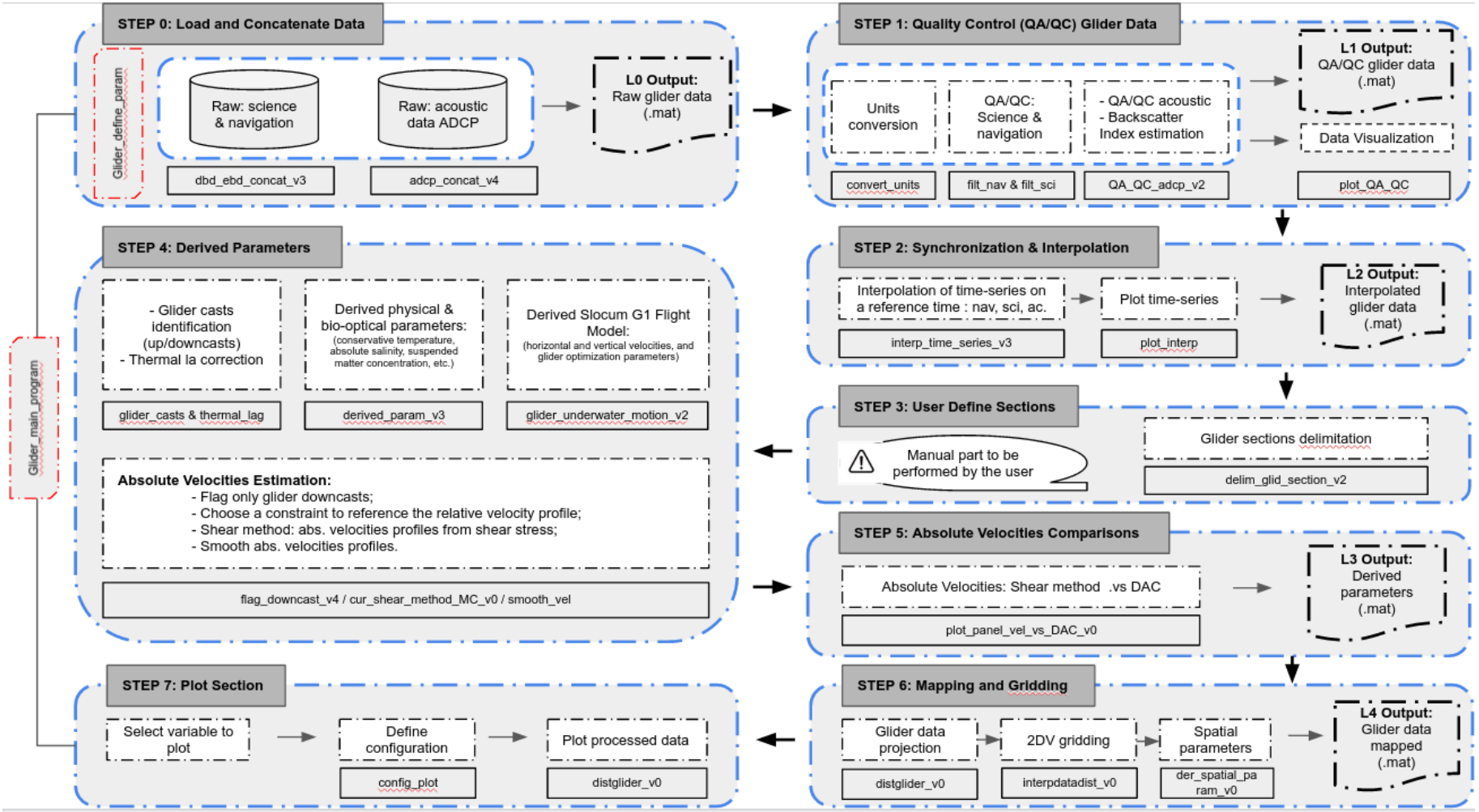

Figure 3.1: Scheme of the Glider-ADCP treatment chain step by step (initial step "0" to the final one "step 7"). The white rectangles show the processing action performed in each of the modules. The grey rectangles represent the codes (. m) associated with the action boxes. Black and grey arrows show dependencies between the different modules and the different action boxes, respectively. Five levels of outputs (L0 to L4) are produced from the processing chain. Finally, the rectangles with red outlines are the two main scripts of the toolbox.

detailed and applied in section 3.4 (i.e., Processing Steps). The latter script, *Glider_ADCP_define_param.m*, is the script that declares the parameters chosen by the user for each processing step and that is loaded in the *Glider_Adcp_main_program.m* in the initial step (step 0). The parameterization stage is essential to ensure the correct processing of data in steps 1 to 6 and is also described in section 3.4.

3.3. The Glider-ADCP

3.3.1. Explorer ADCP setup

An Explorer Doppler Velocity Log with Acoustic Doppler Current Profiling capacity (Explorer ADCP) was integrated into a special payload bay on the Slocum glider (Fig. 3.2a). The Explorer ADCP has a downward facing transducer which was tilted forward by 11°, enabling to compensate for the pitch of the glider during downcasts. The inclination of the transducer optimized the three-beam measurements on the 26° pitched glider downcasts with the three forward ADCP beams oriented 15° from vertical, and with the fourth, 45° aft relative to the glider (Fig. 3.2b). The offset of 11° represents the best compromise between optimizing for beam position and minimizing the hydrodynamics drag penalties of the mounting (Mullison et al., 2013). However, this fixed forward configuration rendered the device unsuitable for collecting measurements during ascent. Indeed, the non-rotated orientation of the head does not allow respecting the assumption about symmetry (beam pairs), during upcast measurements as shown in Fig. 3.2b (Mullison et al., 2013). For this reason, only downcast measurements were used in this study (black line in Fig. 3.2c).

3.3.2. Glider operation

In this study, we deployed a Slocum glider equipped with a CTD, an optical payload, and a downward looking ADCP (Fig. 3.2a). The Teledyne Webb Research Slocum glider (G1) can autonomously dive to typically up to 200 m water depth. The adjustment of its buoyancy allows it

to navigate along a saw-tooth path through the water column (Fig. 3.2c). Continuously CTD and optical measurements are acquired by the glider along its ascent and descent, according to the sampling frequency user-defined. Also, ADCP periodically records: (i) echo intensity measurements to estimate backscatter index, which is a proxy of SPM concentration, (ii) the relative velocities measurements to estimate absolute velocities, and (iii) the bottom track measurements, which is the direct measure of speed over the ground when in range of the bottom. In this study, we used an Explorer ADCP of 614 kHz, which allows measuring echo intensity and relative velocity in the water column, only during downcast (see section 3.1), to a maximum range of 40–50 m (gridding area in Fig. 3.2c). From this device frequency, the first bottom track measurements are detectable around 50 meters until 2 m above the seabed (green line in Fig. 3.2c), which corresponds to the inflection point of the glider. During surfacing, the glider uses GPS positioning to estimate the difference between the expected surface location from underwater dead reckoning and the GPS fixes. Such position difference, dependent on the duration of the dive, allowed to estimate the depth-averaged current (DAC) between two surfacings (Fig. 3.2d) (Eriksen et al., 2001; Rudnick et al., 2018). Also during surfacing, the glider records GPS fixes, to transfer data to land and to receive any new information about its route configuration. This operation takes between 10–15 min, where the glider is subject to wind and currents forcing, resulting in surface drift (red line in Fig. 3.2c). In coastal environments, multiple yos (upcast/downcast pairs) are the standards (Fig. 3.2d) to limit the glider's surfacing to reduce the risk of collision with ships or topography (coast). During a sequence of multiple yos, the glider dive to typically 2 m above the bottom and ascent to 1 m from the surface (dashed line blue in Fig. 3.2c), leading to an under-sampling of the surface layer (0–1 m).

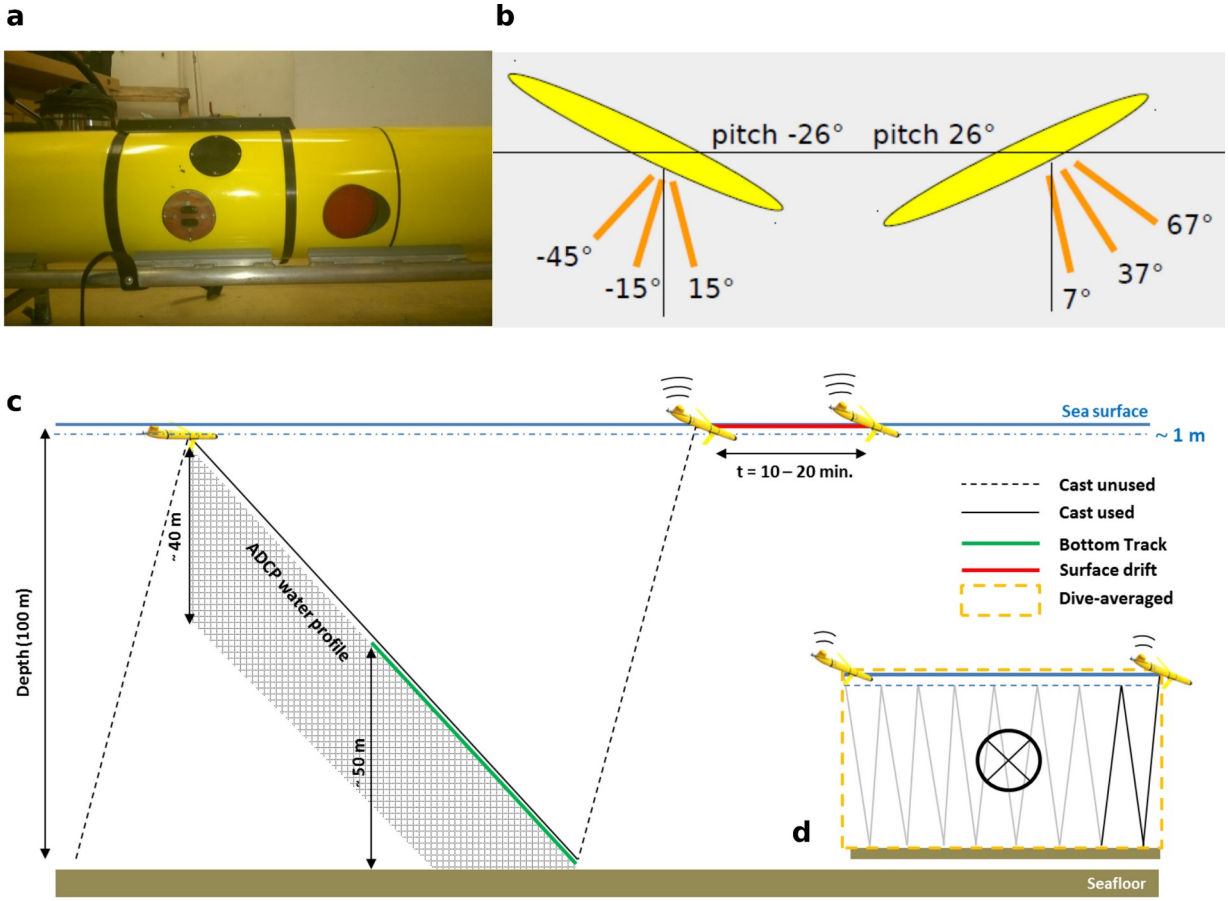

Figure 3.2: (a) A view of the BBFLCD optical payload (black) and Explorer ADCP payload (red) integrated into a G1 Slocum glider (photo credit: Gaël Many). (b) Flight orientations showing relative beam angles from a downward looking Explorer ADCP. (c, and d) Glider operation and data acquisition.

3.3.3. Glider deployments

Three deployments of a Slocum glider equipped with an active acoustic sensor were carried out in 2016, 2017, and 2018 over the micro-tidal continental shelf of the Gulf of Lions in the NW Mediterranean (Fig. 3.3a), as part of programs to study sediment flux dynamics during extreme events (flood and storm). A total of 3 months of acquisition, 31 sections, and more than 12,700 profiles were recorded for these deployments and were used to develop the toolbox. In this study, the dataset provided to run the glider-ADCP toolbox corresponds to the deployment carried out in winter 2017 (Fig. 3.3b). Examples of profiles of the experiments are used to illustrate the toolbox capacities in section 3.4.

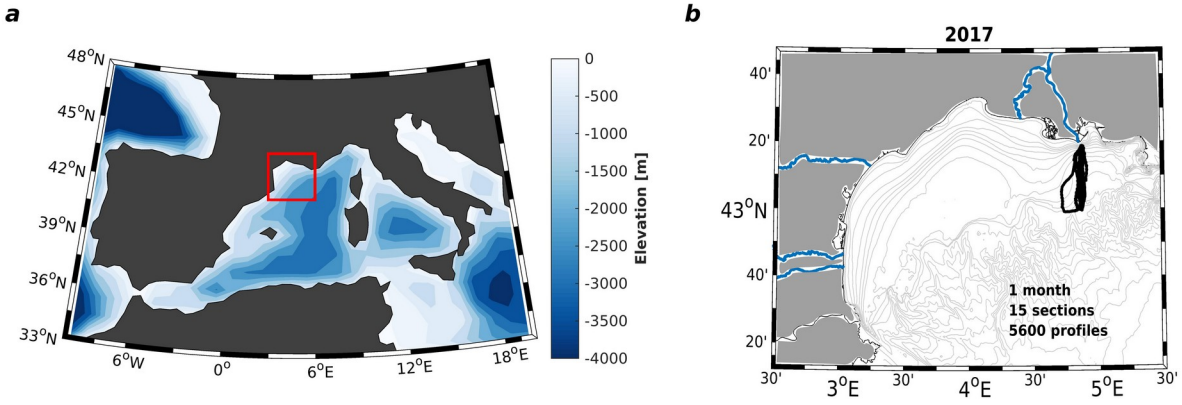

Figure 3.3: (a) Western Mediterranean, the Gulf of Lions is located by a red square. (b) Glider-ADCP deployment (black lines) over the Gulf of Lions shelf in winter 2017.

3.4. Processing steps

3.4.1. User-defined parameters

Glider_ADCP_define_param.m is one of the two main scripts of the toolbox. In this script, we have defined the set of variables involved in data processing and on which the user can adjust the values according to the scientific processes studied. The main parameters to be filled in are:

- Conversion and calibration of sensors values;
- The magnetic declination for glider compass;
- The configuration of ADCP (pitch inclination, conversion factor) and threshold values for control quality data (correlation signal, velocity intensity, time lag, bottom track offset);
- The reference time to synchronize and interpolate data;
- Glider parameters that will be optimized in the flight model (glider volume, mass, hull compressibility, and parasite drag);
- Options for the parameters optimization;

- Parameters to process acoustic data (bin size, standard deviation of a single ping measurement, number of iterations for Monte-Carlo simulations, vertical and horizontal filters);
- Reference positions and projection angle for mapping the data;
- Vertical and horizontal resolution for gridding processed data.

3.4.2. Step 1: quality control of glider data – output level 1 files

The different sensors are processed separately because the temporal data are not synchronized and may have different sampling resolutions. In this study case, the navigation and science bay has a sampling frequency of 4 s and acoustic data of 10 s. During this step, first simple unit conversions and factory calibrations are applied to the science, navigation, and acoustic bay. In a second stage, several filters are applied:

Science and navigation data—the compass data are corrected for magnetic declination, gaps of pressure are removed, as well as glider position outliers, and null values. Figure 3.4 shows that ~8% of the navigation, ~55% of CTD, and ~51% of bio-optical data are removed after applying these filters. The majority of the removed data are empty cells because the time vector increments every 2 s. Even though science and navigation have the same sampling rate (4 s), dead reckoning estimates the position of the glider at each time increment, explaining the small amount of data removed for navigation.

Acoustic data—raw ADCP data were subjected to a quality checking algorithm to mask low-quality data as well as to correct data. Following Todd et al. (2017), a pipeline of operations was set up: to correct the speed of sound using an average salinity value of 38; to correct time lag; to correct the real depth of each bin from roll and pitch effects; to mask instrumental data according to the factory threshold of 64 counts of the correlation signal (Gordon, 1996); to mask relative water

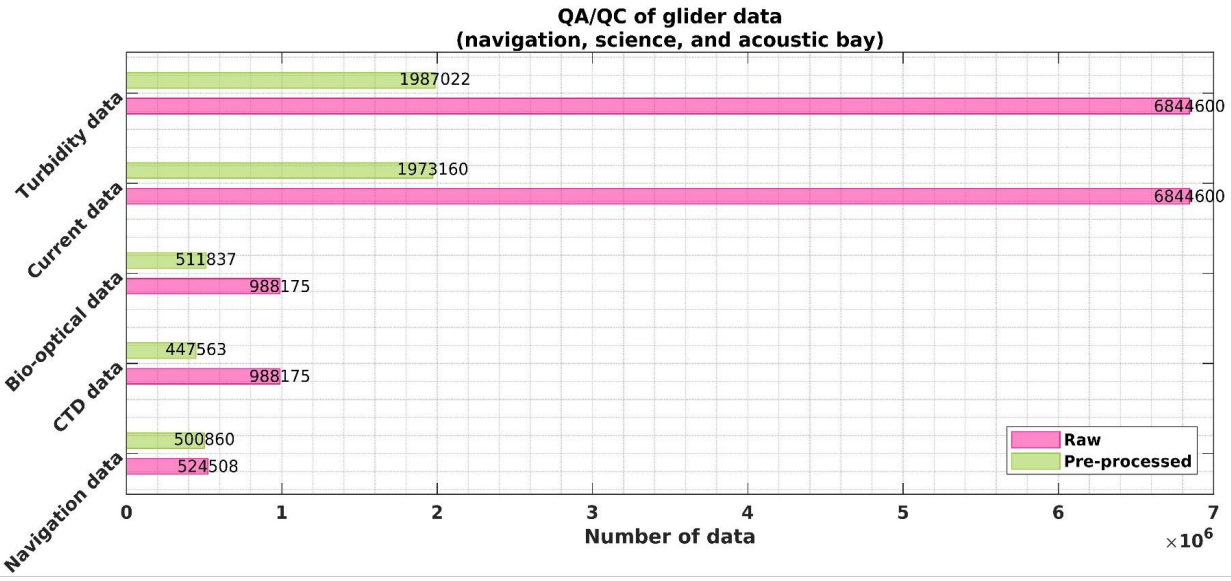

Figure 3.4: Control quality (QA/QC) carried out on glider data: for navigation, science (science and bio-optical), and acoustic bay (current and turbidity). Raw and pre-processed data after applying the thresholds defined in the Glider_ADCP_define_param.m are in pink and green, respectively.

velocities and bottom-track velocities that exceed 0.75 m s^{-1}. Figure 3.4 shows that ~70% of currents and turbidity data are removed. The acoustic data are very noisy, and applying only the factory threshold reduces the data range by 50 to 60%. At the end of these operations, the L1 matrix file containing pre-processed glider data is generated.

3.4.3. Step 2: synchronization & interpolation – output level 2 files

During this step, the user defines the temporal limits of the study, as well as the time step between two measurements. The data from each sensor are synchronized and interpolated to this new reference time. The user should be careful to choose a time step in accordance with the sampling rate of the sensors. In our study case, we chose to synchronize CTD, bio-optical, and navigation data with ADCP data, which have the lowest resolution acquisition, and interpolate to the same periodicity (10 s). Figure 3.5 shows an example of the interpolation of navigation (pitch, roll, heading), CTD (temperature), and bio-optical (backscatter and chlorophyll-a) data. At the end

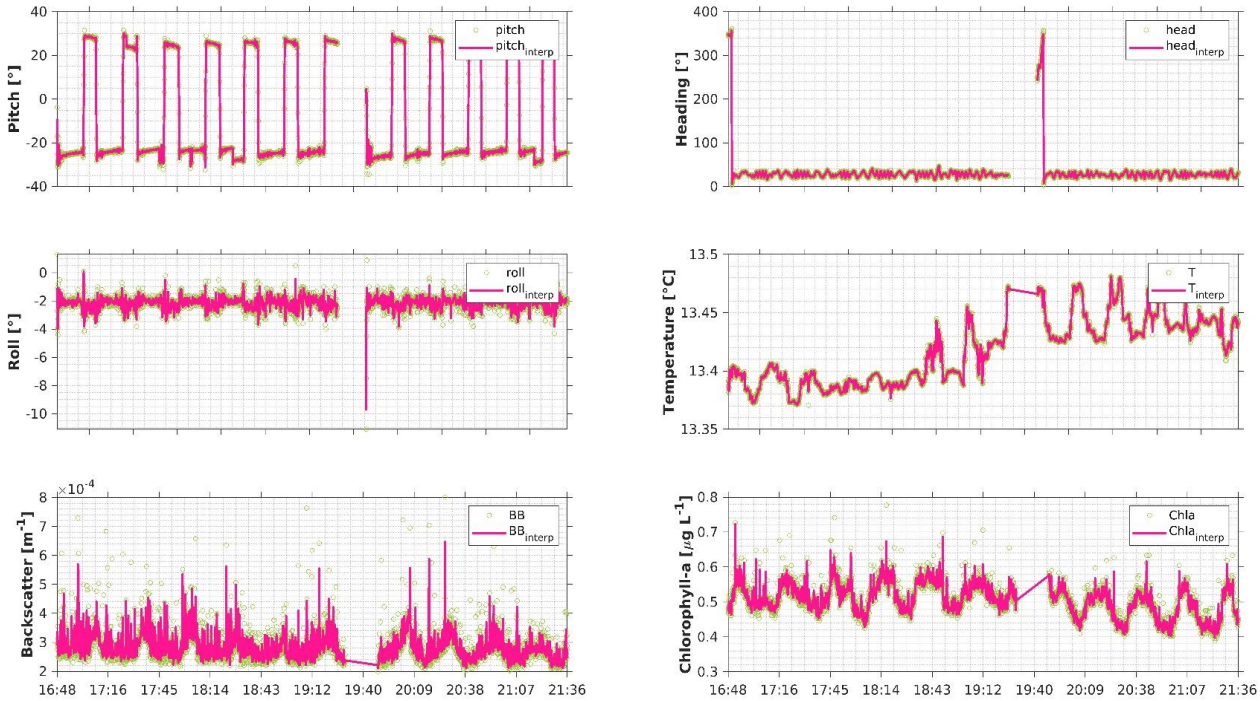

Figure 3.5: Interpolation of glider time series: raw data and interpolated data are in green and pink, respectively.

of these operations, the L2 matrix file containing synchronized and interpolated glider time series is generated.

3.4.4. Step 3: user-defined sections

During this step, the user defines manually one or more sections over the deployment, called section(s) of interest(s) (SOI[s]). Data processing will be performed on the SOI(s). It is necessary to choose a positioning variable (longitude or latitude) to be plotted as a function of time. Then a dialog box is displayed, where the user defines the number of sections to process (Fig. 3.6). Finally, each section chosen needs to be delimited by two clicks on the plot, (start and endpoints). Figure 3.6 shows an example where latitude is chosen to delimit a SOI.

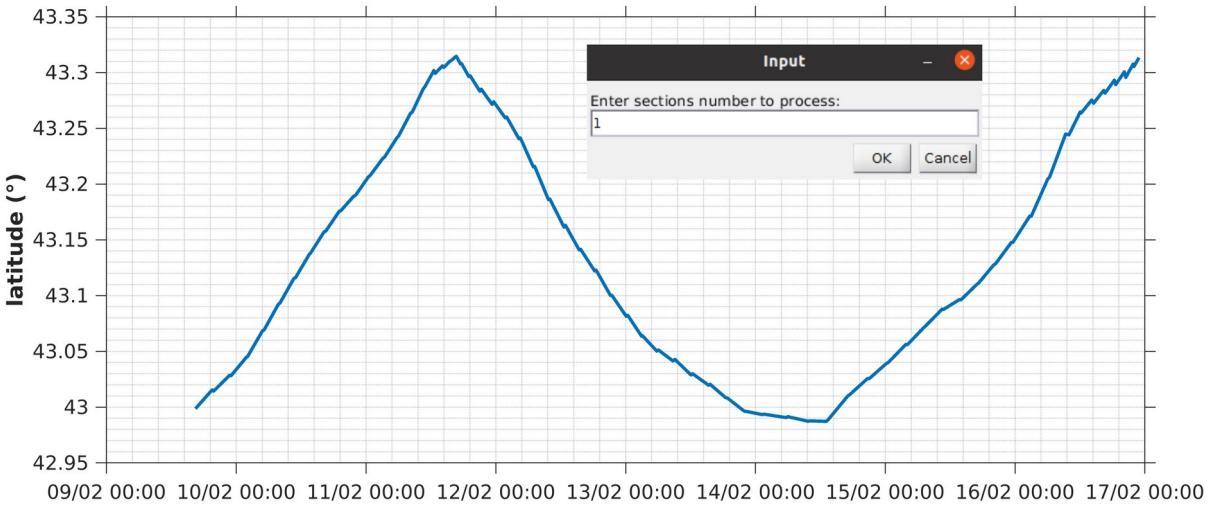

Figure 3.6: Latitude as a function of time to delimit section of interest (SOI). The user needs to select the number of sections to keep for data processing.

3.4.5. Step 4: derived parameters – data processing

The objective of this step is to output well-referenced trajectory data with derived measurements and corrections over the SOI. To generate the derived measurements and corrections, operations are applied in the following order:

3.4.5.1. Glider profiles and thermal lag corrections

First, the pressure of the different sensors (CTD, ADCP, and glider navigation) are compared and adjusted to obtain a reference pressure vector. A gradient threshold on the reference pressure is used to identify dive and ascent glider profiles. At this stage, the thermal-lag correction on CTD data is applied, following the work of Garau et al. (2011). This operation is very time-consuming. The user needs to select several combined profiles (dive/ascent) for which the correction is calculated. Then the average correction is applied to the whole time series. Figure 3.7 shows the result of the average thermal lag correction on a temperature and conductivity profile, after a calculation made on 50 combined profiles of ascents and dives.

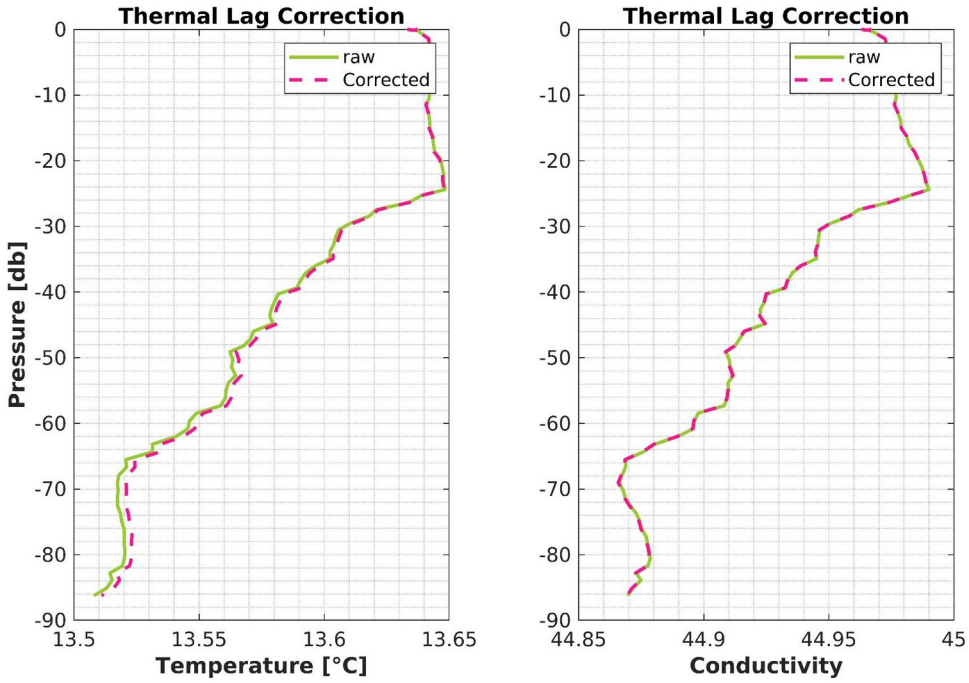

Figure 3.7: A profile of temperature and conductivity with raw data (green) and corrected from thermal lag (pink), following the work of Garau et al. (2011).

3.4.5.2. Physical and bio-optical parammeters

Once the thermal lag is corrected a series of physical parameters can be derived. Salinity, potential temperature, depth, density, Brunt-Väisälä frequency, and others were derived using the TEOS-10 equation (McDougall and Barker, 2011). Furthermore, this toolbox was designed to study hydro-sedimentary processes. The user can load the calibration file of the optical sensor used during the glider deployment, and the suspended particulates matter concentration is derived from the calibration coefficients.

3.4.5.3. Glider flight model

At this stage, a series of operations is applied to estimate vertical and horizontal glider velocities relative to the water in each point of its path, based on a glider quasi-static flight model developed by Merckelbach et al. (2010). Parameters of the glider flight and their origins are presented in Table 1, adapted from Margirier et al. (2017).

Table 1: Parameters of the glider flight, their origins, and their typical value adapted from Margirier et al. (2017)

Parameter	Description	Origin	Typical value	Unit
F_d	Buoyancy frequency	Computed		N
F_g	Gravitational force	Computed		N
F_L	Lift force	Computed		N
F_d	Drag force	Computed		N
U	Glider velocity	Computed		m s^{-1}
U_{glider}	Glider horizontal velocity	Computed		m s^{-1}
W_{glider}	Glider vertical velocity	Computed		m s^{-1}
W_{water}	Water vertical velocity	Computed		m s^{-1}
α	Attack angle	Computed	+/- 2-3	°
γ	Glide angle	Computed		°
θ	Pitch angle	Measured by glider sensors	+/- 26	°
P	Water pressure	Measured by glider sensors		Pa
T	Water temperature	Measured by glider sensors		°C
ρ	Water density	Measured by glider sensors		kg m^{-3}
C_{D0}	Parasite drag	Optimized	0.13	rad^{-2}
ε	Hull compressibility	Optimized	1.1 x 10^{-9}	Pa^{-1}
V_g	Glider volume	Optimized	0.065	L
T_0	Reference water temperature	Characteristic of the glider	13.1	°C
g	Acceleration of gravity	Characteristic of the glider	9.81	m s^{-2}
m_g	Glider mass	Optimized	66.6	kg
ΔV_g	Pumped volume	Characteristic of the glider	0.23	L
S	Wing surface area	Characteristic of the glider	0.1	m^2
C_{D1}	Induced drag	Characteristic of the glider	2.88	rad^{-2}
a	Lift coefficient	Characteristic of the glider	6.1	rad^{-1}
α_T	Thermal expansion coefficient	Characteristic of the glider	7.05 x 10^{-5}	K^{-1}

The glider is modeled in a steady-state flight (no acceleration) in still water. The lift, drag, weight, and buoyancy forces must balance. A schematic view of the forces exerted on the glider is represented in Figure 3.8a, with F_b, F_g, F_L, F_d, respectively the buoyancy, gravity, lift and drag force. Typical values of the different parameters are given in Table 1.

$$F_b = g\rho\left(V_g\left(1-\epsilon P+\alpha_T\left(T-T_0\right)\right)+\Delta V_g\right) \quad (3.1)$$

$$F_g = m_g g \quad (3.2)$$

$$F_L = \frac{1}{2}\rho S U^2 a\alpha \quad (3.3)$$

$$F_d = \frac{1}{2}\rho S U^2\left(C_{D_0}+C_{D_1}\alpha^2\right) \quad (3.4)$$

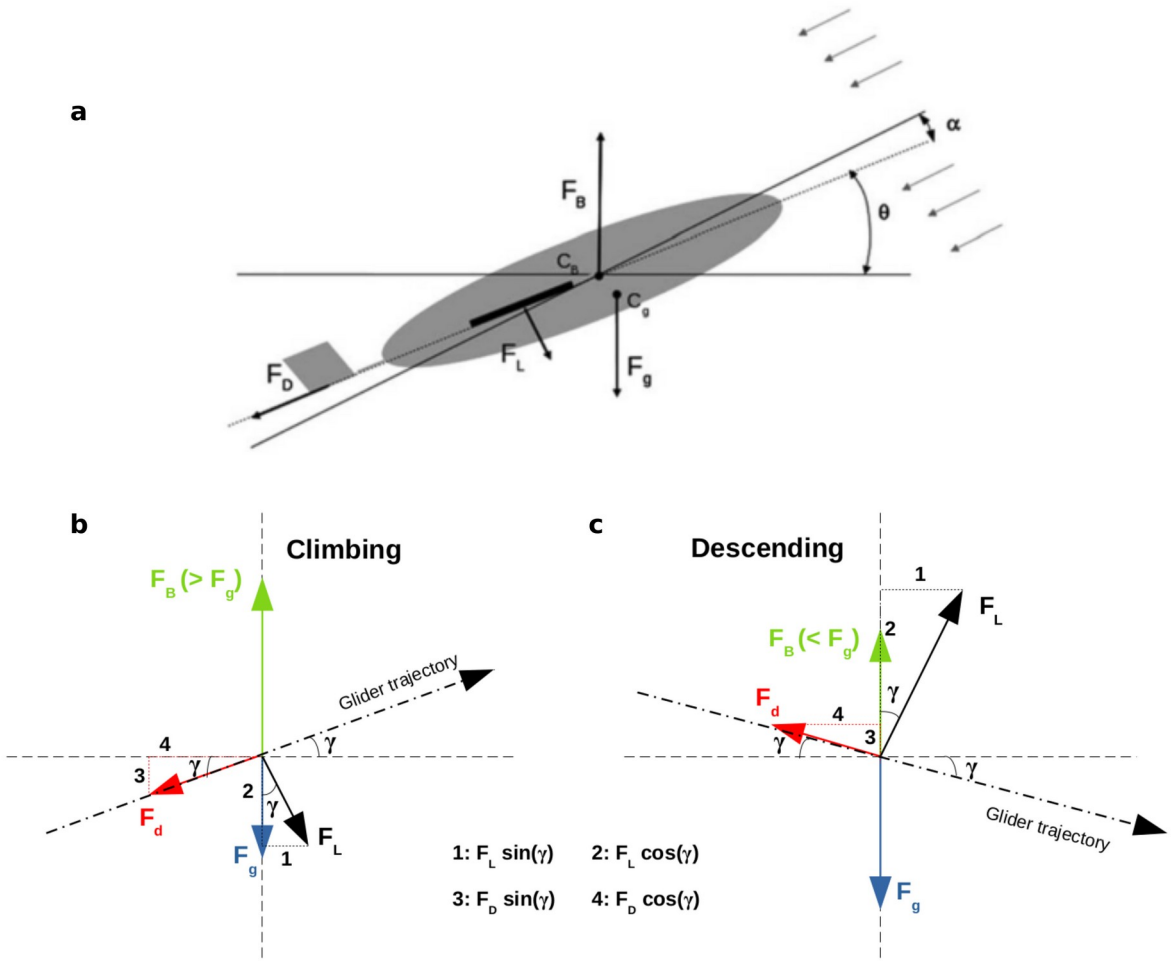

Figure 3.8: (a) Schematic view of a glider flight on a vertical plane: buoyancy force F_b, gravity F_g, lift F_L, and drag F_d; the sum of attack angle α and pitch θ makes the glide angle γ from Margirier et al. (2017). (b) Diagram of force balance on the Slocum glider during a climb (b) and a dive (c). Forces are defined in (a) and γ is the glide angle.

The projections of the glider-static equilibrium on the vertical and horizontal during a climb (Fig. 3.8b) and a descent (Fig. 3.8c) thus give:

$$(z_{climb}): F_B - \cos(\gamma) F_L - \sin(\gamma) F_d - F_g = 0 \qquad (z_{descent}): F_B + \cos(\gamma) F_L + \sin(\gamma) F_d - F_g = 0 \tag{3.5}$$

$$(x_{climb/descent}): \cos(\gamma) F_d - \sin(\gamma) F_L = 0 \tag{3.6}$$

Using equation 3.5, it is possible to determine the glider velocity along its path, U, from equations 3.1 and 3.3.

$$U_{climb}=\sqrt{\frac{2(F_b-F_g)\sin(\gamma)}{\rho S[C_{D_0}+(C_{D_1})\alpha^2]}} \qquad U_{descent}=\sqrt{\frac{-2(F_b-F_g)\sin(\gamma)}{\rho S[C_{D_0}+(C_{D_1})\alpha^2]}} \qquad (3.7)$$

Despite the negative sign, solving equation 3.7 on the descent, gives a positive speed which is identical to the climb. There is only one unknown, the angle of attack, α, which is written from the equation 3.6, and solving with an iterative method.

$$\alpha=\frac{C_{D_0}+C_{D_1}\alpha^2}{a\tan(\theta+\alpha)} \qquad (3.8)$$

We then obtain the glider's vertical (eq. 3.9) and horizontal (eq. 3.10) velocities.

$$W_{glider}=U\sin(\alpha+\theta) \qquad (3.9)$$

$$U_{glider}=U\cos(\alpha+\theta) \qquad (3.10)$$

Taking into account the compass of the glider, β, we derive the east-west (u_h) and noth-south (v_h) horizontal components of the current.

$$u_h=U\cos(\alpha+\theta)\sin(\beta) \qquad (3.11)$$

$$v_h=U\cos(\alpha+\theta)\cos(\beta) \qquad (3.12)$$

To assess the quality of the flight model, we compared the vertical glider velocity estimated from optimization and the pressure sensor (Fig. 3.9). The vertical water velocity is estimated as the difference between the velocity derived from the rate of change of pressure and that predicted by the glider flight model. Vertical movements of the water are minimized (the model makes the hypothesis there are none) over a 24h period (long enough to consider that the mean vertical velocities are null) (Margirier et al., 2017). The term on the left in equation 3.13 is therefore equal to zero.

$$w_{water}=\frac{dz_p}{dt}-w_{glider} \qquad (3.13)$$

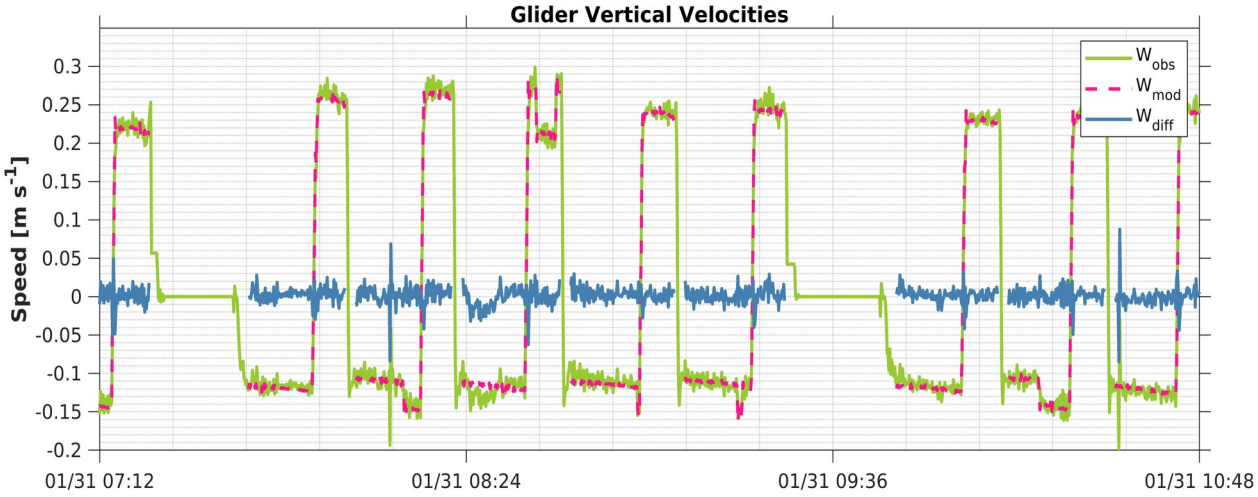

Figure 3.9: Flight parameters and resulting water vertical velocity in a steady-state hypothesis. Glider vertical velocity (w_{glider}) (pink), pressure gradient induced velocity $(\frac{dz_p}{dt})$ (green), and water vertical velocity (w_{water}) (blue).

As expected, the vertical water motion is on average equal to zero (in blue, Fig. 3.9), assuming still water in the flight model. Furthermore, the robustness of the method is highlighted by the fact that the extracted vertical velocities are not affected by the glider vertical movement (dive/ascent). Indeed, when the glider switches from a downward to an upward motion, the water vertical velocity remains coherent (variation <5 cm s^{-1}). During the second dive, we can see a spike in the data. This is probably because the pitching battery moved, and we use a steady-state model. The steady-state model does not include these changes and adapts instantly, in contrast to the glider. These spikes are filtered in the toolbox.

The validation of the glider flight model allowed us to recalculate the glider's velocity in each component and at each point of its path in the water column. The steady-state flight model requires four calibration parameters, the parasite drag coefficient (C_{D_0}), glider volume (at atmospheric pressure) (V_g), hull compressibility (ϵ) and the glider mass (m_g), which are found by minimizing a cost function based on the variance of calculated vertical water velocity.

$$J(C_{D0}, \epsilon, V_g, m_g) = \sum \left(\frac{d z_p}{dt} - w_{glider}\right)^2 \qquad (3.14)$$

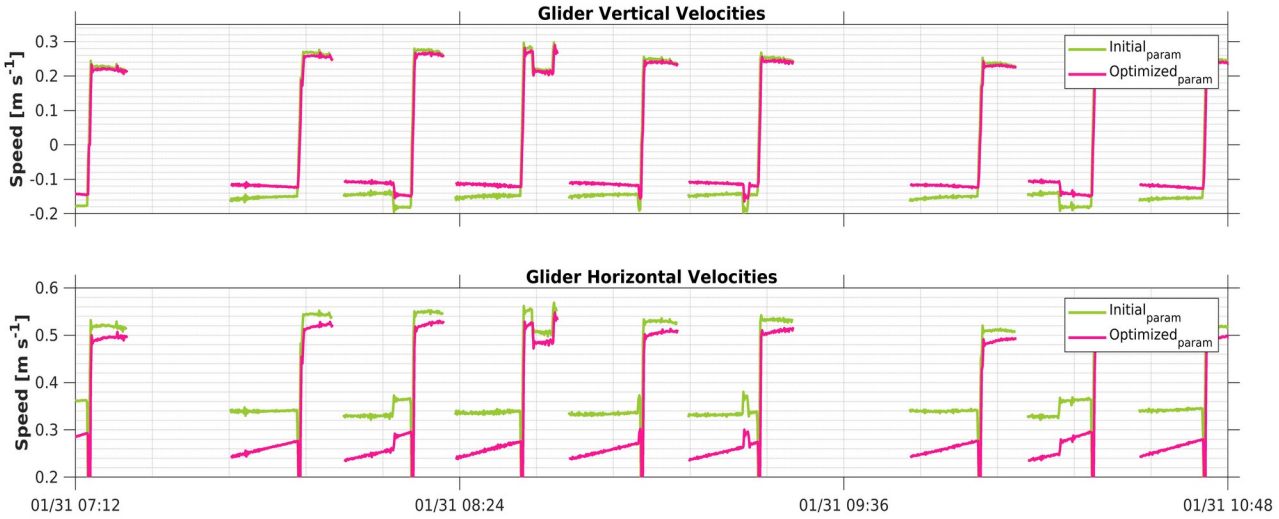

Figure 3.10: Glider's velocity components: (top) vertical velocity, and (bottom) horizontal velocity. The glider's velocity from the initial parameters is shown in green, while those from the optimized parameters from the quasi-steady flight model (Merckelbach et al., 2010) are in pink.

Figure 3.10 shows that with the initial parameters the vertical and horizontal glider's velocities are overestimated, especially during a dive. An average difference of about 3 and 15 cm s^{-1} is found between the initial and optimized velocities for the vertical and horizontal components, respectively. While during upcast, vertical velocities are similar and a difference of 5 cm s^{-1} is found on the horizontal component. The optimized average velocities are therefore of the order of 0.15 and 0.25 m s^{-1} in descent for the vertical and horizontal components, respectively, and of 0.25 and 0.5 m s^{-1} for upcast. The accuracy of the glider motion is fundamental to derive the absolute water velocities.

3.4.5.4. Absolute velocities and backscatter index

3.4.5.4.1. Backscatter index estimates

The received level (RL) of the acoustic return along each beam was converted into the backscatter index (BI, in dB) from Mullison, (2017) .

$$BI = 10\,log_{10}\left(10^{(Kc(RL-Er/10))}-1\right)+TL_w+TL_g \qquad (3.15)$$

where Kc is the count to dB factor (0.61 for the ADCP used in this work), RL the received level in counts, Er the noise in counts (50 counts), TLw the loss due to absorption by seawater (Francois and Garrison, 1982), and TLg the loss due to geometrical spreading. The computation of the speed of sound was based on the Explorer temperature sensor and an average salinity value of 38.

ADCP provides a series of overlapping profiles (Fig. 3.11a) over a typical vertical range of O(20) m after the control quality (Fig. 3.11b). The successive profiles of the backscatter index were stacked to reconstruct the profile over the entire water column from the median values of the overlapping data at each level (Visbeck, 2002). The associated uncertainty corresponds to the standard deviation of the stacked values for each bin (in this study case is 1 m depth bin). A final three-point centered moving-average filter was applied to eliminate the high-frequency noise (Fig. 3.11c).

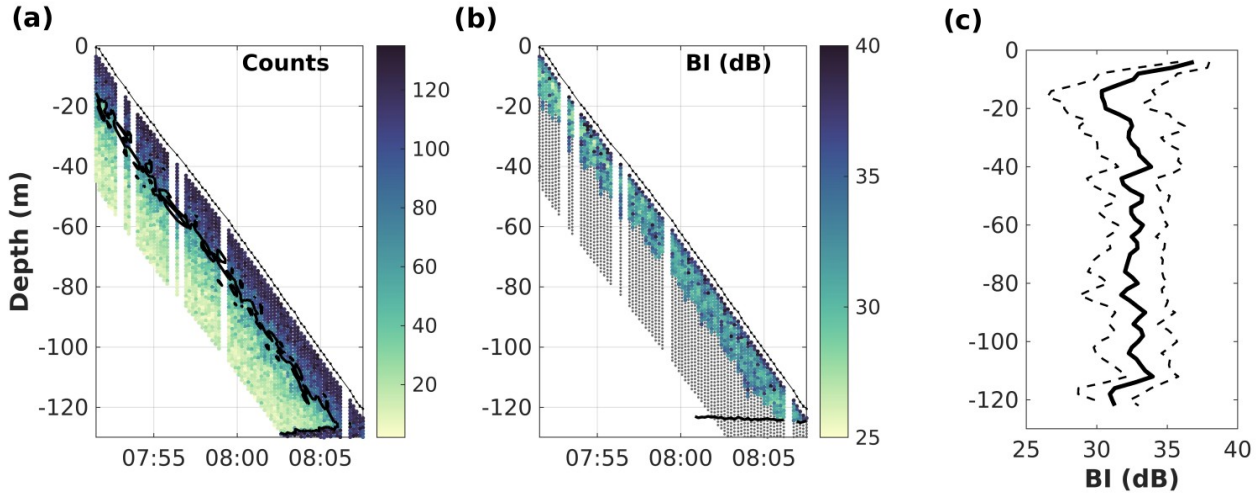

Figure 3.11: Example of measurements carried out by the Acoustic Doppler Current Profiler (ADCP) during a descent of the glider. (a) The swath of the count signal for each cell of the multiple water profiles. The threshold of 64 counts used to discard erroneous values is shown in black. (b) Filtered backscatter index (BI) measurements (dB). Discarded values are shown in gray. A black line shows bottom detection. (c) Reconstructed median backscatter index profile and associated standard deviation from Gentil et al. (2020).

3.4.5.4.2. Absolute velocities estimates

At this step, the selection of downcasts only is carried out from the glider-ADCP toolbox, due to the ADCP setup (see section 3.3.1). As backscatter index profiles, the successive relative velocity profiles were stacked to reconstruct the profile over the entire water column from the median values of the overlapping data at each level (Fig. 3.12a-b). During post-processing, methods are used to remove the glider's motion (u_{glider}) from relative velocity measurements of ADCP (u_{ADCP}) and to apply absolute velocity constraints to obtain profiles of absolute horizontal currents (u_{ocean}). The ADCP measurement principle according to the time (t) and depth at each bin (i) is as follows:

$$u_{ADCP}^{(t,i)} = u_{ocean}^{(t,i)} + u_{glider}^{(t,i)} \quad (3.16)$$

In this study, three methods were used to estimate the absolute velocities: (i) the "shear" method, (ii) the "direct" method, and (iii) the "inverse" method, described below.

(i) The "shear" method—is based on the work of Firing and Gordon, (1990), with the assumption that glider velocity is constant for each profile and can, therefore, be eliminated. After reconstructing the shear of the current over the whole water column (Fig. 3.12c), its integration allows obtaining a relative water velocity profile (Fig. 3.12d). At this step, a constraint is required, corresponding to a barotropic velocity component, to derive absolute water velocity profiles. Absolute velocity is estimated by adjusting the relative velocity profile to the current velocity measured by the barotropic constraint (Fig. 3.12e). The user chooses the constraint to apply from the toolbox, either the depth-averaged current (DAC), either the bottom track (BT) (Fig. 3.12e). When the glider performs multiple yos (downcast/upcast) between two surfacings, as is often the case in coastal deployments, we recommend using the BT if it meets the quality control (i.e., no offset). Indeed, the BT is specific to each downcast, while the DAC is calculated between two

surfacings (i.e., on 6 downcasts in our study case). Furthermore, the lack of ADCP data during upcast and in the surface layer may result in a bias between the average ADCP data and the DAC.

Uncertainties regarding absolute water velocities vary depending on the ADCP settings (mainly cell size, instrument frequency, pulse length, and the number of pings per ensemble) (Gordon, 1996). The user must fill in the error (standard deviation) associated with single ping measurements in the *Glider_define_param* script. To estimate the uncertainty of the relative velocity estimates, we performed a Monte-Carlo simulation based on 500 iterations, with initial velocity values sampled randomly according to a normal distribution centered on the measured value for each bin of each profile during the downcast. Finally, an average standard deviation of the absolute velocity—calculated from the sum of variances of the relative velocities and the constraint selected—is estimated (Fig. 3.12e).

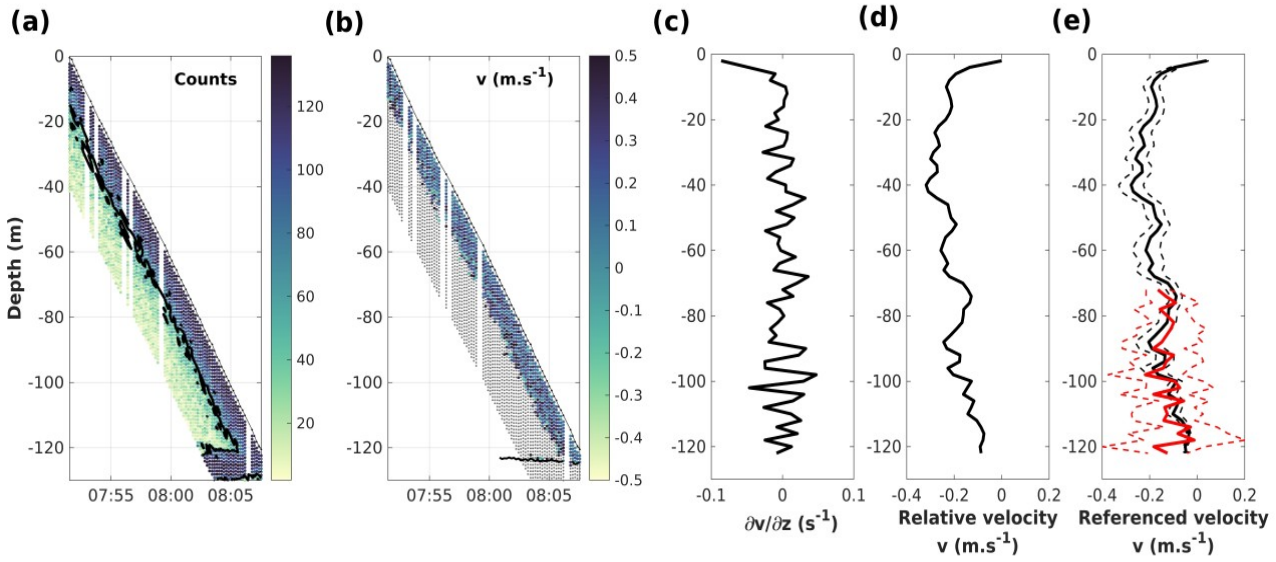

Figure 3.12: Example of measurements carried out by the ADCP during a descent of the glider. (a) The swath of the counts signal for each cell of successive water profiles. The empirical threshold of 64 counts used to discard erroneous velocity values is shown in black. (b) Filtered raw northward velocity measurements (m s^{-1}). Discarded values are shown in grey. The black line shows bottom detection. (c) Mean profile reconstructed after stacking successive profiles of the vertical derivatives of measured currents. (d) Integrated relative velocity profile. (e) Absolute velocity profile (black line) after adjustment with near-bottom current measurements derived from bottom tracking (red line), dashed lines indicate uncertainties (standard deviation) for each variable from Gentil et al. (2020).

A moving average on vertical (depth) and horizontal (time) windows can be applied on the absolute velocities of the SOI (to be defined in *Glider_define_param.m*) because the "shear method" is relatively noisy.

(ii) The "direct" method—is based on the work of Merckelbach et al. (2010), with the estimation of glider motions by a steady-state flight model (see section 3.4.5.3, equations 3.1 to 3.12). The horizontal glider velocity is then subtracted from the ADCP measurements at each depth. Uncertainties regarding absolute water velocities are calculated from the sum of variances of the relative velocities and glider motion from the steady-state flight model.

(iii) The "Inverse" method—considers a system of equations formed by the relationships between the known ADCP velocity measurements (d), unknown current and glider speeds (m), and known uncertainties or noise (n). Constraints can be added to this system such as the measured glider speeds near the bottom from the bottom track, and the glider motions determined from an optimized flight model. Each of these constraints is assigned a weight (Todd et al., 2017; Visbeck, 2002) that can be adjusted by the user. The equation system is written in matrix form (Visbeck, 2002).

$$d = G\,m + n \tag{3.17}$$

where the vector d represents all ADCP velocities from different depths within the water column. n represents the noise due to imperfect measurements d and imperfect prediction of the absolute velocity field by Gm. The unknown ocean velocity profile and motion of the glider are combined into a single vector, which are related to the observations d by the model matrix G, as shown in the example below. This method is particularly flexible because additional constraints can be added, by simply adding rows to the initial vector d and matrix G. The system of linear equations including all available constraints is generally over-constrained (i.e., more independent equations than unknowns).

$$\mathbf{d} = \begin{bmatrix} u_{1,1} \\ u_{1,2} \\ u_{1,3} \\ u_{2,1} \\ \vdots \\ u_{3,1} \\ \vdots \\ u_{20,3} \end{bmatrix}, \quad \mathbf{m} = \begin{bmatrix} u_{\text{glid},1} \\ u_{\text{glid},2} \\ u_{\text{glid},3} \\ \vdots \\ u_{\text{glid},20} \\ \text{—} \\ u_{\text{ocean},1} \\ u_{\text{ocean},2} \\ u_{\text{ocean},3} \\ \vdots \\ u_{\text{ocean},10} \end{bmatrix}, \quad \mathbf{G} = \left\{ \begin{array}{ccccc|ccccc} 1 & 0 & 0 & \cdots & 0 & 1 & 0 & 0 & \cdots & 0 \\ 1 & 0 & 0 & \cdots & 0 & 0 & 1 & 0 & \cdots & 0 \\ 1 & 0 & 0 & \cdots & 0 & 0 & 0 & 1 & \cdots & 0 \\ 0 & 1 & 0 & \cdots & 0 & 0 & 1 & 0 & \cdots & 0 \\ \vdots & \vdots & \vdots & \ddots & \vdots & \vdots & \vdots & \vdots & \ddots & \vdots \\ 0 & 0 & 1 & \cdots & 0 & 0 & 0 & 1 & \cdots & 0 \\ \vdots & \vdots & \vdots & \ddots & \vdots & \vdots & \vdots & \vdots & \ddots & \vdots \\ 0 & 0 & 0 & \cdots & 1 & 0 & 1 & 0 & \cdots & 1 \end{array} \right\} \begin{matrix} \\ \\ \\ \\ \\ \\ \\ \\ \\ \lfloor u_{\text{ocean},10} \rfloor \end{matrix}.$$

In this case, there is no unicity of solutions. The solutions of the systems are given by equation 3.16. To solve this system of linear equations, we use the least squares method (pseudo-solutions), minimizing the squared error between d and its estimated value d^{pre}. The error prediction, which the least squares method tries to minimize, is given by equation 3.17.

$$m = [G\,G^T]^{-1} G^T d \tag{3.18}$$

$$E = \sum_{i=1}^{N} (d_i - d_i^{pre})^2 \tag{3.19}$$

The three methods, presented above, should give similar results for the estimation of absolute velocities in the water column. However, despite a good optimization of the glider vertical velocity from the steady-state flight model (Fig. 3.9), the glider horizontal velocity appears particularly weak around 0.25 m s^{-1} (Fig. 3.10b) compared to the expected velocity of around 0.35-0.4 m s^{-1}. The difference between the calculated and expected glider horizontal velocity is of the same order of magnitude as the difference between the absolute velocities estimated from the "shear" and the "direct" method. In addition, the "direct" method does not allow estimating absolute velocities for the first 10 m. This is the depth by which the glider has traveled several body lengths after its inflection point and for which acceleration terms can be reasonably neglected (Merckelbach et al., 2010). Concerning the "inverse method", it has the advantage of being particularly flexible

since multiple constraints can be easily incorporated (Todd et al., 2017). However, glider horizontal velocity derived from the flight model cannot be used as a constraint due to the uncertainties on the magnitude mentioned previously. Therefore, only one constraint is available to reference the relative water velocity profile in our study case, the bottom track. This constraint can only be applied to the lower part of the profile when the seabed is in the range of the ADCP measurements. The lack of additional constraints makes it impossible to reference the relative velocity profile at the upper part of the water column. For all these reasons, we chose to use the "shear" method to estimate absolute velocities in the water column in this thesis work. The "inverse" and "direct" methods have therefore not been implemented in the toolbox.

3.4.6. Step 5: validation of current measurements – output level 3 files

At this step, the robustness of the absolute velocity estimate is assessed, from an "external" current measurement, the DAC (see section 3.2 for the calculation). To assess the quality of the ADCP measurements compared to this independent estimate of the currents, we contrasted the residual current velocities and direction computed from the downcast ADCP data between two surfacings with the corresponding DAC estimates (Fig. 3.13). The two estimates of the integrated average current over the water column were broadly comparable and reproduced the main inversions and intensifications of the currents. Statistical analysis is performed with the eastward and northward components considered separately. The Taylor diagram shows a good agreement between the DAC (used as a reference) and the ADCP-derived residual currents (Fig. 3.14). The correlation coefficient for the east-west and north-south components is 0.95 and 0.88, respectively, with a *p-value* <0.001. Furthermore, the average standard deviation is between 0.04 and 0.08 m s^{-1}, while the average RMSD is between 0.04 and 0.06 m s^{-1}. These results give us some confidence in the "shear" method used to estimate absolute velocities. In this chapter, we showed the results on

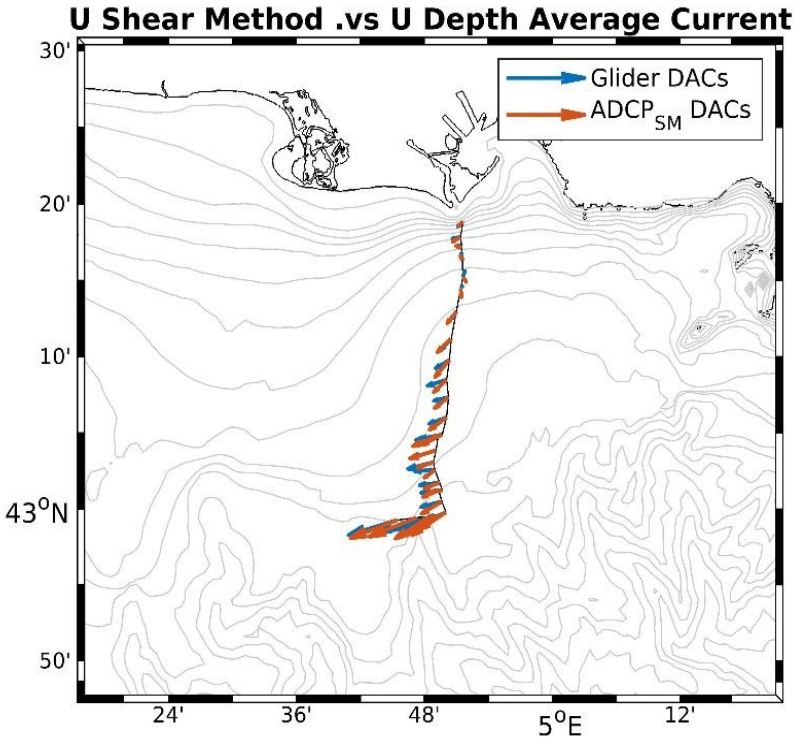

Figure 3.13: Comparison of depth-averaged current (DAC) vs. ADCP-derived current from the "shear method", on the section of interest.

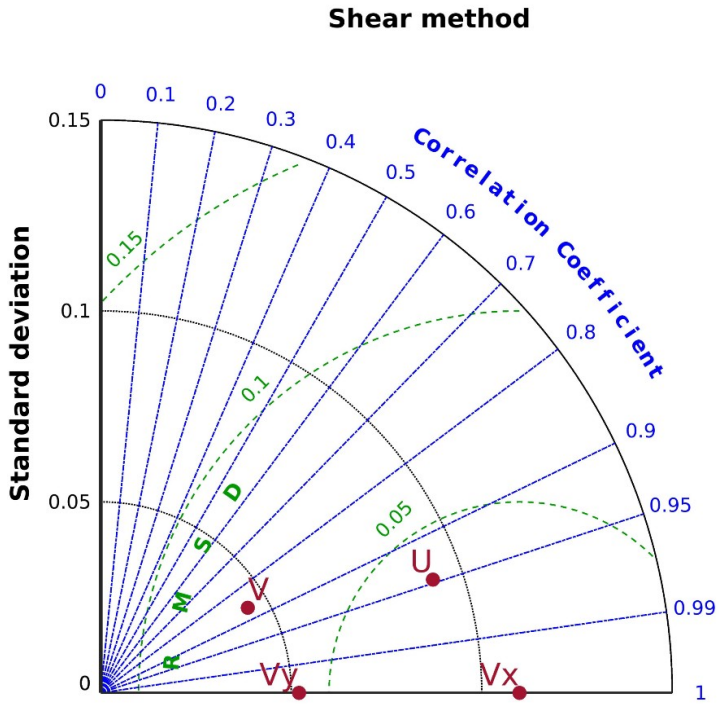

Figure 3.14: Taylor's diagram compares DACs (Vx, Vy), and ADCP-derived residual current (U, V)—respectively for each component of eastward and northward velocity—along the section of interest, for the "shear method".

one glider section for the toolbox, but these ADCP and DAC velocities were compared across all deployments and will be presented in Chapter 4. Finally, the L3 matrix file containing all derived parameters is generated.

3.4.7. Step 6: mapping & gridding – output level 4 files

For some applications or analyses, the user may find it more convenient to use the data projected along a section, instead of as continuous measurements along the glider trajectory. In this step, the glider data are projected from reference positions entered by the user (latitude/longitude). This allows us to estimate the distances (km) of each profile from a point of origin (the coast in our study case). Figure 3.15 shows the projection of glider data and distance from the coast estimated on the SOI. It is often more convenient, computationally efficient, and required for certain calculations to work with data that is on a regular grid. Projected glider data are interpolated on a regular 2DV grid (distance, depth) defined by the user. Once the data are projected and gridded, it is possible to estimate some spatiotemporal parameters such as currents perpendicular to the glider trajectory by the geostrophic approach (i.e., Coriolis force and impact of the horizontal density gradient). At the end of these operations, the L4 matrix file containing the final processed glider data is generated.

3.4.8. Step 7: plot sections

In the last step of the glider-ADCP toolbox, the processed data are plotted if the user selected it in the *Glider_ADCP_define_param.m*. A dialog box is displayed with the different physical, bio-optical, and acoustic variables to represent. Figure 3.16 shows an example with processed temperature on the SOI in spatial and temporal dimensions.

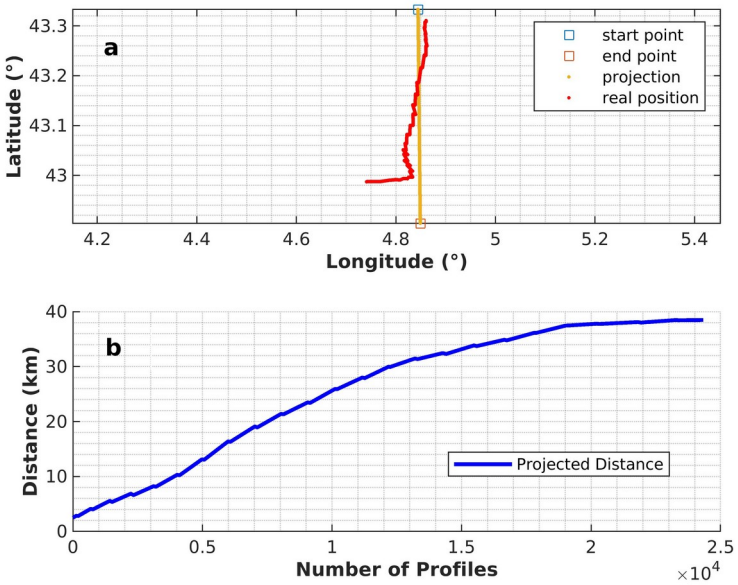

Figure 3.15: (a) The red line corresponds to the glider section and the orange line is the projected section from the two reference positions. (b) Distance from the coast (km) estimated along the glider projected section.

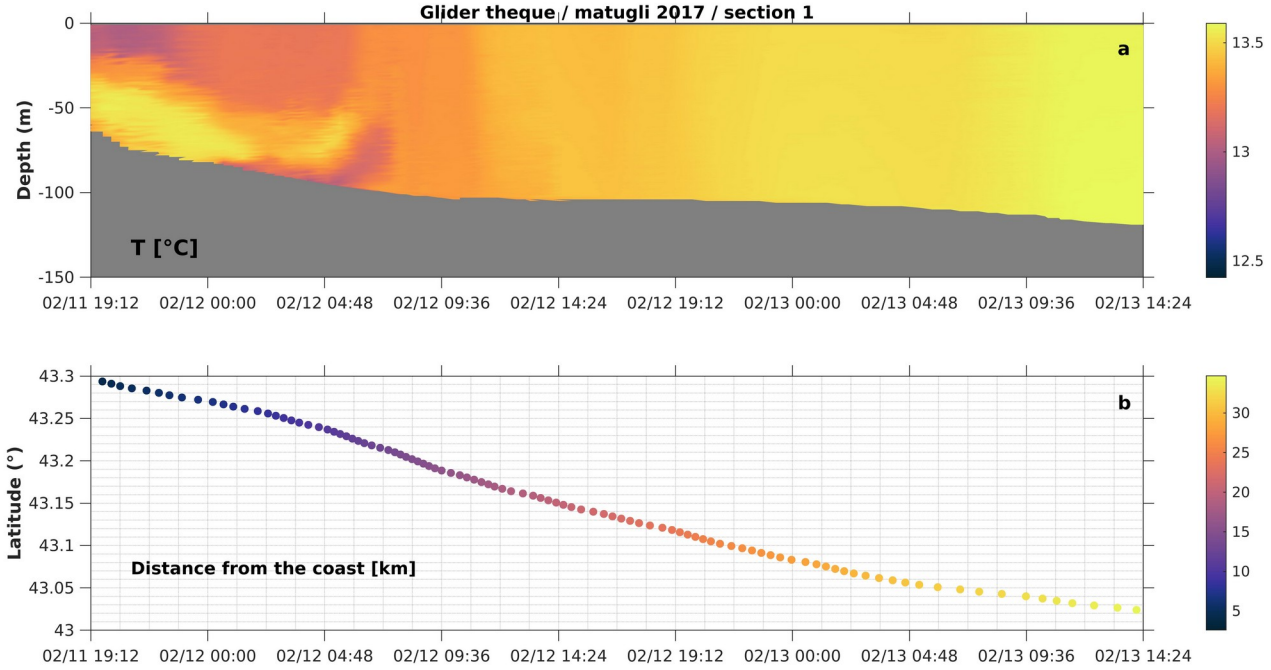

Figure 3.16: (a) Glider time series of temperature. (b) Glider distance from the coast (km) as a function of time.

References

Davis, R. E., Eriksen, C. C., Jones, C. P., 2002. Autonomous buoyancy-driven underwater gliders. The technology and applications of autonomous underwater vehicles 37–58.

EGO gliders data management team, 2017. EGO Gliders NetCDF Format Reference Manual.

Eriksen, C.C., Osse, T.J., Light, R.D., Wen, T., Lehman, T.W., Sabin, P.L., Ballard, J.W., Chiodi, A.M., 2001. Seaglider: A long-range autonomous underwater vehicle for oceanographic research. IEEE Journal of oceanic Engineering 26, 424–436.

Firing, E., Gordon, R. L., 1990. Deep ocean acoustic Doppler current profiling. Presented at the Proceedings of the IEEE Fourth Working Conference on Current Measurement, IEEE, pp. 192–201.

Francois, R., Garrison, G., 1982. Sound absorption based on ocean measurements. Part II: Boric acid contribution and equation for total absorption. The Journal of the Acoustical Society of America 72, 1879–1890.

Garau, B., Ruiz, S., Zhang, W.G., Pascual, A., Heslop, E., Kerfoot, J., Tintoré, J., 2011. Thermal lag correction on Slocum CTD glider data. Journal of Atmospheric and Oceanic Technology 28, 1065–1071.

Gentil, M., Many, G., Durrieu de Madron, X., Cauchy, P., Pairaud, I., Testor, P., Verney, R., Bourrin, F., 2020. Glider-Based Active Acoustic Monitoring of Currents and Turbidity in the Coastal Zone. Remote Sensing 12, 2875.

Gordon, R. L., 1996. Acoustic Doppler current profiler-Principles of operation: A practical primer. Rd Instruments 54, 54.

Gregor, L., Ryan-Keogh, T.J., Nicholson, S.-A., Du Plessis, M., Giddy, I., Swart, S., 2019. GliderTools: A Python toolbox for processing underwater glider data. Frontiers in Marine Science 6, 738.

Liblik, T., Karstensen, J., Testor, P., Alenius, P., Hayes, D., Ruiz, S., Heywood, K., Pouliquen, S., Mortier, L., Mauri, Ejm., 2016. Potential for an underwater glider component as part of the Global Ocean Observing System. Methods in Oceanography 17, 50–82.

Margirier, F., Bosse, A., Testor, P., l'Hévéder, B., Mortier, L., Smeed, D., 2017. Characterization of convective plumes associated with oceanic deep convection in the northwestern Mediterranean from high-resolution in situ data collected by gliders. Journal of Geophysical Research: Oceans 122, 9814–9826.

MATLAB, 2018. 9.7.0.1190202 (R2019b). The MathWorks Inc., Natick, Massachusetts.

McDougall, T.J., Barker, P. M., 2011. Getting started with TEOS-10 and the Gibbs Seawater (GSW) oceanographic toolbox. SCOR/IAPSO WG 127, 1–28.

Merckelbach, L., Berger, A., Krahmann, G., Dengler, M., Carpenter, J.R., 2019. A dynamic flight model for Slocum gliders and implications for turbulence microstructure measurements. Journal of Atmospheric and Oceanic Technology 36, 281–296.

Merckelbach, L., Smeed, D., Griffiths, G., 2010. Vertical water velocities from underwater gliders. Journal of Atmospheric and Oceanic Technology 27, 547–563.

Miles, T., Slade, W., Glenn, S., 2021. Sediment resuspension and transport from a glider integrated Laser In Situ Scattering and Transmissometry (LISST) particle analyzer. Journal of Atmospheric and Oceanic Technology.

Miles, T. N., Kohut, J., Slade, W., Gong, D., 2018. Suspended particle characteristics from a glider integrated LISST sensor. Presented at the OCEANS 2018 MTS/IEEE Charleston, IEEE, pp. 1–5.

Mullison, J., 2017. Backscatter estimation using broadband acoustic doppler current profilers-updated. Presented at the Proceedings of the ASCE Hydraulic Measurements & Experimental Methods Conference, Durham, NH, USA, pp. 9–12.

Mullison, J., DeCollibus, C., Allsup, B., 2013. An investigation of the accuracy of current profile measurements from a glider-mounted ADCP operating in shallow water. Presented at the 2013 OCEANS-San Diego, IEEE, pp. 1–8.

Palmer, M.R., Stephenson, G.R., Inall, M.E., Balfour, C., Düsterhus, A., Green, J.A.M., 2015. Turbulence and mixing by internal waves in the Celtic Sea determined from ocean glider microstructure measurements. Journal of Marine Systems 144, 57–69.

Rudnick, D. L., 2016. Ocean research enabled by underwater gliders. Annual review of marine science 8, 519–541.

Rudnick, D. L., Davis, R. E., Eriksen, C. C., Fratantoni, D. M., Perry, M. J., 2004. Underwater gliders for ocean research. Marine Technology Society Journal 38, 73–84.

Rudnick, D. L., Sherman, J. T., Wu, A.P., 2018. Depth-average velocity from Spray underwater gliders. Journal of Atmospheric and Oceanic Technology 35, 1665–1673.

Teledyne Webb Research, 2012. Slocum G2 Glider Maintenance Manual.

Testor, P., de Young, B., Rudnick, D. L., Glenn, S., Hayes, D., Lee, C. M., Pattiaratchi, C., Hill, K., Heslop, E., Turpin, V., 2019. OceanGliders: a component of the integrated GOOS. Frontiers in Marine Science 6, 422.

Todd, R. E., Rudnick, D. L., Sherman, J. T., Owens, W. B., George, L., 2017. Absolute Velocity Estimates from Autonomous Underwater Gliders Equipped with Doppler Current Profilers. Journal of Atmospheric and Oceanic Technology 34, 309—333. https://doi.org/10.1175/JTECH-D-16-0156.1

Troupin, C., Beltran, J.P., Heslop, E., Torner, M., Garau, B., Allen, J., Ruiz, S., Tintoré, J., 2015. A toolbox for glider data processing and management. Methods in Oceanography 13, 13–23.

Visbeck, M., 2002. Deep velocity profiling using lowered acoustic Doppler current profilers: Bottom track and inverse solutions. Journal of atmospheric and oceanic technology 19, 794–807.

Wolk, F., Lueck, R., Laurent, L.S., 2009. Turbulence measurements from a glider. Presented at the OCEANS 2009, IEEE, pp. 1–6.

Chapter 4.

Glider-based active acoustic monitoring of currents and turbidity in the coastal zone

remote sensing MDPI

Chapter 4. Glider-based active acoustic monitoring of currents and turbidity in the coastal zone

---

Mathieu Gentil [1,*], Gaël Many [2,1], Xavier Durrieu de Madron [1], Pierre Cauchy [1,3], Ivane Pairaud [4], Pierre Testor [5], Romaric Verney[6] and François Bourrin [1] ,

[1] CEFREM, CNRS, Université de Perpignan Via Domitia, 52 Avenue Paul Alduy, 66860 Perpignan, France ; demadron@univ-perp.fr (X. D.d.M.) ; fbourrin@univ-perp.fr (F.B.)

[2] LA, Observatoire Midi-Pyrénées, 14 Avenue Edouard Belin, 31400 Toulouse, France ; gael.many@outlook.fr (G.M.)

[3] COAS, School of Environmental Sciences, University of East Anglia, Norwich NR4 7TJ, UK; p.cauchy@uea.ac.uk (P.C.)

[4] LOPS, CNRS— IFREMER-IRD-UBO, ZI de la Pointe du Diable, CS 10070, 29280 Plouzané, France ; ivane.pairaud@ifremer.fr (I.P.)

[5] CNRS-Sorbonne Universités (UPMC Univ. Pierre et Marie Curie, Paris 06) — CNRS-IRD-MNHN, UMR 7159, Laboratoire d'Océanographie et de Climatologie (LOCEAN), Institut Pierre Simon Laplace (IPSL), 4 place Jussieu, F-75005 Paris, France ; testor@locean-ipsl.upmc.fr (P.T.)

[6] IFREMER, DHYSED, ZI Pointe du Diable, 29280, Plouzané, France ; romaric.verney@ifremer.fr (R.V.)

* Correspondence: mathieu.gentil@univ-perp.fr (M.G.)

Received: 15 July 2020; Accepted: 31 August 2020; Published: 4 September 2020

Table of Contents

Table of figures

Index of table

Abstract

The recent integration of Acoustic Doppler Current Profilers (ADCPs) onto underwater gliders changes the way current and sediment dynamics in the coastal zone can be monitored. Their endurance and ability to measure in all weather conditions increases the probability of capturing sporadic meteorological events, such as storms and floods, which are key elements of sediment dynamics. We used a Slocum glider equipped with a CTD (Conductivity, Temperature, Depth), an optical payload, and an RDI 600 kHz phased array ADCP. Two deployments were carried out during two contrasting periods of the year in the Rhone River region of freshwater influence (ROFI). Coastal absolute currents were reconstructed using the shear method and bottom tracking measurements, and generally appear to be in geostrophic balance. The responses of the acoustic backscatter index and optical turbidity signals appear to be linked to changes of the particle size distribution in the water column. Significantly, this study shows the interest of using a glider-ADCP for coastal zone monitoring. However, the comparison between suspended particulate matter dynamics from satellites and gliders also suggests that a synoptic view of the processes involved requires a multiplatform approach, especially in systems with high spatial and temporal variability, such as the Rhone ROFI area.

Keywords: glider; optics; acoustics; satellite; coastal hydrodynamics; suspended particulate matter; particulate fluxes; Gulf of Lions; Mediterranean

4.1. Introduction

Sediment dynamics on continental margins play an essential role in marine habitats and ecosystems dynamics, in the dispersion and sequestration of land-derived chemical elements (e.g., carbon, contaminants) and, in the long term, the evolution of continental shelf morphology (Durrieu de Madron et al., 2008). This dynamic is influenced by multiple forcings (river discharges, currents, wind, waves), which strongly affect the spatiotemporal variability of suspended particulate matter (SPM) distribution. Operational monitoring of SPM is thus necessary to improve sediment transport and ecosystem modelling, with a final goal to prevent long-term damage to coastal waters (Ody et al., 2016).

Over the past decade, technological advances in ocean color satellite observation have made it possible to describe the variability of SPM dynamics in the surface layer of the coastal zone on large spatial and temporal scales (Doxaran et al., 2009; Gohin, 2011; Ody et al., 2016). However, satellite data cannot provide information on the vertical structure of SPM dynamics in the water column. Until recently, most in-situ observations of SPM transport in the water column were gathered at a few fixed locations over the shelves. However, in situ monitoring throughout the water column is essential to characterize the spatiotemporal variability of the processes involved in sediment transport and deposition in coastal areas (Bourrin et al., 2015a). Autonomous underwater vehicles (AUVs), such as gliders, appear to be useful tools for the monitoring of coastal hydrodynamics, sediment transport, and coastal ecosystems, especially during extreme events such as floods and storms, which are critical elements of sediment dynamics and particulate transport in the coastal zone (Bourrin et al., 2015a; Glenn et al., 2008; Miles et al., 2015, 2013).

Gliders driven by variable buoyancy (Davis et al., 2002) an measure a large number of environmental variables at the same time, collecting data which they transmit in near real time. Glider-based monitoring allows sampling of the entire water column and continental shelf over long

periods. Gliders markedly supplement the fixed measurements of buoys and moorings, as well as data collected during shipborne surveys, which are shorter, potentially less frequent, and weather-sensitive. They are becoming increasingly important for the collection of oceanographic measurements in observing programs (Liblik et al., 2016; Rudnick, 2016; Testor et al., 2010). Several recent studies have dealt with the integration of Acoustic Doppler Current Profilers (ADCPs) on gliders for applications in the open ocean as well as the coastal zone (Ellis et al., 2015; Ma et al., 2019; Todd, 2017; Todd et al., 2011). However, few of them have dealt with sediment transport (Miles et al., 2015, 2013). The sampling strategy for most of the latter studies was based on high-frequency measurements over short periods (a few hours to a week). Endurance deployments to monitor currents and turbidity are necessary in order to fill the gap in measurements concerning SPM dynamics at the regional scale, and to validate hydro-sedimentary models (Ouillon, 2018).

In this study, a Slocum glider equipped with a CTD, optical sensors and an ADCP was tested in conjunction with ocean color satellite images to evaluate its capacity to monitor the interplay of hydrographic features, water circulation and particulate matter distribution in the coastal zone. The study area is located in the region of freshwater influence (ROFI) of the Rhone River in the Gulf of Lions (NW Mediterranean), and measurements encompass two different seasons with stratified and non-stratified hydrological conditions. The sampling strategy was adapted to target a continuous observation period of several weeks so as to capture sporadic events, such as storms or floods. The objectives of this work are: (i) to evaluate the performance of current estimations by ADCP with reduced sampling frequency allowing endurance deployment, (ii) to evaluate the complementarity between the evaluation of turbidity derived from acoustic backscattering of an ADCP and optical measurements, (iii) to estimate SPM fluxes at the scale of a continental shelf, and (iv) to assess the

complementarity between the glider and satellite platforms to monitor the turbidity in the Rhone's ROFI.

4.2. Materials and methods

4.2.1. Deployment strategy

A glider equipped with an ADCP was deployed within the Rhone ROFI during two measuring campaigns (Fig. 4.1 a,b). The first one lasted for 30 days (from October 26 to November 21, 2016), in autumnal conditions of thermal stratification, with a pycnocline at around 50–60 m depth. The second campaign lasted for 35 days (from January 30 to March 3, 2017), and took place in winter during unstratified conditions. However, for both deployments, haline stratification conditions could be observed along some sections up to 40 m depth, depending on the Rhone River inflow. Fourteen and seventeen cross-shelf sections were carried out in 2016 and 2017 respectively, among which were six and twelve complete sections from the river mouth to the shelf edge (40 km offshore – 120 m depth). Each section was generally performed in 1.5-2 days. During these two glider deployments, no significant flood or storm was recorded.

Concomitant sea surveys were carried out on board the R/V Tethys II at the same location from 2-11 November 2016 for the autumnal conditions, and from 24 January to 3 February 2017 for the winter conditions. During these surveys, water samples were collected at specific depths for the determination of SPM concentration in the water column.

4.2.2. Environmental data

Satellite data: spatial maps of daily SPM concentrations (Fig. 4.1a,b), with 1 km resolution, were obtained from the Moderate Resolution Imaging Spectroradiometer (MODIS) on the Aqua satellite (Level-2 reflectance products). Products, analysis, and calibrations used were provided by

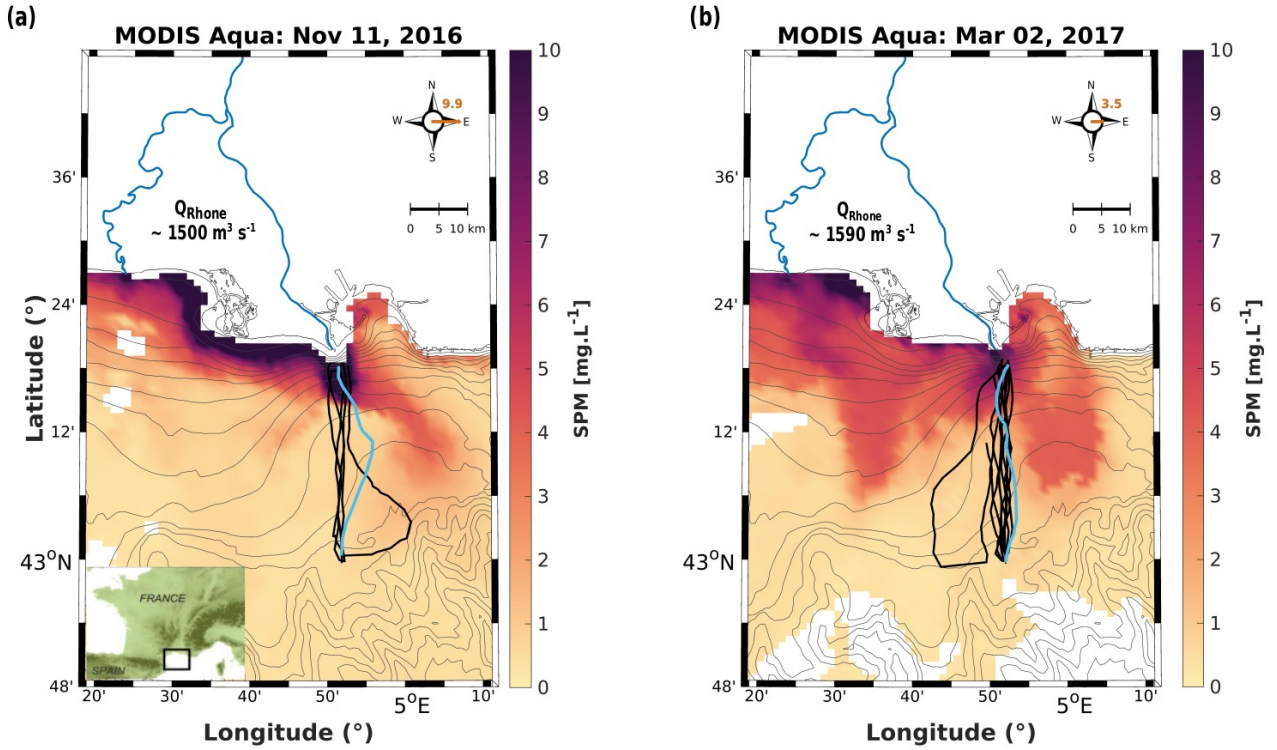

Figure 4.1: Moderate Resolution Imaging Spectroradiometer (MODIS) Aqua images of suspended particulate matter (SPM) concentration for (a) November 11th 2016, with a flow from the Rhone River of about 1500 m^3 s^{-1} and (b) March 2nd 2017, with a flow of about 1590 m^3 s^{-1}. Clouds are shown as white patches and wind speed (in m s^{-1}) and direction are specified. Depth contours are shown in gray and represent the 10 m isobaths from the coast. The glider track and sections of interest are shown as thick black and blue lines, respectively, for each deployment.

IFREMER, and OC5 IFREMER algorithms for SPM concentrations estimations were obtained from Gohin, (2011).

Rhone River discharge time series: hourly water discharges of the Rhone River were measured at the Beaucaire-Tarascon gauging station (code V7200015) and were provided by the French national data bank "HYDRO" (http://www.hydro.eaufrance.fr). Solid discharges were estimated using a calibration established for the Rhone River (Sadaoui et al., 2016), based on the fitting of rating curves to existing SPM-flow data pairs.

Meteorological time series: hourly (10-min burst average) wind speed and direction were measured at the Météo-France station of Cap-Couronne (43 °20.23'N; 5 °01.38'E). Data were provided by the Publithèque database.

4.2.3. Glider data

4.2.3.1. Glider system, CTD, and optical sensors

The autonomous underwater glider (depth range 30–200 m) used for this work is a Teledyne Webb Research Slocum G1 (Davis et al., 2002). It uses a variable buoyancy engine to move in a saw-tooth pattern from the surface (0–1 m depth) to typically 2 m above bottom. For this experiment, the glider was carefully ballasted to enter into and measure both the low-density waters (<27.5 kg m^{-3}) of the Rhone ROFI and the denser outer shelf waters (>29 kg m^{-3}). The chosen settings allowed the glider to descend and ascend through the water column with a pitch angle of approximately 26°, and horizontal and vertical speeds of 0.4 and 0.2 m s^{-1}, respectively. The glider surfaced every six down- and up-casts (yos) in order to obtain GPS fixes so as to transfer data to land and to receive any new information about its route or configuration. For the subsequent data analyses, the glider's surfacings were removed because of very noisy data, likely due to bubbles or provoked by rapid changes in heading and attitude on the surface. Conductivity, temperature, and pressure measurements were made using a pumped SeaBird 41cp CTD. Conductivity and temperature measurements were corrected for thermal lag effects (Garau et al., 2011). Salinity, density, Brunt—Väisälä frequency, and dynamic-height anomaly were derived using the TEOS-10 equation (McDougall and Barker, 2011). An optical backscatter sensor (Wetlabs BB2FLS) provided light scattering measurements (expressed in m sr^{-1}) at a wavelength of 700 nm for turbidity, and at 695 nm for fluorescence of chlorophyll-a. The sampling frequency was 4 s for CTD and optical sensors and 10 s for ADCP sensors. CTD and optical data were synchronized with ADCP data and interpolated to the same periodicity (10 s).

4.2.3.2. Optical data processing

Optical signal calibration: the BB2FLS sensor provided light scattering measurements (β [θ, λ]) at specific angles θ = 124° in the backward direction (Sullivan et al., 2013). The particulate backscattering coefficients (bbp_{700}, in m^{-1}) were derived using the following equation:

$$bbp(\lambda) = 2\pi . X . (\beta_p(\theta, \lambda)) \quad (4.1)$$

where X is an adjustment factor provided by the manufacturer according to particle type [1.077], and β_p [θ, λ] is the volume scattering function of the particles. The light backscattering measurements at 700 nm (bbp_{700}) from the ship- and glider-based Wetlabs instruments were used to derive SPM concentrations from in situ gravimetric SPM measurements. Data were binned into classes of 0.005 m^{-1} to improve the calibration. The outliers of each bin, above and below 1.5 times the upper and lower quartile, were removed. Then, a least squares regression method accounting for the dispersion of observations was used to estimate the relationship between the SPM concentration (mg L^{-1}) and the turbidity at 700 nm (eq. 4.2).

$$[SPM]_{OPT} = (104.2 \pm 9.1) bbp_{700} + (0.81 + 0.3) (r^2 = 0.88) \quad (4.2)$$

Schlieren effects: the stratified water column shows varying refractive indices associated with density gradient that can cause light scattering, resulting in optical artifacts known as Schlieren effects (Styles, 2006). The refraction index of seawater, n, is a function of temperature, salinity, pressure, and wavelength of the optical backscattering. The empirical equation of Quan and Fry, (1995) was used to calculate n at 700 nm. For both seasons (autumn and winter), the hydrological profiles (temperature, salinity, density, Brunt—Väisälä frequency) and the refraction index of seawater profiles (Fig. 4.2a,b,d,e) were compared with the optical backscattering signal to assess the presence of Schlieren effects.

Spike analyses: spikes were recorded by all optical measurements as rapid, transient, and often large increases in optical signals. Spikes result from the interception by optical instruments of coarse particles, such as aggregates and biological debris (Briggs et al., 2011), which are scarce relative to the fine particles that induce most of the turbidity signal. We used a similar spike analysis on our data to characterize the presence of large particles (Fig. 4.2c,f). A 5-point running minimum filter followed

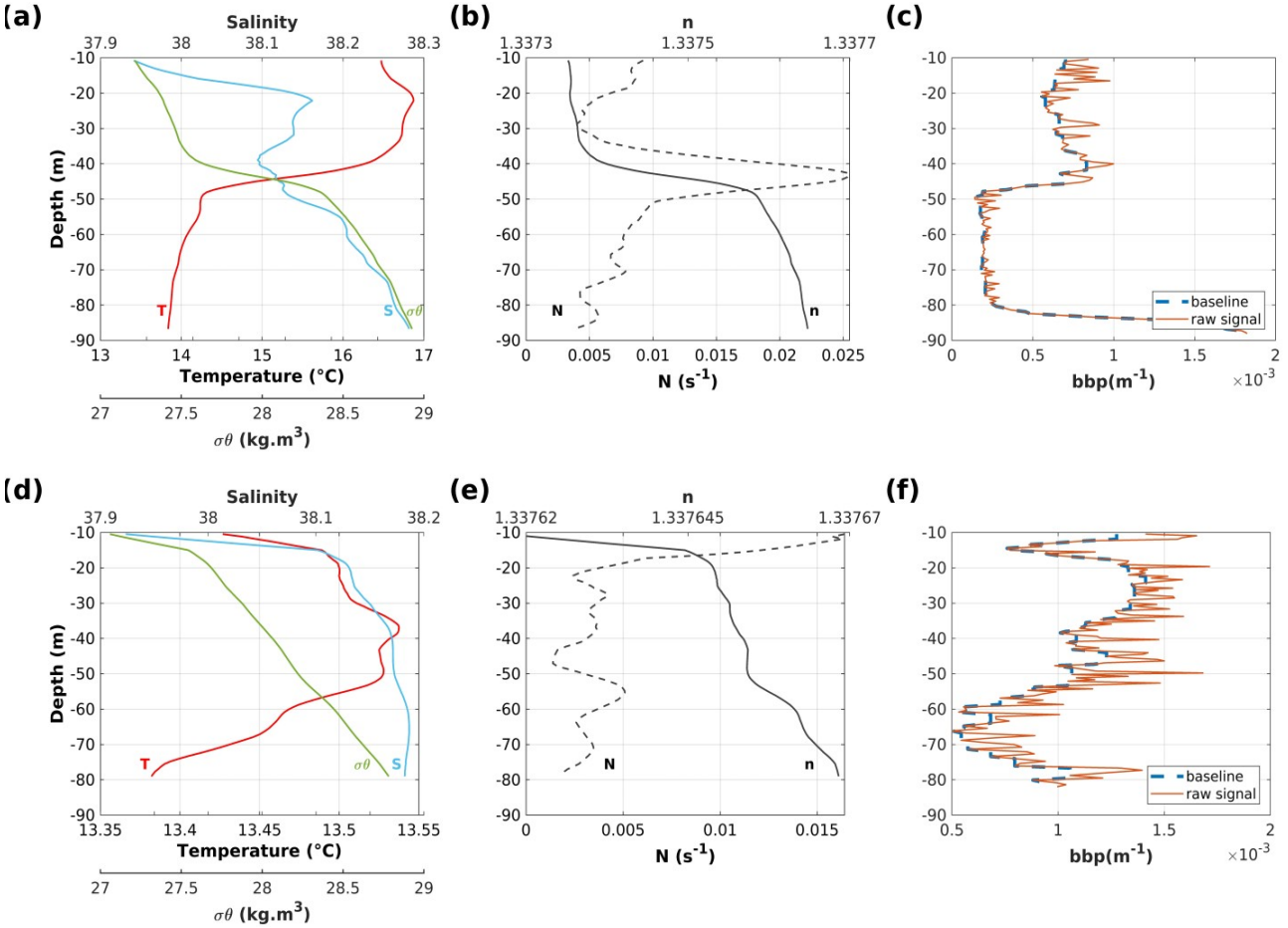

Figure 4.2: (a,d) Water-column profiles of salinity (S), temperature (T), and density (σθ); (b,e) index of refraction of seawater (n) and Brunt–Väisälä frequency profiles (N); and (c,f) backscattering profiles of bbp_{700} of Wetlabs BBFL2 (raw-signal) and the baseline extract from a filter 5-point running minimum followed by a 5-point running maximum applied on the bbp_{700} measurements. The top panels correspond to the autumnal season (November, 2016) showing a seasonal thermocline around 50 m depth characteristic of the coastal area surrounding the Rhone region of freshwater influence (ROFI) area. The lower panels correspond to the winter season, with a homogeneous water column (15–80 m depth), except in subsurface waters due to the Rhone River plume.

by a 5-point running maximum was applied on the raw optical backscattering data at 700 nm (one measurement every meter depth) for the determination of the background (baseline) at each profile (Fig. 4.2c,f). Then, spike height was calculated by subtracting the baseline from the raw optical profile.

4.2.3.3. ADCP settings

An Explorer Doppler Velocity Log with Acoustic Doppler Current Profiling capacity (Explorer ADCP) was integrated into a special payload bay on the Slocum glider. It allowed to measure echo intensity and velocity profiles in the water column. The Explorer ADCP has a downward-facing transducer which was tilted forward by 11°, enabling to compensate for the pitch of the glider during downcasts. The inclination of the transducer optimized the three-beam measurements on the 26° pitched glider downcasts with the three forward ADCP beams oriented 15° from vertical, and with the fourth, 45° aft relative to the glider. This fixed forward configuration rendered the instrument unsuitable for collecting velocity profile data during upcasts (Mullison et al., 2013), so for this reason, only downcasts measurements were used in this study. Dedicated high accuracy attitude and compass sensors were used by the ADCP to monitor the beam orientation and were carefully calibrated before deployment. Velocities used in this work were associated with Earth coordinates using dead reckoning and were bin-mapped.

During a glider descent, the ADCP periodically recorded echo intensity and relative water velocities along water profiles (WP). A sampling frequency of 0.1 Hz was set to optimize the duration of the glider deployment. This sampling frequency (ensemble of 1 ping every 10 s) allowed sampling of WPs spaced on average every 4 m along the glider trajectory and 1.7 m vertically. The maximum range of each WP was 40 m. Results were thus organized along a diagonal swath, with overlapping measurements at each depth (Fig. 4.3a and 4.4a). A blanking distance of 2 m close to the transducer was generally observed for this ADCP and data were vertically averaged into 1 m cell sizes. For echo intensity measurements, a correction was applied on cell depths to avoid the effect of the pitched transducer (Ordonez et al., 2012). The real depth of each cell was thus calculated, taking into account the pitch and roll effects, the blanking distance, and the depth of the glider. Finally, to properly estimate the backscatter index and the relative water velocities, the factory threshold of 64 counts of

the correlation signal (Gordon, 1996) was used to discard erroneous values. This threshold generally reduced the usable part of the profiles to about 20 m from the transducer (Fig. 4.3b and 4.4b).

4.2.3.4. ADCP data processing

4.2.3.4.1. Estimation of backscatter index

The received level (RL) of the acoustic return along each beam was converted into the backscatter index (BI, in dB) (eq. 4.3) (Deines, 1999; Gostiaux and van Haren, 2010; Mullison, 2017):

$$BI = 10\,log_{10}\left(10^{(Kc(RL-Er/10))}-1\right)+TL_w+TL_g \quad (4.3)$$

where Kc is the count to dB factor (0.61 for the ADCP used in this work), RL the received level in counts, Er the noise in counts (50 counts for the ADCP used in this work), TL_w the loss due to absorption by seawater (Francois and Garrison, 1982), and TL_g the loss due to geometrical spreading. The computation of the speed of sound was based on the Explorer temperature sensor and an average salinity value of 38.

The successive profiles of the backscatter index were stacked (bins of 1 m) to reconstruct the profile over the entire water column from the median values of the overlapping data at each level. The number of overlapping data ranged between 1 for the first bin at the surface and 12 on average over most of the profile. The associated uncertainty corresponds to the standard deviation of the stacked values for each 1 m depth bin. A final three-point centered moving-average filter was applied to eliminate the high-frequency noise (Fig. 4.3c).

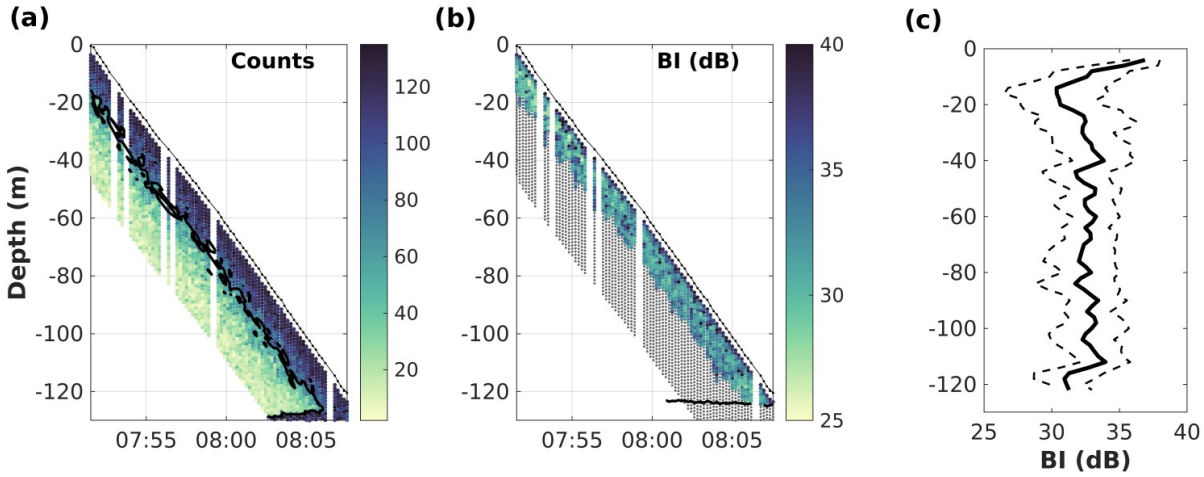

Figure 4.3: Example of measurements carried out by the Acoustic Doppler Current Profiler (ADCP) during a descent of the glider. (a) Swath of the counts signal for each cell of the multiple water profiles. The threshold of 64 counts used to discard erroneous velocity values is shown in black. (b) Filtered backscatter index (BI) measurements (dB). Discarded values are shown in gray. A black line shows bottom detection. (c) Reconstructed median backscatter index profile and associated standard deviation.

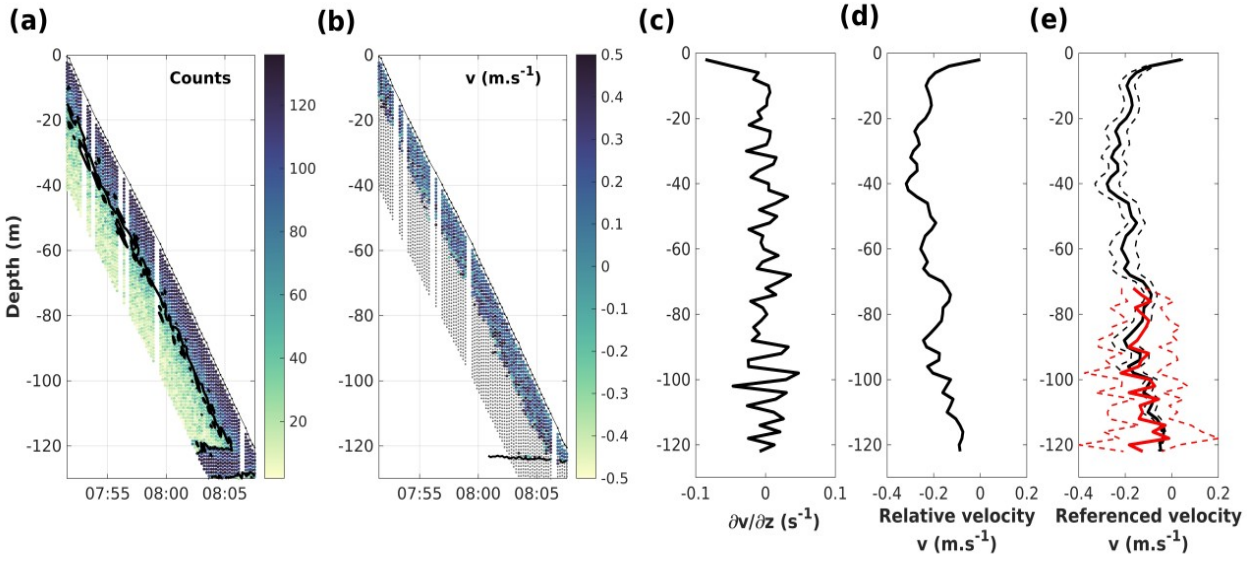

Figure 4.4: (a) Swath of the counts signal for each cell of successive water profiles. The empirical threshold of 64 counts used to discard erroneous velocity values is shown in black. (b) Filtered raw northward velocity measurements (m s^{-1}). Discarded values are shown in gray. The black line shows bottom detection. (c) Mean profile reconstructed after stacking the successive profiles of the vertical derivatives of measured currents. (d) Integrated relative velocity profile. (e) Absolute velocity profile (black line) after adjustment with near-bottom current measurements derived from bottom tracking (red line); dashed lines indicate uncertainties (standard deviation) for each variable.

4.2.3.4.2. Water velocity estimates

ADCP measurements combine glider motion with current velocity. In order to derive current velocities, several methods are available. For the "direct" method, the glider motions are estimated by a steady-state flight model (Frajka-Williams et al., 2011; Merckelbach et al., 2010), and then subtracted from the ADCP data. For the velocity inversion method (Visbeck, 2002), a set of linear equations is solved to estimate absolute water velocities from a combination of velocity-referencing constraints (navigational data, shipboard ADCP measurements, bottom tracking, etc.). The shear method (Firing and Gordon, 1990; Fischer and Visbeck, 1993; Thurnherr et al., 2015) is based on the assumption that glider speed is constant for each profile and can, therefore, be eliminated. After reconstructing the shear of the current over the whole water column, its integration allows to obtain a relative water velocity profile. Integrated relative velocities do not include glider motion bias but require an integration constant corresponding to a barotropic velocity component (profile referencing from a single constraint) in order to derive absolute water velocities profiles. In this study, the shear method was preferred over the velocity inversion method since bottom tracking was the only constraint that could be used to reference the profile. The "direct" method gives similar results except for the first 10 m, where data cannot be estimated. This is the depth by which the glider has traveled several body lengths after its inflexion point and for which acceleration terms can be reasonably neglected (steady-state flight model) (Merckelbach et al., 2010).

The different steps of the shear method were applied independently to E–W and N–S components to (i) calculate single-ensemble shear by vertically differentiating ADCP velocity profiles (Fig. 4.4c); (ii) grid the resulting shear estimates in depth space (median values of shear current per 1 m cell); (iii) vertically integrate shear to yield the relative velocity profile (Fig. 4.4d), and (iv) estimate absolute velocities by adjusting relative velocity profiles to the current velocities

measured by bottom tracking. Estimation of velocity started at a depth of 3 m, due to the position of the ADCP under the glider and a blanking distance of 2 m.

Uncertainties regarding absolute water velocities vary depending on the ADCP settings (mainly cell size, instrument frequency, pulse length, and number of pings per ensemble) (Gordon, 1996). The standard deviation of single ping measurements for 1 m cell size at 614 kHz is about 0.066 m s^{-1}. To estimate the uncertainty of the relative velocity estimates, we performed a Monte-Carlo simulation based on 500 iterations, with initial velocity values sampled randomly according to a normal distribution centered on the measured value for each bin of each WP during the downcast. The probability distribution of the resulting outcomes for all the downcasts collected during the two surveys yielded an average standard deviation of 0.04 m s^{-1}. In addition, the uncertainty concerning the near-bottom current velocity determined by bottom tracking was estimated as the average standard deviation after stacking the data, and amounted to 0.12 m s^{-1}. Finally, an average standard deviation of the absolute velocity—calculated from the sum of the variances of the relative velocities and the absolute near-bottom current—was estimated at 0.13 m s^{-1}.

Geostrophic velocities were estimated using the observed density field. This allowed to determine the degree to which the flow perpendicular to the glider track (generally in the E–W direction during this experiment) can be associated with the horizontal density gradient. The cross-track component of the velocities is thus derived by adjusting the integrated geostrophic velocities in the water column—calculated from the dynamic-height anomaly differences between each pair of downcasts and with a subsurface reference level (5 m, i.e., minimum depth common to each profile)—to the corresponding depth-averaged velocities from ADCP measurements.

4.3. Results

4.3.1. Observations context

Six and 12 complete cross-shelf sections were carried out from the river mouth to the shelf edge, respectively, for the autumnal and winter periods. Analyses (depth-averaged current [DAC] comparison vs. ADCP integrated mean current, geostrophy, and optic vs. acoustic) were done on all sections. For convenience and clarity, we chose one section for each deployment (section 2 on November 11–13, 2016, and section 3 on February 5–7, 2017) to illustrate key hydrological, hydrodynamical, and biogeochemical features. The high variability of hydrological and hydrodynamical structures is also addressed in Section 4.4.

During both deployments, variable wind conditions were observed. Several south-easterly (i.e., marine) wind events of 5–10 m s^{-1} occurred during both seasons. North-westerly (i.e., continental) winds were observed during the two selected sections (Fig. 4.5a, b), with maximum

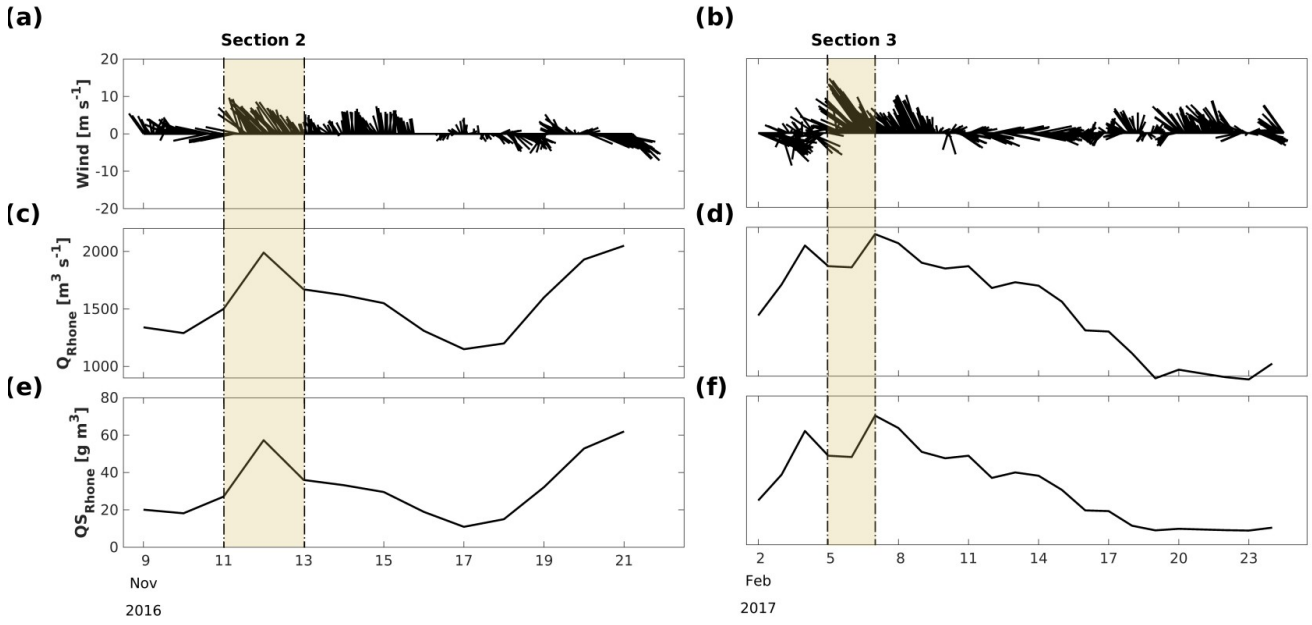

Figure 4.5: Time-series of atmospheric conditions at Cap-Couronne station (40°20.23'N; 5°01.38'E) for (a) autumnal and (b) winter conditions. Black lines correspond to hourly (10-min burst average) wind speed and direction. By convention, wind direction indicates its origin. The shaded area corresponds to the sections chosen to illustrate hydrological, hydrodynamical, and biogeochemical features.

wind speeds of 21 m s^{-1} in February 2017. For both deployments, the Rhone River discharges fluctuated between 650–1950 m3 s^{-1} and 800–2,100 m^3 s^{-1}, respectively, in autumnal and winter conditions. River discharges were around 1,500 and 1,900 m^3 s^{-1} for the selected sections, i.e., close to the mean annual flow of the Rhone River (1,700 m^3 s^{-1}) (Fig. 4.5c,d).

The shallowest part of the Rhone River submarine delta was not sampled because the glider was unable to make dives in water depths of less than 30 m. Subsequently, glider sections were divided into two parts: the mid shelf (4–20 km) and the outer shelf (>20 km).

4.3.2. Hydrological conditions

Observations along the selected sections (Fig. 4.6) revealed the offshore extension of the Rhone River surface plume with fresher, colder, and lighter water. During the two study periods, the plume was pushed offshore by continental N—NW winds. The plume extended as far as the shelf break (Fig. 4.6c,d) with a thickness of less than 10 m near the coast, and a thickening up to 15 m offshore. These continental inputs resulted in haline stratification, as shown by the Brunt—Väisälä frequency ($N^2 > 1.3 \times 10^{-3}$ s^{-1}) in the upper water layer (<30 m depth) (Fig. 4.6g ,h).

During the autumnal period, thermal stratification around 50–60 m depth was observed (Fig. 4.6a, c, e, left panel). Colder (<15.5 °C), saltier (>38.3 g kg^{-1}), and denser water (>28.5 kg m^{-3}) was covered by warmer (≈15.5–18 °C), fresher (≈37.8–38.3 g kg^{-1}), and lighter water (≈27.8–28.5 kg m^{-3}). This seasonal stratification was characterized by Brunt—Väisälä frequencies between 0.8 and 1.3 $\times 10^{-3}$ s^{-1} (Fig. 4.6g).

During the winter season, the water column became homogeneous below the river plume with temperatures around 13.5–14 °C, salinity around 38–38.5 g kg^{-1}, and density anomalies around 28.5–28.8 kg m^{-3} (Fig. 4.6b, d, f, right panel). The Rhone River plume offshore extension varied significantly during the winter deployment due to wind variability.

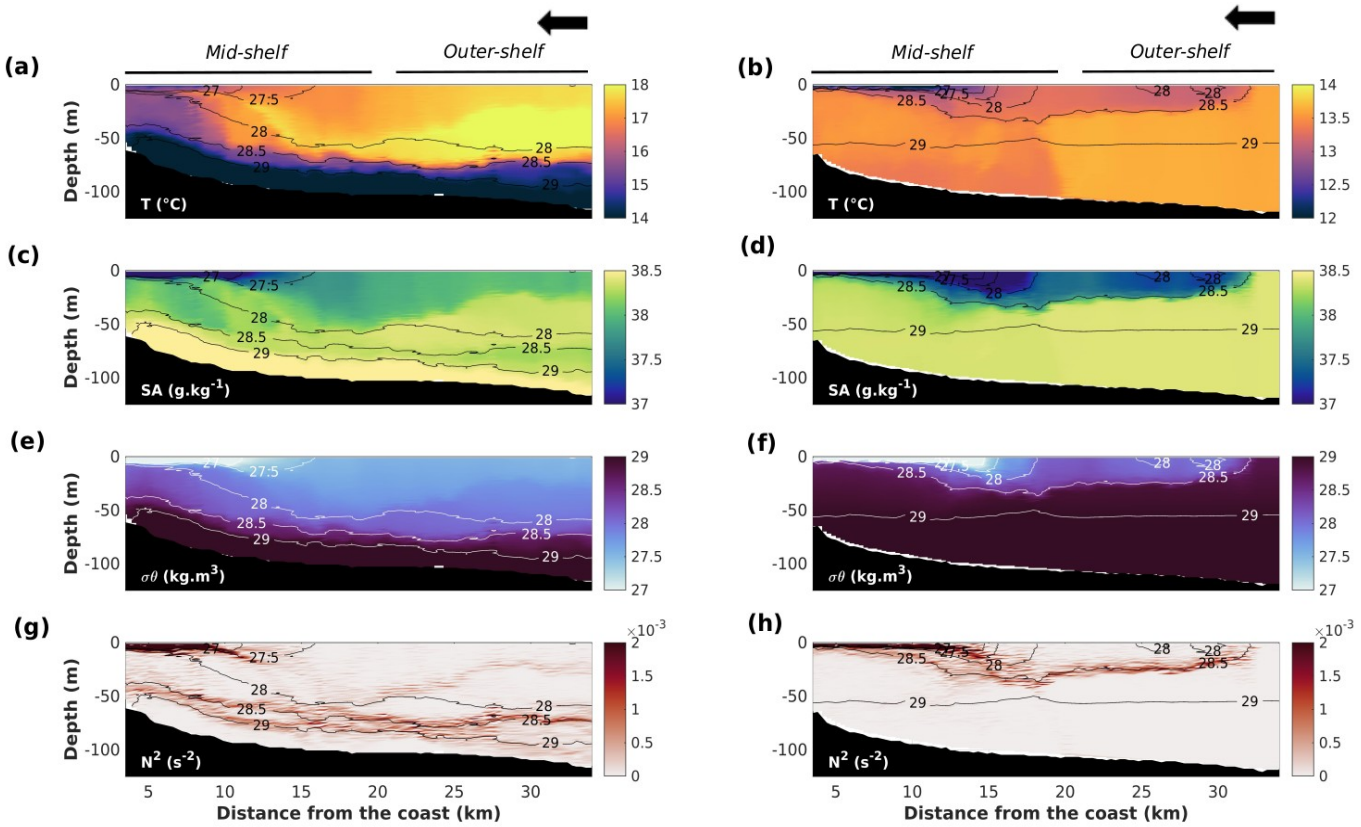

Figure 4.6: Hydrological variables: (a,b) temperature, (c,d) absolute salinity, (e,f) density anomalies, and (g,h) the Brunt–Väisälä frequency. The isopycnals are superimposed on all plots and indicated by black or white lines. The left panels correspond to autumnal conditions, from November 11 to 13, 2016. The right panels correspond to winter conditions, from February 5 to 7, 2017. The black arrow at the top of each panel indicates the direction of the glider's motion.

4.3.3. Hydrodynamical conditions

4.3.3.1. Validation of current measurements

After multiple yos (about six), the glider used GPS positioning to estimate the difference between the expected surface location as calculated through underwater dead reckoning, and the actual new position. Such position difference, relative to the time of dive, allowed the glider to estimate the depth-averaged current (DAC) between two surfacings (Davis et al., 2002). To assess

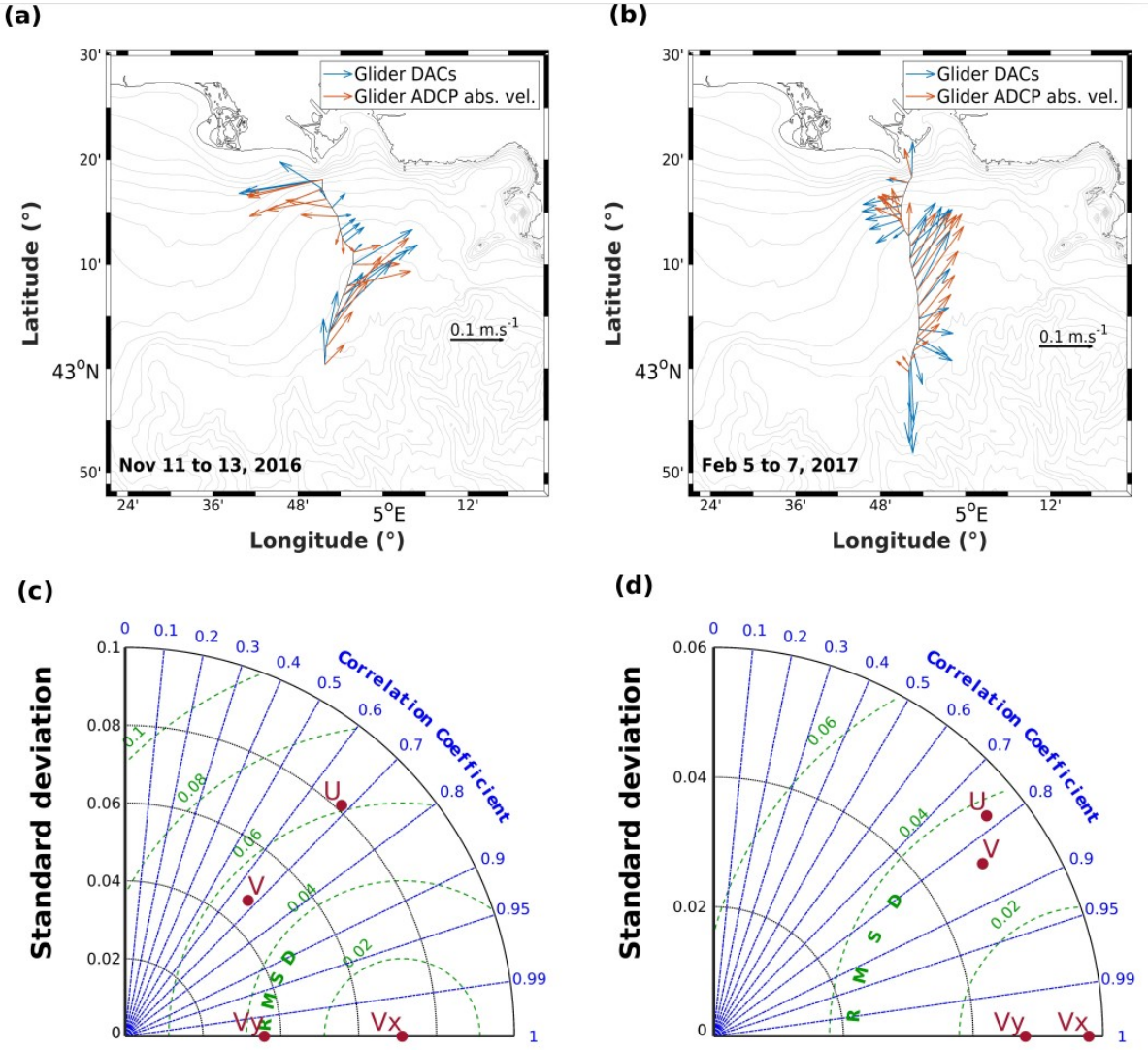

Figure 4.7: Comparison of depth-averaged current (DAC) vs. ADCP-derived residual current on sections of interest, respectively (a) from November 11 to 13, 2016 and (b) from February 5 to 7, 2017. Taylor's diagram comparing the DACs (Vx, Vy) and ADCP-derived residual current (U,V)—respectively for each component of eastward and northward velocity—across an entire deployment, (c) the autumn (November 2016) and (d) winter seasons (February 2017).

the quality of the ADCP measurements compared to this independent estimate of the currents, we contrasted the residual current velocities and direction computed from the downcast ADCP data between two surfacings with the corresponding DAC estimates (see the example on a section in Fig. 4.7a, b). The two estimates of the integrated average current over the water column were broadly comparable and reproduced the main inversions and intensifications of the currents for both periods.

This comparison was also carried out for all sections of each deployment, with the eastward and northward components considered separately (Fig. 4.7c, d). The Taylor diagrams showed a good agreement between the DAC (used as a reference) and the ADCP-derived residual currents. The correlation coefficient for the 2016 and 2017 surveys, respectively, was 0.69 and 0.78 for u, and 0.68 and 0.84 for v. Furthermore, the average standard deviation was 0.06 and 0.05 m s^{-1}, while the average RMSD was around 0.06 and 0.04 m s^{-1}, respectively, for the 2016 and 2017 deployments.

4.3.3.2. Characteristics of observed coastal currents

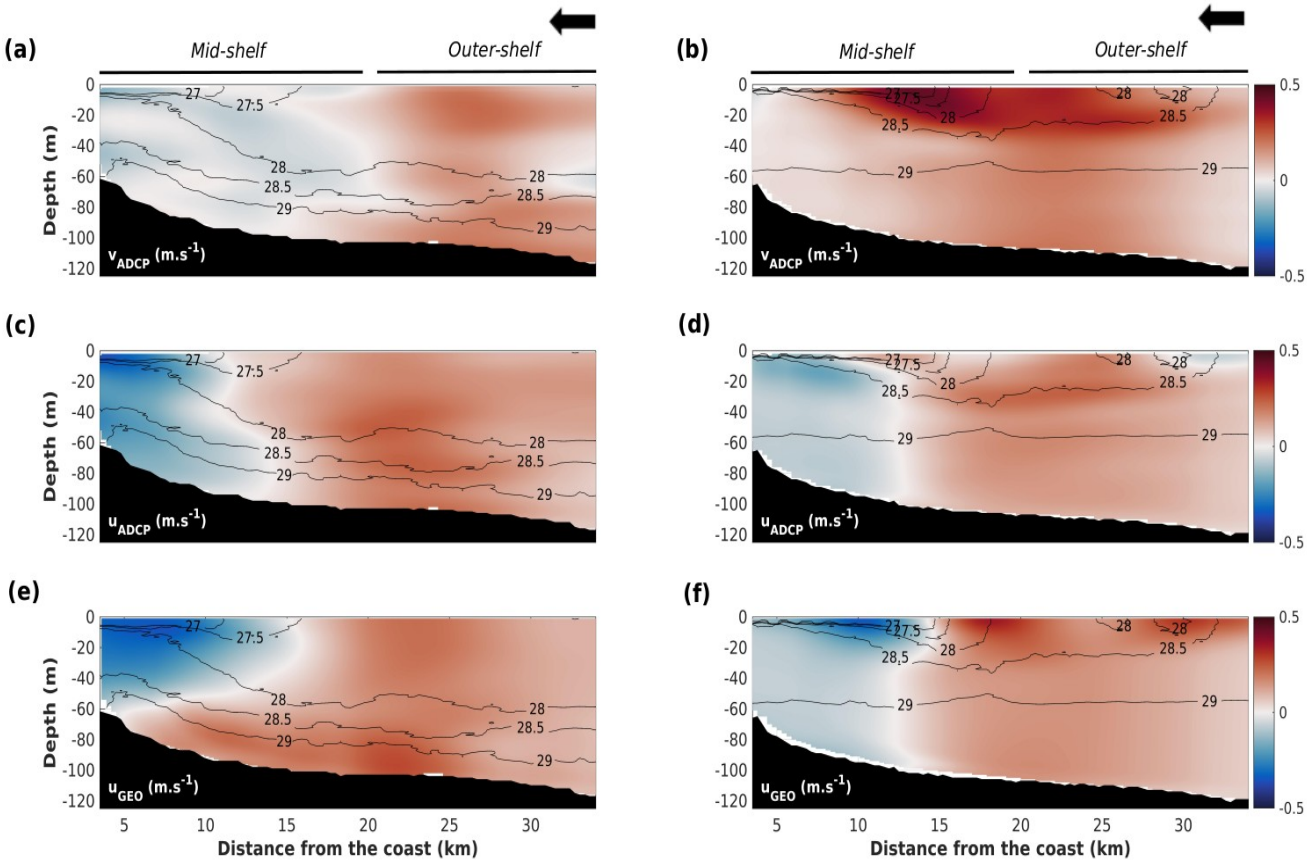

Figure 4.8: Hydrodynamical variables: (a,b) northward velocity, (c,d) eastward velocity, (e,f) and eastward geostrophic velocity. The left panels correspond to the autumnal season, from November 11 to 13, 2016. The right panels correspond to the winter season, from February 5 to 7, 2017. The black arrow at the top of each panel indicates the direction of the glider's motion.

Figure 4.8 shows the components of the cross-shelf (N–S) and along-shelf (E–W) currents derived from ADCP measurements for the selected sections. For the E–W and N–S components, current velocity (starting at 3 m under the surface) was generally homogeneous throughout the water column, with a maximum intensity of 0.5 m s^{-1}. However, strong northward subsurface currents were sometimes observed on the outer shelf, as in the section dating from 5 to 7 February 2017 (Fig. 4.8b). A westerly coastal current ($v \approx -0.4$ m s^{-1}) was often observed during autumnal conditions on the mid shelf (up to 13 km) (Fig. 4.8c). During winter conditions, the inner part of the slope current was observed at the shelf edge (not shown here).

4.3.4. Cross-shelf variability of biogeochemical variables

Optical and acoustic turbidity sections observed for the two selected periods are presented in Figure 4.9. Surface optical turbidity (Fig. 4.9a, b) and, incidentally, suspended particulate matter concentrations (Fig. 4.9c,d) decreased rapidly seaward from 6 mg L^{-1} next to the river mouth to 1 mg L^{-1} at the shelf break for both periods. Highest concentrations were observed in the plume. However, on some sections, a thin bottom nepheloid layer was observed with an SPM concentration around 2 mg L^{-1}. Finally, from November 11 to 13, 2016 an intermediate nepheloid layer extended over the mid shelf from 5 to 50 m depth, with a concentration of around 3 mg L^{-1}.

The concentration of chlorophyll-a was maximum in the surface layer, and its depth distribution was limited by the stratification. A chlorophyll-a rich layer (1–2 µg L^{-1}), with maximum thickness on the mid shelf (10–20 km offshore), was visible in November 2016 (Fig. 4.9e). During February 2017, chlorophyll-a concentration was both low (<0.5 µg L^{-1}) and homogeneous in the water column (Fig. 4.9f).

Observations show that the acoustical backscatter index (Fig. 4.9g, h) and optical spikes (Fig. 4.9i, j) were higher on the mid shelf for both deployments. An increase in the intensity of the spike signal was observed at the base of the intermediate nepheloid layer along the seasonal

pycnocline (around 50–60 m depth) from November 11 to 13, 2016 (Fig. 4.9i). During the autumnal deployment, the strong density stratification of the water column induced a significant change of the refractive index (Fig. 4.2a, b). The absence of a turbidity anomaly on either side of this interface indicates there was no Schlieren effect.

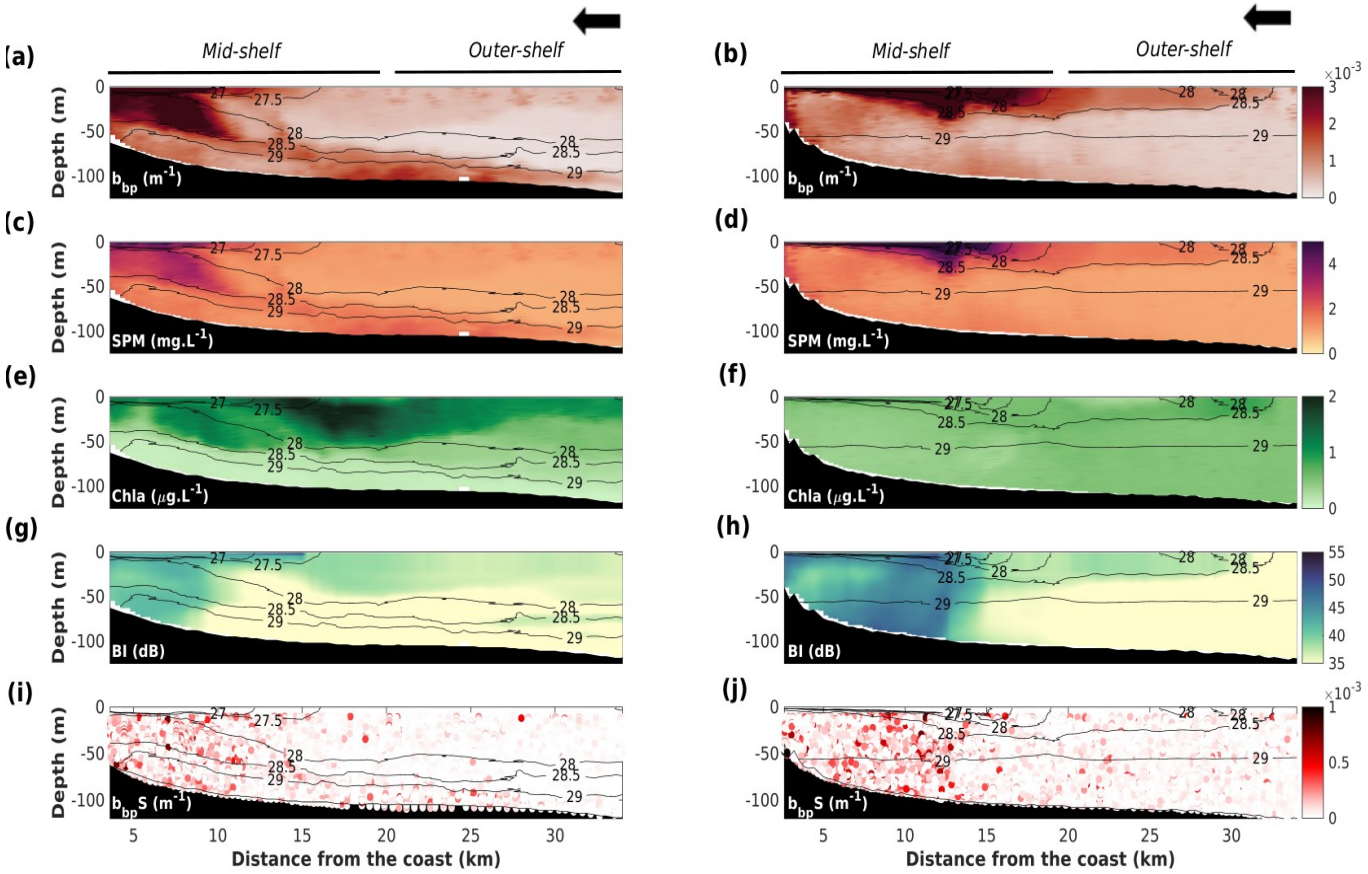

Figure 4.9: Turbidity measurements: (a,b) optical backscattering, (c,d) suspended particulate matter, (e,f) chlorophyll-a, (g,h) acoustic backscatter index, and (i,j) optical backscatter spikes. The left panels correspond to the autumnal season, from November 11 to 13, 2016. The right panels correspond to the winter season, from February 5 to 7, 2017. The black arrow at the top of each panel indicates the direction of the glider's motion.

4.4. Discussion

4.4.1. Currents observation by glider-mounted ADCP

Validation of absolute water velocities: differences are observed between the DAC computed using glider drift and dead reckoning, and the ADCP sensor. The ADCP samples neither during upcasts (transducer misalignment) nor at the surface (blanking distance close to the transducer and downward position), which may explain the main differences. However, the correlation coefficients between both components of the residual currents computed from glider drift and the ADCP range between 0.69 and 0.84. These highly significant correlations (*p*-value <0.001), with a mean bias between 0.05 and 0.06 m s^{-1}, give us some confidence in the method used for the estimation of absolute velocities.

The average uncertainty of the absolute current profile derived from the shear method is estimated at 13 cm s^{-1}, mainly due to the bottom tracking uncertainty which is about 12 cm s^{-1}. The ADCP sampling rate is likely the main parameter affecting the quality of the bottom tracking measurements, as our sampling frequency (0.1 Hz—1 ping per ensemble) was 10 times lower than that used in other studies (1 Hz—10 pings per ensemble) (Ma et al., 2019; Miles et al., 2015). Nevertheless, in yet another study, the total uncertainty estimated from the shear method and a similar instrument (DVL mounted on a Slocum glider)—but with a higher temporal resolution (1 Hz sampling frequency, ensembles averaging every 3.5 s)—was also close to 10 cm s^{-1} (Ordonez et al., 2012). An error velocity of 6 cm s^{-1} has previously been achieved using the inverse method with several constraints (DAC, surface current, and modelled velocity) and a high sampling frequency (1 Hz) (Ma et al., 2019). In spite of a higher uncertainty in current measurement, the chosen sampling strategy in our study allows deployments of several weeks. This choice was motivated by our intention to capture sporadic events, which are key elements of sediment dynamics in the coastal zone. Future deployments using different optimizations of sampling

parameters (increasing the size of the bins, reducing the number of bins, increasing the acquisition frequency [Gordon, 1996], and doubling the bottom tracking pings [Mullison et al., 2013]) should be investigated in order to assess the reduction of uncertainty in current estimations, while continuing to maintain autonomy.

Coastal current dynamics: the geostrophic component of the along-shelf flow (Fig. 4.8e, f) shows that the main structures of the ADCP-derived absolute currents were preserved. A least squares regression method was used to estimate the relationship between the geostrophic and absolute velocities, for all sections (Table 4.1). Coefficients of determination (r^2) were highly variable (0.02–0.99) from one section to another for both seasons. Coefficients of determination of all the data were high, between 0.69 and 0.8, respectively, in the autumn and winter seasons (Table 4.1). The local density field, which is affected by the freshwater input from the Rhone River, appears to play a major role in the coastal current dynamics.

Table 4.1: Results of linear regression analysis of eastward geostrophic currents with eastward ADCP currents for both deployments. Asterisks in the table indicate the sections of interest.

	Observation Time	**No. of Data**	**r^2**
Nov 1 to Nov 12, 2016	Section 1	10,738	0.15
	Section 2*	10,399	0.59
	Section 3	10,023	0.35
	Section 4	10,156	0.02
	Section 5	9752	0.68
	Section 6	10,256	0.72
Total		**61,324**	**0.69**
Jan 30 to Mar 3, 2017	Section 1	10,343	0.84
	Section 2	10,214	0.75
	Section 3*	10,661	0.61
	Section 4	10,307	0.68
	Section 5	10,615	0.74
	Section 6	10,221	0.79
	Section 7	9507	0.99
	Section 8	10,184	0.61
	Section 9	10,444	0.64
	Section 10	10,146	0.4
	Section 11	10,433	0.47
Total		**113,075**	**0.8**

However, wind may be a cause of non-geostrophic motion. The intense NW gusts of February 5–7, 2017 (shaded area on Fig. 4.5b), with speeds up to 21 m s^{-1}, pushed the fresh surface (0–3 m depth) water offshore inducing a strong northward subsurface counter-current (3–30 m depth) (Fig. 4.8b). Satellite measurements of sea surface temperature in summer (Millot, 1979), and hydrodynamic modeling studies (Estournel et al., 2003; Petrenko et al., 2008; Reffray et al., 2004; Schaeffer et al., 2011) have, indeed, described the presence of coastal upwelling in this region under the effect of N—NW winds. Moreover, near-inertial currents are recurrent on the Gulf of Lions shelf, where they tend to be triggered by windy events (Millot, 1990; Petrenko, 2003). They appear as rotational movements with characteristic diameters of a few kilometers and currents of about 10 cm s^{-1}. Using the method of unwrapping the phase of the shear vector of the current (Chereskin et al., 1989), between 3 and 40 m depth on glider sections, we were able to isolate periods when currents had a rotating component with a frequency close to the local Coriolis frequency (17.5 h) (Fig. 4.10a). Figure 4.10b shows the clockwise near-inertial current component of a few cm s^{-1} superimposed on a baroclinic mean current. These inertial currents were observed at the end of the section on the outer shelf following a strong NW wind episode that lasted several days. Current data collection ceases while the glider negotiates the half turn necessary for changing direction. Unfortunately, these data gaps prevent from observing the integrality of an inertial period.

Gliders thus appear to be unique tools for high resolution characterization of such transient phenomena throughout the entire water column and across the continental shelf.

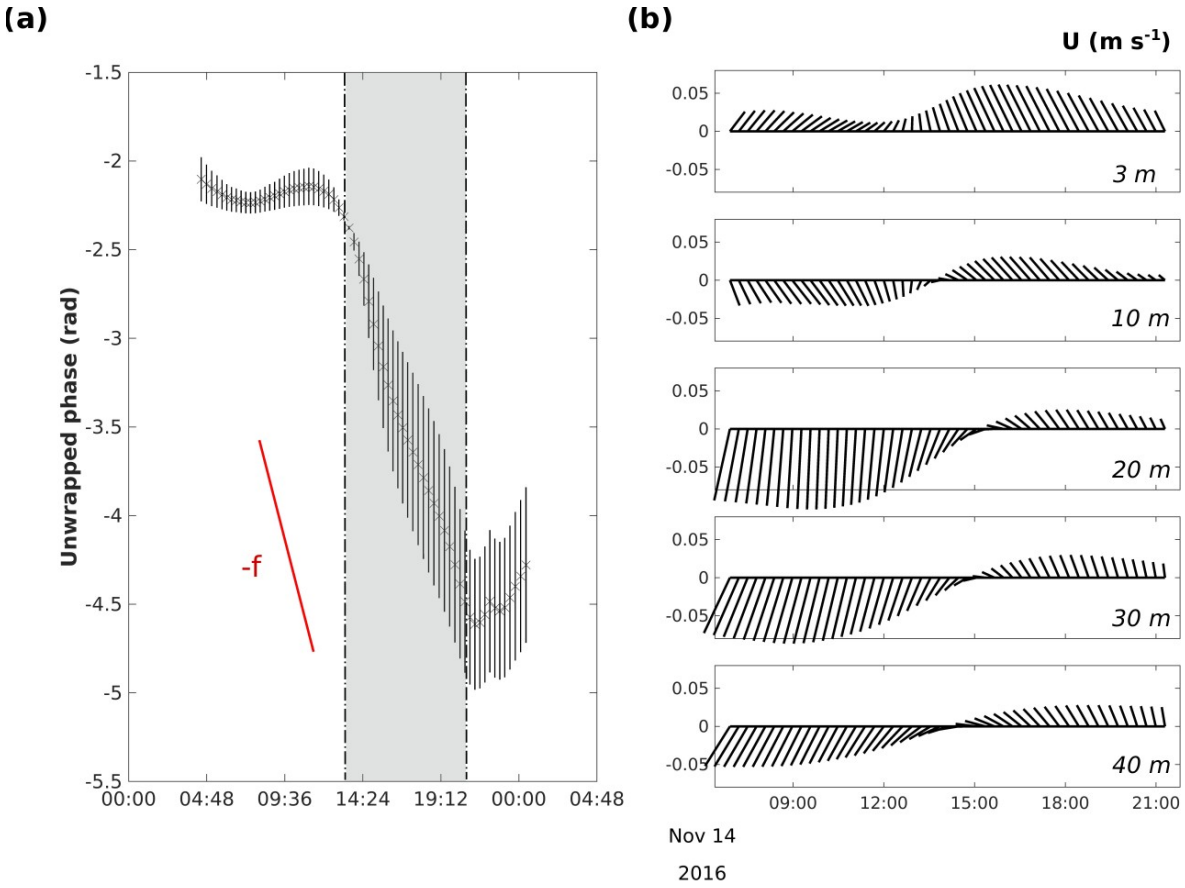

Figure 4.10: (a) Phase unwrapping of the horizontal current shear (3–40 m) from November 14 to 15, 2016. The negative slope corresponding to the Coriolis factor (-f) is shown. The shaded area corresponds to the portion of the period during which inertial oscillations are observed. (b) Horizontal currents from November 14 to 15, 2016, at 3, 10, 20, 30, and 40 m depth. From 10 m depth, the profiles show a clockwise oscillation of the currents.

4.4.2. Turbidity observation by glider optical and ADCP sensors

Optical and acoustic signals vary significantly with respect to particle concentration and to particle properties such as size, nature, and shape (Downing, 2006; Lynch et al., 1994). In addition, particle abundance in the Rhone River ROFI decreased by six orders of magnitude, ranging between particles of a few µm and those of 300 µm in size (Many et al., 2016). In this study, we hypothesize that optical spikes and acoustic backscatter sample a similar size range of particles.

Optical backscatter sensors that sample a small volume (approximately 1.10^{-6} m^3) are preferentially sensitive to fine particles. Indeed, measured optical turbidity for a given concentration

of suspended particles increases with decreasing particle size, due to both increased abundance and to light scattering from smaller particles. Although not very abundant, aggregates with sizes between a few tens and a few hundreds of microns (Many et al., 2016) often appear as spikes on the optical signal.

For acoustical measurements, the ADCP used in this work, with a frequency of 614.4 kHz, has a peak sensitivity for particles of 775 µm in diameter (Lohrmann, 2001), which represents the upper limit of the observed aggregates. Its sensitivity is 10–170 times lower for particles of 200 and 50 µm in diameter, respectively. Finally, the ADCP samples large insonified volumes—e.g., considering bins of 1 m and an acoustic beam width of 2°, the volume derived from the "footprint" of a single beam ranges between 1.10^{-3} m^3 at 2 m and about 1 m^3 at 20 m from the transducer—which may contain a significant number of aggregates.

A comparison of the different optical turbidity and acoustic backscatter index sections during the two deployments reveals both similarities (e.g., sections 5 and 6 in November 2016; Fig. 4.11) and dissimilarities (e.g., sections 2, 3, and 4 in February 2017; Fig. 4.12). For sections with similarities, mainly in the autumnal season, the distribution of optical spikes reproduces the main structures of both optical turbidity and acoustic backscatter index (Fig. 4.9a, g, i; Fig. 4.11). This concordance suggests that both instruments perceive signals from a narrower particle size distribution, mostly consisting of fine and micro-aggregate particles, in an equivalent manner. The presence of the intermediate nepheloid layer can thus be explained by the accumulation along the pycnocline of fine particles and micro aggregates that are insufficiently dense to move across this density interface.

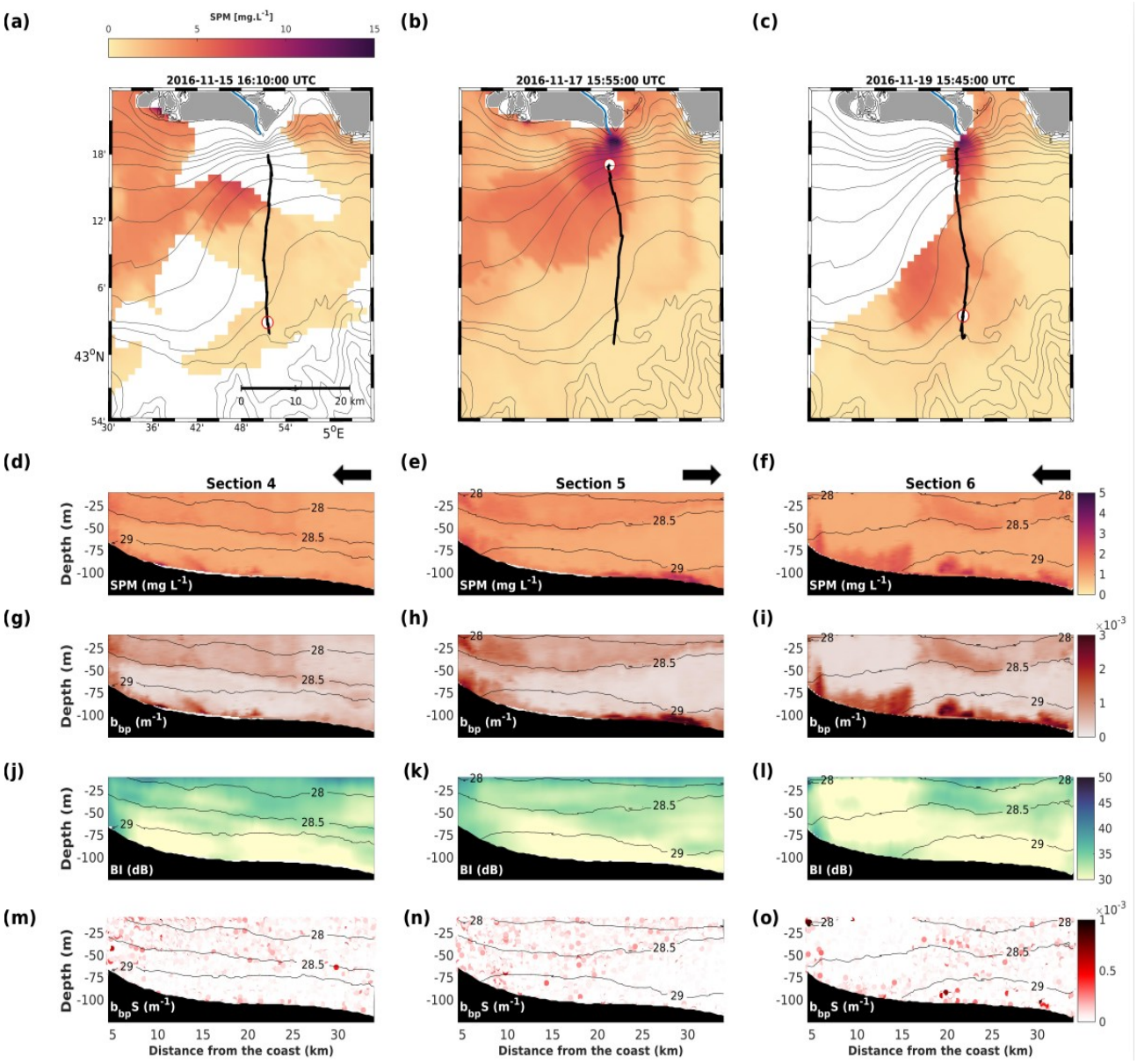

Figure 4.11: Surface turbidity from MODIS images (a—c) and glider measurements in the autumnal season: (d—f) suspended particle matter, (g—i) optical backscattering, (j—l) acoustic backscatter index, and (m—o) optical backscatter spikes. The left panels are estimates for section 4, from November 15 to 17, 2016. The center panels are estimates for section 5, from November 17 to 18, 2016. The right panels are estimates for section 6, from November 19 to 21, 2017. The black arrows indicate the glider's direction. For the top panels, the glider's location at the time the satellite image was taken is shown by the red circle, and clouds and land are shown as white patches and gray areas, respectively.

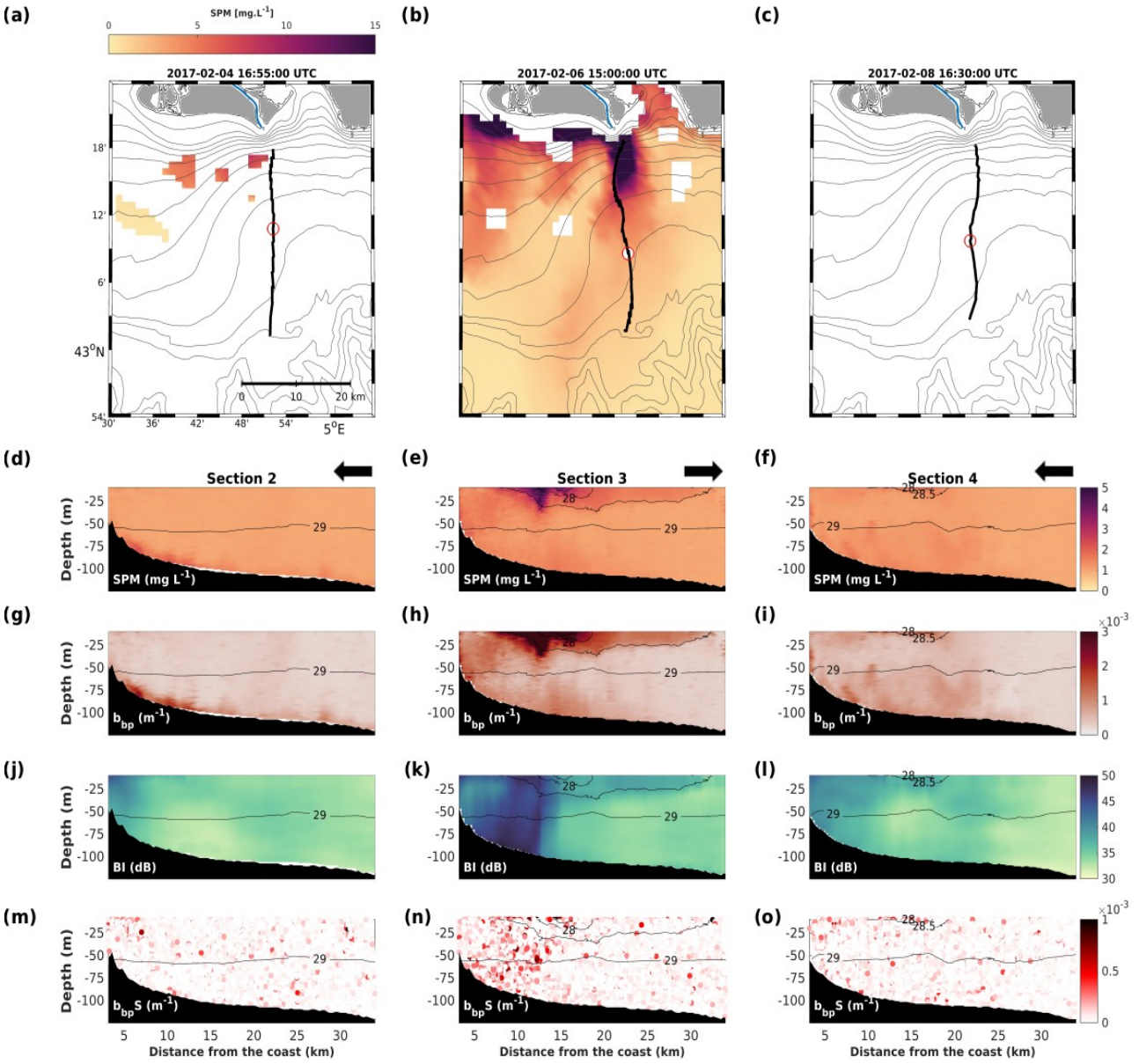

Figure 4.12: Surface turbidity from MODIS images (a—c) and glider measurements in the winter season: (d—f) suspended particle matter, (g—i) optical backscattering, (j—l) acoustic backscatter index, and (m—o) optical backscatter spikes. The left panels are estimates for section 3, from February 04 to 05, 2017. The center panels are estimates for section 4, from February 5 to 7, 2017. The right panels are estimates for section 5, from February 7 to 9, 2017. The black arrows indicate the glider's direction. For the top panels, the glider's location at the time the satellite image was taken is shown by the red circle, and clouds and land are shown as white patches and gray areas, respectively.

For sections with substantial dissimilarities, mainly during the winter season, it can be seen that the distribution of optical spikes differs from optical turbidity structures, but strongly corresponds to acoustic backscatter index structures (Fig. 4.9b, h, j; Fig. 4.12). This suggests that there are indeed two distinct (fine vs. large), relatively abundant particle size populations. The optical backscatter sensor detects these two populations through the base signal on one hand and the spikes on the other hand (Fig. 4.9b, j; Fig. 4.12), while the ADCP mainly senses the coarser fraction. This interpretation is in agreement with observations on particle size distribution in the Rhone ROFI area completed at the beginning of the February 2017 deployment (Many et al., 2016). Using LISST-100 and LISST-HOLO in situ grain sizers, those authors showed the concomitant abundance of fine particles (<30 μm), micro aggregates (between 30 and 100 μm), and large aggregates (up to 400 μm) on the proximal part of the mid shelf, at both the surface and the bottom. They revealed the presence of large particles—both aggregates and planktonic organisms (e.g., copepods)—in the surface layer further offshore, where we observe an increase in acoustic backscatter index, corresponding to the increase in chlorophyll-a concentration (Fig. 4.9e, g).

Our study illustrates the complementarity between concomitant optical and acoustic backscatter measurements from a glider to characterize the dynamics of different particle size populations. These results are consistent with observations made on the New Jersey shelf, which focused on intercomparison of acoustic and optical sensors to estimate sediment resuspension and transport. However, this information remains qualitative in nature, and there is currently no single glider-based instrument for the accurate description of variability and size of SPM in the water column. Recent technological advances have made it possible to integrate a Sequoia LISST-Glider (Miles et al., 2018) or a Hydroptics UVP6-LP (www.hydroptic.com/index.php/public/Page/product_item/UVP6-LP), and more quantitative estimates can legitimately be expected soon.

4.4.3. Estimates of SPM fluxes

Sediment transport plays a key role in the dynamics of coastal areas. However, the quantification of these fluxes on the continental shelf is still poorly documented, as over the last two decades measurements have been carried out mainly in a single given location, using bottom-mounted instruments (Bourrin et al., 2008b, 2008a ; Guillén et al., 2006 ; Palanques et al., 2008). In the Rhone ROFI area, quantitative studies have been derived solely from modelling (Dufois et al., 2014; Gangloff, 2017). However, the combined measurement of currents and particle concentration along a glider's trajectory has allowed us to estimate along- and cross-shore SPM fluxes. We calculated the integrated SPM fluxes throughout the water column by considering homogeneous currents and SPM concentrations in the surface and bottom layers not sampled by the glider. The fluxes were then cumulated over the entire length of each section. We estimated the uncertainty on cumulative SPM fluxes by propagating the average relative uncertainties related to the currents (~70%) and SPM concentrations (~35%). Relative error was seen to increase with decreasing SPM and water fluxes, ranging from 20% to 600%.

The along-shelf (E–W) and cross-shelf (N–S) SPM fluxes for the different glider sections are variable but generally remain lower than ±5 kg s^{-1} (Fig. 4.13). The highest value (8 kg s^{-1}) corresponds to the period from February 5 to 7, 2017, during which a strong NW wind induced an upwelling on the shelf, with the highest subsurface current (up to 0.5 $m.s^{-1}$) and SPM concentration (~6 mg L^{-1}) (Fig. 4.8b and 4.9d).

In the absence of storm or flood events, however, estimated SPM fluxes remain low, about one order of magnitude lower than the SPM fluxes from the Rhone River during the same periods (10–130 kg s^{-1}). This suggests a significant deposition next to the river mouth in line with Lansard, (2004); Maillet et al. (2006); and Noël, (1996). Estimated SPM fluxes are also three orders of magnitude lower than those observed on the Catalan shelf in the Gulf of Lions during stormy

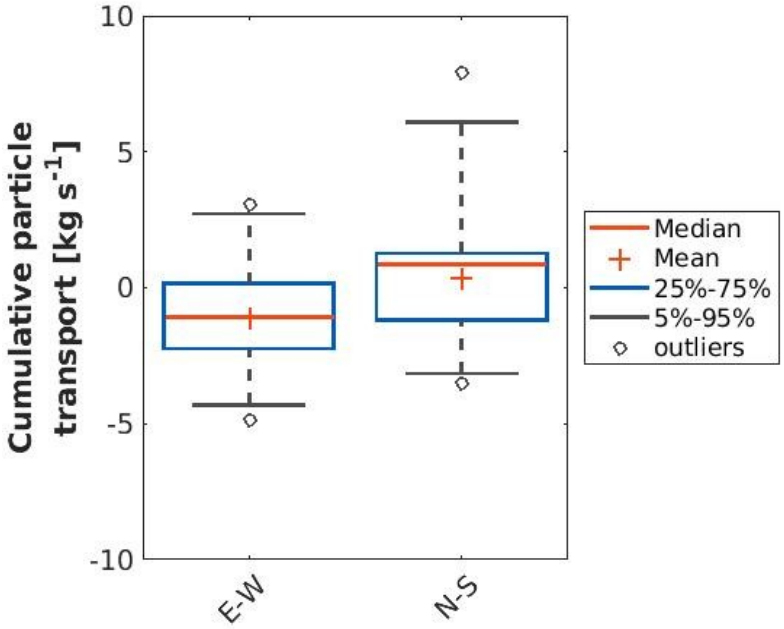

Figure 4.13: Distribution of cumulative along- (E–W) and cross-shelf (N–S) particle transport (kg s^{-1}) for all the sections performed during autumnal and winter deployments.

conditions (Bourrin et al., 2015). We see here the difficulty of estimating SPM flows with a reasonable level of certainty because this requires accurate conversion of optical turbidity or acoustic backscatter index signals into SPM concentration. This step therefore remains challenging because of the great variability in the nature of the suspended particulate material, especially in coastal areas and during storms or flood events.

4.4.4. SPM dynamics from glider vs. satellite observations

Several studies have emphasized the value of combining satellite and glider measurements to accurately characterize SPM dynamics in coastal areas, especially during extreme events (Bourrin et al., 2015; Castelao et al., 2008; Miles et al., 2015). We compared satellite images of surface SPM concentrations with those observed by the glider close to the surface in order to assess their complementarity in terms of monitoring turbidity in the Rhone's ROFI. The relationship between SPM derived from glider/MODIS measurements can be expressed as $SPM_{MODIS} = 2.6 \times$

SPM_{Glider}, with a coefficient of determination of 0.87, which is very similar to observations already made in this area (Many et al., 2018).

The Rhone's ROFI is a complex system in which the high spatial and temporal variability of the river plume can shift by several kilometers in a few hours, depending on wind and river discharge conditions. For stable conditions, or when satellite data are partial (Fig. 4.11a, c) or lacking (Fig. 4.12a, c) due to cloud cover, glider measurement near the surface ensures some continuity between daily satellite snapshots. The complementarity of the glider as a tool resides primarily in the fact that gliders make it possible to describe the vertical extension of superficial structures in the water column, such as the turbid plumes of rivers.

Conversely, when conditions are very changeable it is more difficult to correlate the surface structures as seen by satellites with the glider's observations that couple space and time. Figure 4.14 shows a glider section and the associated satellite images of November 8, 9, and 10, 2016. Daily satellite images (Fig. 4.14a—c) show significant variability of the Rhone River plume which the glider observations (Fig. 4.14d) fail to capture. Throughout the section, which was covered in two days, the glider was in the plume on the first day only (Fig. 4.14a), when the plume was located near the river mouth. The plume was then deflected by the wind on the following days and moved offshore (Fig. 4.14b, c), away from the glider.

This example shows the limits of agreement between these two observation platforms in a system with high spatial and temporal variability. However, the above-mentioned complementarity proves useful in systems where variability is lower and compatible with the time it takes the glider to traverse the monitoring section.

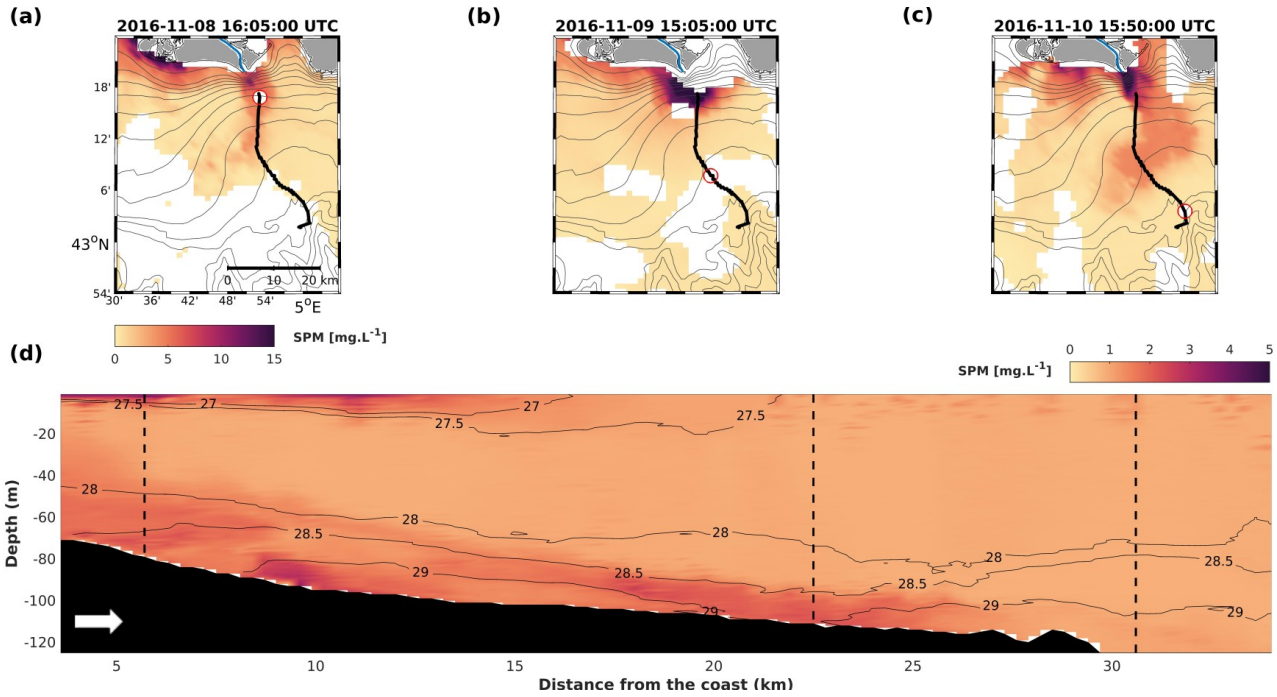

Figure 4.14: (a–c) Surface turbidity from MODIS images, for the glider's section 1 in November 2016. Clouds and land are shown as white patches and gray areas, respectively. (d) Glider turbidity observations in the water column along the cross-shelf track. The black line indicated the glider's path and the white arrow shows its direction. The glider's location at the time the satellite image was taken is shown by the red circle and by dashed black lines in the upper and lower panels, respectively.

4.5. Conclusion

In this study, we successfully deployed a glider equipped with a CTD, an optical payload, and a 600 KHz phased array ADCP to monitor currents and turbidity in the Rhone River ROFI during two contrasted periods (autumn and winter). The major outcomes and conclusions of this study are as follows:

- In line with previous studies, our comparison of currents estimated from ADCP data with the DAC confirms that this system is suitable for measuring currents in coastal areas, with an uncertainty of 0.13 m s^{-1}. The repeated glider transects across the shelf show the importance of freshwater input from the Rhone River as one of the main drivers of local hydrodynamics.

- In order to qualify the results by comparison with the DAC, we employed the shear method to determine absolute currents. We applied the bottom track constraint to near-bottom currents. Unfortunately, this constraint was seen to have a fairly high uncertainty due to the low ADCP sampling frequency.
- Coincident optical and acoustic backscatter measurements show complementarity in the characterization of small and large suspended particles, respectively. Analysis of optical spikes and acoustic backscatter indicates the presence of coarse particles on the proximal part of the mid shelf close to the river mouth, where hydrological conditions likely favor the formation of macro flocs.
- The calculated SPM fluxes and their uncertainties (20–600%) are highly variable. Furthermore, the SPM fluxes on the shelf are one order of magnitude lower than the concomitant SPM fluxes from the nearby Rhone River, which suggests a significant deposition of particulate matter at the river mouth.
- The combination of both satellite and glider SPM measurements is important for monitoring both surface and subsurface parts of the river plume.
- The sampling strategy used in this study showed that the monitoring of currents and turbidity in the coastal zone over periods ranging from several weeks to several months is feasible. This technique enables the capture of difficult to monitor sporadic events such as storms or floods, which is essential both for improving existing knowledge of coastal circulation and sediment transport, and for the validation of hydro-sedimentary regional models.

In future work we plan to continue estimating currents using the inverse method, simultaneously using independent estimates of current velocities using bottom tracking, a flight model, and the DAC. This should enable to reduce the uncertainty in current estimates and to extend the study area beyond the continental shelf, where bottom tracking is inoperative. We also intend to optimize sampling (by increasing the size of the bins, reducing the number of bins,

increasing the acquisition frequency) so as to reduce uncertainties while maintaining a large autonomy. For the estimation of SPM fluxes, we foresee improving the calibration of the optical sensor (by increasing the number of measurements and triplicates) and carrying out an independent calibration of the acoustic sensor, which may allow us to discriminate coarse particle (acoustic) and fine particle (optic) fluxes. Future use of glider-based direct measurements of particle size will allow to better characterize the entire spectrum of suspended particles and their dynamics.

Author Contributions: Conceptualization, methodology, and writing, M.G., G.M., F.B., X.D.M., I.P., P.T., R.V.; analyses, M.G., G.M., P.C, F.B., X.D.M.; funding acquisition, F.B., X.D.M. All authors have read and agreed to the published version of the manuscript.

Funding: The corresponding author is funded through a PhD grant of French Occitanie Region. This work was funded by the MATUGLI project (ANR-14-ASTR-0021-01) under the ANR ASTRID DGA Program and the MISTRALS-MERMEX Program.

Acknowledgments: We thank N. Briggs for his help on optical spike characterization. We thank the Parc National des Gliders of the DT INSU, CNRS for the integration of the ADCP, glider deployment, and piloting. We also thank the captain and crews of the R/V Tethys II for their help during sampling.

Conflicts of Interest: The authors declare no conflict of interests.

References

Bourrin, F., de Madron, X. D., Heussner, S., Estournel, C., 2008a. Impact of winter dense water formation on shelf sediment erosion (evidence from the Gulf of Lions, NW Mediterranean). Continental Shelf Research 28, 1984–1999.

Bourrin, F., Friend, P.L., Amos, C.L., Manca, E., Ulses, C., Palanques, A., De Madron, X.D., Thompson, C.E., 2008b. Sediment dispersal from a typical Mediterranean flood: the Têt River, Gulf of Lions. Continental Shelf Research 28, 1895–1910.

Bourrin, F., Many, G., De Madron, X. D., Martín, J., Puig, P., Houpert, L., Testor, P., Kunesch, S., Mahiouz, K., Béguery, L., 2015. Glider monitoring of shelf suspended particle dynamics and transport during storm and flooding conditions. Continental Shelf Research 109, 135–149.

Briggs, N., Perry, M. J., Cetinić, I., Lee, C., D'Asaro, E., Gray, A. M., Rehm, E., 2011. High-resolution observations of aggregate flux during a sub-polar North Atlantic spring bloom. Deep Sea Research Part I: Oceanographic Research Papers 58, 1031–1039.

Castelao, R., Glenn, S., Schofield, O., Chant, R., Wilkin, J., Kohut, J., 2008. Seasonal evolution of hydrographic fields in the central Middle Atlantic Bight from glider observations. Geophysical Research Letters 35.

Chereskin, T., Levine, M. D., Harding, A., Regier, L., 1989. Observations of near-inertial waves in acoustic Doppler current profiler measurements made during the Mixed Layer Dynamics Experiment. Journal of Geophysical Research: Oceans 94, 8135–8145.

Davis, R. E., Eriksen, C. C., Jones, C. P., 2002. Autonomous buoyancy-driven underwater gliders. The technology and applications of autonomous underwater vehicles 37–58.

Deines, K. L., 1999. Backscatter estimation using broadband acoustic Doppler current profilers. Presented at the Proceedings of the IEEE Sixth Working Conference on Current Measurement (Cat. No. 99CH36331), IEEE, pp. 249–253.

Downing, J., 2006. Twenty-five years with OBS sensors: The good, the bad, and the ugly. Continental Shelf Research 26, 2299–2318.

Doxaran, D., Froidefond, J.-M., Castaing, P., Babin, M., 2009. Dynamics of the turbidity maximum zone in a macrotidal estuary (the Gironde, France): Observations from field and MODIS satellite data. Estuarine, Coastal and Shelf Science 81, 321–332.

Dufois, F., Verney, R., Le Hir, P., Dumas, F., Charmasson, S., 2014. Impact of winter storms on sediment erosion in the Rhone River prodelta and fate of sediment in the Gulf of Lions (North Western Mediterranean Sea). Continental Shelf Research 72, 57–72.

Durrieu de Madron, X., Wiberg, P. L., Puig, P., 2008. Sediment dynamics in the Gulf of Lions: The impact of extreme events.

Ellis, D., Washburn, L., Ohlmann, C., Gotschalk, C., 2015. Improved methods to calculate depth-resolved velocities from glider-mounted ADCPs. Presented at the 2015 IEEE/OES Eleveth Current, Waves and Turbulence Measurement (CWTM), IEEE, pp. 1–10.

Estournel, C., Durrieu de Madron, X., Marsaleix, P., Auclair, F., Julliand, C., Vehil, R., 2003. Observation and modeling of the winter coastal oceanic circulation in the Gulf of Lion under wind conditions influenced by the continental orography (FETCH experiment). Journal of Geophysical Research: Oceans 108.

Firing, E., Gordon, R. L., 1990. Deep ocean acoustic Doppler current profiling. Presented at the Proceedings of the IEEE Fourth Working Conference on Current Measurement, IEEE, pp. 192–201.

Fischer, J., Visbeck, M., 1993. Deep velocity profiling with self-contained ADCPs. Journal of atmospheric and oceanic technology 10, 764–773.

Frajka-Williams, E., Eriksen, C. C., Rhines, P.B., Harcourt, R. R., 2011. Determining vertical water velocities from Seaglider. Journal of Atmospheric and Oceanic Technology 28, 1641–1656.

Francois, R., Garrison, G., 1982. Sound absorption based on ocean measurements. Part II: Boric acid contribution and equation for total absorption. The Journal of the Acoustical Society of America 72, 1879–1890.

Gangloff, A., 2017. Devenir des apports solides du Rhône dans le Golfe du Lion : étude de la dynamique du panache turbide du Rhône en réponse aux forçages hydrométéorologiques.

Garau, B., Ruiz, S., Zhang, W.G., Pascual, A., Heslop, E., Kerfoot, J., Tintoré, J., 2011. Thermal lag correction on Slocum CTD glider data. Journal of Atmospheric and Oceanic Technology 28, 1065–1071.

Glenn, S., Jones, C., Twardowski, M., Bowers, L., Kerfoot, J., Kohut, J., Webb, D., Schofield, O., 2008. Glider observations of sediment resuspension in a Middle Atlantic Bight fall transition storm. Limnology and Oceanography 53, 2180–2196.

Gohin, F., 2011. Annual cycles of chlorophyll-a, non-algal suspended particulate matter, and turbidity observed from space and in situ in coastal waters. Ocean Science 7, 705–732.

Gordon, R. L., 1996. Acoustic Doppler current profiler-Principles of operation: A practical primer. Rd Instruments 54, 54.

Gostiaux, L., van Haren, H., 2010. Extracting meaningful information from uncalibrated backscattered echo intensity data. Journal of Atmospheric and Oceanic Technology 27, 943–949.

Guillén, J., Bourrin, F., Palanques, A., De Madron, X. D., Puig, P., Buscail, R., 2006. Sediment dynamics during wet and dry storm events on the Têt inner shelf (SW Gulf of Lions). Marine Geology 234, 129–142.

Lansard, B., 2004. Distribution et remobilisation du plutonium dans les sédiments du prodelta du Rhône (Méditerranée nord-occidentale).

Liblik, T., Karstensen, J., Testor, P., Alenius, P., Hayes, D., Ruiz, S., Heywood, K., Pouliquen, S., Mortier, L., Mauri, Ejm., 2016. Potential for an underwater glider component as part of the Global Ocean Observing System. Methods in Oceanography 17, 50–82.

Lohrmann, A., 2001. Monitoring sediment concentration with acoustic backscattering instruments. Nortek Technical Note 3, 1–5.

Lynch, J. F., Irish, J.D., Sherwood, C.R., Agrawal, Y. C., 1994. Determining suspended sediment particle size information from acoustical and optical backscatter measurements. Continental Shelf Research 14, 1139–1165.

Ma, W., Wang, Y., Wang, S., Zhang, Hongwei, Zhang, Han, Gong, Q., 2019. Absolute Current Estimation and Sea-Trial Application of Glider-Mounted AD2CP. Journal of Coastal Research 35, 1343–1350.

Maillet, G.M., Vella, C., Berné, S., Friend, P. L., Amos, C.L., Fleury, T. J., Normand, A., 2006. Morphological changes and sedimentary processes induced by the December 2003 flood event at the present mouth of the Grand Rhône River (southern France). Marine Geology 234, 159–177.

Many, G., Bourrin, F., de Madron, X.D., Ody, A., Doxaran, D., Cauchy, P., 2018. Glider and satellite monitoring of the variability of the suspended particle distribution and size in the Rhône ROFI. Progress in oceanography 163, 123–135.

Many, G., Bourrin, F., de Madron, X.D., Pairaud, I., Gangloff, A., Doxaran, D., Ody, A., Verney, R., Menniti, C., Le Berre, D., 2016. Particle assemblage characterization in the Rhone River ROFI. Journal of Marine Systems 157, 39–51.

McDougall, T.J., Barker, P. M., 2011. Getting started with TEOS-10 and the Gibbs Seawater (GSW) oceanographic toolbox. SCOR/IAPSO WG 127, 1–28.

Merckelbach, L., Smeed, D., Griffiths, G., 2010. Vertical water velocities from underwater gliders. Journal of Atmospheric and Oceanic Technology 27, 547–563.

Miles, T., Glenn, S. M., Schofield, O., 2013. Temporal and spatial variability in fall storm induced sediment resuspension on the Mid-Atlantic Bight. Continental Shelf Research 63, S36—S49.

Miles, T., Seroka, G., Kohut, J., Schofield, O., Glenn, S., 2015. Glider observations and modeling of sediment transport in Hurricane Sandy. Journal of Geophysical Research: Oceans 120, 1771–1791.

Miles, T. N., Kohut, J., Slade, W., Gong, D., 2018. Suspended particle characteristics from a glider integrated LISST sensor. Presented at the OCEANS 2018 MTS/IEEE Charleston, IEEE, pp. 1–5.

Millot, C., 1990. The gulf of Lions' hydrodynamics. Continental shelf research 10, 885–894.

Millot, C., 1979. Wind induced upwellings in the Gulf of Lions. Oceanologica Acta 2, 261–274.

Mullison, J., 2017. Backscatter estimation using broadband acoustic doppler current profilers-updated. Presented at the Proceedings of the ASCE Hydraulic Measurements & Experimental Methods Conference, Durham, NH, USA, pp. 9–12.

Mullison, J., DeCollibus, C., Allsup, B., 2013. An investigation of the accuracy of current profile measurements from a glider-mounted ADCP operating in shallow water. Presented at the 2013 OCEANS-San Diego, IEEE, pp. 1–8.

Noël, M.-H., 1996. Le plutonium comme traceur du transfert et de l'accumulation des apports particulaires du Rhône en Méditerranée Nord Occidentale.

Ody, A., Doxaran, D., Vanhellemont, Q., Nechad, B., Novoa, S., Many, G., Bourrin, F., Verney, R., Pairaud, I., Gentili, B., 2016. Potential of high spatial and temporal ocean color satellite data to study the dynamics of suspended particles in a micro-tidal river plume. Remote Sensing 8, 245.

Ordonez, C.E., Shearman, R.K., Barth, J.A., Welch, P., Erofeev, A., Kurokawa, Z., 2012. Obtaining absolute water velocity profiles from glider-mounted acoustic Doppler current profilers. Presented at the 2012 Oceans-Yeosu, IEEE, pp. 1–7.

Ouillon, S., 2018. Why and how do we study sediment transport? Focus on coastal zones and ongoing methods. Water 2018, 10(4), 390; https://doi.org/10.3390/w10040390.

Palanques, A., Guillén, J., Puig, P., de Madron, X. D., 2008. Storm-driven shelf-to-canyon suspended sediment transport at the southwestern Gulf of Lions. Continental Shelf Research 28, 1947–1956.

Petrenko, A., Dufau, C., Estournel, C., 2008. Barotropic eastward currents in the western Gulf of Lion, north-western Mediterranean Sea, during stratified conditions. Journal of Marine Systems 74, 406–428.

Petrenko, A., 2003. Variability of circulation features in the Gulf of Lion NW Mediterranean Sea. Importance of inertial currents. Oceanologica acta 26, 323–338.

Quan, X., Fry, E. S., 1995. Empirical equation for the index of refraction of seawater. Applied optics 34, 3477–3480.

Reffray, G., Fraunié, P., Marsaleix, P., 2004. Secondary flows induced by wind forcing in the Rhône region of freshwater influence. Ocean Dynamics 54, 179–196.

Rudnick, D. L., 2016. Ocean research enabled by underwater gliders. Annual review of marine science 8, 519–541.

Sadaoui, M., Ludwig, W., Bourrin, F., Raimbault, P., 2016. Controls, budgets and variability of riverine sediment fluxes to the Gulf of Lions (NW Mediterranean Sea). Journal of Hydrology 540, 1002–1015.

Schaeffer, A., Garreau, P., Molcard, A., Fraunié, P., Seity, Y., 2011. Influence of high-resolution wind forcing on hydrodynamic modeling of the Gulf of Lions. Ocean Dynamics 61, 1823–1844.

Styles, R., 2006. Laboratory evaluation of the LISST in a stratified fluid. Marine Geology 227, 151–162.

Sullivan, J.M., Twardowski, M.S., Ronald, J., Zaneveld, V., Moore, C.C., 2013. Measuring optical backscattering in water, in: Light Scattering Reviews 7. Springer, pp. 189–224.

Testor, P., Meyers, G., Pattiaratchi, C., Bachmayer, R., Hayes, D., Pouliquen, S., Petit de la Villeon, L., Carval, T., Ganachaud, A., Gourdeau, L., 2010. Gliders as a component of future observing systems. OceanObs' 09.

Thurnherr, A., Symonds, D., Laurent, L.S., 2015. Processing explorer ADCP data collected on slocum gliders using the LADCP shear method. Presented at the 2015 IEEE/OES Eleventh Current, Waves and Turbulence Measurement (CWTM), IEEE, pp. 1–7.

Todd, R. E., 2017. High-frequency internal waves and thick bottom mixed layers observed by gliders in the Gulf Stream. Geophysical Research Letters 44, 6316–6325.

Todd, R. E., Rudnick, D. L., Mazloff, M. R., Davis, R. E., Cornuelle, B. D., 2011. Poleward flows in the southern California Current System: Glider observations and numerical simulation. Journal of Geophysical Research: Oceans 116.

Visbeck, M., 2002. Deep velocity profiling using lowered acoustic Doppler current profilers: Bottom track and inverse solutions. Journal of atmospheric and oceanic technology 19, 794–807.

Chapter 5.

Sediment dynamics on the outer-shelf of the Gulf of Lions during an onshore storm: an approach based on acoustic glider and numerical modelling

Chapter 5. Sediment dynamics on the outer-shelf of the Gulf of Lions during an onshore storm: an approach based on acoustic glider and numerical modelling

---

Mathieu Gentil [1,*], Claude Estournel [2], Xavier Durrieu de Madron [1], Gaël Many [3], Travis Miles [4], Patrick Marsaleix [2], Serge Berné [1], François Bourrin [1],

[1] CEFREM, CNRS, Université de Perpignan Via Domitia, 52 Avenue Paul Alduy, 66860 Perpignan, France ;

[2] LEGOS, Université de Toulouse, CNES, CNRS, IRD, UPS, Toulouse, France ;

[3] IDYST, Université of Lausanne, Switzerland;

[4] Rutgers, The State University of New Jersey, New Brunswick, New Jersey ;

* Correspondence: mathieu.gentil@univ-perp.fr

Submitted to Continental Shelf Research: 20 October 2021.

Highlights:

- Active acoustic underwater glider monitors near-bed sediment processes during a 5-year return period storm;
- Waves are the primary driver of sediment resuspension for depths >90 m on the shelf;
- Numerical simulations suggest an along shelf transfer by successive jumps associated with onshore storms.

Table of Contents

Table of figures

Abstract

Describing and quantifying storm-induced sediment dynamics enables improved mapping of the fate of sediments over continental shelves, which is necessary to understand their role in the structure and dynamics of marine ecosystems, nutrient cycling, and dispersion of pollutants. Storms are episodic processes that can lead to massive sediment resuspension and transport on continental shelves. However, the quantification of sediment dynamics during storms remains a challenge, because these events are spatially under-sampled due to their intermittency and intensity. This paper quantifies processes that drive sediment dynamics and their spatiotemporal variability over the outer shelf of the Gulf of Lions (NW Mediterranean), during a 5-year return period storm, using an active acoustic glider combined with a hydrodynamic model (SYMPHONIE). The glider-ADCP (Acoustic Doppler Current Profiler) provides valuable near-bed data, showing for the first time that waves are the primary driver of sediment resuspension for depths greater than 90 m on the shelf. Also, this mobile profiling sensor platform proved invaluable validation of current vertical profiles of the hydrodynamic model during the storm, while observations of this type of event are generally lacking in the coastal continuum due to their rarity. The combination of observations with numerical simulations suggest an along shelf sediment transfer by successive jumps associated with onshore storms, from the main input (the Rhone River) to the output (the Cap de Creus) area of the Gulf of Lions' shelf. This study highlights the complementarity between numerical modelling and new technology observations designed to spatially extend the measurement of sediment resuspension and transport during extreme events.

Keywords: Storm event, Wave-current interaction, Sediment dynamics, Acoustic-glider, Hydrodynamic model, Gulf of Lions, Mediterranean

5.1. Introduction

5.1.1. Coastal storm and sediment dynamics

Sediment dynamics over continental shelves is strongly influenced by multiple forcings (river discharges, currents, wind, waves). Among them, coastal storm-driven mixing events are episodic processes (Chang et al., 2001; Wiggert et al., 2000; Zedler et al., 2002)**,** especially important in micro-tidal environments (Paladini de Mendoza et al., 2018). Both waves and currents can generate bottom shear stress that can result in potentially massive sediment resuspension, through non-linear interactions (Grant and Madsen, 1979; Soulsby et al., 1993; Van Rijn and Kroon, 1993). However, the quantification of sediment resuspension and transport on continental shelves during storms remains a challenge. Enriching the documentation of the hydro-sedimentary conditions that control sediment resuspension and transport are crucial to predict the fate of sediment and pollutants that are introduced onto the shelf and which might be reworking and off-shelf export (Bosnic et al., 2017; Ferré et al., 2010).

Most *in-situ* observations of wave-current interactions and sediment resuspension are gathered at few fixed locations on the shelf, from optical and acoustic sensors on tripods and benthic landers (Chang et al., 2001; Drake et al., 1992; Drake and Cacchione, 1986; Jing and Ridd, 1996; Liu et al., 2017; Niu et al., 2020; Palinkas et al., 2010). Such observations provide precise information on the temporal variability of the bottom layer but do not capture the spatial gradients across the entire shelf or evaluate the overall sediment transport. To fill this gap and understand sediment dynamics at regional scales, three-dimensional hydrodynamic models have been used (Dalyander et al., 2013; Dufois et al., 2008; King et al., 2019; Styles and Glenn, 2005; Ulses et al., 2008a)**.** However, these studies face the difficulty of modelling hydrodynamic parameters under extreme conditions as well as sediment behavior in a wide range of sand-mud mixtures associated with a variety of complex bedforms. In this context, the combination of numerical modelling and

new autonomous ocean observing technologies designed to spatially extend the measurement of sediment resuspension and transport appears promising (Miles et al., 2015).

Underwater gliders are becoming increasingly important for the collection of oceanographic measurements in observing programs (Liblik et al., 2016; Rudnick, 2016; Testor et al., 2019). These systems are low power long-term duration (>30 days) autonomous underwater vehicles that can carry a range of interchangeable sensor packages and sample the water column on large spatial scales (>100 km). Several studies have shown the ability of autonomous gliders equipped with physical and optical sensors to study the spatial and temporal variability of sediment resuspension on continental shelves (Glenn et al., 2008), especially in stormy conditions (Bourrin et al., 2015; Many et al., 2018; Miles et al., 2021, 2013). The recent integration of Acoustic Doppler Current Profilers (ADCPs) onto gliders allows describing the baroclinic conditions in the water column, essential to understand physical processes that occur during storms and to quantify sediment transport on continental shelves (Gentil et al., 2020; Miles et al., 2015).

Here we present a study combining glider observations and modelling approach to characterize processes responsible for sediment resuspension and to quantify sediment transport during a marine storm in the Gulf of Lions (GoL) shelf in the north-western Mediterranean.

5.1.2. The Gulf of Lions

5.1.2.1. Sediment features

During the last decades, the GoL has been targeted by numerous observational programs dealing with the present-day particle flux dynamics (Durrieu de Madron et al., 2008; Weaver et al., 2006). Sediment source on the GoL shelf is essentially dependent upon suspended matter inputs from the Rhone River (8.4 Mt yr^{-1} +/- 4.5 t yr^{-1}) in the northeast, and to a lesser extent to several small rivers along the central and western part of the gulf (Sadaoui et al., 2016). The shelf presents contrasted sedimentological features (Aloısi, 1986; Berne et al., 1998; Monaco, 1971) (Fig. 5.1a)

with: (i) a sandy inner shelf (<30 m), (ii) a mid shelf mud-belt (30–90 m) characterized by deposition of cohesive sediments mainly from the Rhone River, and (iii) coarser sediments with muddy sand patches on the outer shelf (>90 m).

Muddy sands of the outer shelf are homogeneous and bioturbated (Bassetti et al., 2006), as shown by Figure 5.2. The sandy fraction corresponds to relict "offshore sands", which cover many continental shelves around the world, at water depths generally between 80 and 120 m (Emery, 1968). These sediments represent littoral relict formations from the last eustatic low stage that were reworked during the first phase of the eustatic sea-level rise (Bassetti et al., 2006; Berne et al., 1998; Perez Belmonte, 2003). In this part of the shelf, sand ripples and large bedforms (dunes) are often found as reported by Albarracin et al. (2014) and references therein. The muddy fraction has a more recent origin and is mainly sourced from the Rhone River. In the GoL, sand ripples blanketed with mud may be remobilized from the outer shelf and supply sediments to canyon heads (Gaudin et al., 2006). Understanding the evolution of these deposits requires taking into account present-day sediment dynamics.

5.1.2.2. Hydrodynamic features

The GoL is a low-energy wave-dominated area (Guizien, 2009), where tides have small amplitudes (a few cm) and associated currents are very weak of a few mm s^{-1} (Carrère et al., 2012). Various observational (Bonnin et al., 2008; Bourrin et al., 2015, 2008; Ferré et al., 2005; Guillén et al., 2006; Martín et al., 2013; Ogston et al., 2008; Palanques et al., 2008, 2006) and modelling (Dufois et al., 2008; Ferré et al., 2008; Ulses et al., 2008b) studies emphasized the role of severe E-SE storms on the resuspension and redistribution of the shelf sediments. The E-SE storms have a marked seasonal impact with a maximum occurrence during autumn and winter (Mikolajczak et al., 2020).

Coastal buoys have shown that during storms, sediment resuspension is primarily driven by waves for depths <30 m (Guillén et al., 2006; Pruski et al., 2019). However, such events are very difficult to observe over the shelf, mainly because of the difficulties of maintaining equipment in such regions exposed to trawling activities. To fill these gaps, modelling studies were carried out to gain an insight into the hydro-sedimentary processes on the coastal continuum. Ulses et al. (2008b) showed, for an east storm event, that the influence of waves on resuspension on the outer shelf can be neglected in contrast to strong near-bottom currents that may generate resuspension. However, Dufois et al. (2008) showed from a 1-year simulation that waves can generate a maximum bottom shear stress of 0.08 N m^{-2} over depths of 100 m for severe E-SE storms. These conclusions are shared by Palanques et al. (2008), who found wave shear stresses higher than 0.12 N m^{-2} from extrapolation between observations recorded on the inner shelf and the canyon head during a marine storm.

Given the diversity of storms, the few existing studies targeting some of them are not sufficient to fully understand resuspension and advection processes during these episodic events. There is a lack of measurements in the coastal continuum, especially on the mid and outer shelf. Bourrin et al. (2015) used a glider equipped with physical and optical sensors to detail and quantify cross-shelf sediment dynamics induced by a storm on the Catalan shelf (southwestern part of the GoL). However, the instruments used in this study did not allow the quantification of baroclinic conditions in the water column and their impact on resuspension.

The present work builds on the aforementioned papers. It describes a comprehensive set of observations collected on the shelf coupled with hydrodynamic modelling used to study the fate of muddy sands on outer continental shelves. The methods and tools used to characterize hydro-sedimentary processes under storm events are described in section 5.2. Section 5.3 then presents the physical processes driving the sediment resuspension, and transport on a muddy sand outer shelf.

Finally, the glider-ADCP contribution to describe the episodic events and their impact on the spatiotemporal variability of sediment dynamics is discussed in section 5.4.

5.2. Data and methods

5.2.1. Glider observation

5.2.1.1. Sampling strategy

A glider equipped with a CTD (Conductivity, Temperature, Depth), an optical payload, and an ADCP was deployed in the central part of the GoL (Fig. 5.1a) in February-March 2018. The sampling strategy was adapted to target a continuous observation period of more than 30 days to sample short-term energetic events. In total, 11 cross-shelf sections were carried out from the mid shelf (5 km offshore to 30 m depth) to the shelf edge (55 km offshore to 100 m depth) (Fig. 5.1a). Each section was generally performed in 2.5-3 days. This long deployment permitted monitoring of a storm event on the shelf from 1st to 2nd March 2018.

5.2.1.2. Glider system and sensors

The autonomous underwater glider (depth range 30–200 m) used for this study is a Teledyne Webb Research Slocum G1 (Davis et al., 2002). The glider is driven primarily through small changes in buoyancy that allow it to "glide" forward through the water column on the descent, to typically 2 m above bottom, and ascend to 0–1 m from the surface. The chosen settings allowed the glider to descend and ascend through the water column with a pitch angle of approximately 26°, and horizontal and vertical speeds of 0.3 and 0.15 m s^{-1}, respectively. The glider surfaced every six down- and up-casts (yos) to obtain GPS fixes and transfer data to land, and to receive any new information about its route configuration and sampling strategy.

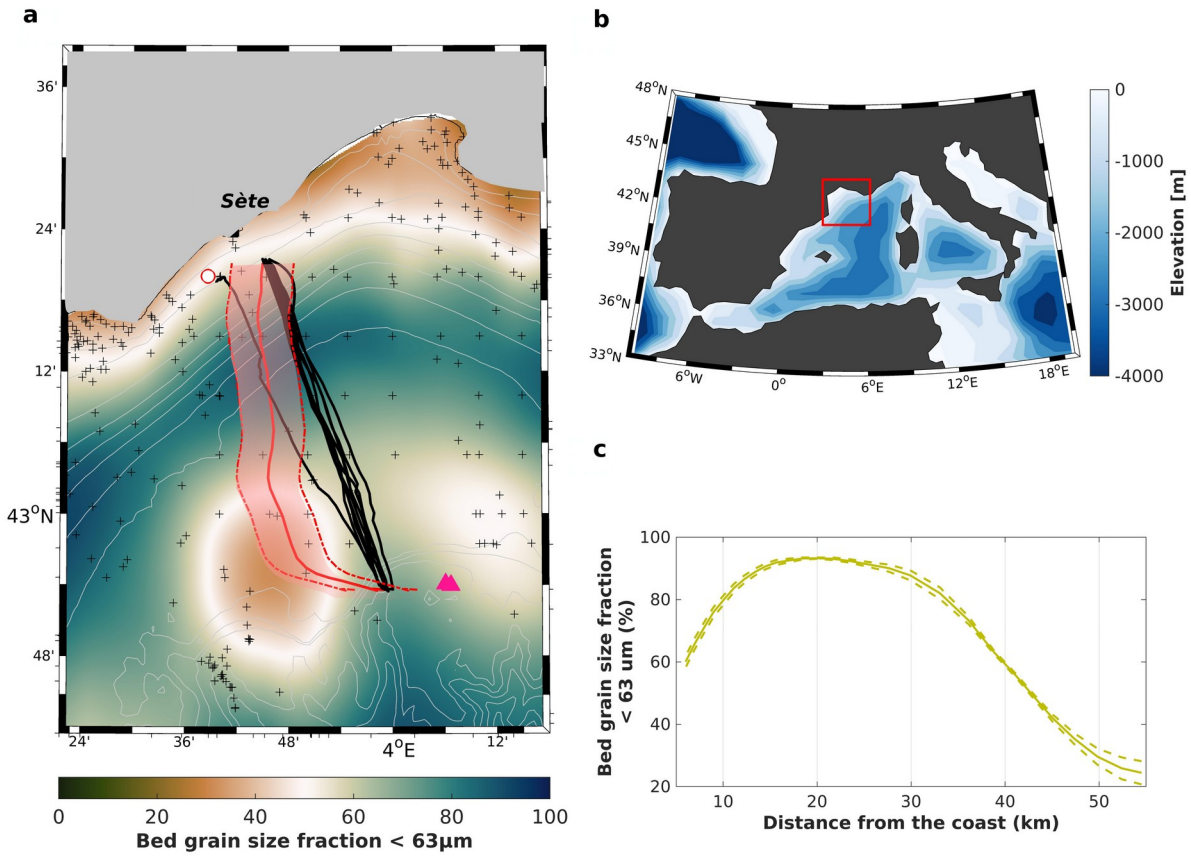

Figure 5.1: (a) Map of the glider track (solid black and red lines) superimposed on shelf surface sediment characteristics of the central part of the Gulf of Lions, interpolated from the granulometric samples (black crosses). The location of the coastal buoy (red and white circle), the meteorological station (black square), and the bedform images of Fig. 5.2 (pink triangles) are also shown. The solid red lines indicate the glider sections of interest for this study. (b) General map of western Mediterranean, where the Gulf of Lions is located by a red square. (c) Content of fine sediment (<63 µm) (solid green line) in bottom sediment as a function of the distance from the coast. Uncertainty on the pelitic fraction (dashed green line) has been derived from interpolated surface sediment characteristics (red-shaded area in Fig. 1a) along the glider section during storm conditions.

The glider was equipped with a suite of sensors that allow for sustained observations throughout the deployment. Conductivity, temperature, and pressure measurements were made using a pumped SeaBird 41cp CTD. An optical backscatter sensor (ECO-FLNTU) provided light scattering at 700 nm calibrated in NTU (Normalized Turbidity Units) and the fluorescence of chlorophyll-a. Using a sampling frequency of 0.5 Hz and a fall speed of approximately 0.15 m s^{-1}, the glider collects ~3 measurements per meter from all sensors yielding a detailed look at the water

column vertical structure. An Explorer Doppler Velocity Log with Acoustic Doppler Current Profiling capacity (Explorer ADCP) at 614 kHz was integrated into a special payload bay on the Slocum glider. It measures echo intensity and water velocity profiles. The Explorer ADCP has a downward-facing transducer tilted 11° forward, which enables it to compensate for the pitch of the glider during downcast. The inclination of the transducer optimized the three-beam measurements on the 26° pitched glider during the downcast. This fixed forward configuration rendered the instrument unsuitable for collecting velocity profile data during upcast (Mullison et al., 2013). Dedicated high accuracy attitude and compass sensors were used by the ADCP to monitor the beam orientation and were calibrated before deployment, following the procedure of PNI Sensor Corporation, (2013). During a glider descent, the ADCP periodically recorded echo intensity and relative water velocities to a maximum range of 20 m. A sampling frequency of 0.33 Hz was set to optimize the duration of the glider deployment. This sampling frequency (ensemble of 3 pings every 10 s) allowed sampling of profiles spaced on average every 1.2 m along the glider trajectory and 0.6 m vertically.

5.2.1.3. Glider data processing

Science and navigation data—During surfacing, the glider used GPS positioning to estimate the difference between the expected surface location from underwater dead reckoning and the GPS fixes. Such position difference, dependent on the duration of the dive, allowed to estimate the depth-averaged current (DAC) between two surfacings (Eriksen et al., 2001; Rudnick et al., 2018). Conductivity and temperature measurements were corrected for thermal lag effects (Garau et al., 2011). Salinity, density, and Brunt-Väisälä frequency were derived using the TEOS-10 equation (McDougall and Barker, 2011). CTD and optical measurements were synchronized with ADCP data and interpolated to a periodicity of 4 s.

Acoustic data—were processed to retrieve the Backscatter Index (BI) from echo intensities and absolute velocities from relative velocities using the method detailed in Gentil et al. 2020. ADCP measurements were organized along a diagonal swath, with overlapping measurements at each depth (see Fig. 3 in Gentil et al., 2020). For echo intensity measurements, a correction was applied on cell depths to avoid the effect of the pitched transducer (Ordonez et al., 2012). The real depth of each cell was thus calculated, taking into account the pitch and roll effects, the blanking distance, and the depth of the glider. Finally, to properly estimate the backscatter index and the relative water velocities, the factory threshold of 64 counts of the correlation signal was used to discard erroneous values (Gordon, 1996).

The received level of the acoustic return along each beam was converted into BI (dB) using equations of Mullison (2017), derived from the work of Gostiaux and van Haren, (2010), and Deines (1999). Then, the successive profiles of the BI were stacked into bins of 2 m, to reconstruct the profile over the entire water column from the median values of the overlapping data at each level. A final three-point centered moving-average filter was applied to eliminate the high-frequency noise.

Velocities used in this work were converted from beam coordinates to Earth coordinates and were bin-mapped using ADCP attitude sensor outputs. Successive relative water profiles were reconstructed following the same method used for BI profiles. During post-processing, techniques are used to remove the glider's motion from relative velocity measurements of ADCP and to apply absolute velocity constraints to obtain profiles of absolute horizontal currents. Absolute velocities were derived using the shear method (de Fommervault et al., 2019; Fischer and Visbeck, 1993; Gentil et al., 2020). The different steps of the shear method were applied independently to E-W and N-S components to (i) calculate single-ensemble shear by vertically differentiating ADCP velocity profiles; (ii) grid the resulting shear estimates in depth space (median values of shear current per

2 m cell); (iii) vertically integrate shear to yield the relative velocity profile, and (iv) estimate absolute velocities by adjusting relative velocity profiles to the current velocities measured by DAC. DAC has been chosen to reference the relative water velocity profiles because erroneous values have been observed on bottom track profiles, indicating an acquisition trouble during the deployment. Estimation of velocity started at a depth of 3 m, due to the position of the ADCP under the glider and a blanking distance of 2 m.

Uncertainty in BI profiles corresponds to the standard deviation of the stacked values for each 2 m depth bin. For relative velocity, the standard deviation of single ping measurements for 2 m cell size at 614 kHz is about 0.03 m s^{-1} (Gordon, 1996). To estimate the uncertainty of the relative velocity estimates, we performed a Monte-Carlo simulation based on 500 iterations, with initial velocity values sampled randomly according to a normal distribution centered on the measured value for each bin of each profile during the downcast. Finally, an average standard deviation of the absolute velocity—calculated from the sum of variances of the relative velocities and the DAC—was estimated at 0.06 m s^{-1}.

5.2.2. Additional observation assets

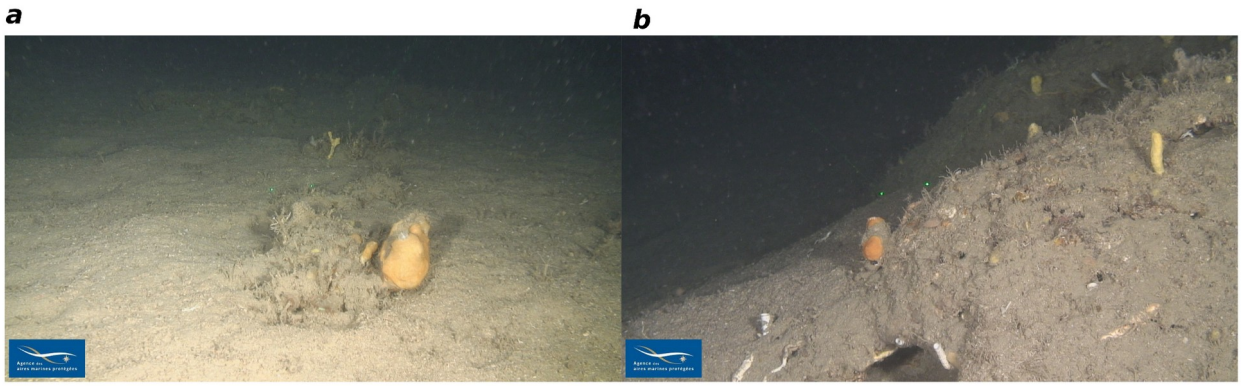

Figure 5.2: Seabed images (Agence des aires marines protégées et al., 2012) of muddy sands over the outer shelf of the Gulf of Lions (characterized by yellow patches in Fig. 5.1a), at 96 (a) and 105 m (b) depth, located at 42 °53.059'N; 4°04.162'E and 42 °53.066'N; 4°04.125'E, respectively (marked by pink triangles in Fig. 5.1a).

Geological Settings—Shelf surface sediment map is determined by interpolating sediment samples (black crosses in Fig. 5.1a) on a regular grid of 100 m, using the data-interpolating variational analysis (DIVA) method (Troupin et al., 2012). Sediment samples were compiled from numerous grab samples and piston cores acquired over the last ca. 40 years, as part of French and European projects (Augris et al., 2013). The resulting surface sediment map is very similar to the distribution described by Got and Aloisi, (1990). In the vicinity of the glider track, close examination of sediment samples suggests a representative median grain size between 10 and 30 µm for the mid shelf, whereas the outer shelf has a representative median grain size between 40 and 70 µm, and is composed of muddy sands (Bassetti et al., 2006)**.** Uncertainty about the pelitic fraction has been estimated from the median of the interpolated sediment characteristics (Fig. 5.1c) over a 5 km band on both sides of the glider track (red shaded area in Fig. 5.1a). Figure 5.2 shows photos of the bedform and the biological stands on the outer shelf of the GoL, at the vicinity of the study area (pink triangles in Figure 5.1a).

Coastal buoy time series—waves were monitored at 30 m water depth (43 °22.261'N; 3°46.777'E) (red and white circle in Fig. 5.1a), every 30 min with a directional wave buoy (Datawell®). The main wave characteristics (significant and maximum height, mean period, and direction) were retrieved from the CANDHIS database (http://candhis.cetmef.developpement-durable.gouv.fr).

Meteorological time series—hourly (10 min burst average) wind speed and direction were measured at the Météo-France station of Sète (34,301,002) located at 43 °23.50'N; 3°41.31'E (black square in Fig. 5.1a). Data were provided by MeteoFrance and are available in the Publithèque database (https://donneespubliques.meteofrance.fr/).

5.2.3. Hydrodynamical modelling

The 3-D ocean circulation model SYMPHONIE (Marsaleix et al., 2019, 2008) is based on the Navier-Stokes primitive equations solved on an Arakawa horizontal curvilinear C-grid and a VQS vertical coordinate (Estournel et al., 2021), under the hydrostatic and Boussinesq approximations. The model makes use of an energy-conserving finite difference method described by Marsaleix et al. (2008), a forward-backward time stepping scheme, a Jacobian pressure gradient scheme (Marsaleix et al., 2009), the equation of state of Jackett et al. (2006), and the K-epsilon turbulence scheme implemented following Michaud et al. (2012). The lateral open boundary conditions, based on radiation conditions combined with nudging conditions, are described in Marsaleix et al. (2006). The bipolar horizontal grid is the same as that of Mikolajczak et al. (2020) —see their Fig. 1b—with a resolution between 300 and 500 m over the entire GoL continental shelf. The vertical VQS grid has 40 levels in total and about 20 on the continental shelf to reduce truncation errors associated with the sigma coordinate while maintaining an accurate description of the bathymetry. A particularly important property of this coordinate for this study is that it preserves the horizontal continuity of the bottom current (i.e., without the blocking effect of staircase coordinates). Among the numerous applications of SYMPHONIE in the Mediterranean, simulations targeting wind-induced circulation on the Gulf of Lions' shelf have been analyzed and validated by Estournel et al. (2003) and Petrenko et al. (2008).

The simulation is initialized and forced at the open boundaries by a "parent" simulation of the entire Mediterranean Basin carried out with the SYMPHONIE model (Estournel et al., 2021; see their Fig. 6 for comparison with the average SST in January 2018). The forcing at the air/sea interface is done by the COARE3.0 bulk formulas fed by ECMWF hourly forecasts. Taking into account the recommendations of Van Sebille et al. (2020) regarding the effects of waves on transport, a simplified parameterization of the effect of waves on currents is introduced into the

model. This parameterization, similar to that of McWilliams and Restrepo (1999) and Jorda et al. (2007), only retains the leading terms of the current/wave interactions (i.e., neglecting the quadratic terms, the Vortex force in particular). The horizontal components of the Stokes drift (u_s, v_s), are in practice added to the Eulerian current for the calculation of advection and the transport divergence giving the variation of the surface elevation. As pointed out by Jorda et al. (2007), the modified momentum equations add the Stokes-Coriolis force (Van Sebille et al., 2020; Xu and Bowen, 1994) to the Coriolis term (i.e. $+fu \rightarrow +f(u+u_s)$ and $-fv \rightarrow -f(v+v_s)$). Finally, similarly to Jorda et al. (2007), a wave-induced increase of the bottom stress is applied (see section 5.2.5.5 Eq. 5.7). The characteristics of waves are interpolated in space and time from the fields obtained with the Wavewatch 3 model (section 5.2.4).

The simulation is initialized on 13 December 2017 and runs until the storm studied here (early March 2018).

5.2.4. Wave modelling

The wave characteristics (significant height, period, direction, and Stokes drift) are calculated with the Wavewatch 3 wave generation and propagation model (Tolman, 2009) using the grid of the parent model (see above) throughout the Mediterranean. The model is forced by the wind using the same product as above (ECMWF wind). Outputs are archived hourly.

5.2.5. Diagnostics

Glider data have been analyzed in the context of other available datasets such as coastal buoys, granulometric samples, meteorological time series, and hydrodynamic modelling. Diagnostics were implemented to characterize hydrometeorological events, the suspended

particulate matter properties, the physical processes that drive sediment dynamics in the bottom boundary layer, and their transport across the GoL shelf.

5.2.5.1. Wave event return period

Wave events return period was derived from coastal buoy time series to assess the intensity of hydro-meteorological events. The erroneous wave data were eliminated by the method of Butel et al. (2002). Cumulative probability distribution of the monthly maximum of H_{m0} (significant spectral wave height) and $T_{(0,2)}$ (mean spectral period) were computed to estimate the return period of wave events in a period from February 2006 to July 2020. The monthly maxima were extracted from the 30 min interval wave data and the GEV (generalized extreme value) distribution has been applied using the Maximum Likelihood method (Prescott and Walden, 1980), classically used to describe the probability distribution of episodic events (floods, rainfalls or waves). This analysis was done using MATLAB and the WAFO toolbox (Brodtkorb et al., 2000)**.**

5.2.5.2. Suspended particulates matter

Suspended particulates matter (SPM) properties were inferred from coincident optical and acoustic backscatter measurements carried out by the glider (Gentil et al., 2020). A spike analysis has been applied to characterize the presence of large particles, using the method described by Briggs et al. (2011). Spikes were recorded by all optical measurements as rapid transient, and often large increases in optical signals. A 5-point running minimum filter followed by a 5-point running maximum was applied on the raw optical backscattering profiles at 700 nm for the determination of the background (baseline) of each profile. Then, spike height was calculated by subtracting the baseline from the raw optical profile.

5.2.5.3. The bottom boundary layer and surface-mixed layer

The bottom boundary layer (BBL) and surface mixed layer (SML) depths were estimated from the density profiles as the depth where the difference between the density and the reference value at 3 meters above the seabed for the BBL, and below the surface for the SML was equal to 3 x 10^{-2} kg m^{-3} (Perlin et al., 2007). Based on density profile observations, this threshold density deviation has been preferred to 6 x 10^{-4} kg m^{-3}, used by Perlin et al. (2007) to assess the well-mixed BBL.

5.2.5.4. The Rouse profile

As in Glenn et al. (2008) and Miles et al. (2013), we use optical backscatter profiles averaged over 1.5 hours as a proxy for sediment concentration to study sediment resuspension in the BBL from the Rouse profile. Previous studies have clearly defined the Rouse profile above the wave boundary layer in the unstratified layer, where the suspended sediment concentration decays with distance from the seabed (Glenn et al., 2008; Glenn and Grant, 1987; Miles et al., 2013; Styles and Glenn, 2000) as:

$$C_{(z)} = C_r \left[\frac{z}{z_r}\right]^{[-\gamma wf/\kappa u^x]} \quad (5.1)$$

where $C_{(z)}$ is the vertical concentration profile, C_r is the sediment concentration at the reference height z_r, γ is a constant ratio of eddy viscosities and diffusivities, wf is the particle fall velocity, κ is the von Karman's constant and u^x the friction velocity.

5.2.5.5. The bottom shear stress

The bottom shear stress (BSS) was estimated to assess the physical processes that drive the sediment resuspension. When dealing with currents only, the method to calculate the BSS (eq. 5.2)

consists in assuming a logarithmic velocity profile close to the bottom to characterize the friction velocity (eq. 5.3).

$$\tau_c = \rho u_c^{x\,2} \tag{5.2}$$

$$u_c^x = \frac{\kappa u_{(z)}}{\ln(z/z_0)} \tag{5.3}$$

where, ρ is the density of water, u_c^x the friction velocity, κ the Von Karman constant (0.4), z the height of the measurement above the bottom, $u_{(z)}$ is the associated current velocity, and z_0 the bottom roughness.

Waves are also able to generate bottom shear stress (here noted τ_w) expressed from (eq. 5.4).

$$\tau_w = 0.5 \rho f_w U_b^{\,2} \tag{5.4}$$

where f_w is the wave friction factor expressed by (Swart, 1974):

$$f_w = 0.3 \text{ if } A/k_s < 1.57$$

and beyond:

$$f_w = 0.00251 \exp[5.21 (A/k_s)^{-0.19}] \tag{5.5}$$

where A the orbital half excursion near the bottom estimated from the Symphonie hydrodynamic model, U_b the orbital velocity, and k_s the physical roughness related to the bottom roughness height through $z_0 = k_s/30$, in turbulent condition. A variety of models have been developed for predicting the non-linear combined wave- and current-induced BSS (Grant and Madsen, 1979; Holmedal et al., 2003; Shi and Wang, 2008; Soulsby et al., 1993). We used the Soulsby et al. (1993) formulation, widely used in the calculation of the BSS under the wave-current interaction (Jia et al., 2014). It allows estimating the wave-current shear stress (τ_{cw}) maximum within a wave period from the current alone shear stress (τ_c) and the wave alone shear stress (τ_w):

$$\tau_{cw} = [(\tau_m + \tau_w |\cos\varphi|)^2 + (\tau_w \sin\varphi)^2]^{0.5} \tag{5.6}$$

where (τ_m) is the shear stress averaged over the wave period which reflects the enhancement of turbulence by wave motions:

$$\tau_m = \tau_c\left(1+1.2\left[\frac{\tau_w}{\tau_w+\tau_c}\right]^{3.2}\right) \quad (5.7)$$

and φ is the angle between the wave propagation and the current calculated when glider measurements are available in the bottom boundary layer.

5.2.5.6. The bottom roughness

The bottom roughness (z_0) is an important parameter for the prediction of sediment transport (resuspension and vertical diffusivity in the BBL) as well as for calculating the current profile near the sea bed. The bottom roughness depends on the physical roughness composed of three distinct elements (Nielsen, 1992): (1) the sediment grain size; (2) the morphology of the bed, including sedimentary bed structures such as ripples and morphological characteristics induced by benthic communities; and (3) the roughness associated with the near-bottom sediment transport. The resulting total physical roughness is assumed to be equivalent to the addition of the partial ones (Nielsen, 1992; Xu and Wright, 1995). Given the lack of information on the sediment properties (size distribution and bedforms) along the glider's path, it was decided to compute a range of bottom shear stress from an empirical range of bottom roughness based on two values. In cohesive muddy sand environments, a typical value found in the literature is 10^{-4} m (Ogston et al., 2008; Soulsby, 1997). This value was chosen as the low value of our physical roughness range. However, Figure 5.2 shows the presence of biogenic material in abundance on the seabed of the outer shelf, such as indicated in Bassetti et al. (2006) with craters around 10 cm in diameter (see the two green points in Figure 5.2b indicating a scale of 8 cm). For these reasons, a high value of 10^{-3} m was chosen, as found from observations where bedforms and biogenic material are observed (Cheng et al., 1999; Guillén et al., 2008; Peine et al., 2005).

5.2.5.7. SPM fluxes

Horizontal SPM fluxes are computed from current velocity and SPM concentration. SPM concentration was derived from a calibration (eq. 5.8) carried out in 2015 on the Gulf of Lions from the ship- and the same glider-based ECO-FLNTU instrument during similar conditions.

$$[SPM]_{OPT} = (1.27 \pm 0.45)\, xNTU + (1.05 \pm 0.85) \quad (5.8)$$

The integrated SPM fluxes were calculated throughout the water column, considering homogeneous currents and SPM concentrations in the portions of the surface and bottom layers not sampled by the glider. We estimated the uncertainty on SPM fluxes by propagating the average relative uncertainties related to the currents (0.06 m s^{-1}) from glider-ADCP data processing, and SPM concentrations (1 mg L^{-1}) from the calibration.

5.3. Results

5.3.1. Storm conditions

The hydro-sedimentary dynamics is studied along three periods from 26 February to 4 March 2018: (1) pre-storm, (2) storm, and (3) post-storm, indicated in Figure 5.3. Pre-storm conditions are characterized by a low-energy swell around 1 m high and a period of 4 s (Fig. 5.3b). At the beginning of the storm period (1st March), winds shift from north to southeast with an intensity of 15 m s^{-1} (Fig. 5.3a). These southeast winds were related to a peak swell at the Sète buoy on 1 March (Fig. 5.3b) characterized by a significant wave height (H_s) of ~5.5 m, a maximum wave height (H_{max}) of 11 m, a period (T_s) around 10 s, and a direction of 100° (Fig. 5.3c). The wave statistical analysis carried out over a period from 2006 to 2020 from the Sète buoy data showed a return period of 5.4 years for this event. In the post-storm period, the significant wave height dropped drastically. In total, the storm lasted 42 hours.

The glider was deployed approximately 5 km offshore in the Gulf of Lions and progressed perpendicular to the isobaths from the coast at ~30 m depth to the shelf edge at ~200 m depth (26 to 28 February in pre-storm conditions), and back to the coast (1 to 4 March in storm and post-storm conditions) (see the road in Fig. 5.3d). Because storm currents are often faster than the typical maximum glider forward speed of about 0.3 m s^{-1}, passing storms can be readily identified in the glider track data as a deviation from the across shelf line. During the storm, the glider's deviation shows a south-westerly depth-averaged current on the outer shelf (Fig. 5.3d), which is a typical circulation under onshore winds in the GoL (Mikolajczak et al., 2020; Ulses et al., 2008a). However, a stop of the glider acquisition is observed at the beginning of the storm (green line) due to the data transfer (surfacing) and the change of ADCP configuration.

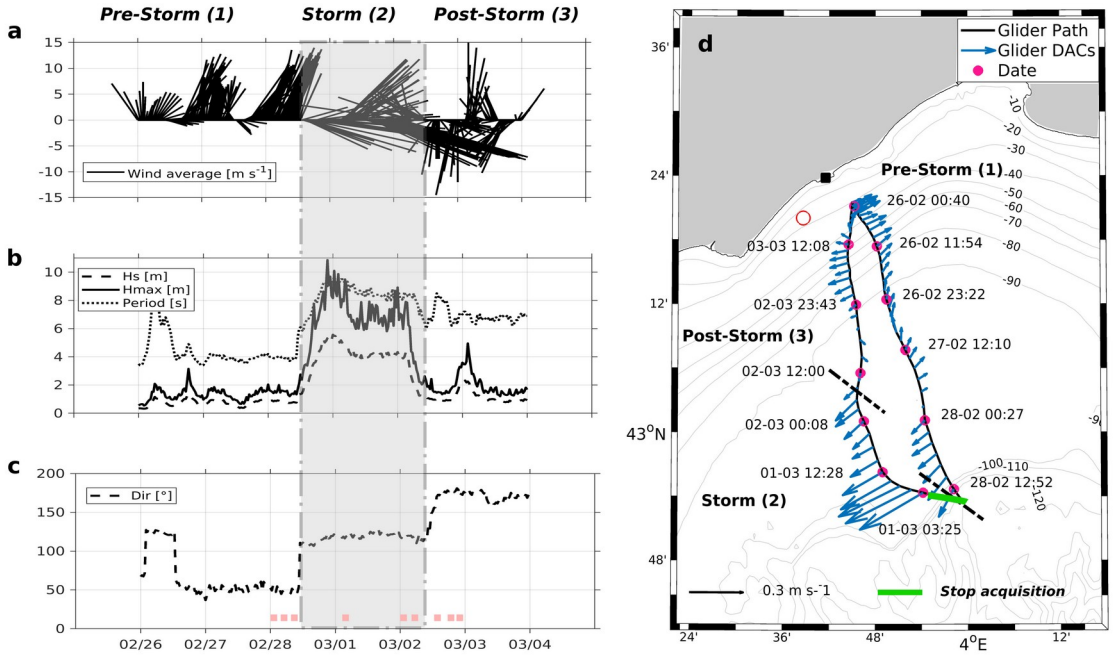

Figure 5.3: (a) Wind speed and direction time series at the Météo-France station (black square in Fig. 5.3d). By convention, wind direction indicates its origin. (b, c) Buoy time series (red circle in Fig. 5.3d) of significant wave height (Hs), maximum wave height (Hmax), wave period, and wave direction (Dir). The red squares, in panel c, indicate the time of the nine profiles displayed in Fig. 5.5. (d) Depth averaged current superimposed on cross shelf glider tracks from 02/26 to 03/04. The temporal evolution of the meteorological conditions is indicated by periods 1,2,3.

5.3.2. Cross-shelf glider sections

Figure 5.4 shows a time series of hydrological, hydrodynamical, and biogeochemical properties of the water column for the three periods (pre-storm, storm, and post-storm).

During pre-storm conditions, a 2- to 3-layer system according to the temperature (Fig. 5.4d) and salinity (Fig. 5.4g) is observed. The interface between these layers is marked by an increase of the Brunt-Väisälä frequency, highlighting the stratification of the water column (Fig. 5.4j). Two cold (<10 °C) and low salinity (<37 g kg^{-1}) patches are observed at the surface at the two ends of the transect and correspond to the dispersion of the Rhone River plume over the GoL shelf. The seasonal pycnocline is marked by the isopycnal 28.9 kg m^{-3}, separating cold (<12 °C) and less salty (<38 g kg^{-1}) subsurface waters, from warmer and saltier bottom waters. Currents (Fig. 5.4b, e, h) show a weak depth-averaged intensity (<0.1 m s^{-1}) from the northeastern part over the mid shelf, turning into the southwestern part over the outer shelf (Fig. 5.3d). The vertical shear is low in the water column but increases close to the bottom where velocity decreases. Biogeochemical properties show subsurface waters rich in chlorophyll-a (~1.5-2 μg L^{-1}) (Fig. 5.4l). In addition, an increase of optical backscatter (~1.5 NTU, Fig. 5.4c), shows the presence of a thin bottom nepheloid layer with a concentration of ~3 mg L^{-1}, and a subcritical Richardson number (<0.25), suggesting Kelvin-Helmholtz instabilities (Fig. 5.4k).

On 1st March during the storm period, the 28.9 kg m^{-3} isopycnal shifted in the water column from 55 to 80 m depth, switching to a two-layer system with homogenization of temperature and salinity in the subsurface and bottom waters (Fig. 5.4d, g). During this event, the currents have a maximum magnitude of around 0.5 m s^{-1} and are on average two to three times larger than pre-storm conditions and oriented southwest (Fig. 5.4b, e, h). In addition, the bottom nepheloid layer is up to 20 m thick, where Kelvin Helmholtz instabilities are still present and the concentration deduced from the optical backscatter is twice as high (6 mg L^{-1}) as under pre-storm conditions. An

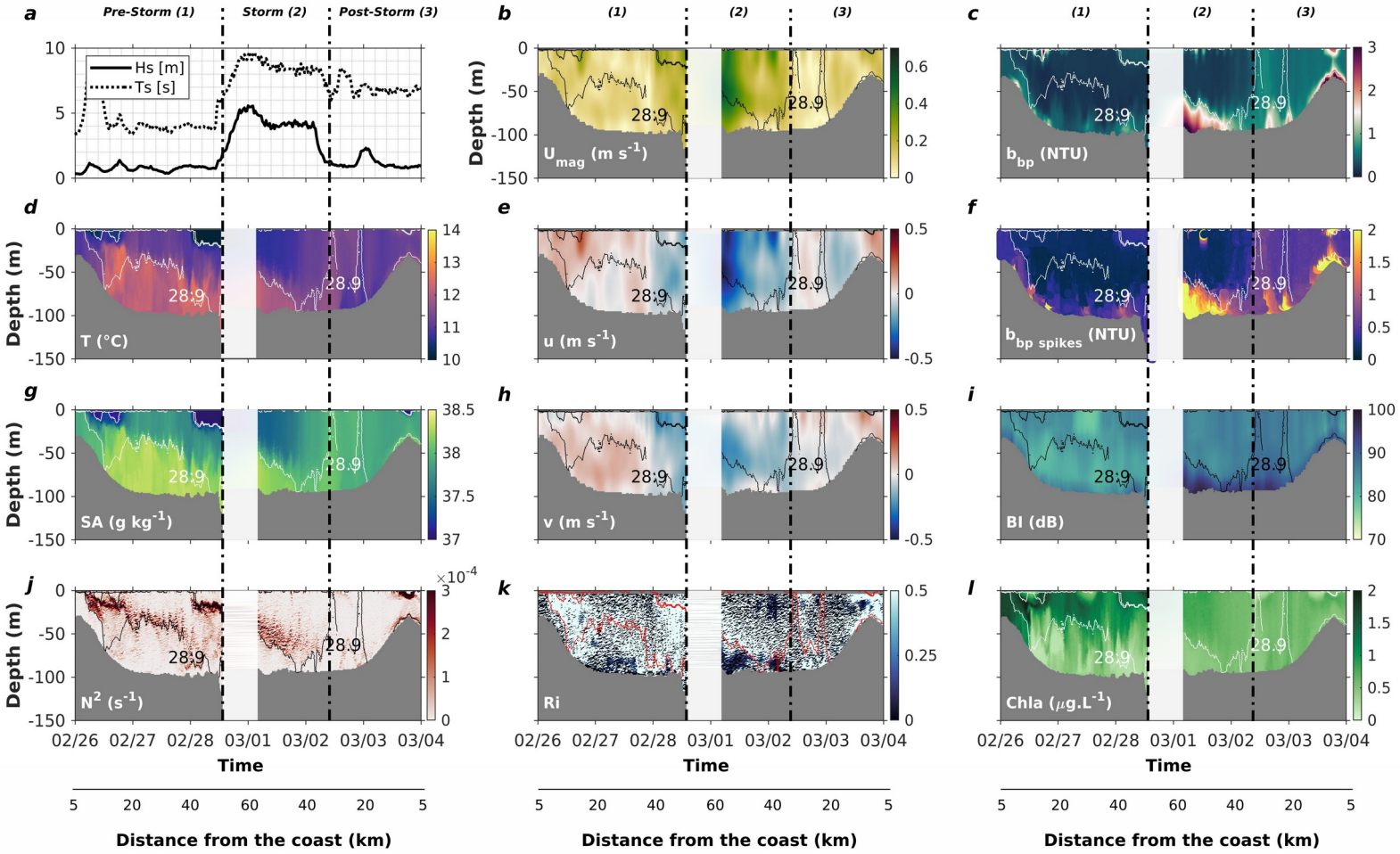

Figure 5.4: Time series of (a) significant wave heights (Hs) and wave period (Ts), and glider time-series observations of hydrological ((d) temperature, (g) absolute salinity, (j) Brunt-Väisälä frequency), hydrodynamical ((b) current speed, (e) eastward velocities, (h) northward velocities, (k) Richardson number) and biogeochemical properties ((c) optical backscatter, (f) optical backscatter spikes, (i) acoustic backscatter index, (l) chlorophyll-a). The isopycnal 28.9 kg m^{-3} is superimposed on all plots and indicated by a solid black, white, or red line. Numbers 1–3 indicate three different storm regimes discussed in the text.

increase of the acoustic and optical spikes signal (Fig. 5.4f, i) is also observed and indicates the likely presence of large particles in the bottom nepheloid layer.

On 2 March at 12:00, the system transitioned toward a homogeneous water layer as the isopycnal 28.9 kg m^{-3} reaches the surface, with a temperature of ~11.5 °C, a salinity of ~38.3 g kg^{-1}, and currents falling at ~ 0.1 m s^{-1} throughout the water column. During this post-storm condition, the distribution of particles extends throughout the water column with higher values in optical and acoustic backscatter than during pre-storm conditions, while concentration in chlorophyll-a dropped by a factor three near the coast (~0.5 μg L^{-1}).

5.3.3. Sediment dynamics observation

5.3.3.1. Sediment resuspension

Optical backscatter profiles averaged over 1.5 hours were used to study sediment resuspension in the water collumn from the Rouse profiles. Profiles were normalized using the backscatter observed at a reference height of 4 m above bottom, close to the bottom inflection point of the glider's sawtooth trajectory. As prescribed by the Rouse profile, the relative backscatter profiles decay along a straight line in the BBL when plotted on this log-log scale (Fig. 5.5).

Figure 5.5 shows three density anomaly and optical backscatter profiles for each of the three periods: pre-storm (a-c), storm (d-f), and post-storm conditions (g-i), represented in Figure 5.3c by red squares. The dynamics of the BBL and SML are highly variable over time. From 1 March, where significant wave height and period increase, we observe a thickening of the bottom and surface mixed layers on profiles d to f (blue and red squares, Fig. 5.5), related to a supercritical Richardson number (Fig. 5.4k) in the bottom boundary layer. A few hours after the end of the storm (Fig. 5.5g), the pycnocline appears to have been eroded via a complete mixing of the wind-driven surface layer and the bottom boundary layer. When the pycnocline was eroded, the normalized

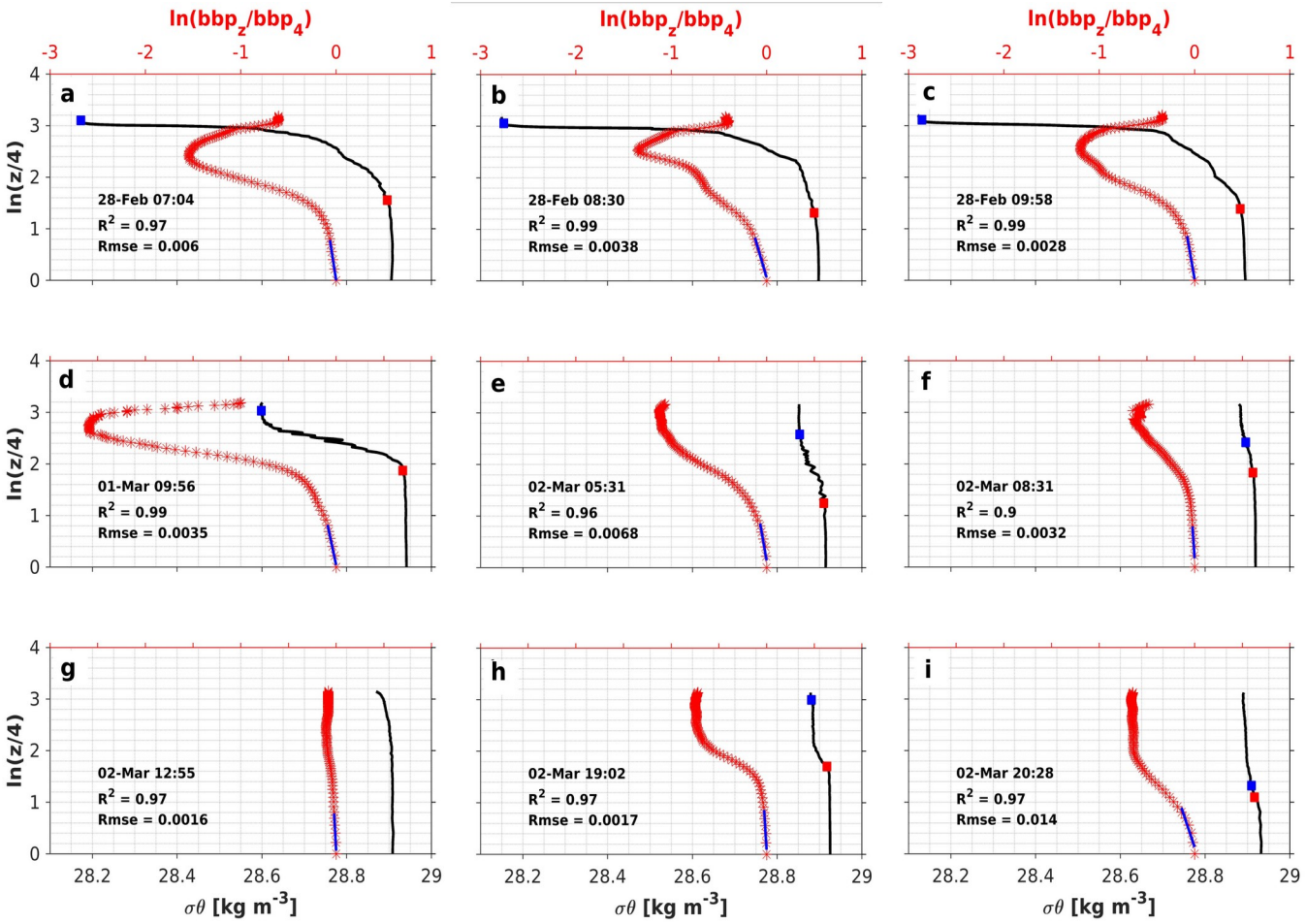

Figure 5.5: X-axes are density profiles (black line, bottom scale) and logarithm of the normalized backscatter (top scale). Y-axis is the natural logarithm of depth divided by z_r. A straight line was fitted (blue line) to the normalized backscatter values below the bottom boundary layer whose thickness is indicated by a red square. The surface mixed-layer depth is also indicated (blue square).

backscatter profile is Rouse-like over the full water column, increasing vertical mixing of resuspended sediment in the entire water column. As observed in Glenn et al. (2008) and Miles et al. (2013), the small amount of stratification caused by the temperature and salinity structure appears to be enough to inhibit the vertical turbulent flux of sediment and significantly limit the amount of resuspended material reaching the upper water column (Fig. 5.5 a-f and 5.5h-i).

5.3.3.2. *Sediment fluxes*

During pre-storm conditions, current magnitude, SPM concentrations, and cumulative SPM fluxes in the BBL are weak, around 0.1 m s^{-1}, 2 mg $L^{-1,}$ and 4 mg m^{-2} s^{-1} respectively (Fig. 5.6 b-d). From 1 March the significant wave height increases rapidly (1 to 5 m, Fig. 5.6a), as do the currents (0.1 to 0.4 m s^{-1}, Fig. 5.6b), and SPM concentrations (2 to 5 mg L^{-1}, Fig. 5.6c) in the water column. Under these forcings, the thickness of the BBL increases to more than 20 m above the bottom as shown in Fig. 5.5d to f. During this period, cumulative SPM fluxes throughout the BBL reach up to 45 mg m^{-2} s^{-1} (Fig. 5.6d) oriented along the isobaths (Fig. 5.6e), approximately 10 times higher than during pre- and post-storm conditions. The maximum cumulative SPM fluxes in the water column are around 60 mg m^{-2} s^{-1}, estimated during the storm event (Fig. 5.6e). This observation shows that

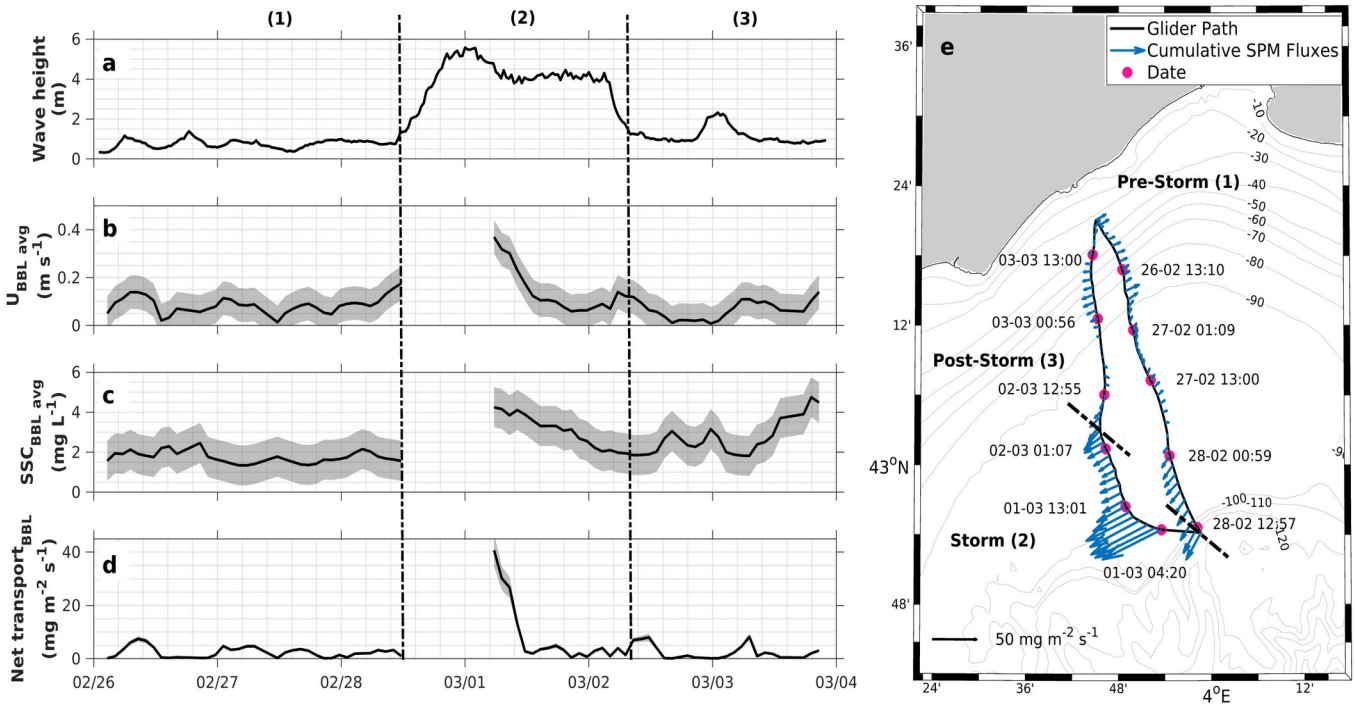

Figure 5.6: Time series of (a) significant wave height, and hydro-sedimentary parameters in the bottom boundary layer: (b) depth-averaged currents, (c) SPM average concentration, (d) vertical cumulative SPM fluxes. The shaded grey area is the average uncertainty. (e) Map of vertical cumulative SPM fluxes (orange arrows) and cross shelf glider tracks (black lines) from 26 February to 04 March.

the majority of the sediment fluxes are in the bottom layer since they represent 66% of the total SPM fluxes in the water column. After the storm, the average SPM concentration remains relatively high (~3.5 mg L^{-1}, about twice the pre-storm concentrations) in the entire water column, and persists more than 40 h after the end of the storm.

5.3.4. Model validation

To validate the wave and current simulations, we calculated correlation coefficients and root-mean-square-error between modeled and observed significant waves height at the coastal buoy and depth averaged currents along the glider track.

Simulated wave heights (Fig. 5.7b) are underestimated during the peak of the storm (around 00.00 h on 1 March), up to 1.2 m difference from the observed values. Outside this peak, during the high wave event (~4.5 m) and the pre- and post-storm periods, the simulation is in line with observations, as confirmed by a highly significant correlation (p-value <0.001, r^2 = 0.93), and a RMSE of 0.41 m (Fig. 5.7d).

To assess modeled currents, we compared the hourly mean depth-averaged values extracted from the nearest grid point to each glider surfacing, to depth and time-averaged glider currents using dead reckoning (see section 5.2.1.3 Glider data processing). The SYMPHONIE simulated currents are in good agreement in intensity and direction with the observed glider currents for the majority of the deployment (Fig. 5.7a) with the area of minimum current in the middle of the glider path and the reversal of the current between the pre and post storm periods in the vicinity of the inner shelf. The complex correlation coefficient between the model and glider is 0.84, with a RMSE of 0.06 m s^{-1} (Fig. 5.7c), which is a value identical to the uncertainty of the absolute velocity estimated from the ADCP. However, Fig. 5.7c shows that the model underestimates the strong and weak currents compared to the glider.

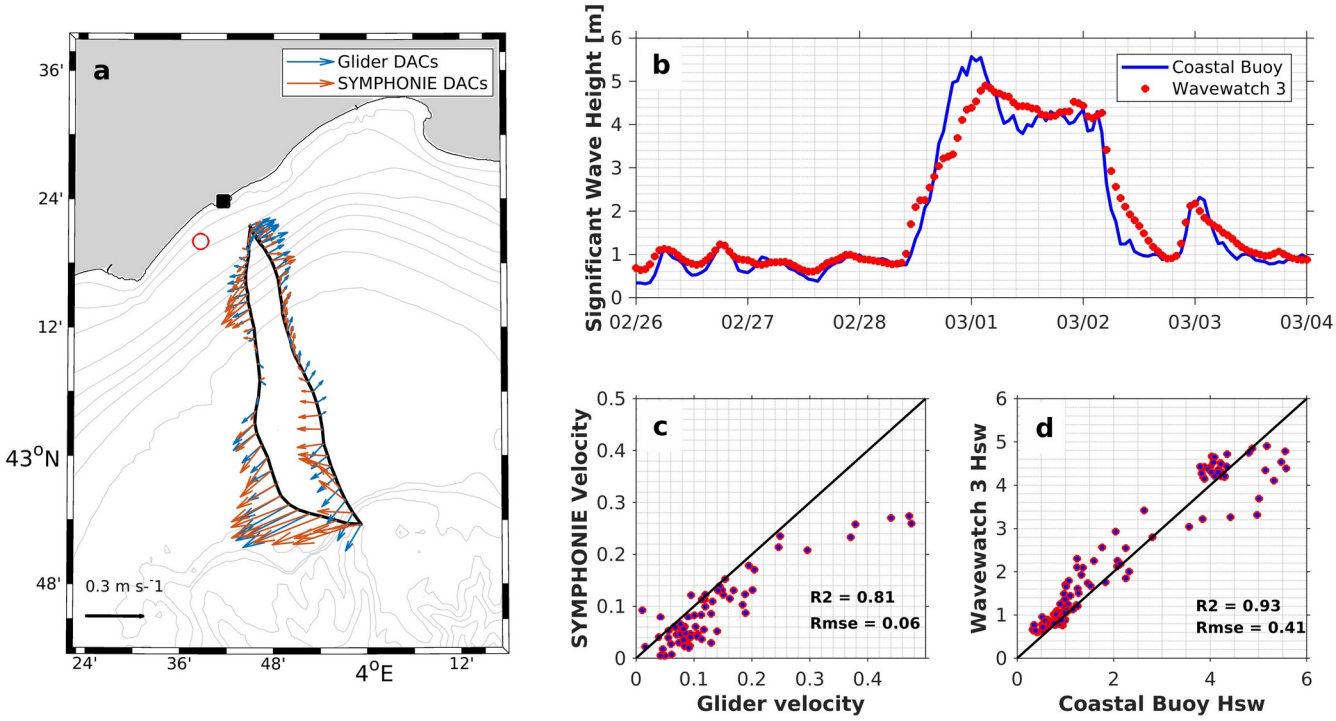

Figure 5.7: (a) Depth-averaged currents simulated with SYMPHONIE (orange arrows) and deduced from the glider dead reckoning (blue arrow); (b) Significant wave heights measured at the buoy (blue) and simulated with Wavewatch 3 (red). (c, d) Correlations and RMSE between modeled and observed depth-averaged currents and significant wave heights, respectively.

5.3.5. Physical processes driving resuspension

5.3.5.1. Along the glider path

Figure 5.8 shows the time series of the bottom shear stress generated by waves and currents and their combined impact as a function of the distance to the coast. The current-induced (and combined) bottom shear stress was calculated from the glider data and by the SYMPHONIE model collocated in time and space with the glider. The wave-induced shear stress was calculated from Wavewatch 3 results rather than the series measured at the buoy to account for wave inhomogeneity along the glider path. As mentioned before, given the limited information on the surface sediment along the glider path, we chose to perform a sensitivity analysis to the bottom roughness with values of 10^{-4} m (green line) and 10^{-3} m (pink line).

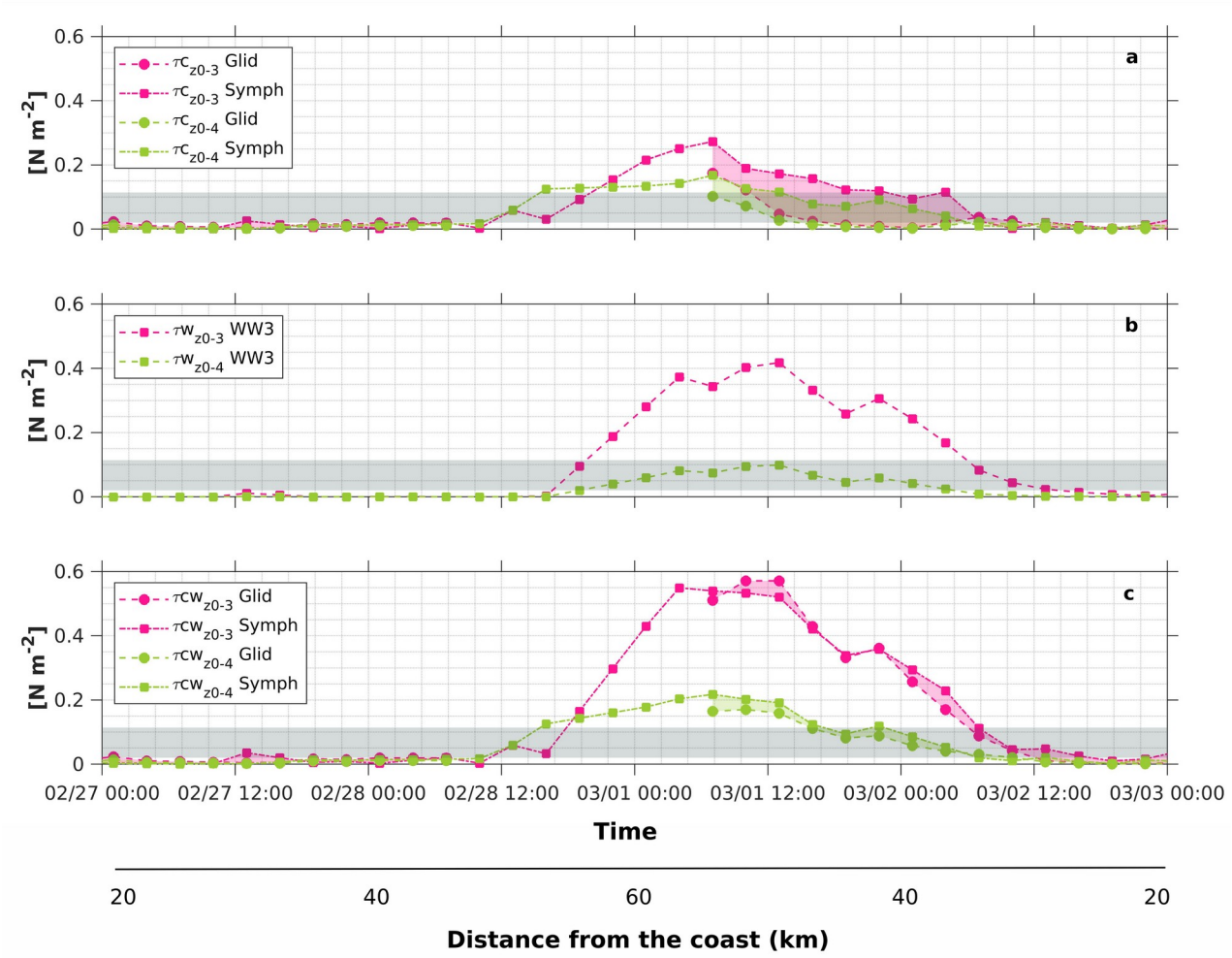

Figure 5.8: Comparisons of bottom shear stress (BSS) derived from the glider (circle) and SYMPHONIE / Wavewatch 3 models (square) for (a) currents, (b) waves (no glider), and (c) wave-current interactions along the glider path with two values of the bottom roughness, 10^{-4} m (green) and 10^{-3} m (pink). Typical resuspension critical shear stress for the muddy sands of the GoL is indicated by the grey band. Note that the glider does not produce any observations at the beginning of the storm between 28 February 3 p.m. and 01 March 5:00.

During pre-storm conditions, the glider sails offshore on a bottom depth ranging from 30 to 95 m. Over this period, currents and waves are too weak to generate bottom shear stress larger than 0.03 N m^{-2} whatever the bottom roughness value used. From 1 March, when the marine storm impacts the shelf, the glider is over the outer shelf (>90 m). The highest values recorded at the offshore end of the transect range between 0.1 and 0.25 N m^{-2} for the current-induced bottom stress depending on whether we consider the model or the glider and depending on the two values of the

roughness (Fig. 5.8a). For the wave-induced shear stress highest values are between 0.1 and 0.45 N m^{-2} (Fig.. 5.8b). Note that the model overestimates the current-induced bottom stress compared to the glider due to a current in the BBL stronger than in the observations despite similar depth-averaged currents. Whatever the value of bottom roughness, Figure 5.8 shows that currents, waves, or the interaction of these two forcings are likely to resuspend sediment. Indeed, critical shear stress for muddy sands of the outer shelf are ranging from 0.03 to 0.11 N m^{-2} (grey band, Fig. 5.8) (Ahmad et al., 2011; Soulsby, 1983). The sensitivity analysis shows that for a bottom roughness of 10^{-4} m, the wave and current stresses are of the same magnitude (~0.15 N m^{-2}) at the swell peak, while the wave stress can be up to 2 times the current stress (~0.45 and 0.22 N m^{-2}, respectively), for a bottom roughness of 10^{-3} m, making it the main contributor to total bottom shear stress (τ_{cw} in Fig. 5.8c).

5.3.5.2. Overall spatial variability

Thanks to the convincing comparison between the combined wave current BSS from observations and simulation, the simulation is used to describe this stress at the scale of the Gulf of Lions during the storm. Maps of the wave-current BSS averaged from 0:00 a.m. to 03:00 h on 1 March, during the storm, calculated for both values of the bottom roughness are plotted in Figure 5.9a and b. The depth-averaged currents superimposed on the figures are westward and along isobaths on the shelf, which is a classical circulation during marine storms in the GoL. The entire Gulf of Lions was affected by the storm, but the currents in the central part of the shelf explored by the glider were weaker than those to the west and east, where the narrower shelf accelerated the flow. The significant wave height averaged over the same period as the bottom stress is shown in Fig. 5.9c. In shallow water, BSS is larger due to a greater interaction between the bottom and the swell. Comparison of the BSS distribution with representative surface granulometric

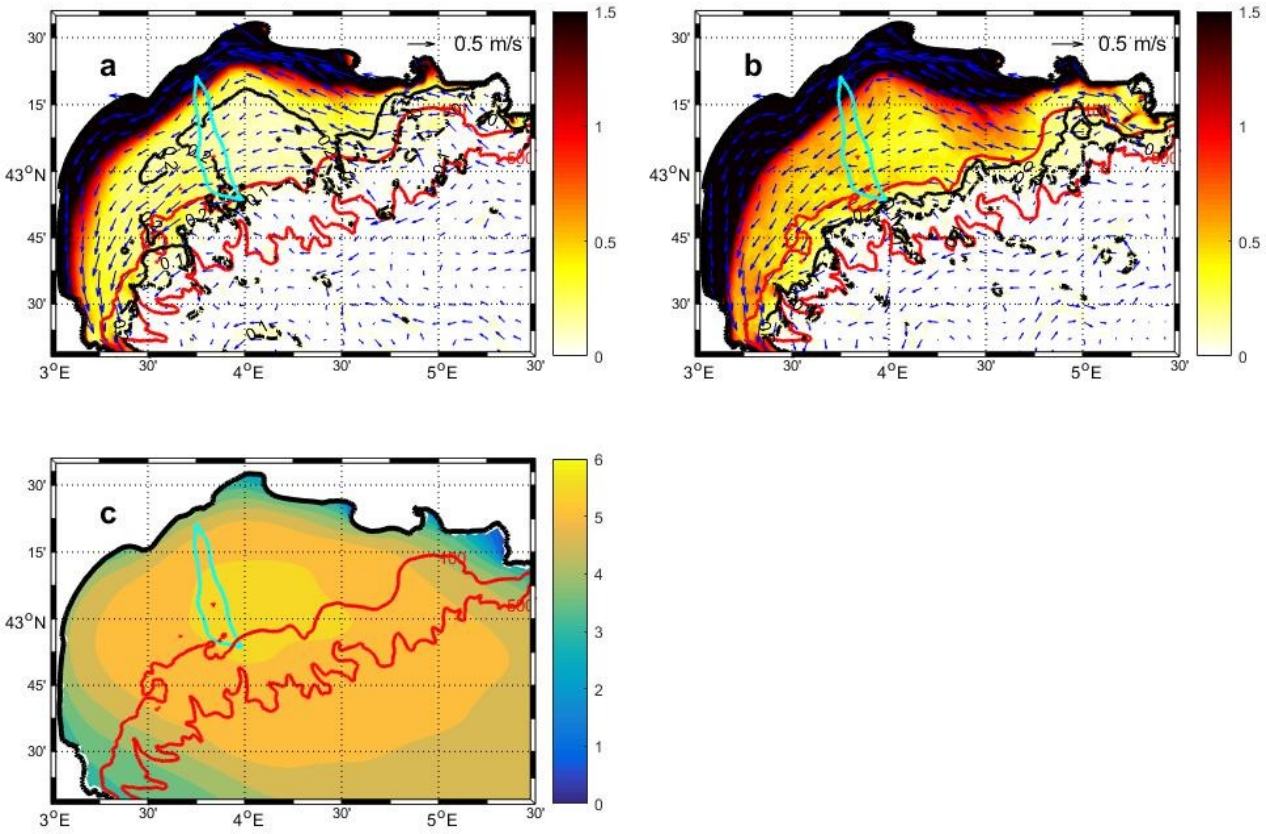

Figure 5.9: (a) and (b) background color: wave-current bottom shear stress (N m^{-2}) averaged between 00:00 and 03:00 h on 1 March 2018 from the simulations using a roughness of 10^{-4} (a) and 10^{-3} m (b). Note that the colorbar has been saturated on the inner shelf to focus on the deeper areas. The black lines correspond to the 0.2 (solid line) and 0.1 (dashed line) N m^{-2} isolines. The depth-averaged currents are superimposed. (c) Significant wave height (m) calculated by Wavewatch 3 averaged over the same period. For the three maps, the red lines correspond to the 100 m and 500 m isobaths, and the cyan line corresponds to the glider path.

sediment distribution data (not shown here) shows that resuspension may occur during this storm over the outer shelf (isobaths>90 m). Indeed, minimum values of 0.1 and 0.3 N m^{-2} are observed on the 100 m isobath (Fig. 5.9 a-b), with the 10^{-4} and 10^{-3} m z_0 simulation, respectively. These values are close to the resuspension critical shear stress assessed for muddy sands as discussed above.

5.4. Discussion

Acoustic and optical data sets from winter glider transects have shown, outside of storm periods, the existence of a 2- or 3-layer vertical stratification characterized by the presence of a low

salinity water layer from the Rhone River. This upper layer, in the first tens of meters, is cooled by air-sea fluxes, while the bottom layer is characterized by the presence of more salty offshore water. This stratification produces a decoupling of currents accelerated in the surface layer by the wind, and also of passive tracers such as chlorophyll-a largely concentrated in the surface layer or suspended matter in the bottom layer. The arrival of an offshore storm (5 years of return period) associated with a strong swell can unstratify the water column up to 90 m depths. This storm induces resuspension on the outer shelf. The vertical mixing is then sufficiently strong to allow the diffusion of the suspended matter over the entire water column. Similar observations were recorded on the meso-tidal Mid-Atlantic Bright shelf (Glenn et al., 2008; Miles et al., 2013).

The importance of currents and surface waves was examined in the bottom boundary layer during the storm, to assess mechanisms driving the sediment resuspension on the muddy sands of the outer shelf. The glider-ADCP provides valuable near-bed data to describe the sediment dynamics, but the resolution used was not sufficient to derive the bottom roughness, a key parameter for quantifying bottom shear stress. We have therefore set a range of values based on the available particle size samples, seabed images close to the glider path, and typical values used in the literature for muddy sands with biological contents (Guillén et al., 2008; Ogston et al., 2008; Peine et al., 2005; Soulsby, 1997). Bottom shear stress computation from glider-ADCP shows that current-, wave-, and wave-current-induced stress are able to remobilize sediments from the seabed. Observations highlights that wave-induced stress (0.15 to 0.45 N m^{-2}) can be up two times greater than the current-induced stress (0.15 to 0.22 N m^{-2}) in the selected bottom roughness ranges (10^{-4} to 10^{-3} m). Therefore, waves stress would be primarily responsible for sediment resuspension observed by the glider for depths greater than 90 m. The commonly accepted view is that near-bottom currents are the main mechanism for sediment resuspension on the outer shelf of the GoL (Bassetti et al., 2006; Ulses et al., 2008b), where depths limit the effect of surface waves to only the most

severe storms (Dufois et al., 2008; Palanques et al., 2008). This study shows for the first time detailed observations of waves impact on the sediment resuspension over the outer shelf, which is an under-monitored area. The modeled wave-current-induced stress, during the peak of the storm, shows conditions conducive to sediment resuspension over the whole shelf (inner-, mid-, and outer-shelf). Bottom shear stress intensity is enough to remobilize at least the uppermost sediment layer (mud) that blankets the outer shelf, and up to the relict coarser sands (~150 μm) found beneath the surface layer for bottom roughness of 10^{-4} and 10^{-3} m, respectively.

Previous studies have highlighted alongshore transport as the dominant feature of storm-driven sediment transport on continental shelves (Miles et al., 2015, 2013; Ogston and Sternberg, 1999; Styles and Glenn, 2005). This alongshore transport induced by eastern storms also exists in the Gulf of Lions (Bourrin et al., 2015 ; Guillén et al., 2006 ; Palanques et al., 2008, 2006 ; Ulses et al., 2008a). However, the quantification of the sediment transport on continental shelves is still poorly documented or associated with very high uncertainty (Gentil et al., 2020). The combination of the glider observations and the model results allows characterizing the advection of particles resuspended during the storm from the spatiotemporal variability of currents. Strong westward currents (~0.4 m s^{-1}) persist between 28 February at 4 p.m. and 2 March 10:00, during which period a fraction of the resuspended material on the outer shelf is advected as the glider shows a sustained increase in turbidity in the water column during two days (Fig. 5.4). Cumulative SPM fluxes throughout the water column from glider observations were estimated according to the method described in section 5.2.5.7. Considering a southwestward SPM transport along the glider's outer-shelf section of 0.86 ± 0.17 t s^{-1} during the storm period, the total SPM mass transported during this 42-hour period amounts to $1.3 \times 10^5 \pm 2.5 \times 10^4$ t. The outer shelf particulate fluxes (0.86 t s^{-1}) are significant, as they would represent 20% of the estimated coastal SPM fluxes during an onshore storm (4 t s^{-1}), according to Bourrin et al. (2015). These observations emphasize the necessity to

monitor the outer shelf to improve our understanding of SPM dynamics at the shelf scale. However, the glider performs the open ocean-coast section over 3 days, i.e. about 4 periods of inertial oscillation (~17.5 h) in the Gulf of Lions. The variability of currents on scales smaller than the transit time along the transect, generally does not allow to assume a steady state. This non-simultaneity of the measurements along the transect, represents the main limitation of the contribution of the glider to the study of transport at the scale of the shelf, if it is used alone. On the other hand, if it is used in conjunction with fixed moorings and/or in connection with the modeling, its contribution is indisputable. To evaluate the displacement of suspended matter at the regional scale, Lagrangian particles were positioned in the model current fields along the "storm" transect of the glider and throughout the water column. The particles were released at the beginning of the storm every 10 m, from 20 m below the surface to the bottom. Deposition was neglected to simulate the particles that remain in suspension throughout this period. Figure 5.10 shows the trajectories of the particles, all points combined. The 2-day storm associated with currents of ~0.4 m s^{-1}, produces a displacement of SPM of ~68 km to the southwest. The storm duration is not sufficient for the material resuspended in the central part of the shelf (study area) to be exported from the Gulf of Lions. However, it is likely that this matter will be exported during the next storm, even if it is moderate. Indeed, the muddy sediment deposits in the southwestern part of the GoL are easily remobilized (compared to the mid-shelf) due to the narrowing of the shelf producing a strengthening of the storm-induced bottom currents (DeGeest et al., 2008). The material is likely transferred from the proximal zone of the Rhone to the southwestern outlet of the Gulf of Lions in a discontinuous manner, with a jump of a few tens of kilometers at each storm. Annual storms are probably sufficient to produce these jumps up to 60 m depth along the mid shelf mud belt, where most of the along-shelf transport is probably concentrated. Concerning the outer shelf, a hypothesis would be a seeding in suspended matter to the south/south-west of the Rhone by the plume which

extends towards the open sea in the dominant conditions of northern wind (Estournel et al., 1997). Although the extremity of the plume is lightly loaded with suspended matter, the recurrence of these situations could be the cause of the deposits that drape the outer shelf sands. Furthermore, Ekman transport in the bottom nepheloid layer, induced by the general cyclonic circulation of the Gulf of Lions, contributes to the advection of fine sediments from the shelf to the open sea, feeding the outer shelf (Durrieu de Madron and Panouse, 1996). Following this initial deposition, southwestward transport would occur during the most energetic storms. This transfer model, which indicates temporary deposits, would be consistent with Miralles et al. (2005) observations, showing that sedimentation rates in the central part of the GoL are around 0.1 cm year^{-1} at scales of several decades. This study improves knowledge of the fate of the muddy sands over the outer shelf of the Gulf of Lions—also found on many continental margins into the world.

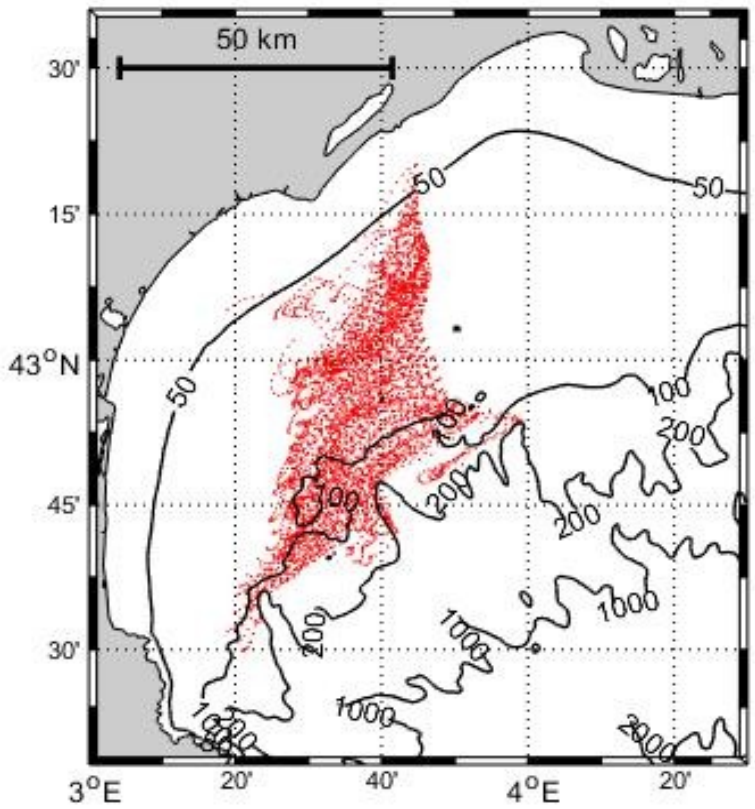

Figure 5.10: Along shelf transport of resuspended muds (all points combined) from the glider section during the 2-day storm (from 28 February 16.00 to 2 March 10.00).

5.5. Conclusion

This study highlights the importance of utilizing novel ocean observation technology, such as active acoustic glider to extend the measurement of sediment resuspension and transport in the coastal zone. The continuing observations of near-bottom currents and sediment concentration profiles using both acoustic and optical sensors mounted on glider platforms, prompt to show for the first time, to our knowledge, the role of surface wave forcing in the resuspension of sediment at depths >90 m over the shelf. ADCP measurements proved invaluable validation of current vertical profiles of the hydrodynamic model during this severe storm, while observations of this type of event are generally lacking in the coastal continuum due to their rarity. This is particularly important for improving model forecasting, in a context where extreme events such as storms are expected to become more intense by the end of the century in the Mediterranean as a result of human influences on climate (Romero and Emanuel, 2013).

Future advances that may improve bottom shear stress estimates from the glider-ADCP, would be to increase near-bed high-frequency measurements, enabling to estimate friction velocity from turbulence methods (direct covariance and turbulent kinetic energy). These methods are less variable than the log profile method used in this study and allow to get away from the bottom roughness, which is hard to estimate in real-time. Similarly, the recent integration of a Laser In Situ Scattering and Transmissometry (LISST) sensor into gliders allows observation of the details of suspended particle size and concentration, opening up new perspectives in understanding particle aggregation and settling processes at regional scales. Improved in situ observations of particle properties will be valuable for the validation of sediment resuspension and transport model to assess the impact of episodic events in the coastal zones.

References

Agence des aires marines protégées, COMEX, GIS Posidonie, Equipe scientifique — MEDSEACAN 2008-2012, 2012. Programme de reconnaissance des têtes de canyons de la Méditerranée française.

Augris, C., Agin, G., Berne, S., Arnaud, M., Guizien, K., Chatelain, M., Labrune, C., Carbonnel, P., Maillet, G., Grenz, C., Vella, C., Nittrouer, C. C., Bourrin, F., Certain, R., Durrieu De Madron, X., Garlan, T., Dufois, F., Jouet, G., Dennielou, B., Simplet, L., (2013). Seabed substrate database from a compilation of sediment samples taken during oceanographic campaigns carried out in the Gulf of Lion by Ifremer, CEFREM, IRSN, CEREGE, FOB, MIO, LECOB, The Conseil Général de l'Hérault and Rhône-Méditerranée-Corse Water Agency. Results of grain size analysis performed on samples. SEANOE. https://doi.org/10.17882/81430

Ahmad, M., Dong, P., Mamat, M., Wan Nik, W., Mohd, M., 2011. The critical shear stresses for sand and mud mixture. Appl. Math. Sci 5, 53–71.

Albarracín, S., Alcántara-Carrió, J., Montoya-Montes, I., Fontán-Bouzas, Á., Somoza, L., Amos, C.L., Salgado, J.R., 2014. Relict sand waves in the continental shelf of the Gulf of Valencia (Western Mediterranean). Journal of Sea Research 93, 33–46.

Aloısi, J., 1986. Sur un modele de sédimentation deltaıque : contribution a la connaissance des marges passives. These de Doctorat d'Etat, Université de Perpignan.

Bassetti, M.-A., Jouet, G., Dufois, F., Berné, S., Rabineau, M., Taviani, M., 2006. Sand bodies at the shelf edge in the Gulf of Lions (Western Mediterranean): Deglacial history and modern processes. Marine Geology 234, 93–109.

Berne, S., Lericolais, G., Marsset, T., Bourillet, J.F., De Batist, M., 1998. Erosional offshore sand ridges and lowstand shorefaces; examples from tide-and wave-dominated environments of France. Journal of Sedimentary Research 68, 540–555.

Bonnin, J., Heussner, S., Calafat, A., Fabres, J., Palanques, A., De Madron, X.D., Canals, M., Puig, P., Avril, J., Delsaut, N., 2008. Comparison of horizontal and downward particle fluxes across canyons of the Gulf of Lions (NW Mediterranean): Meteorological and hydrodynamical forcing. Continental Shelf Research 28, 1957–1970.

Bosnic, I., Cascalho, J., Taborda, R., Drago, T., Hermínio, J., Rosa, M., Dias, J., Garel, E., 2017. Nearshore sediment transport: Coupling sand tracer dynamics with oceanographic forcing. Marine Geology 385, 293–303.

Bourrin, F., Friend, P. L., Amos, C.L., Manca, E., Ulses, C., Palanques, A., De Madron, X. D., Thompson, C.E., 2008. Sediment dispersal from a typical Mediterranean flood: the Têt River, Gulf of Lions.

Continental Shelf Research 28, 1895–1910.

Bourrin, F., Many, G., De Madron, X. D., Martín, J., Puig, P., Houpert, L., Testor, P., Kunesch, S., Mahiouz, K., Béguery, L., 2015. Glider monitoring of shelf suspended particle dynamics and transport during storm and flooding conditions. Continental Shelf Research 109, 135–149.

Briggs, N., Perry, M. J., Cetinić, I., Lee, C., D'Asaro, E., Gray, A. M., Rehm, E., 2011. High-resolution observations of aggregate flux during a sub-polar North Atlantic spring bloom. Deep Sea Research Part I: Oceanographic Research Papers 58, 1031–1039.

Brodtkorb, P.A., Johannesson, P., Lindgren, G., Rychlik, I., Ryden, J., Sjö, E., 2000. WAFO-a Matlab toolbox for analysis of random waves and loads. Presented at the The tenth international offshore and polar engineering conference, International Society of Offshore and Polar Engineers.

Butel, R., Dupuis, H., Bonneton, P., 2002. Spatial variability of wave conditions on the French Atlantic coast using in-situ data. Journal of Coastal Research 96–108.

Chang, G., Dickey, T., Williams III, A., 2001. Sediment resuspension over a continental shelf during Hurricanes Edouard and Hortense. Journal of Geophysical Research: Oceans 106, 9517–9531.

Cheng, R.T., Ling, C., Gartner, J.W., Wang, P., 1999. Estimates of bottom roughness length and bottom shear stress in South San Francisco Bay, California. Journal of Geophysical Research: Oceans 104, 7715–7728.

Dalyander, P.S., Butman, B., Sherwood, C.R., Signell, R.P., Wilkin, J.L., 2013. Characterizing wave-and current-induced bottom shear stress: US middle Atlantic continental shelf. Continental Shelf Research 52, 73–86.

Davis, R. E., Eriksen, C. C., Jones, C. P., 2002. Autonomous buoyancy-driven underwater gliders. The technology and applications of autonomous underwater vehicles 37–58.

de Fommervault, O., Besson, F., Beguery, L., Le Page, Y., Lattes, P., 2019. SeaExplorer Underwater Glider: A New Tool to Measure depth-resolved water currents profiles. Presented at the OCEANS 2019-Marseille, IEEE, pp. 1–6.

DeGeest, A., Mullenbach, B., Puig, P., Nittrouer, C., Drexler, T.M., de Madron, X. D., Orange, D., 2008. Sediment accumulation in the western Gulf of Lions, France: the role of Cap de Creus canyon in linking shelf and slope sediment dispersal systems. Continental Shelf Research 28, 2031–2047.

Deines, K. L., 1999. Backscatter estimation using broadband acoustic Doppler current profilers. Presented at the Proceedings of the IEEE Sixth Working Conference on Current Measurement (Cat. No. 99CH36331), IEEE, pp. 249–253.

Drake, D. E., Cacchione, D. A., 1986. Field observations of bed shear stress and sediment resuspension on

continental shelves, Alaska and California. Continental Shelf Research 6, 415–429.

Drake, D. E., Cacchione, D. A., Grant, W. D., 1992. Shear stress and bed roughness estimates for combined wave and current flows over a rippled bed. Journal of Geophysical Research: Oceans 97, 2319–2326.

Dufois, F., Garreau, P., Le Hir, P., Forget, P., 2008. Wave-and current-induced bottom shear stress distribution in the Gulf of Lions. Continental Shelf Research 28, 1920–1934.

Durrieu de Madron, X., Panouse, M., 1996. Transport de matière particulaire en suspension sur le plateau continental du Golfe du Lion. Situation estivale et hivernale. Comptes rendus de l'Académie des sciences. Série 2. Sciences de la terre et des planètes 322, 1061–1070.

Durrieu de Madron, X., Wiberg, P. L., Puig, P., 2008. Sediment dynamics in the Gulf of Lions: The impact of extreme events.

Emery, K., 1968. Relict sediments on continental shelves of world. AAPG Bulletin 52, 445–464.

Eriksen, C.C., Osse, T.J., Light, R.D., Wen, T., Lehman, T.W., Sabin, P.L., Ballard, J.W., Chiodi, A.M., 2001. Seaglider: A long-range autonomous underwater vehicle for oceanographic research. IEEE Journal of oceanic Engineering 26, 424–436.

Estournel, C., Durrieu de Madron, X., Marsaleix, P., Auclair, F., Julliand, C., Vehil, R., 2003. Observation and modeling of the winter coastal oceanic circulation in the Gulf of Lion under wind conditions influenced by the continental orography (FETCH experiment). Journal of Geophysical Research: Oceans 108.

Estournel, C., Kondrachoff, V., Marsaleix, P., Vehil, R., 1997. The plume of the Rhone: numerical simulation and remote sensing. Continental shelf research 17, 899–924.

Estournel, C., Marsaleix, P., Ulses, C., 2021. A new assessment of the circulation of Atlantic and Intermediate Waters in the Eastern Mediterranean. Progress in Oceanography *(in press)*.

Ferré, B., Durrieu De Madron, X., Estournel, C., Ulses, C., Le Corre, G., 2008. Impact of natural (waves and currents) and anthropogenic (trawl) resuspension on the export of particulate matter to the open ocean: application to the Gulf of Lion (NW Mediterranean). Continental Shelf Research 28, 2071–2091.

Ferré, B., Guizien, K., De Madron, X.D., Palanques, A., Guillén, J., Grémare, A., 2005. Fine-grained sediment dynamics during a strong storm event in the inner-shelf of the Gulf of Lion (NW Mediterranean). Continental Shelf Research 25, 2410–2427.

Ferré, B., Sherwood, C.R., Wiberg, P. L., 2010. Sediment transport on the Palos Verdes shelf, California. Continental Shelf Research 30, 761–780.

Fischer, J., Visbeck, M., 1993. Deep velocity profiling with self-contained ADCPs. Journal of atmospheric and oceanic technology 10, 764–773.

Garau, B., Ruiz, S., Zhang, W.G., Pascual, A., Heslop, E., Kerfoot, J., Tintoré, J., 2011. Thermal lag correction on Slocum CTD glider data. Journal of Atmospheric and Oceanic Technology 28, 1065–1071.

Gaudin, M., Berné, S., Jouanneau, J.-M., Palanques, A., Puig, P., Mulder, T., Cirac, P., Rabineau, M., Imbert, P., 2006. Massive sand beds attributed to deposition by dense water cascades in the Bourcart canyon head, Gulf of Lions (northwestern Mediterranean Sea). Marine Geology 234, 111–128.

Gentil, M., Many, G., Durrieu de Madron, X., Cauchy, P., Pairaud, I., Testor, P., Verney, R., Bourrin, F., 2020. Glider-Based Active Acoustic Monitoring of Currents and Turbidity in the Coastal Zone. Remote Sensing 12, 2875.

Glenn, S., Jones, C., Twardowski, M., Bowers, L., Kerfoot, J., Kohut, J., Webb, D., Schofield, O., 2008. Glider observations of sediment resuspension in a Middle Atlantic Bight fall transition storm. Limnology and Oceanography 53, 2180–2196.

Glenn, S. M., Grant, W. D., 1987. A suspended sediment stratification correction for combined wave and current flows. Journal of Geophysical Research: Oceans 92, 8244–8264. https://doi.org/10.1029/JC092iC08p08244

Gordon, R.L., 1996. Acoustic Doppler current profiler-Principles of operation: A practical primer. Rd Instruments 54, 54.

Gostiaux, L., van Haren, H., 2010. Extracting meaningful information from uncalibrated backscattered echo intensity data. Journal of Atmospheric and Oceanic Technology 27, 943–949.

Got, H., Aloisi, J., 1990. The Holocene sedimentation on the Gulf of Lions margin: a quantitative approach. Continental Shelf Research 10, 841–855.

Grant, W. D., Madsen, O.S., 1979. Combined wave and current interaction with a rough bottom. Journal of Geophysical Research: Oceans 84, 1797–1808.

Guillén, J., Bourrin, F., Palanques, A., De Madron, X. D., Puig, P., Buscail, R., 2006. Sediment dynamics during wet and dry storm events on the Têt inner shelf (SW Gulf of Lions). Marine Geology 234, 129–142.

Guillén, J., Soriano, S., Demestre, M., Falqués, A., Palanques, A., Puig, P., 2008. Alteration of bottom roughness by benthic organisms in a sandy coastal environment. Continental Shelf Research 28, 2382–2392.

Guizien, K., 2009. Spatial variability of wave conditions in the Gulf of Lions (NW Mediterranean Sea). Vie

et milieu 59, 261.

Holmedal, L. E., Myrhaug, D., Rue, H., 2003. The sea bed boundary layer under random waves plus current. Continental Shelf Research 23, 717–750.

Jackett, D. R., McDougall, T.J., Feistel, R., Wright, D. G., Griffies, S. M., 2006. Algorithms for density, potential temperature, conservative temperature, and the freezing temperature of seawater. Journal of Atmospheric and Oceanic Technology 23, 1709–1728.

Jia, L., Ren, J., Nie, D., Chen, B., Lv, X., 2014. Wave-current bottom shear stresses and sediment re-suspension in the mouth bar of the Modaomen Estuary during the dry season. Acta Oceanologica Sinica 33, 107–115.

Jing, L., Ridd, P. V., 1996. Wave-current bottom shear stresses and sediment resuspension in Cleveland Bay, Australia. Coastal Engineering 29, 169–186.

Jordá, G., Bolaños, R., Espino, M., Sánchez-Arcilla, A., 2007. Assessment of the importance of the current-wave coupling in the shelf ocean forecasts. Ocean Science 3, 345–362.

King, E., Conley, D., Masselink, G., Leonardi, N., McCarroll, R., Scott, T., 2019. The impact of waves and tides on residual sand transport on a sediment-poor, energetic, and macrotidal continental shelf. Journal of Geophysical Research: Oceans 124, 4974–5002.

Liblik, T., Karstensen, J., Testor, P., Alenius, P., Hayes, D., Ruiz, S., Heywood, K., Pouliquen, S., Mortier, L., Mauri, Ejm., 2016. Potential for an underwater glider component as part of the Global Ocean Observing System. Methods in Oceanography 17, 50–82.

Liu, X., Zhu, C., Zheng, J., Guo, L., Yin, P., Jia, Y., 2017. The observations of seabed sediment erosion and resuspension processes in the Jiaozhou Bay in China. Acta Oceanologica Sinica 36, 79–85.

Many, G., Bourrin, F., de Madron, X.D., Ody, A., Doxaran, D., Cauchy, P., 2018. Glider and satellite monitoring of the variability of the suspended particle distribution and size in the Rhône ROFI. Progress in oceanography 163, 123–135.

Marsaleix, P., Auclair, F., Estournel, C., 2009. Low-order pressure gradient schemes in sigma coordinate models: The seamount test revisited. Ocean Modelling 30, 169–177.

Marsaleix, P., Auclair, F., Estournel, C., 2006. Considerations on open boundary conditions for regional and coastal ocean models. Journal of Atmospheric and Oceanic Technology 23, 1604–1613.

Marsaleix, P., Auclair, F., Floor, J.W., Herrmann, M. J., Estournel, C., Pairaud, I., Ulses, C., 2008. Energy conservation issues in sigma-coordinate free-surface ocean models. Ocean Modelling 20, 61–89.

Marsaleix, P., Michaud, H., Estournel, C., 2019. 3D phase-resolved wave modelling with a non-hydrostatic

ocean circulation model. Ocean Modelling 136, 28–50.

Martín, J., Durrieu de Madron, X., Puig, P., Bourrin, F., Palanques, A., Houpert, L., Higueras, M., Sanchez-Vidal, A., Calafat, A.M., Canals, M., 2013. Sediment transport along the Cap de Creus Canyon flank during a mild, wet winter. Biogeosciences 10, 3221–3239.

McDougall, T.J., Barker, P. M., 2011. Getting started with TEOS-10 and the Gibbs Seawater (GSW) oceanographic toolbox. SCOR/IAPSO WG 127, 1–28.

McWilliams, J.C., Restrepo, J. M., 1999. The wave-driven ocean circulation. Journal of Physical Oceanography 29, 2523–2540.

Michaud, H., Marsaleix, P., Leredde, Y., Estournel, C., Bourrin, F., Lyard, F., Mayet, C., Ardhuin, F., 2012. Three-dimensional modelling of wave-induced current from the surf zone to the inner shelf. Ocean Science 8, 657–681.

Mikolajczak, G., Estournel, C., Ulses, C., Marsaleix, P., Bourrin, F., Martín, J., Pairaud, I., Puig, P., Leredde, Y., Many, G., 2020. Impact of storms on residence times and export of coastal waters during a mild autumn/winter period in the Gulf of Lion. Continental Shelf Research 207, 104,192.

Miles, T., Glenn, S. M., Schofield, O., 2013. Temporal and spatial variability in fall storm induced sediment resuspension on the Mid-Atlantic Bight. Continental Shelf Research 63, S36—S49.

Miles, T., Seroka, G., Kohut, J., Schofield, O., Glenn, S., 2015. Glider observations and modeling of sediment transport in Hurricane Sandy. Journal of Geophysical Research: Oceans 120, 1771–1791.

Miles, T., Slade, W., Glenn, S., 2021. Sediment resuspension and transport from a glider integrated Laser In Situ Scattering and Transmissometry (LISST) particle analyzer. Journal of Atmospheric and Oceanic Technology.

Miralles, J., Radakovitch, O., Aloisi, J.-C., 2005. 210Pb sedimentation rates from the Northwestern Mediterranean margin. Marine Geology 216, 155–167.

Monaco, A., 1971. Contribution à l'étude géologique et sédimentologique du plateau continental du Roussillon (Golfe du Lion).

Mullison, J., 2017. Backscatter estimation using broadband acoustic doppler current profilers-updated. Presented at the Proceedings of the ASCE Hydraulic Measurements & Experimental Methods Conference, Durham, NH, USA, pp. 9–12.

Mullison, J., DeCollibus, C., Allsup, B., 2013. An investigation of the accuracy of current profile measurements from a glider-mounted ADCP operating in shallow water. Presented at the 2013 OCEANS-San Diego, IEEE, pp. 1–8.

Nielsen, P., 1992. Coastal bottom boundary layers and sediment transport. World scientific.

Niu, J., Xu, J., Li, G., Dong, P., Shi, J., Qiao, L., 2020. Swell-dominated sediment re-suspension in a silty coastal seabed. Estuarine, Coastal and Shelf Science 242, 106,845.

Ogston, A., Sternberg, R., 1999. Sediment-transport events on the northern California continental shelf. Marine Geology 154, 69–82.

Ogston, A.S., Drexler, T.M., Puig, P., 2008. Sediment delivery, resuspension, and transport in two contrasting canyon environments in the southwest Gulf of Lions. Continental Shelf Research 28, 2000–2016.

Ordonez, C.E., Shearman, R.K., Barth, J.A., Welch, P., Erofeev, A., Kurokawa, Z., 2012. Obtaining absolute water velocity profiles from glider-mounted acoustic Doppler current profilers. Presented at the 2012 Oceans-Yeosu, IEEE, pp. 1–7.

Paladini de Mendoza, F., Bonamano, S., Martellucci, R., Melchiorri, C., Consalvi, N., Piermattei, V., Marcelli, M., 2018. Circulation during storms and dynamics of suspended matter in a sheltered coastal area. Remote Sensing 10, 602.

Palanques, A., de Madron, X. D., Puig, P., Fabres, J., Guillén, J., Calafat, A., Canals, M., Heussner, S., Bonnin, J., 2006. Suspended sediment fluxes and transport processes in the Gulf of Lions submarine canyons. The role of storms and dense water cascading. Marine Geology 234, 43–61.

Palanques, A., Guillén, J., Puig, P., de Madron, X. D., 2008. Storm-driven shelf-to-canyon suspended sediment transport at the southwestern Gulf of Lions. Continental Shelf Research 28, 1947–1956.

Palinkas, C., Ogston, A., Nittrouer, C., 2010. Observations of event-scale sedimentary dynamics with an instrumented bottom-boundary-layer tripod. Marine Geology 274, 151–164.

Peine, F., Bobertz, B., Graf, G., 2005. Influence of the blue mussel Mytilus edulis (Linnaeus) on the bottom roughness length (z0) in the south-western Baltic Sea. Baltica 18, 13–22.

Perez Belmonte, L., 2003. Enregistrement de la dernière transgression dans le Golfe du Lion. DEA Thesis, Université Lille 1, 52.

Perlin, A., Moum, J., Klymak, J., Levine, M., Boyd, T., Kosro, P., 2007. Organization of stratification, turbulence, and veering in bottom Ekman layers. Journal of Geophysical Research: Oceans 112.

Petrenko, A., Dufau, C., Estournel, C., 2008. Barotropic eastward currents in the western Gulf of Lion, north-western Mediterranean Sea, during stratified conditions. Journal of Marine Systems 74, 406–428.

Prescott, P., Walden, A., 1980. Maximum likelihood estimation of the parameters of the generalized extreme-value distribution. Biometrika 67, 723–724.

Pruski, A.M., Buscail, R., Bourrin, F., Vétion, G., 2019. Influence of coastal Mediterranean rivers on the

organic matter composition and reactivity of continental shelf sediments: The case of the Têt River (Gulf of Lions, France). Continental Shelf Research 181, 156–173.

Romero, R., Emanuel, K., 2013. Medicane risk in a changing climate. Journal of Geophysical Research: Atmospheres 118, 5992–6001.

Rudnick, D. L., 2016. Ocean research enabled by underwater gliders. Annual review of marine science 8, 519–541.

Rudnick, D. L., Sherman, J. T., Wu, A.P., 2018. Depth-average velocity from Spray underwater gliders. Journal of Atmospheric and Oceanic Technology 35, 1665–1673.

Sadaoui, M., Ludwig, W., Bourrin, F., Raimbault, P., 2016. Controls, budgets and variability of riverine sediment fluxes to the Gulf of Lions (NW Mediterranean Sea). Journal of Hydrology 540, 1002–1015.

Shi, J.Z., Wang, Y., 2008. The vertical structure of combined wave—current flow. Ocean Engineering 35, 174–181.

Soulsby, R., 1997. Dynamics of marine sands.

Soulsby, R. L., 1983. The bottom boundary layer of shelf seas, in: Elsevier Oceanography Series. Elsevier, pp. 189–266.

Soulsby, R. L., Hamm, L., Klopman, G., Myrhaug, D., Simons, R., Thomas, G., 1993. Wave-current interaction within and outside the bottom boundary layer. Coastal engineering 21, 41–69.

Styles, R., Glenn, S. M., 2005. Long-term sediment mobilization at a sandy inner shelf site, LEO-15. Journal of Geophysical Research: Oceans 110.

Styles, R., Glenn, S. M., 2000. Modeling stratified wave and current bottom boundary layers on the continental shelf. Journal of Geophysical Research: Oceans 105, 24119–24139.

Testor, P., de Young, B., Rudnick, D. L., Glenn, S., Hayes, D., Lee, C. M., Pattiaratchi, C., Hill, K., Heslop, E., Turpin, V., 2019. OceanGliders: a component of the integrated GOOS. Frontiers in Marine Science 6, 422.

Tolman, H. L., 2009. User manual and system documentation of WAVEWATCH III TM version 3.14. Technical note, MMAB Contribution 276, 220.

Troupin, C., Barth, A., Sirjacobs, D., Ouberdous, M., Brankart, J.-M., Brasseur, P., Rixen, M., Alvera-Azcárate, A., Belounis, M., Capet, A., 2012. Generation of analysis and consistent error fields using the Data Interpolating Variational Analysis (DIVA). Ocean Modelling 52, 90–101.

Ulses, C., Estournel, C., Bonnin, J., Durrieu de Madron, X., Marsaleix, P., 2008a. Impact of storms and dense

water cascading on shelf-slope exchanges in the Gulf of Lion (NW Mediterranean). Journal of Geophysical Research: Oceans 113.

Ulses, C., Estournel, C., De Madron, X.D., Palanques, A., 2008 b. Suspended sediment transport in the Gulf of Lions (NW Mediterranean): Impact of extreme storms and floods. Continental shelf research 28, 2048–2070.

Van Rijn, L. C., Kroon, A., 1993. Sediment transport by currents and waves, in: Coastal Engineering 1992. pp. 2613–2628.

Van Sebille, E., Aliani, S., Law, K.L., Maximenko, N., Alsina, J.M., Bagaev, A., Bergmann, M., Chapron, B., Chubarenko, I., Cózar, A., 2020. The physical oceanography of the transport of floating marine debris. Environmental Research Letters 15, 023003.

Weaver, P., Canals, M., Trincardi, F., 2006. EUROSTRATAFORM Vol 1: Source to Sink Sedimentation on the European Margin. Special issue of Marine Geology. Marine Geology 234, 1–292.

Wiggert, J., Jones, B., Dickey, T., Brink, K., Weller, R., Marra, J., Codispoti, L., 2000. The Northeast Monsoon's impact on mixing, phytoplankton biomass and nutrient cycling in the Arabian Sea. Deep Sea Research Part II: Topical Studies in Oceanography 47, 1353–1385.

Xu, J., Wright, L., 1995. Tests of bed roughness models using field data from the Middle Atlantic Bight. Continental Shelf Research 15, 1409–1434.

Xu, Z., Bowen, A., 1994. Wave-and wind-driven flow in water of finite depth. Journal of physical oceanography 24, 1850–1866.

Zedler, S., Dickey, T., Doney, S., Price, J., Yu, X., Mellor, G., 2002. Analyses and simulations of the upper ocean's response to Hurricane Felix at the Bermuda Testbed Mooring site: 13–23 August 1995. Journal of Geophysical Research: Oceans 107, 25–1.

Chapter 6.

General conclusion

Table of Contents

Table of figures

Monitoring SPM dynamics involves: (i) estimating sediment fluxes between or within compartments of the coastal zone and (ii) analyzing their spatiotemporal variability at different scales (Ouillon, 2018). In this conclusion, we will discuss the glider's ability to measure currents, turbidity, and fluxes (section 6.1), and to represent their spatiotemporal variability in the coastal zone (section 6.2).

6.1. The glider-ADCP

6.1.1. A new tool to monitor coastal dynamics

Reliable current, SPM concentration, and fluxes data are fundamental in the understanding of marine ecosystems dynamics and their fate. The recent integration of an ADCP onto underwater gliders opens new research perspectives in coastal fields. In this context, we developed a processing chain allowing the simultaneous analysis of hydrological and hydrodynamic data from underwater gliders. This open-source code of this "toolbox" was made available to the community on the GitHub platform (see Chapter. 3). Previously available packages are focused on processing raw glider output, usually limited to physical and bio-optical data (SOCIB, https://github.com/socib/glider_toolbox; UEA, http://www.byqueste.com/toolbox.html; GliderTools, https://github.com/GliderToolsCommunity/GliderTools). Our "toolbox" was developed in a context where no tool existed to process active acoustic data from ADCPs embedded on gliders. Acoustic and optic processing used for hydro-sedimentary purposes is discussed below according to each component.

Currents — In delayed mode data quality control (DMQC), several techniques are used to remove the glider's motion from ADCP measurements and to derive absolute ocean velocity (Gentil et al., 2020; Merckelbach et al., 2010; Todd et al., 2017). The "inverse method", is particularly flexible since multiple constraints, smoothing, and weighting of observations can be easily

incorporated (Todd et al., 2017). This method is particularly suitable when the seabed is out of range of the glider-ADCP (e.g., shelf slope, open ocean). However, this study has shown that in the coastal zone where the bottom track (directly measuring velocity over ground) is often the only available constraint, the "shear method" to derive absolute velocities is very suitable. Indeed, the depth-averaged current constraint, often used for offshore deployments, is less reliable for coastal glider-ADCP surveys, where multiple yos (upcast/downcast) are the standards to limit the glider's surfacing and consecutive surface drift, to reduce the risk of collision with ships or topography (coast). Also, this method has the advantage of being less time-consuming than the "inverse method". Our results show that endurance deployments (>30 days) are feasible with uncertainties around 6 cm s^{-1} from an optimized sampling strategy (Gentil et al., submitted). These uncertainties are comparable to those obtained by other authors (~0.05 to 0.1 m s^{-1}, e.g., Heiderich and Todd, 2020; Jakoboski et al., 2020; Todd et al., 2017). While the latter studies were based on glider high-frequency measurements over short periods (few hours to a week).

Turbidity—SPM size, shape, as well as density, plays a fundamental role in their fate, it is thus essential to characterize the properties of SPM. This study highlighted the complementarity of coincident optical and acoustic measurements to characterize the granulometric populations (fine vs. aggregates) of SPM in the water column (Gentil et al., 2020)**.** Analysis of spikes from optical sensors and acoustic backscatter signals indicates the presence of coarse particles, while the optical signal is more sensitive to fine particulates. However, turbidity results from acoustic sensors are dependent on the device frequency and must be carefully examined before being interpreted. In this study, the ADCP used has a frequency of 614.4 kHz, and a peak sensitivity for particles of 775 µm (Lohrmann, 2001), which represents the upper limit of the observed aggregates in the Rhone ROFI area (Many et al., 2016). The sensitivity signal is 10–170 times lower for particles of 200 and 50 µm in diameter, respectively. This means that acoustics cannot detect all flocs/aggregates and the

coincident optical spikes measurements are thus required to improve the detection of coarse particles in the water column.

SPM fluxes — In the GoL, the description of SPM dynamics is beginning to be known, but quantification of fluxes at various spatiotemporal scales from observations is rare (Bourrin et al., 2015; Many, 2016). This work has shown that uncertainties of fluxes are very sensitive to the uncertainties related to the currents and SPM concentration estimates. Results showed that with (i) a non-optimized sampling strategy (1 ping every 10 s) of the ADCP, and (ii) a limited coverage of water samples without triplicates, the resulting uncertainty on the SPM fluxes could exceed 100% (Gentil et al., 2020)**.** However, from a good SPM calibration (glider measurements carried out on the bathysonde with water samples) and an optimized ADCP configuration in endurance deployment (1 ping every 3 s), the uncertainty on SPM fluxes are significantly reduced (~20%) (Gentil et al., submitted).

Results emphasized the ability of gliders to measure currents, turbidity, and fluxes at high spatiotemporal resolution in the water column over continental shelves. These estimates are fundamental parameters in the improvement, validation of hydro-sedimentary models (Miles et al., 2015). Our “toolbox” has proven its efficiency since it has been used in the data processing of two scientific papers (Gentil et al., 2020; Gentil et al., submitted), presented in chapters 4 and 5 of this thesis. However, the glider-ADCP “toolbox” is instrument-dependent and can currently only process data from an RDI Doppler Velocity Log (ADCP) from a Slocum glider. This “toolbox” is not intended to be developed further in the future. Its use on a larger scale in the scientific community would require: (i) that it be accessible on free software (as Python) and (ii) that it be able to handle all glider-ADCP combinations.

6.1.2. Towards a real-time data processing

Real-time data supply information about the ocean surface and interior that can be used in various operational systems and services (Legler et al., 2015). It is a critical component of operational monitoring of SPM dynamics, which is necessary to improve sediment transport and ecosystem modeling, with the final goal to prevent short—and long-term damage to coastal waters (e.g., dispersion of pollutants, seabed erosion) (Ody et al., 2016). Many teams are actively working on quality control of real-time data from underwater glider platforms (Schofield et al., 2015). Recent studies have shown the value of using real-time data from gliders for diverse applications as: to direct the ship-based sampling on the New Jersey coast (Schofield et al., 2007), to track sand tiger sharks and sturgeon off the east coast of the United States (Schofield et al., 2015), or even to provide temperature and salinity profiles for assimilation into a real-time marine forecasting system in Northern South China Sea (Peng et al., 2019).

To our knowledge, there is no system for real-time monitoring of SPM dynamics from a glider equipped with optical and acoustic sensors. In this context, a new project supported by the CEFREM and the University of Perpignan in partnership with companies (ALSEAMAR and CENTRALWEB) aims to develop a tool to measure and transmit currents, turbidity data and in fine the SPM fluxes at various spatial (from the meter to the hundreds of kilometers) and temporal (from the second to several months) scales of the coastal zone, in real-time. The protocols for cleaning and processing acoustic data to estimate turbidity (backscatter index) and currents in real-time, took advantage of the work of Gentil et al. (2020) and the “toolbox” developed in this thesis. The new tool developed will eventually allow the monitoring of coastal water quality in the context of the Marine Strategy Framework Directive, but also the monitoring of current and underwater visibility for military applications.

6.1.3. Towards “best practices” in glider data processing

This study showed that the integration of new sensors such as the ADCP implies that a newcomer to glider data analysis is exposed to several issues and time-consuming tasks that are not common when processing data from more traditional platforms (see Chapter. 3; and in Gregor et al., 2019). To avoid this issue, the *Oceangliders* (https://www.oceangliders.org/) program started in 2016 to support active coordination and enhancement of the worldwide glider activity. A major objective of this program is to provide interoperable and intercomparable glider data in global databases, in real-time and delayed mode, through the development of “best practices” to benefit a broader community. The concept of best practice has been defined by Pearlman et al. (2019) as follows: “*a best practice is a methodology that has repeatedly produced superior results relative to other methodologies with the same objective; to be fully elevated to a best practice, a promising method will have been adopted and employed by multiple organizations”*. To follow this concept the glider community is writing a reference document for submission to Frontiers in Marine Sciences (Testor et al., in prep). It is intended to be an initial summary paper to help establish best practices and standards in DMQC in sections dedicated to each area of glider activity (currents, oxygen, SPM, etc.). Throughout my Ph.D., I developed skills in the glider’s data processing for hydro-sedimentary purposes. In this context, I joined this community-based effort initiated by *Oceangliders* to contribute to the development of DMQC data for ocean currents and particle dynamics from glider platforms. Also, I joined the GliderTools community, to work on integrating best practices on DMQC data into an open-source toolbox, to be shared by a wider community.

6.2. SPM dynamics monitoring in the GoL

SPM dynamics in coastal waters usually shows high-frequency dynamics. This work highlighted the mechanisms that enable the resuspension and transport of SPM and their spatiotemporal variability over the GoL shelf, according to different forcings (Rhone River plume

and marine storm). The data acquired during two experiments conducted respectively in 2016 and 2017 at the level of the ROFI area and in 2018 on the continental shelf of the GoL, were analyzed by combining them with other data from traditional platforms (moorings, ships, satellites) or numerical simulations.

6.2.1. Contribution of autonomous underwater glider-ADCP platform

Glider-ADCP observations were decisive to determine how (i) the properties of SPM were affected by the hydrological conditions in the ROFI area, and (ii) the particulate along- and cross-shelf transport were affected by the marine storm. High-resolution (i.e., approx. 1 profile/200 m and 1 section per 2 days) observations permitted to understand resuspension and transport with high accuracy. Observations can be summarized as follows:

- In the ROFI, analysis of optical spikes and acoustic backscatter indicates the presence of coarse particles on the proximal part of the mid-shelf close to the river mouth, where hydrological conditions likely favor the formation of macro flocs. These results are consistent with the observations of Many et al. (2016) from occasional one-off measurements with a LISST-holographic (Laser In Situ Scattering and Transmissometry particle analyzer).
- On the continental shelf, the remarkable spatiotemporal resolution of glider sampling has shown that during storm conditions, pycnocline erosion from complete mixing of the wind-driven surface layer and the bottom boundary layer increases the vertical mixing of resuspended sediment throughout the water column.
- The observations of near-bottom currents and sediment concentration profiles using both acoustic and optical sensors mounted on glider platforms show for the first time, to our knowledge, the role of surface wave forcing in the resuspension of sediment at depths >90 m over the shelf during a storm event.

- The continuous measurements of hydrodynamic properties from the glider-ADCP proved valuable validation of current vertical profiles of hydrodynamic models during a storm, while observations of this type of event are generally lacking in the coastal continuum due to their rarity.

This study highlighted the importance of utilizing novel ocean observation technology, such as active acoustic glider to describe sediment dynamics in the coastal zone over periods of several weeks to several months, essential for capturing flood and storm events. While these events were considered as episodic, they occurred over large areas and appeared as key processes in the regulation of sediment dynamics over the shelves, espcially for micro-tidal shelves like the GoL.

6.2.2. Towards a better characterization of SPM properties

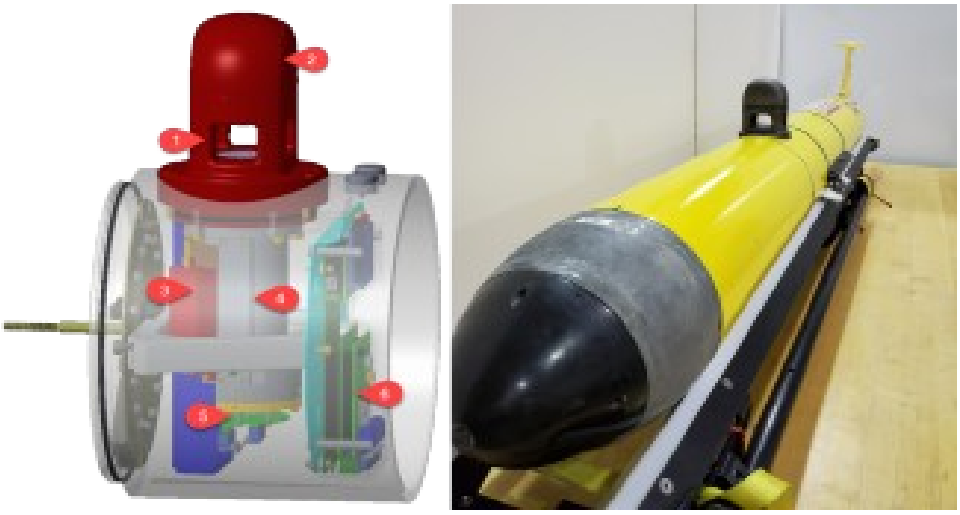

Figure 6.1: A schematic view of the LISST-glider (left) shows the sample volume (1). The beam collimation optics and reference detector are also contained in the optical head (2), connected to a fiber-coupled diode laser module (3). The scattered light is received through the lens tube (4). The primary ring detectors and transmission sensor (5) are mounted on an XY stage that is used to adjust the instrument alignment, which can then be locked into place. An electronics section (6) digitizes the analog signals from the scattering detectors, controls the sampling process, logs the full scattering dataset, and calculates beam attenuation particle size metrics (i.e., mean size and total concentration). A view of the LISST-glider integrated into a G2 Slocum glider (description and schema/photo from Miles et al., 2021).

The measurement of the concentration and size of SPM is a critical parameter to better understand the sedimentary dynamics, the fluxes of carbon, pollutants, and biological particles in coastal areas. This work highlighted the contribution of gliders equipped with acoustic and optical sensors in the differentiation of granulometric populations in the water column. However, current sensors give only partial information about the size (partitioning in “large” and “fine”) and concentration of SPM. This lack of knowledge on the properties of the material leads to uncertainties on quantitative resuspension and particle transfer budgets.

The recent integration of a LISST particle analyzer onto underwater gliders (Fig. 6.1) opens new perspectives on the understanding of the spatiotemporal variability of particulate material in the coastal zone (Miles et al., 2021, 2018). This system uses laser diffraction as a composition insensitive method for sizing ensembles of particles in a sample volume. The near forward scattering of light onto concentric detector rings paired (Fig. 6.1) with inversion algorithms can be used to estimate particle size distributions and volume concentration (Miles et al., 2021). A collaboration has been started in 2020 with Rutgers University through the METPAG (« MEsures de la Taille des PArticules à l’aide de Gliders ", particle size measurements using gliders) project, led by the CEFREM, to deploy a glider-LISST in the GoL. The objective of this project is (i) to document the role of flocculation on the SPM dynamics in the ROFI area, and (ii) to describe the spatiotemporal variability of the coast-water SPM transfer mechanisms. A glider-LISST deployment was carried out in February 2021 in the Rhone river ROFI area which is of particular interest in a source-to-sink approach in terms of sediment advection, settling, and deposition. As the strategy used in this thesis, an endurance deployment (>30 days) was performed. Figure 6.2 shows an example of preliminary results. Data from traditional sensors used on a glider (physical and bio-optical) show the presence of an intermediate nepheloid layer along the pycnocline (left panel in Fig. 6.2). This intermediate nepheloid seems to detach from the surface on the proximal part of the

shelf around 20 m depth (24 Feb 00:00) to feed the bottom nepheloid layer on the mid-shelf around 80 m depth (23 Feb 18:00). Throughout the intermediate nepheloid layer, particles of 50 to 350 µm are observed at concentrations between 1 and 8 µL L^{-1} (right panel in Fig. 6.2). These values are in agreement with observations made by Many et al. (2019) from an onboard LISST-holographic, showing that floc sizes are centered around 20–500 µm in the Rhone ROFI area. However, the data process still needs to be refined to take into account sensor drifts due to the potential impact of biofouling and Schlieren effects in highly stratified areas (as the surface plume). The combination of the different optical data and the water samples will allow us to better estimate the density of the

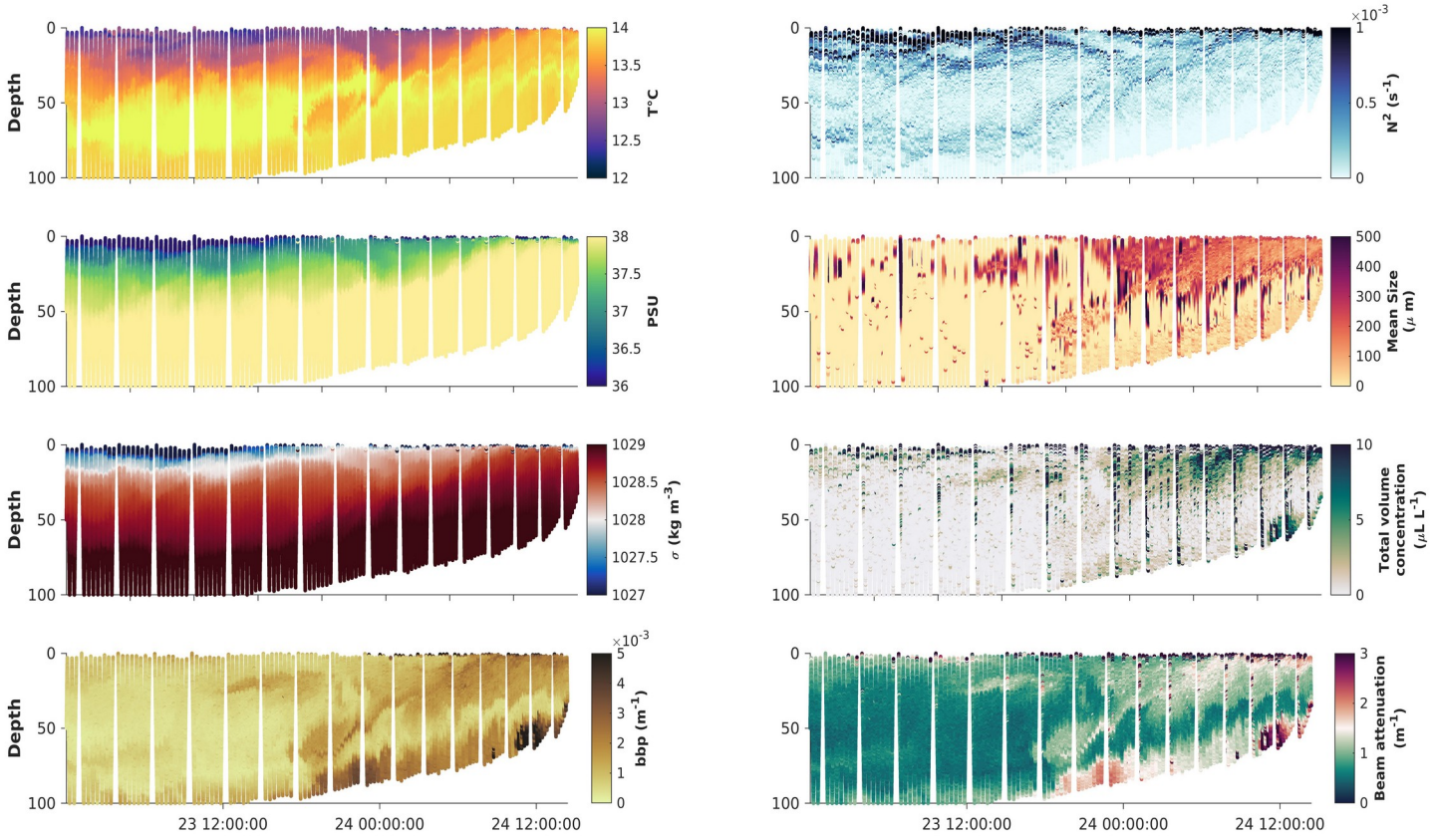

Figure 6.2: Glider cross-sections of temperature, salinity, potential density, optical backscatter (from top to bottom on the left panel), buoyancy frequencies, mean particle size, total volume concentration, and beam attenuation (from top to bottom on the right panel).

particles to better understand their fate. These preliminary results show that glider-LISST measurements combined with CTD and bio-optical measurements, providing an unprecedented view of suspended particle characteristics and hydrography from a single profiling sensor in the GoL. This should allow refining the knowledge on the properties of the particles in the bottom boundary layer, which is critical for the characterization of bottom roughness to assess resuspension events and transfer mechanisms during energetic processes (e.g., Chapter 5).

6.3. Future challenges of glider observations in the coastal zone monitoring

6.3.1. Towards a multi-platform approach

Gliders have shown their ability for monitoring SPM dynamics and properties over continental shelves, especially during flooding and storm conditions (Bourrin et al., 2015; Glenn et al., 2008; Many et al., 2018; Miles et al., 2021; 2015; 2013; Gentil et al., 2020; and submitted), where observations are typically sparse. As reported by Testor et al. (2019), gliders are nowadays a mature technology used by researchers around the world. They became the tool of choice for those who require continuous sampling of ocean properties over a range of user-controllable depths (Williams et al., 2008). However, glider integration in a multi-platform approach is crucial (i) to address the different spatiotemporal scales of coastal zone processes, and (ii) for the miniaturized onboard sensor validation.

This study showed that in a complex system, such as the Rhone river ROFI area, glider observations may fail to capture the large spatiotemporal variability of the river plume, which can shift by several kilometers in a few hours depending on wind and river flow conditions (e.g., Chapter 4). In this context, the glider needs to be combined with other observation platforms to provide a synoptic view of the water column (e.g., satellite observations to monitor surface

structures). On the other hand, researchers continue to add new sensors to these vehicles. For instance, in this study, we developed the glider-ADCP data chain processing. These sensors need to be calibrated and validated under real conditions, before being used to address scientific issues. Despite the use of a multi-platform approach, this study lacks external measurements to assess the robustness of the current and turbidity estimates from the embedded ADCP. To fill this gap we compared different methods to estimate absolute velocities using different methods (flight model, shear, inverse) to differentiate the speeds of the glider from those of the current. For future missions, the use of traditional platforms equipped with optical and acoustic sensors should provide the necessary data to validate the glider's onboard sensors.

6.3.2. Towards a sustainable observation

The endurance of observing systems is very challenging due to their costs, maintenance, control of data quality, or logistics. All play an important role in creating and maintaining a sustained observation system (Liblik et al., 2016). However, sustainable ocean observations are needed to build an operational system for SPM monitoring to help to predict the fate of the coastal zones.

In this context, UNESCO developed the Global Ocean Observing System (GOOS) over two decades ago to coordinate the national efforts in terms of sustained ocean observations around the world (Testor et al., 2019). In this framework, OceanGlider works on the integration of gliders as a component of integrated GOOS along the ocean observation value chain (Fig. 6.3). The purpose is to provide a framework for glider survey design to post-mission processing and services to increase the societal benefits (Testor et al., in prep). This global system has been adapted to local levels to be operational and adapted to societal requirements. Gliders are now integrated into several coastal

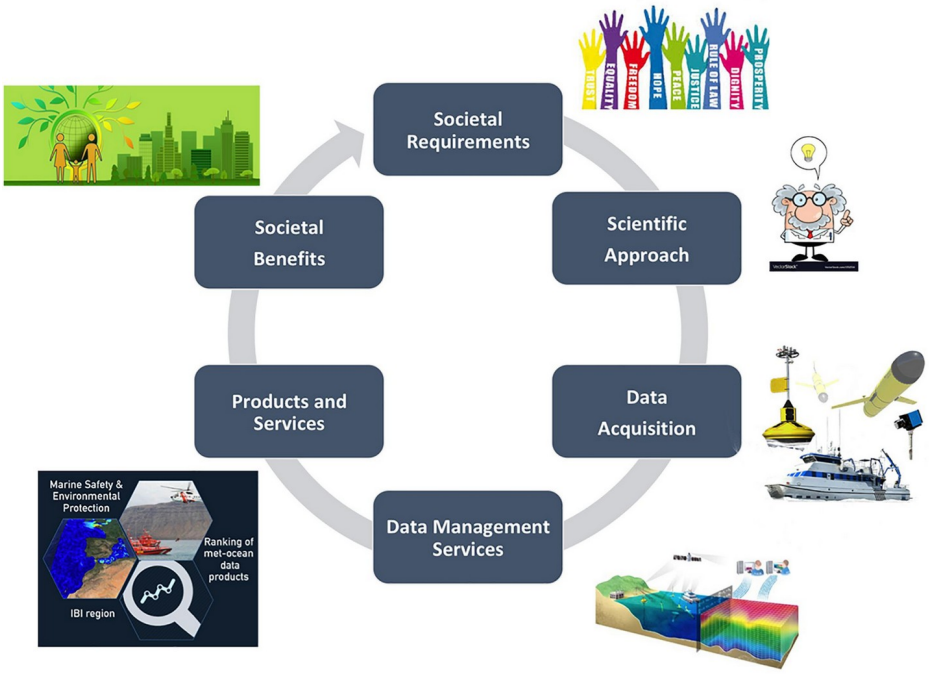

Figure 6.3: The ocean observing value chain, from Pearlman et al., (2019).

observing systems into the world, such as the United States Integrated Ocean Observing Systems (US IOOS; Willis, 2013) or the Coastal Observing SYstem for the Northern and Arctic seas (COSYNA; Stanev et al., 2011)**.** These operating systems provide a framework to support glider "endurance lines" which is essential for long-term monitoring. "Endurance lines" ensure multi-scale monitoring and are enabled to capture sub-seasonal to seasonal variability in highly complex systems such as the coastal zones, which are subject to continental and oceanic influences.

In the Western Mediterranean, glider "endurance lines" allow monitoring the long-term variability of hydrological, hydrodynamical, and biogeochemical processes in a "choke point" for the Ibiza channel (Heslop et al., 2012), and the open sea of the GoL through the MOOSE (Mediterranean Ocean Observing System for the Environment) program. These data have enabled considerable advances in the knowledge of deep-water formation and variability in the northwestern Mediterranean Basin, which is essential to understand the general circulation of the Mediterranean (Bosse et al., 2021; Heslop et al., 2012; Margirier et al., 2020). Despite the difficulties (marine traffic, fisheries activities with trawling, etc.), it is now crucial to integrate gliders as sustained

platforms in the coastal zone of the GoL to complete offshore measurements to study SPM dynamics in a source-to-sink approach (i.e., land-sea continuum). The launch of the S3 JERICO (Joint European Research Infrastructure for Coastal Observatories, https://www.jerico-ri.eu/) project in 2020 appears to be a fantastic opportunity. This project supports the implementation of a regionally structured observation system, and the GoL has been selected as a pilot site for this experimental phase. The framework provided by JERICO is essential for the integration of gliders as a sustainable observation platform in the GoL, as successfully operated in other world regions (e.g., US and Northern and Arctic Seas thanks to IOOS and COSYNA).

On a global scale, these systems are fundamental to achieving the goals of the Decade of Ocean Science for Sustainable Development, because they provide many of the physical and biochemical ocean data to reach a high level of understanding of marine ecosystems. To achieve this, we emphasize that the glider integration into local ocean observing systems is essential to support long-term observation with the final goal to prevent damage to coastal waters. Finally, the ability of underwater gliders to operate autonomously and transmit data via satellite communication in near-real-time, represents a real opportunity to continue researching in these times when oceanographers must stay at home due to the Covid-19 pandemia.

References

Agrawal, Y. C., Pottsmith, H.C., 2000. Instruments for particle size and settling velocity observations in sediment transport. Marine Geology 168, 89–114.

Bosse, A., Testor, P., Damien, P., Estournel, C., Marsaleix, P., Mortier, L., Prieur, L., Taillandier, V., 2021. Wind-Forced Submesoscale Symmetric Instability around Deep Convection in the Northwestern Mediterranean Sea. Fluids 6, 123.

Bourrin, F., Many, G., De Madron, X. D., Martín, J., Puig, P., Houpert, L., Testor, P., Kunesch, S., Mahiouz, K., Béguery, L., 2015. Glider monitoring of shelf suspended particle dynamics and transport during storm and flooding conditions. Continental Shelf Research 109, 135–149.

Firing, E., Gordon, R. L., 1990. Deep ocean acoustic Doppler current profiling. Presented at the Proceedings of the IEEE Fourth Working Conference on Current Measurement, IEEE, pp. 192–201.

Gentil, M., Many, G., Durrieu de Madron, X., Cauchy, P., Pairaud, I., Testor, P., Verney, R., Bourrin, F., 2020. Glider-Based Active Acoustic Monitoring of Currents and Turbidity in the Coastal Zone. Remote Sensing 12, 2875.

Gentil, M., Estournel, C., Durrieu de Madron, X., Many, G., Miles, T., Marsaleix, P., Berné, S., Bourrin, F., 2021. Sediment dynamics on the outer-shelf of the Gulf of Lions during an onshore storm: an approach based on acoustic glider and numerical modelling. Submitted to Continental Shelf Research.

Gregor, L., Ryan-Keogh, T.J., Nicholson, S.-A., Du Plessis, M., Giddy, I., Swart, S., 2019. GliderTools: A Python toolbox for processing underwater glider data. Frontiers in Marine Science 6, 738.

Heiderich, J., Todd, R. E., 2020. Along-stream evolution of Gulf Stream volume transport. Journal of Physical Oceanography 50, 2251–2270.

Heslop, E. E., Ruiz, S., Allen, J., López-Jurado, J. L., Renault, L., Tintoré, J., 2012. Autonomous underwater gliders monitoring variability at “choke points” in our ocean system: A case study in the Western Mediterranean Sea. Geophysical Research Letters 39.

Jakoboski, J., Todd, R.E., Owens, W.B., Karnauskas, K.B., Rudnick, D.L., 2020. Bifurcation and upwelling of the equatorial undercurrent west of the Galapagos archipelago. Journal of Physical Oceanography 50, 887–905.

Legler, D.M., Freeland, H.J., Lumpkin, R., Ball, G., McPhaden, M., North, S., Crowley, R., Goni, G., Send, U., Merrifield, M., 2015. The current status of the real-time in situ global ocean observing system for operational oceanography. Journal of Operational Oceanography 8, s189—s200.

Liblik, T., Karstensen, J., Testor, P., Alenius, P., Hayes, D., Ruiz, S., Heywood, K., Pouliquen, S., Mortier, L., Mauri, Ejm., 2016. Potential for an underwater glider component as part of the Global Ocean Observing System. Methods in Oceanography 17, 50–82.

Lohrmann, A., 2001. Monitoring sediment concentration with acoustic backscattering instruments. Nortek Technical Note 3, 1–5.

Many, G., 2016. Impacts of storm and flood events on suspended particulate matter dynamics in the Gulf of Lions. Contributions of gliders to a multi-platform approach.

Many, G., Bourrin, F., de Madron, X.D., Pairaud, I., Gangloff, A., Doxaran, D., Ody, A., Verney, R., Menniti, C., Le Berre, D., 2016. Particle assemblage characterization in the Rhone River ROFI. Journal of Marine Systems 157, 39–51.

Many, G., de Madron, X.D., Verney, R., Bourrin, F., Renosh, P., Jourdin, F., Gangloff, A., 2019. Geometry, fractal dimension and settling velocity of flocs during flooding conditions in the Rhône ROFI. Estuarine, Coastal and Shelf Science 219, 1–13.

Margirier, F., Testor, P., Heslop, E., Mallil, K., Bosse, A., Houpert, L., Mortier, L., Bouin, M.-N., Coppola, L., D'ortenzio, F., 2020. Abrupt warming and salinification of intermediate waters interplays with decline of deep convection in the Northwestern Mediterranean Sea. Scientific Reports 10, 1–11.

Merckelbach, L., Smeed, D., Griffiths, G., 2010. Vertical water velocities from underwater gliders. Journal of Atmospheric and Oceanic Technology 27, 547–563.

Miles, T., Seroka, G., Kohut, J., Schofield, O., Glenn, S., 2015. Glider observations and modeling of sediment transport in Hurricane Sandy. Journal of Geophysical Research: Oceans 120, 1771–1791.

Miles, T., Slade, W., Glenn, S., 2021. Sediment resuspension and transport from a glider integrated Laser In Situ Scattering and Transmissometry (LISST) particle analyzer. Journal of Atmospheric and Oceanic Technology.

Miles, T. N., Kohut, J., Slade, W., Gong, D., 2018. Suspended particle characteristics from a glider integrated LISST sensor. Presented at the OCEANS 2018 MTS/IEEE Charleston, IEEE, pp. 1–5.

Ody, A., Doxaran, D., Vanhellemont, Q., Nechad, B., Novoa, S., Many, G., Bourrin, F., Verney, R., Pairaud, I., Gentili, B., 2016. Potential of high spatial and temporal ocean color satellite data to study the dynamics of suspended particles in a micro-tidal river plume. Remote Sensing 8, 245.

Ouillon, S., 2018. Why and how do we study sediment transport? Focus on coastal zones and ongoing methods. Water 2018, 10(4), 390; https://doi.org/10.3390/w10040390.

Pearlman, J., Bushnell, M., Coppola, L., Karstensen, J., Buttigieg, P. L., Pearlman, F., Simpson, P., Barbier, M., Muller-Karger, F. E., Muñoz-Mas, C., 2019. Evolving and sustaining ocean best practices and

standards for the next decade. Frontiers in Marine Science 6, 277.

Peng, S., Zhu, Y., Li, Z., Li, Y., Xie, Q., Liu, S., Luo, Y., Tian, Y., Yu, J., 2019. improving the Real-time Marine forecasting of the northern South china Sea by Assimilation of Glider-observed T/S Profiles. Scientific reports 9, 1–9.

Schofield, O., Jones, C., Kohut, J., Kremer, U., Miles, T., Saba, G., Webb, D., Glenn, S., 2015. Developing coordinated communities of autonomous gliders for sampling coastal ecosystems. Marine Technology Society Journal 49, 9–16.

Schofield, O., Kohut, J., Aragon, D., Creed, L., Graver, J., Haldeman, C., Kerfoot, J., Roarty, H., Jones, C., Webb, D., 2007. Slocum gliders: Robust and ready. Journal of Field Robotics 24, 473–485.

Stanev, E., Schulz-Stellenfleth, J., Staneva, J., Grayek, S., Seemann, J., Petersen, W., 2011. Coastal observing and forecasting system for the German Bight—estimates of hydrophysical states. Ocean Science 7, 569–583.

Testor, P., de Young, B., Rudnick, D. L., Glenn, S., Hayes, D., Lee, C. M., Pattiaratchi, C., Hill, K., Heslop, E., Turpin, V., 2019. OceanGliders: a component of the integrated GOOS. Frontiers in Marine Science 6, 422.

Testor, P., Thomsen, S., Heslop, E., Palmer, M., in prep. Towards OceanGliders Best Practices. In prep for Frontiers in Marine Sciences.

Todd, R. E., Rudnick, D. L., Sherman, J. T., Owens, W. B., George, L., 2017. Absolute Velocity Estimates from Autonomous Underwater Gliders Equipped with Doppler Current Profilers. Journal of Atmospheric and Oceanic Technology 34, 309–333. https://doi.org/10.1175/JTECH-D-16-0156.1

Visbeck, M., 2002. Deep velocity profiling using lowered acoustic Doppler current profilers: Bottom track and inverse solutions. Journal of atmospheric and oceanic technology 19, 794–807.

Williams, C. D., Bachmayer, R., deYoung, B., 2008. Progress in predicting the performance of ocean gliders from at-sea measurements. Presented at the OCEANS 2008, IEEE, pp. 1–8.

Willis, Z., 2013. US Integrated Ocean Observing System (IOOS®) delivering benefits and the Global HF Radar and glider initiative. Presented at the 2013 MTS/IEEE OCEANS-Bergen, IEEE, pp. 1–5.

Annexes

Annex 1. Scientific activity

Peer- reviewed publications

in prep./ submit/ under review

Gentil, M., Miles, T., Blin, P., Durrieu de Madron, X., Many, G., Bourrin, F., Spatio-temporal variability of particle properties in the Rhone River ROFI from glider-LISST measurements. ***In prep*** *for Estuarine, Coastal and Shelf Science*.

Gentil, M., Estournel, C., Durrieu de Madron, X., Many, G., Miles, T., Marsaleix, P., Berné, S., Bourrin, F., Sediment dynamics on the outer-shelf of the Gulf of Lions during an onshore storm: an approach based on acoustic glider and numerical modelling. ***Submitted*** *to Continental Shelf Research.*

Taillandier, V., D'Ortenzio, F., Prieur, L., Conan, P., Coppola, L., Cornec, M., Dumas, F., Durrieu de Madron, X., Fach, B., Fourrier, M., **Gentil, M**., Hayes, D., Husrevoglu, S., Legoff, H., Le Ster, L., Orek, H., Ozer, T., Poulain, P. M., Pujo-Pay, M., Ribeira d'Alcalà, M., Salihoglu, B., Testor, P., Velaoras, D., Wagener, T., Wimart-Rousseau, C., Formation and spreading of the Levantine Intermediate Water during the winter of 2019. ***Under review*** *to J. Geophys. Res. Ocean.*

published

Gentil, M., Floc'h, F., Meunier, T., Ruiz-Angulo, A., Roudaut, G., Perrot, Y., Lebourges-Dhaussy, A. (2021), Internal solitary waves on the NW African shelf: A heuristic approach to localize diapycnal mixing hotspots. *Continental Shelf Research,* https://doi.org/10.1016/j.csr.2021.104492

Gentil, M.; Many, G.; Durrieu de Madron, X.; Cauchy, P.; Pairaud, I.; Testor, P.; Verney, R.; Bourrin, F. (2020), Glider-based Active Acoustic Monitoring of Currents and Turbidity in the Coastal Zone. *Remote Sens.* 2020, *12*, 2875. https://doi.org/10.3390/rs12182875

Professional meetings and abstracts

Gentil, M., Bourrin, F., Durrieu de Madron, X., Estournel, C., Glider observations of resuspension during storm conditions. European Geosciences Union, Vienna, Austria 2021 *(PICO presentation)*.

Gentil, M., Many, G., Bourrin, F., Cauchy, P., Durrieu de Madron, X., Coastal current estimates from glider mounted ADCP. Everyone's Gliding Observatories Meeting, Rutgers University, United-States 2019 *(Oral presentation)*.

Open-source tools

Glider-ADCP pre-stage toolbox: https://github.com/mgentil17/mgentil17

Research cruises

Februrary 2021: MELANGE, Gulf of Gascogne, R/V Thalassa (SHOM), 2 weeks.

March 2020: METPAG, Rhône River ROFI, R/V Téthys II (CEFREM), 1 week.

February 2020: METPAG, Rhône River ROFI, R/V Téthys II (CEFREM), 1 week.

February/March 2019: PERLE 2, Aegean Sea, R/V Pourquoi pas ? (LOMIC), 4 weeks.

Teaching experience

Teaching Aid: Physical Oceanography (30h)	2020
Teaching Aid: Mapping – GIS (10h)	2020
Teaching Aid: Geosciences (15h)	2019

Annex 2. Résumé (français)

Apport des planeurs sous marins au suivi des processus hydro-sédimentaires de la zone côtière

1 Introduction

1.1 La zone côtière et ses enjeux

Les océans côtiers, à l'interface entre les continents et les océans profonds, sont des zones complexes présentant des environnements bio-physiques et géomorphologiques divers, où la terre, l'océan et l'atmosphère interagissent fortement. Cette étude considère les océans côtiers comme les eaux du plateau situées entre la surface et 200 m de profondeur, soit du littoral jusqu'à la pente de la marge continentale.

Ces petites régions (~7% de l'océan global, soit 26×10^6 km^2) jouent un rôle essentiel dans la séquestration des éléments chimiques (carbone), le bilan sédimentaire des marges continentales, ainsi que la structure des habitats benthiques. Elles sont le réceptacle des matières organiques, inorganiques, naturelles et anthropiques d'origine terrestre (comme les sédiments, les nutriments dissous et particulaires). Bien que relativement petites, elles représentent 10 à 30% de la productivité primaire globale des océans, 80% de l'enfouissement de la matière organique, et 90% des prises de pêche mondiales. De plus, environ 35% de la population mondiale vit à moins de 100 km du littoral et ce pourcentage devrait atteindre 75% au cours des prochaines décennies.

Une gestion intégrée et une exploitation durable des ressources des océans côtiers reposent sur une connaissance détaillée du fonctionnement de ces écosystèmes et des principaux facteurs affectant leur variabilité et état de santé. L'observation des zones côtières et de leur lien avec les phénomènes météorologiques, climatiques et biogéochimiques est nécessaire pour prévoir les évolutions futures et diminuer les pressions sur ces écosystèmes. Cependant, notre connaissance de la dynamique des océans côtiers reste partielle. En effet, les processus océaniques fonctionnent sur

des échelles temporelles allant d'une fraction de seconde à plusieurs décennies et spatiales allant du millimètre à des milliers de kilomètres (Fig. 1). L'imbrication des échelles spatiales et temporelles des processus côtiers rend l'échantillonnage particulièrement difficile. Dans cette thèse, nous nous concentrons sur les processus hydro-sédimentaires, notamment ceux liés à la dynamique des matières en suspension (MES) sur les marges continentales.

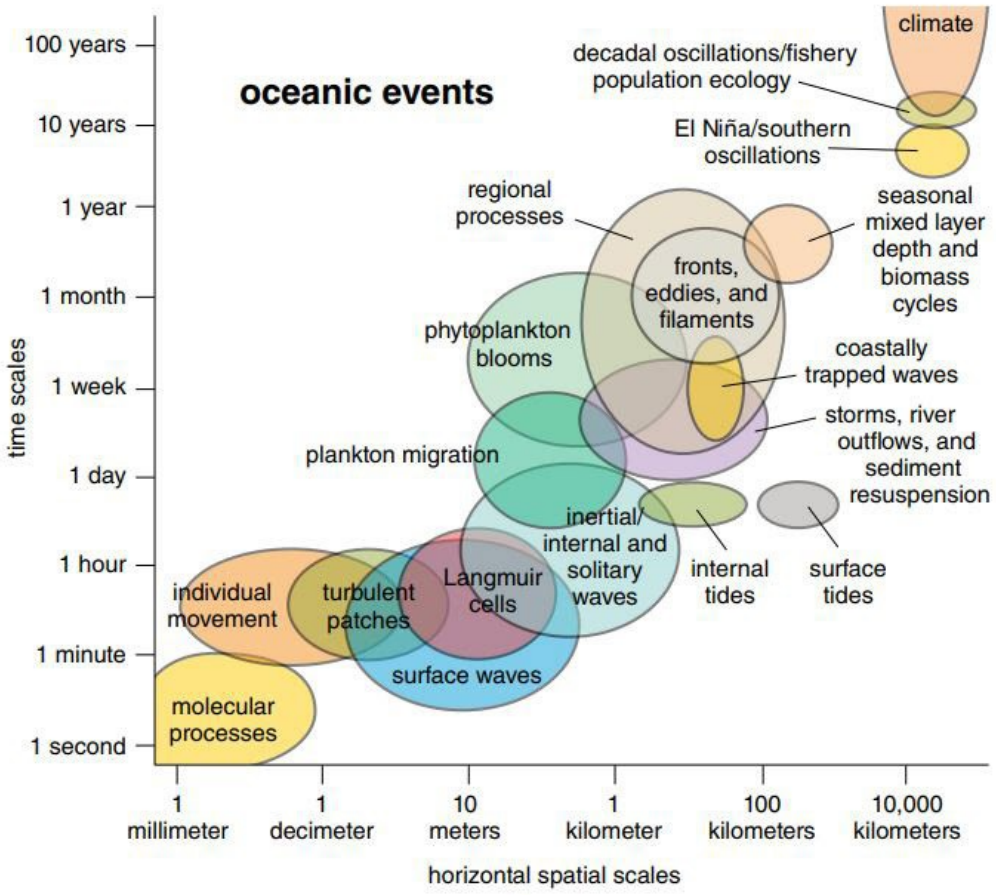

Figure 1: Les processus océaniques se déroulent à différentes échelles temporelles et spatiales, et ces événements ont souvent une incidence les uns sur les autres.

1.2 L'observation de la dynamique hydro-sédimentaire

L'étude de la dynamique des MES dans les zones côtières est d'une importance majeure pour comprendre la qualité de l'eau, les flux de carbone et la dynamique des écosystèmes. Le suivi des MES implique : (i) l'estimation des flux sédimentaires entre ou au sein des compartiments de la zone côtière et (ii) l'analyse de leur variabilité spatio-temporelle. Comme les processus présentés en Figure 1, les processus hydro-sédimentaires présentent des échelles spatio-temporelles disparates.

De nombreux programmes d'observation au cours des dernières décennies ont utilisé des bouées côtières et des mouillages, équipés de capteurs optiques et acoustiques, pour comprendre la remise en suspension et le transport des sédiments sur les plateaux continentaux. Ces observations fournissent des informations précises sur la variabilité temporelle de la colonne d'eau en un point fixe, mais ne sont pas en mesure de décrire les gradients spatiaux sur l'ensemble du plateau afin d'évaluer le transport global des particules en suspension. L'utilisation de navires de recherche et des mesures satellite ont permis d'aborder la composante spatiale à l'échelle de la zone côtière. Cependant, les navires de recherche sont sensibles aux conditions météorologiques et les observations par satellites fournissent un instantané de la distribution des MES limités à la couche de surface et aux jours sans nuages. Ces caractéristiques instrumentales ne permettent pas d'échantillonner les événements extrêmes tels que les tempêtes et les inondations, qui sont pourtant les principaux moteurs de la dynamique sédimentaire dans la zone côtière, en particulier sur les plateaux micro-tidaux. Pour combler ces lacunes et comprendre la dynamique sédimentaire à l'échelle régionale, des modèles hydrodynamiques tridimensionnels ont été utilisés. Cependant, avec le développement de ces études régionales, de nouvelles technologies sont nécessaires pour compléter les mesures ponctuelles sur la remise en suspension et le transport des sédiments obtenues à l'aide de bouées et mouillages. L'amélioration de notre capacité à comprendre, simuler et prévoir la dynamique sédimentaire dans la zone côtière nécessite d'améliorer la résolution, l'étendue et la durée des mesures océanographiques. Les récents développements technologiques ont conduit à l'apparition de nouvelles plateformes d'observations robotisées. Ces plateformes autonomes, telles que les planeurs sous-marins ou "gliders", semblent être particulièrement prometteuses pour l'échantillonnage de la zone côtière à différentes échelles spatio-temporelles.

1.3 L'émergence des gliders

Les gliders sont des véhicules sous-marins autonomes de faible puissance et de longue durée (>30 jours) qui peuvent transporter une gamme de capteurs interchangeables et échantillonner la colonne d'eau sur de grandes échelles spatiales (>100 km). Les gliders n'ont pas d'hélices et sont

principalement entraînés par de petits changements de flottabilité qui leur permettent de "planer" vers l'avant dans la colonne d'eau lors de la descente, jusqu'à 2 m au-dessus du fond, et de remonter à 0-1 m de la surface, décrivant une trajectoire en dents de scie.

Ces plateformes sont devenues de plus en plus importantes pour la collecte de mesures océanographiques dans les programmes d'observation au cours de la dernière décennie. La capacité du glider à fonctionner de manière autonome dans toutes les conditions météorologiques, pour des missions pouvant durer plusieurs mois avec un échantillonnage haute-fréquence, a permis de compléter les mesures acquises à l'aide de bouées, mouillages et navires de recherche (Fig. 2). Dans ce contexte, de nombreux capteurs développés pour les plateformes traditionnelles (bouée, mouillage, navire de recherche) ont été miniaturisés et intégrés sur les gliders. Une nouvelle génération d'instruments de mesure est récemment devenue disponible pour les gliders, avec (i) des capteurs optiques, permettant de caractériser les propriétés des MES, (ii) des profileurs de courant à effet Doppler (ADCP) permettant de mesurer les courants et la turbidité, et (iii) des capteurs à diffraction laser (LISST) permettant une mesure directe de la taille et de la concentration des particules. Ces développements technologiques ouvrent de nouvelles perspectives dans la compréhension des processus hydro-sédimentaires dans la zone côtière avec un accroissement considérable des mesures dans la colonne d'eau. Cependant, les gliders n'ont pas encore atteint le même niveau de maturité que les plateformes de surveillance océanographique plus traditionnelles. Cela implique qu'un nouveau venu dans l'analyse des données de glider est exposé à de nombreux problèmes et à des tâches fastidieuses qui ne sont pas courantes lors du traitement des données provenant de plateformes classiques. Aujourd'hui, il existe un besoin d'exploiter et de gérer les flux de données en temps réel et différé, provenant de ces nouveaux capteurs complexes.

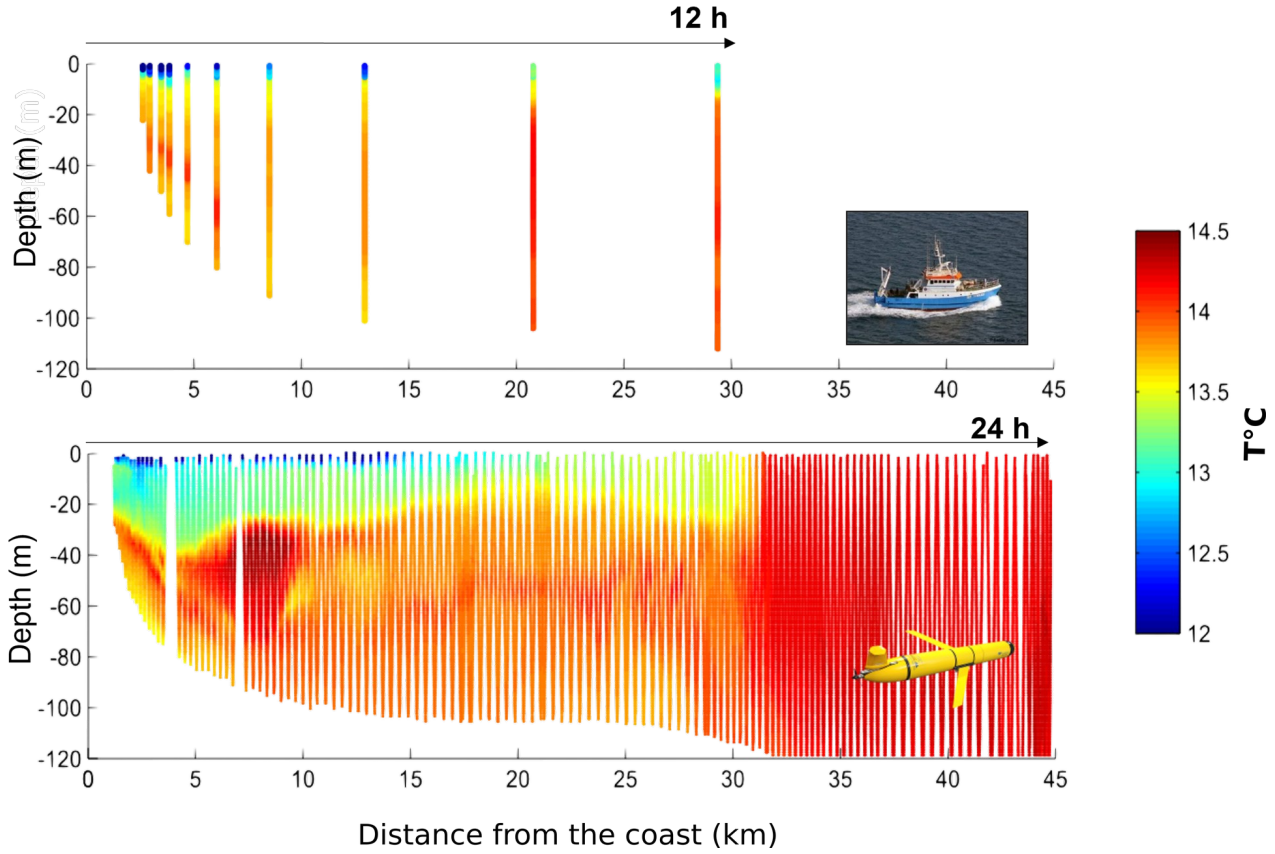

Figure .2: Comparaison de la résolution des observations obtenue à l'aide (i) d'un navire de recherche (en haut) et (ii) d'un glider (en bas) sur une journée. Coupe transversale des conditions de température sur une radiale à l'embouchure du fleuve Rhône.

L'objectif principal de ce doctorat – réalisé au Centre de Formation et de Recherche sur les Environnements Méditerranéens" (CEFREM – UMR 5110 CNRS/UPVD) à l'Université de Perpignan – est de développer la chaîne de traitement et d'explorer la capacité d'un glider, nouvellement équipé d'un profileur acoustique de courant à effet Doppler, pour le suivi des processus hydro-sédimentaires dans la zone côtière, en particulier lors d'événements extrêmes. Il fait suite aux travaux menés dans le cadre des projets CASCADE (CAscading, Storm, Convection, Advection, and Downwelling Events) et TUCPA (Coastal Turbidity and Autonomous Platforms) dans lesquels des gliders équipés de capteurs physiques et bio-optiques ont été déployés dans la zone côtière du Golfe du Lion (GoL) pour décrire les propriétés des MES sur le plateau continental.

Les questions clé, développées dans le cadre de cette thèse pour le suivi de la dynamique des MES (section 1.2), peuvent être résumées comme suivant :

(i) Le glider-ADCP est-il un outil adapté à la mesure des courants, de la turbidité et des flux de MES dans la zone côtière ?

(ii) Le glider-ADCP permet-il de capturer la variabilité spatio-temporelle de la dynamique des MES dans différents compartiments de la zone côtière comme:

- la région sous influence d'eau douce ?

- le plateau continental ?

Cette thèse est organisée autour de 6 chapitres. Le premier présente le contexte de ce travail et est suivi des paramètres régionaux de la zone d'étude. Ces chapitres sont construits autour des précédentes observations réalisées au sein des marges continentales au niveau mondial et du plateau du GoL. Deux articles et une "boîte à outils" composent les chapitres suivants de cette thèse (chapitre 3, 4 et 5). Le chapitre 3 présente la chaîne de traitement permettant d'analyser simultanément les données hydrologiques et hydrodynamiques de glider. Le chapitre 4 détaille : (i) les structures hydrologiques et hydrodynamiques à fine échelle de la région sous influence du panache du Rhône, (ii) l'apport des mesures acoustiques et optiques pour différentier les populations granulométriques (fines vs. agrégats) des particules en suspension, et enfin (iii) la complémentarité du glider avec les données satellites de couleur de l'eau. Le chapitre 5 montre la variabilité spatio-temporelle des courants et de la dynamique sédimentaire induits par une tempête d'est sur le plateau continental du GoL. Enfin, les conclusions générales et les perspectives de cette étude sont abordées dans le Chapitre 6.

2 Principaux résultats

2.1 La "boîte à outils" du glider-ADCP

En l'absence d'une chaîne de traitement disponible, j'ai dû développer au début de mon travail de thèse une "boîte à outils" afin d'analyser et d'interpréter les données de courant et de rétrodiffusion acoustique du glider-ADCP pour des questions hydro-sédimentaires. Dans cette étude, l'accent est mis sur le capteur acoustique actif du glider pour dériver les vitesses absolues et

leur composante barocline (hydrodynamique), ainsi que l'indice de rétrodiffusion (proxy de la concentration en particules) dans la colonne d'eau. Ce chapitre, combiné à une annotation claire du code, fournit un cadre pour traiter les données des gliders acoustiques. Le code source libre de cette “boite à outils” a été mis à disposition de la communauté sur la plateforme GitHub (https://github.com/mgentil17/mgentil17), sans qu'il soit nécessaire de s'inscrire ou de se connecter.

La “boîte à outils” glider-ADCP est composée d'un ensemble de scripts et de fonctions MATLAB conçus pour traiter les données recueillies par un planeur Slocum du constructeur Teledyne Webb Research. Actuellement, la version développée est conçue pour fournir un contrôle qualité des données en mode différé sur les capteurs physiques, bio-optiques et acoustiques intégrés sur le modèle Slocum G1.

La figure 3 présente le flux de travail de la “boîte à outils” glider-ADCP, qui est divisé en 8 étapes. Le traitement des données est organisé autour de deux scripts principaux (rectangles aux contours rouges). Le premier, “Glider_Adcp_main_program.m”, est résumé par la chaîne de traitement (étape 0 à 7) et appelle toutes les fonctions utilisées dans la “boîte à outils”. Pour chaque étape de traitement, les données externes et internes (cases circulaires), les fonctions des modules (rectangles gris) et leurs dépendances (flèches), ainsi que les sorties (figures et fichiers) sont explicitées. La “boîte à outils” est construite pour produire 5 niveaux (L0 à L4) de fichiers MATLAB (.mat), liés aux différents niveaux des étapes de traitement, décrites dans la figure 3. Le second script, “Glider_ADCP_define_param.m”, déclare les paramètres choisis par l'utilisateur pour chaque étape de traitement et est chargé dans “Glider_Adcp_main_program.m” lors de l'étape initiale (étape 0). L'étape de paramétrage est essentielle pour assurer le traitement correct des données dans les étapes 1 à 6.

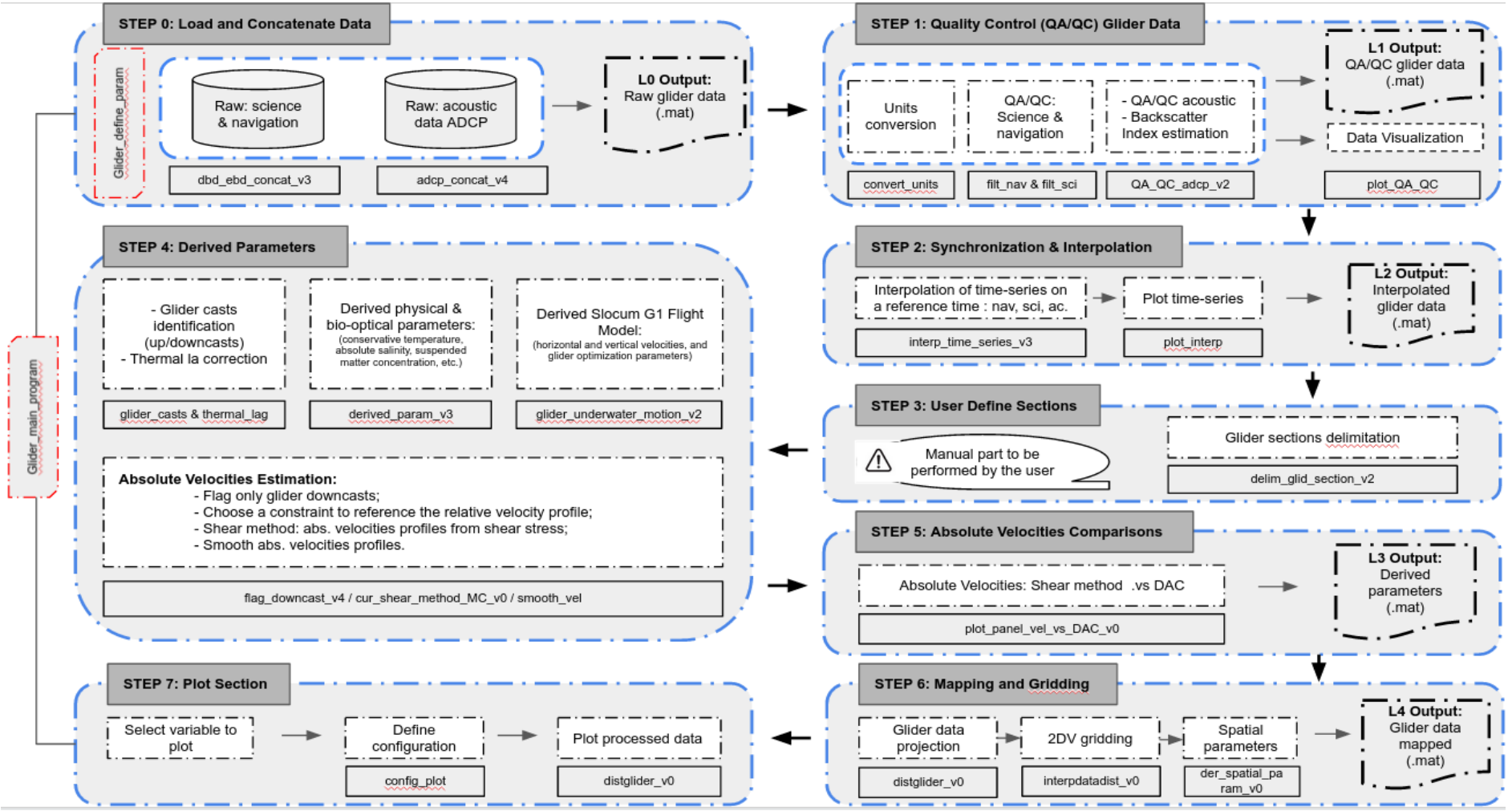

Figure .3: Schéma de la chaîne de traitement Glider-ADCP étape par étape (de l'étape initiale "0" à l'étape finale "7"). Les rectangles blancs représentent l'action de traitement effectuée dans chacun des modules. Les rectangles gris représentent les codes (.m) associés aux actions. Les flèches noir et gris montrent les dépendances entre les différents modules et les différentes actions, respectivement. Cinq niveaux de sorties (L0 à L4) sont produits par la chaîne de traitement. Enfin, les rectangles aux contours rouges sont les deux scripts principaux de la “boîte à outils”.

2.2 Le suivi des courants et de la turbidité au sein de la région sous influence d'eau douce du Rhône

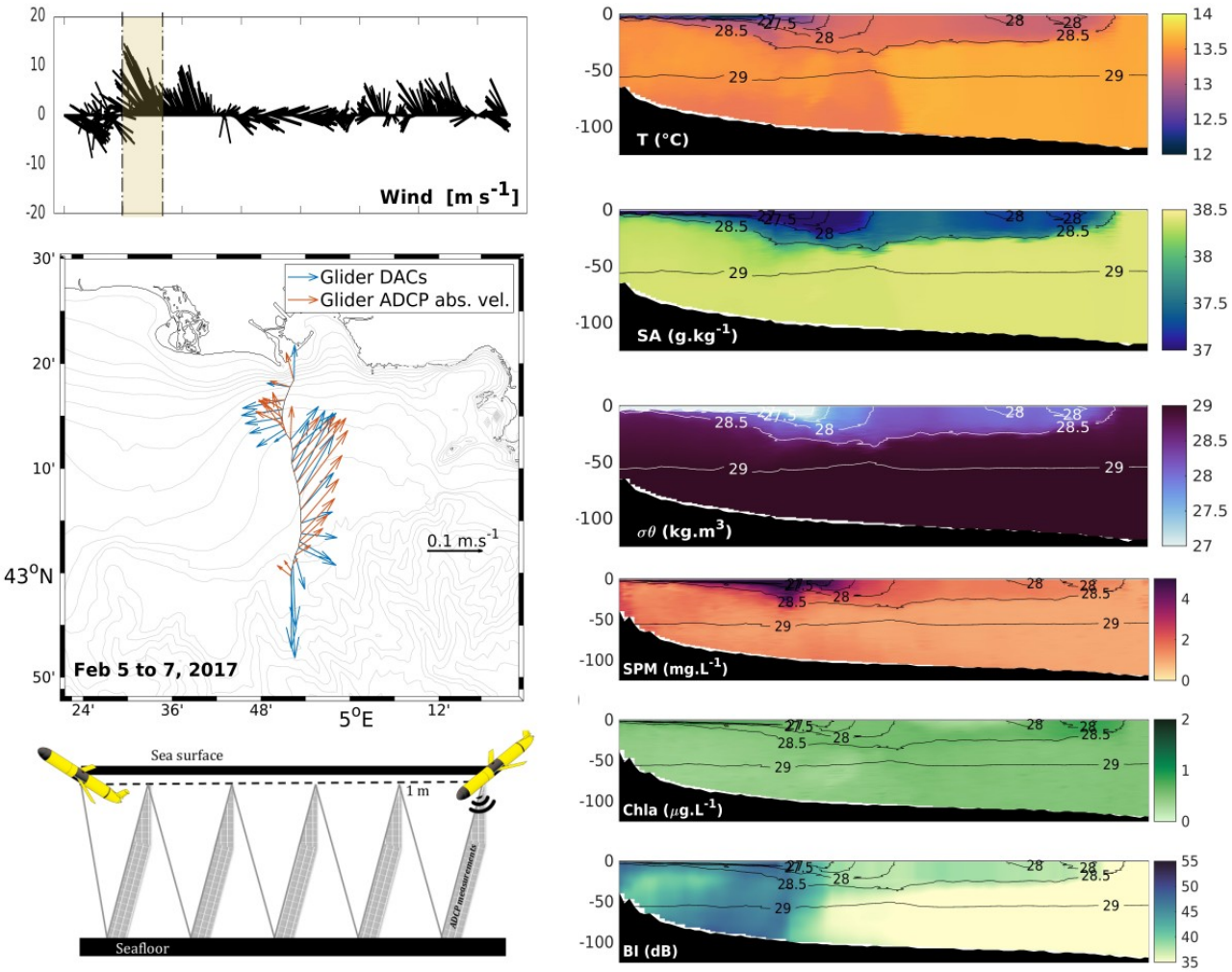

Figure 4: Panels de gauche (de haut en bas) : intensité et direction du vent, estimation des vitesses absolues moyennées sur la profondeur, et fonctionnement de la mesure ADCP à partir d'un glider. Panels de droite (de haut en bas) : température, salinité absolue, anomalie de densité, concentration en MES, concentration en chlorophyll-a et rétrodiffusion acoustique.

Dans cette étude, nous avons déployé avec succès un glider équipé d'une CTD (conductivité, température, profondeur), d'une charge utile optique et d'un ADCP à réseau phasé de 600 KHz pour suivre les courants et la turbidité dans la région sous influence d'eau douce du Rhône pendant deux périodes contrastées (automne et hiver). La capacité du glider-ADCP à : (i) estimer les courants à partir d'une fréquence d'échantillonnage réduite permettant un déploiement d'endurance, (ii) estimer les tailles de particules (fines vs. larges) à partir des mesures acoustiques et optiques, et (iii) estimer les flux de MES à l'échelle du plateau continental, est évaluée. Enfin, la

complémentarité entre les mesures glider-ADCP et satellite pour suivre le panache du Rhône est discutée. Les principaux résultats et conclusions de cette étude sont les suivants :

- En accord avec les études précédentes, notre comparaison des courants, estimés à partir des données ADCP et du courant intégré sur la profondeur, confirme que cette plateforme est adaptée à la mesure des courants dans la zone côtière (panel central à gauche sur la Fig. 4), avec une incertitude de l'ordre de 0,13 m s^{-1}. Les radiales répétées de planeurs à travers le plateau montrent l'importance de l'apport d'eau douce du Rhône comme l'un des principaux forçages de l'hydrodynamique locale.

- La méthode de cisaillement a été utilisée pour estimer les courants absolus. Nous avons appliqué la contrainte de la mesure directe de la vitesse sur le fond ("bottom track") aux vitesses relatives proches du fond. Malheureusement, cette contrainte présente une incertitude assez élevée en raison de la faible fréquence d'échantillonnage de l'ADCP utilisée lors de ce déploiement.

- Les mesures coïncidentes de rétrodiffusion optique et acoustique montrent une complémentarité dans la différenciation des populations granulométriques (fines vs. agrégats) des particules en suspension dans la colonne d'eau. L'analyse des pics optique et de la rétrodiffusion acoustique indique la présence d'agrégats sur la partie proximale du plateau près de l'embouchure de la rivière, où les conditions hydrologiques favorisent probablement leur formation (panels de droite sur la Fig. 4).

- Les flux de MES calculés pour les deux saisons sont très variables, tout comme leurs incertitudes (20-600%). Cependant, cette étude montre que les flux de MES sur le plateau sont d'un ordre de grandeur inférieur à ceux calculés à proximité du Rhône, suggérant un dépôt significatif de particules à l'embouchure du fleuve.

- La combinaison des mesures de MES par satellite et par glider est importante pour surveiller les parties superficielles et souterraines du panache fluvial. En effet, dans un

système complexe comme l'embouchure du Rhône, les observations des gliders peuvent ne pas rendre compte de la grande variabilité spatio-temporelle du panache fluvial, qui peut se déplacer de plusieurs kilomètres en quelques heures en fonction des conditions de vent et de débit du fleuve.

- La stratégie d'échantillonnage utilisée dans cette étude montre que le suivi des courants et de la turbidité dans la zone côtière sur des périodes allant de plusieurs semaines à plusieurs mois est réalisable. Cette stratégie d'observation est adaptée à la capture d'événements sporadiques difficiles à suivre tels que les tempêtes et les inondations. Ces observations sont essentielles pour améliorer les connaissances existantes sur la circulation côtière et le transport sédimentaire, ainsi que pour valider les modèles régionaux hydro-sédimentaires.

2.3 L'impact d'une tempête dans la remise en suspension et le transport des MES sur le plateau du Golfe du Lion

Dans cette étude, le rôle d'une tempête sur la dynamique des MES et le transport particulaire est investigué. Un glider équipé d'une CTD, d'une charge utile optique et d'un ADCP a été déployé durant plus d'un mois dans la partie centrale du GoL, afin de déterminer la variabilité haute-fréquence de l'hydrologie, l'hydrodynamisme ainsi que les flux et propriétés des MES. Ce déploiement d'endurance a permis de capter un événement de tempête sur le plateau du 1er au 2 mars 2018. Ces observations ont été combinées à des simulations numériques afin d'évaluer le transport des sédiments à l'échelle régionale du GoL. Les observations et simulations réalisées peuvent être résumées comme suit :

- L'arrivée d'une tempête au large (période de retour de 5 ans) associée à une forte houle sur le plateau continental a conduit à la dé-stratification de la colonne d'eau jusqu'à des profondeurs supérieures à 90 m. Les observations hautes-résolutions (i.e. un profil tous les 200 m) du glider ont permis de montrer que l'érosion de la pycnocline, due au mélange de la couche de surface poussée par le vent et de la couche limite de fond, augmente le mélange vertical des sédiments remis en suspension dans toute la colonne d'eau. La concentration en

MES reste élevée dans toute la colonne d'eau sur une durée de plus de 40 heures après la fin de la tempête.

- Les observations des profils de courants et de concentration des sédiments acquises à proximité du fond, à l'aide des capteurs acoustiques et optiques montés sur le glider, montrent pour la première fois à notre connaissance, le rôle des vagues de surface dans la remise en suspension des sédiments à des profondeurs >90 mètres sur le plateau continental. La contrainte de fond induite par les vagues serait le principal forçage à l'origine de la resuspension des sédiments sur le plateau externe du GoL durant cette tempête quinquennale (Fig. 5).

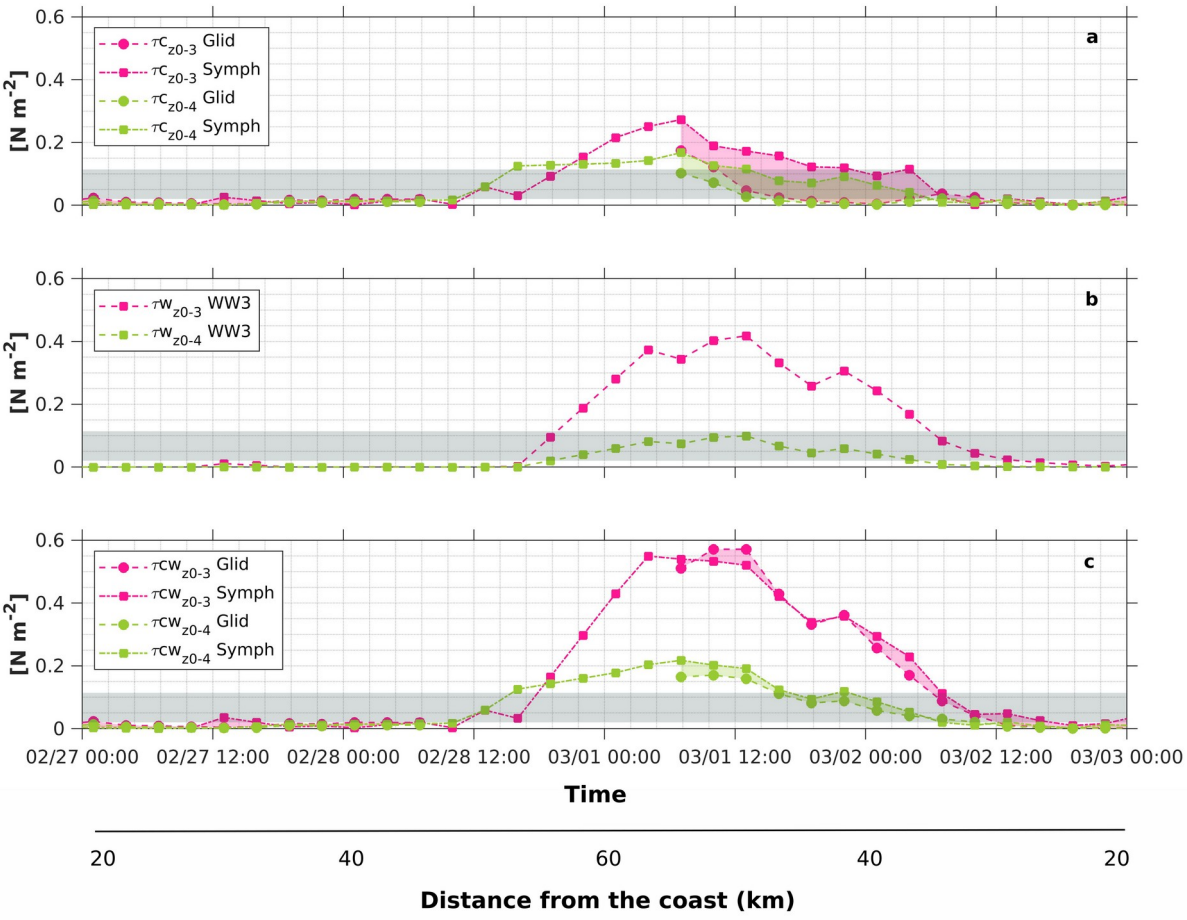

Figure 5: Comparaison de la contrainte de cisaillement de fond dérivée du glider (cercle) et des modèles SYMPHONIE/Wavewatch 3 (carré) pour : (a) les courants, (b) les vagues, et (c) les interactions vagues-courants. Ces contraintes sont calculées le long de la trajectoire du glider, avec deux valeurs de la rugosité de fond, 10^{-4} m (vert) et 10^{-3} m (rose). La contrainte de cisaillement critique typique de la remise en suspension pour les sables vaseux du GoL est indiquée par la bande grise. Notez que le glider ne produit aucune observation au début de la tempête entre le 28 février 15h et le 01 mars 17h.

- Les mesures continues des propriétés hydrodynamiques enregistrées par le glider-ADCP ont permis de valider de manière précieuse les profils verticaux de courants du modèle hydrodynamique pendant une tempête marine, alors que les observations sur ce type d'événement font généralement défaut dans le continuum côtier en raison de leur rareté.

- La combinaison des observations et des simulations numériques montre que la tempête de 2 jours associée à des courants de ~0,4 m s^{-1}, produit un déplacement des MES d'environ 68 km vers le sud-ouest (Fig. 6). Ces résultats suggèrent un transfert de sédiments le long des isobathes par sauts successifs associés à des tempêtes marines, de la zone d'entrée principale (le fleuve Rhône) à la zone de sortie (le Cap de Creus) du plateau du Golfe du Lion.

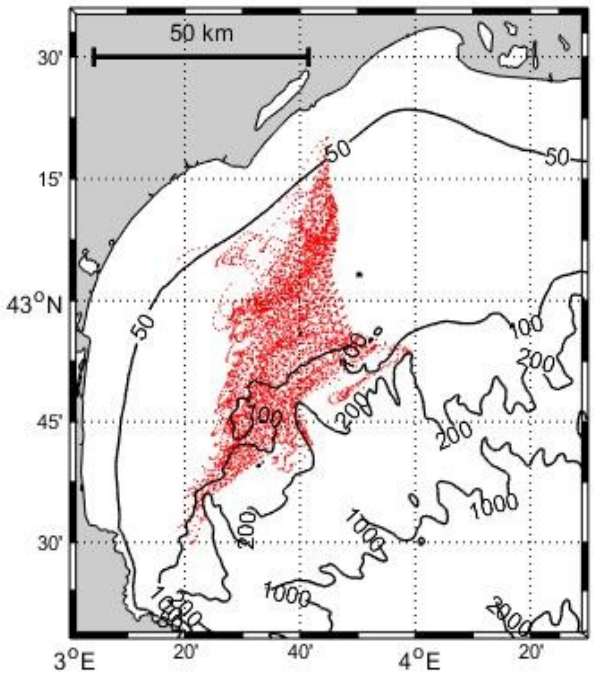

Figure 6: Transport des vases remises en suspension (tout point combinés) le long des isobathes sur plateau continental du GoL à partir de la section du glider pendant la tempête de 2 jours (du 28 février 16:00 au 2 mars 10:00)..

3 Synthèse des observations et perspectives

Le suivi de la dynamique des MES implique : (i) l'estimation des flux sédimentaires entre ou au sein des compartiments de la zone côtière et (ii) l'analyse de leur variabilité spatio-temporelle. Dans cette synthèse, nous discutons de la capacité du glider à mesurer les courants, la

turbidité et les flux (section 3.1), et à représenter leur variabilité spatio-temporelle dans la zone côtière (section 3.2).

3.1 Le glider-ADCP

L'acquisition de données sur les courants, les concentrations et les flux de MES sont fondamentaux pour comprendre la dynamique des écosystèmes marins et leur devenir. Les résultats de cette thèse ont montré la capacité des gliders-ADCP à mesurer les courants, la turbidité et les flux de MES à haute résolution spatio-temporelle dans la zone côtière. L'estimation de ces paramètres est essentielle pour la validation des modèles hydro-sédimentaires. La "boîte à outils" développée dans le cadre de cette thèse a été utilisée dans le traitement des données de deux articles scientifiques (Chapitres 4 et 5). Cependant, cette chaîne de traitement est instrument-dépendante et ne peut actuellement traiter que les données en mode différé provenant d'un profileur de courant RDI (ADCP) monté sur un glider Slocum. Son utilisation à plus grande échelle dans la communauté scientifique nécessiterait : (i) qu'elle soit accessible sur un logiciel libre (comme Python) et (ii) qu'elle soit capable de traiter toutes les combinaisons glider-ADCP.

À notre connaissance, il n'existe pas de système permettant de suivre en temps réel la dynamique des MES à partir d'un glider équipé de capteurs optiques et acoustiques. Or, les données en temps réel fournissent des informations sur la surface et l'intérieur de l'océan, pouvant être utilisées dans divers systèmes et services opérationnels, dans le but de prévenir les dommages à court et long terme des zones côtières (pollutions, érosion). Dans ce contexte, un nouveau projet soutenu par le CEFREM et l'Université de Perpignan en partenariat avec des entreprises (ALSEAMAR et CENTRALWEB) vise à produire un outil capable de mesurer et de transmettre en temps réel les mesures de courant, turbidité et in fine les flux de matières aux diverses échelles spatiales (du mètre à la centaine de kilomètres) et temporelles (de la seconde à plusieurs mois) de la zone côtière. Les protocoles de nettoyage et de traitement des données acoustiques pour estimer la turbidité (indice de rétrodiffusion) et les courants en temps réel, ont bénéficié des résultats de cette thèse. Cet outil pourra à terme aussi bien permettre la surveillance de la qualité des eaux côtière

dans le cadre de la Directive Cadre sur l'Eau et de la Directive Cadre Stratégie sur le Milieu Marin pour les parcs marins par exemple, que la surveillance du courant et de la visibilité sous-marine pour les applications militaires.

Cette étude a montré que l'intégration de nouveaux capteurs tels que l'ADCP implique qu'un nouveau venu dans l'analyse des données de glider est exposé à plusieurs problèmes et tâches chronophages qui ne sont pas courants lors du traitement des données provenant de plateformes plus traditionnelles. Pour éviter ce problème, la communauté scientifique utilisant des gliders s'est regroupée au sein du programme Oceangliders (https://www.oceangliders.org/) afin de fournir des données en temps réel et en mode différé inter-opérables et inter-comparables dans les bases de données mondiales. Un document de synthèse destiné à établir les "bonnes pratiques" en matière de traitement des données est en train d'être rédigé pour soumission à Frontiers in Marine Sciences. Tout au long de mon doctorat, j'ai développé des compétences dans le traitement des données gliders pour des questions hydro-sédimentaires. Dans ce contexte, j'ai rejoint l'effort communautaire initié par Oceangliders pour contribuer au développement des "bonnes pratiques" sur le traitement des mesures de courants et de concentration en particules à partir de gliders. J'ai également rejoint la communauté GliderTools, pour travailler sur le développement d'une "boîte à outils" en libre accès, qui sera partagée par une communauté plus large.

3.2 Le suivi de la dynamique des MES dans le GoL

Ce travail de thèse a mis en évidence les mécanismes permettant la remise en suspension et le transport des MES ainsi que leur variabilité spatio-temporelle sur le plateau continental du GoL en fonction de différents forçages (panache du Rhône, tempête marine). La méthodologie utilisée se base sur une analyse combinée de données provenant de plateformes traditionnelles (mouillages, navires de recherche, satellites), de simulations numériques et de données acquises *in-situ* à partir des gliders, au travers d'expériences conduites au niveau du panache rhodanien (campagnes de 2016 et 2017) et sur le plateau continental du Golfe du Lion (2018).

La première expérience a permis de détailler (i) les structures hydrologiques et hydrodynamiques à fine échelle de la région sous influence du panache du Rhône, (ii) l'apport des mesures acoustiques et optiques pour différentier les populations granulométriques (fines vs. agrégats) des particules en suspension, et enfin (iii) la complémentarité avec les données satellites de couleur de l'eau.

La seconde expérience a permis d'observer la variabilité spatio-temporelle des courants et de la dynamique sédimentaire induits par une tempête d'est sur le plateau continental. Couplée à la modélisation numérique, elle a mis en évidence le rôle des vagues sur la resuspension au niveau du plateau externe, et permis de caractériser les trajectoires et l'étendue du transport particulaire durant cet événement particulièrement énergétique.

Ces résultats soulignent l'importance de l'utilisation de nouvelles technologies d'observation de l'océan, telles que les gliders équipés de capteurs optiques et acoustiques, afin d'étendre la mesure de la remise en suspension et du transport des sédiments en zone côtière. Cependant, des observations durables sont nécessaires pour construire un système opérationnel de suivi de la dynamique des MES afin de prévoir le devenir des zones côtières. En Méditerranée occidentale, les " lignes d'endurance " de gliders permettent de suivre la variabilité à long terme des processus hydrologiques, hydrodynamiques et biogéochimiques dans la partie hauturière du GoL, grâce au programme MOOSE (Mediterranean Ocean Observing System for the Environment). Ces données ont conduit à des avancées considérables dans la connaissance de la formation et de la variabilité des eaux profondes dans le nord-ouest du bassin méditerranéen, essentiel dans la compréhension de la circulation générale de Méditerranée. Malgré les difficultés (trafic maritime, chalutage, etc.), il est maintenant crucial d'intégrer le glider comme plateforme d'observation durable de la zone côtière du GoL, afin de décrire la dynamique des MES dans une approche source-puits (i.e. dans le continuum terre-mer) et compléter les mesures hauturières acquises. Le lancement du projet S3 JERICO (Joint European Research Infrastructure for Coastal Observatories, https://www.jerico-ri.eu/) en 2020, soutient la mise en œuvre d'un système d'observation structuré

au niveau régional, et le GoL a été sélectionné comme site pilote pour cette phase expérimentale. Le cadre fourni par JERICO est essentiel pour l'intégration des gliders comme plateforme d'observation durable dans le GoL, comme cela a été fait avec succès dans d'autres régions du monde (par exemple aux Etats-Unis et dans les mers du Nord et de l'Arctique grâce aux projets IOOS et COSYNA).

4 Conclusion

Cette thèse souligne l'importance des gliders équipés de capteurs optiques et acoustiques pour le suivi des courants et de la turbidité dans la zone côtière sur des périodes de plusieurs semaines à plusieurs mois, essentiels pour capter des événements épisodiques de crues et tempêtes, principaux moteurs de la dynamique sédimentaire sur les marges continentales. À l'échelle mondiale, ces plateformes sont fondamentales pour atteindre les objectifs de la Décennie des sciences océaniques pour le développement durable, car elles fournissent une grande quantité de données physiques et biogéochimiques nécessaire au suivi des écosystèmes marins. Pour y parvenir, nous soulignons que l'intégration des gliders dans les systèmes locaux d'observation de l'océan est essentielle pour soutenir l'observation à long terme. Enfin, la capacité des gliders à fonctionner de manière autonome et à transmettre des données par communication satellite en temps quasi-réel, représente une réelle opportunité de poursuivre la recherche en ces temps où les océanographes doivent rester à la maison en raison de la pandémie de Covid-19.

Abstract (Français)

La dynamique de la matière en suspension joue un rôle majeur dans la qualité de l'eau, les flux de carbone et la dynamique des écosystèmes de l'océan côtier. Cependant, l'imbrication des échelles spatiales (du mètre à la centaine de kilomètres) et temporelles (de la seconde à plusieurs mois) des processus côtiers rend l'étude de la dynamique hydro-sédimentaire délicate, notamment lors d'événements extrêmes, comme les tempêtes et les crues. L'amélioration de notre capacité à comprendre, simuler et prévoir la dynamique des sédiments dans la zone côtière nécessite d'améliorer la résolution, l'étendue et la durée des mesures océanographiques. Dans ce contexte, l'apport des planeurs sous-marins autonomes est examiné, leur conception permettant d'observer sur des périodes longues et à fine échelle l'hydrologie et l'hydrodynamique d'une partie ou de l'ensemble du plateau continental.

L'objectif de cette thèse est d'élaborer une chaîne de traitement et d'explorer la capacité d'un planeur nouvellement équipé d'un profileur de courant acoustique à effet Doppler pour l'étude des processus hydro-sédimentaires, en particulier lors d'événements extrêmes. La méthodologie utilisée se base sur une analyse combinée de données provenant de plateformes traditionnelles (mouillages, navires, satellites), de simulations numériques et de données acquises in situ à partir des planeurs, au travers d'expériences conduites au niveau du panache rhodanien (campagnes de 2016 et 2017) et sur le plateau continental du Golfe du Lion (2018).

La thèse détaille le développement et la validation d'une chaîne de traitement permettant d'analyser simultanément les données hydrologiques et hydrodynamiques de planeurs sous-marins. Le code source libre de cette « boîte à outils » a été mis à disposition de la communauté sur la plateforme GitHub.

La première expérience a permis de détailler (i) les structures hydrologiques et hydrodynamiques à fine échelle de la région sous influence du panache du Rhône, (ii) l'apport des mesures acoustiques et optiques pour différentier les populations granulométriques (fines vs. agrégats) des particules en suspension, et enfin (iii) la complémentarité avec les données satellites de couleur de l'eau.

La seconde expérience a permis d'observer la variabilité spatio-temporelle des courants et de la dynamique sédimentaire induits par une tempête d'est sur le plateau continental. Couplée à la modélisation numérique, elle a mis en évidence le rôle des vagues sur la resuspension au niveau du plateau externe, et permis de caractériser les trajectoires et l'étendue du transport particulaire durant cet événement énergétique.

Ces résultats démontrent clairement l'intérêt des planeurs équipés de capteurs optiques et acoustiques pour le suivi des courants et de la turbidité dans la zone côtière sur des périodes de plusieurs semaines à plusieurs mois, essentiels pour capter des événements épisodiques de crues et tempêtes, principaux moteurs de la dynamique sédimentaire.

Mots-clés : Planeur-acoustique, optique, dynamique sédimentaire, événement extrême, Golfe du Lion, Méditerranée

Abstract (English)

The dynamics of suspended particulate matter play a major role in water quality, carbon fluxes and ecosystem dynamics in the coastal ocean. However, the interlocking spatial (from meters to hundreds of kilometers) and temporal (from seconds to months) scales of coastal processes make the study of hydro-sedimentary dynamics challenging, especially during extreme events such as storms and floods. Improving our ability to understand, simulate and predict sediment dynamics in the coastal zone requires improving the resolution, extent and duration of oceanographic measurements. In this context, the contribution of autonomous underwater gliders, which allow the observation of fine-scale hydrology and hydrodynamics over part or all of the continental shelf, and over long periods of time, is investigated.

The objective of this thesis is to develop the processing chain and to explore the capability of a glider newly equipped with an acoustic Doppler current profiler to study hydro-sedimentary processes, particularly during extreme events. The methodology used is based on a combined analysis of data from traditional platforms (moorings, ships, satellites), numerical simulations and data acquired in situ from gliders, through experiments conducted in the Rhone plume (2016 and 2017 campaigns) and on the continental shelf of the Gulf of Lion (2018).

The thesis details the development and validation of a processing chain allowing the simultaneous analysis of hydrological and hydrodynamic data from underwater gliders. This open-source code of this “toolbox” was made available to the community on the GitHub platform.

The first experiment detailed (i) the fine-scale hydrological and hydrodynamic structures of the region under the influence of the Rhone plume, (ii) the contribution of acoustic and optical measurements to differentiate the granulometric populations (fine vs. aggregates) of suspended particles, and (iii) the complementarity with satellite ocean colour data.

The second experiment observed the spatiotemporal variability of currents and sediment dynamics induced by a strong easterly storm on the continental shelf. Coupled with numerical modeling, it highlighted the role of waves on resuspension on the outer shelf and made it possible to characterize the trajectories and extent of particle transport during this energetic event.

The results clearly demonstrate the interest of gliders equipped with optical and acoustic sensors for monitoring currents and turbidity in the coastal zone over periods of several weeks to several months, essential for capturing episodic flood and storm events, the main drivers of sediment dynamics.

Keywords : Acoustic-Glider, optics, sediment dynamics, extreme events, Gulf of Lions, Mediterranean